FIBER OPTIC SPECTROSCOPY FOR THE OPTIMIZATION OF PHOTODYNAMIC THERAPY

Floor van Leeuwen – van Zaane

ISBN: 978-90-5335-814-6

Layout: Floor van Leeuwen – van Zaane

Cover illustration: © Dr. Daniela Malide, National Institute of Health, Bethesda, MD, USA for 2011 Olympus BioScapes Digital Imaging Competition®
Confocal micrograph of NIH-3T3 cells co-transduced with 5 fluorescent proteins.

Cover design: Ridderprint BV.
Printed by Ridderprint BV.

FIBER OPTIC SPECTROSCOPY FOR THE OPTIMIZATION OF PHOTODYNAMIC THERAPY

Fiber-optische spectroscopie voor het optimaliseren
van fotodynamische therapie

PROEFSCHRIFT

ter verkrijging van de graad van doctor aan de
Erasmus Universiteit Rotterdam
op gezag van de
rector magnificus

Prof.dr. H.A.P. Pols

en volgens besluit van het College voor Promoties.
De openbare verdediging zal plaatsvinden op

woensdag 9 april 2014 om 15:30 uur

door

FLOOR VAN LEEUWEN – VAN ZAANE

geboren te Zaanstad

ERASMUS UNIVERSITEIT ROTTERDAM

Promotiecommissie:

Promotor:	Prof.dr. H.J.C.M. Sterenborg
Overige leden:	Prof.dr. T.E.C. Nijsten Prof.dr. R.J. Baatenburg de Jong Prof.dr. C.W.G.M. Löwik
Copromotor:	Dr. D.J. Robinson

The work in this thesis was conducted at the Center for Optical Diagnostics and Therapy, Department of Radiation Oncology, Postgraduate school Molecular Medicine Erasmus University Medical Center Rotterdam.

The publication of this thesis was further financially supported by: Erasmus MC; Ocean Optics; Rada-pharma International BV; Quantib BV; 'De Hippert' Zaandam BV; Fagron BV.

CONTENTS

chapter 1

General Introduction

Floor van Leeuwen – van Zaane

GENERAL INTRODUCTION

Photodynamic therapy (PDT) is a treatment modality for cancer and premalignant lesions that utilizes a photoactive drug, the photosensitizer, in combination with light. PDT has become the treatment of choice for various malignancies. Furthermore, PDT is under investigation as a potential (palliative) treatment in situations where the possibilities of chemo- and radiotherapy are limited or exhausted. Since both photosensitizer and light have to be present to cause tissue damage, selective damage to the lesion can be achieved by controlling the presence of either one of them to the treatment area. Selective damage can be reached by i) choosing a photosensitizer that is mainly present in the lesion, or ii) preventing normal tissue from being illuminated. However, the success of PDT in reducing/removing (pre-)malignant lesions has been variable. Treatment efficacy can range form non-observable effects to severe damage to normal tissue. Considering the complexity of both the execution of the treatment and damage pathways involved in PDT, some variability in treatment efficacy is not unexpected. However, given the fact that clinical applications of PDT that have proved successful remain small in number, more work is necessary to optimize therapeutic efficacy.

The idea of using sunlight for treatment of certain (skin) abnormalities goes as far back as ancient Egypt and has returned repeatedly over the intervening centuries. Photosensitizing agents and their potential use in treatment were first recognized at the end of the 19th century, when Raab and Von Tappeiner discovered haematoporphyrins in the urine of people suffering from skin photosensitivity [1, 2]. Treatments using a combination of light and a photoactive agent started to be introduced into the clinic from 1975 using haematoporphyrin derivative (HpD) as photosensitizer [3]. With interest piqued, researchers started investigating the mechanisms underlying the seemingly toxic combination of light and photosensitizer. It is shown that the presence of a photosensitizer molecule mediates the transfer of energy from light (photons) to oxygen, thereby creating reactive oxygen species that cause tissue damage [4]. To date, PDT has been clinically used to treat various malignant and non-malignant conditions, ranging from superficial skin lesions [5] to prostate cancer [6], bile duct cancer [7], age-related macular degeneration [8] and the palliative treatment of solid head & neck tumors [9].

FOCUS OF THIS THESIS

This thesis will focus on the use of quantitative fiber optic spectroscopy and optical imaging for the optimization of PDT. PDT has been under investigation both preclinically and in the clinic for several decades, with varying degrees of success. A more complete

understanding of the range of parameters that influence the outcome of PDT will potentially contribute to optimization and control of PDT treatment protocols. This may result in an improved success rate and an increase in the adoption of PDT in existing and new clinical fields.

Recent developments in fiber optic spectroscopy in both the white-light reflectance and fluorescence domains have paved the way for more precise measurements of both treatment inputs and local tissue responses during and after treatment. Local fiber optic observations are combined with optical imaging data to provide a multimodality analysis of the effect of various treatment parameters on local PDT effects observed during and directly after treatment. This thesis focuses on the application of quantitative fiber optic spectroscopy and optical imaging techniques to provide insight into various PDT-related processes, which contribute to the optimization of therapy and can be divided into the following sections:

- The investigation of the relationship between vascular responses during light fractionated ALA-PDT and treatment efficacy using optical imaging and spectroscopy.

- The development of quantitative fiber optic fluorescence spectroscopy and its application in measuring in-vivo photosensitizer pharmacokinetics.

- A comparison of the pharmacokinetics and spectral properties of chlorin e_6 and Bremachlorin based on in-vivo measurements and their relationship to PDT efficacy.

Ultimately, the goal is to use results from these and further investigations to optimize treatment protocols for PDT in order to maximize treatment efficacy. The aim of the remaining introductory text is to provide the background information necessary to understand the underlying principles of the work covered in this thesis.

PRINCIPLES OF PHOTODYNAMIC THERAPY

The mechanism of action of photodynamic therapy is based on the interaction of visible light, photosensitizer and oxygen. Light contains a certain amount of energy in the form of photons. At the intensities and wavelengths utilized in PDT, light is not energetic enough

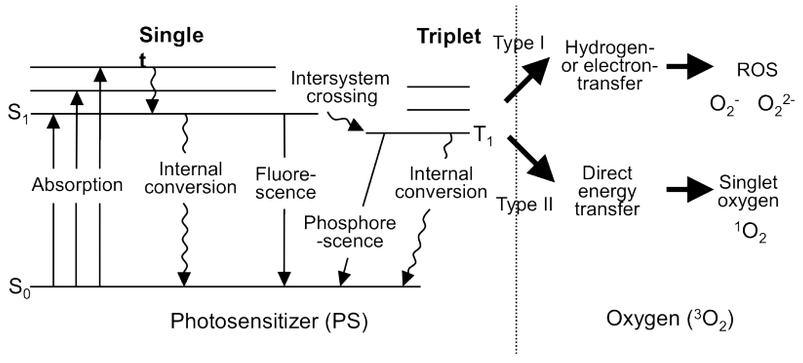

Figure 1.1: *Jablonksi diagram for photosensitizer and oxygen exited states. (Image: Nishiyama et al., Advanced Drug Delivery Reviews, 2009.* ***61****(4))*

to directly damage cells and tissues. Oxygen is present in all cells of the human body, where it plays a major role in the body's process of energy generation. Only when both oxygen and light are in the presence of a photosensitizer, reactive oxygen species are generated and damage is inflicted. An overview of the pathways by which photosensitizers mediate the transfer of energy from photons to oxygen is shown in figure 1.1. Absorption of the treatment light is followed by the transfer of a photosensitizer molecule from the ground state into an excited state (S_1, S_2 etc).

These excited singlet states are highly unstable and therefore very short lived and the molecule will loose the excess of energy, which will happen via one of the following routes: i) internal conversion whereby no photons are emitted, ii) the molecule will fall back to its ground state whereby the excess of energy is emitted as fluorescent light, or iii) the photosensitizer molecule is transformed into its (excited) triplet state (T_1) by intersystem crossing. This energetic state is relatively more stable and has therefore a longer life time. This means that it has a higher probability of interacting with other molecules in the local environment and exchange energy upon collision. When the photosensitizer triplet state molecule directly collides with molecular oxygen (type II reactions), highly reactive singlet oxygen radicals ($^1O_2$) are formed. Another reaction pathway is the direct transfer of energy from photosensitizer triplet state molecules that leads to the production of radicals. These radicals interact with oxygen to form reactive oxygen species (type I reactions) [4]. Reactive oxygen species are known to have harmful effects on cells and cell structures, including damage to lipid membranes and oxidation of amino acids in proteins [10]. Which of these pathways occurs is dependent on factors such as type of photosensitizer, oxygen concentration and molecular environment and may even change during therapy.

PHOTOSENSITIZERS

The first clinical PDT treatments were introduced in 1976 by Dougherty using Hematoporphyrin derivative (HpD) [3]. Over the next three decades, several first generation photosensitizers based on HpD were developed. HpD was improved by purifying the active fraction of oligomers in the mixture, resulting in Photofrin® -the first commercial clinical photosensitizer- that achieved FDA approval for treatment of precancerous lesions and palliative treatment of cancers in the esophagus and tumors in the bronchii [11, 12]. A major drawback of first generation photosensitizers was significant skin photosensitivity, which could last for several weeks and mandates the patient to stay in the (relative) dark.

Several second generation photosensitisers were subsequently introduced: Benzoporphyrin derivative monoacid ring A (BPD-MA, Visudyne®) is a successful photosensitizer with FDA approval for the treatment of abnormal vessels in various eye disorders such as age related macular degeneration [8]. Another second generation photosensitizer is m-tetrahydroxyphenylchlorin (mTHPC or Foscan®), which is approved by the FDA and in Europe for the palliative treatment of head & neck cancers [9]. After systemic administration, high concentrations of mTHPC can be found in plasma, but due to its lipophilicity, photosensitizer localization in (malignant) tissue remains days after injection, providing some tissue selectivity. Drawback is again the prolonged (skin) sensitivity of the patient, which can lead up to 15 days after injection, and the lack of selectivity between tumor and normal tissue.

Chlorins belong to a category of photosensitizers that are investigated in **chapters 5 to 7** of this thesis. Chlorins are reduced porphyrins and belong to the second generation of photosensitizers [13]. In general, these second generation photosensitizers show increased photo activity and an enhanced light absorption in the red region compared with first generation photosensitizers, which allows for a deeper penetration of light and consequently a larger effective treatment volume. Chlorin e_6 (ce6) is a member of this family and has been studied intensively for over two decades [13-15]. Ce6 has some advantageous properties as a clinical photosensitizer; it has low toxicity in the dark, is excreted and/or metabolized from the body within two days and seems to have a higher affinity for cellular internalization in environments with a lower pH such as those found within some tumors. A disadvantage of ce6 is its relatively low lipophilicity, meaning that it has a preference for water-containing environments, such as blood. Therefore, ce6 preferentially remains in the vasculature and does not accumulate significantly in tissue. Cellular membranes or cell structures where reactive oxygen species can cause severe damage, often consist of fat-like structures, for which ce6 lacks a preference. Several compounds have been designed to overcome this and increase cellular uptake of the

photosensitizer. Examples are ce6-PVP, where ce6 is conjugated to a polyvinylpyrrolidone carrier, and the ce6-derivative NPe_6 (mono-L-aspartylchlorin-e_6), which have both been used successfully in phase I clinical trials [16-18].

A new photosensitizing compound, Bremachlorin, consists of a mixture of ce6 (~80%), combined with the photosensitizing agents purpurin 5 (~15%) and chlorin p_6 (~5%), which are both by-products of ce6 synthesis [19, 20]. The main photoactive component of Bremachlorin is thought to be purpurin 5, partly because its rapid interaction with lipo-proteins that enables it to be delivered into tumor cells [21]. Purpurin 5 is too hydrophobic to be administered intravenously, but combined with ce6 and cp6 is achieves the chemical stability required for intravascular administration. It has been suggested that the overall photosensitizing effect of Bremachlorin is larger than its individual components. Part of this thesis is the comparison between ce6 and Bremachlorin.

Another photosensitizer that is the focus of research in this thesis is Protoporphyrin IX (PpIX). Contrary to the aforementioned photosensitizers, PpIX is an endogenous molecule which can be activated by light. PpIX is an intermediate product formed during haem synthesis in mitochondria [22]. Under normal physiological conditions, the amount of PpIX and other intermediates is tightly regulated by various feedback mechanisms, and the concentration present in tissue is too low to be used for therapy. The administration of exogenous 5-aminolevulinic acid (ALA) bypasses the feedback mechanism controlling the concentration of intermediates, and the step transforming PpIX into haem becomes the slowest step in the process [22]. This leads to the accumulation of PpIX to concentrations high enough to allow for photodynamic therapy. PpIX can accumulate in any tissue containing cells with an intact haem synthesis pathway. High PpIX accumulation is observed in tissues like epidermis, gastrointestinal mucosa and various other organs. Muscle, connective tissue and cartilage show low PpIX fluorescence. The increased metabolic activity of tumor cells compared with normal tissue results in (some) selective uptake in tumor tissue. ALA can be applied both systemically and topically [23], the later being regularly clinically used in the treatment of (pre-)malignant skin lesions, where ALA penetrates through the stratum corneum into the epidermis [24]. Research has been done on how deep and into which particular cell types the ALA still generates an excess of PpIX. Of particular interest are endothelial cells, cells forming the vessel wall. Damage to these cells will directly damage vasculature, which is an important damage pathway of PDT [25, 26].

MECHANISMS UNDERLYING PDT INDUCED DAMAGE

Three major damage pathways are identified by which PDT results in destruction of the target tissue through cellular and vascular responses. PDT is also known to activate the immune system and induce immunological responses [27]. Immunological responses to PDT constitute an ongoing research topic, which lies beyond the scope of this thesis. Cellular responses are caused by direct damage to cellular components caused by reactive oxygen species. Cell death can occur in different ways, of which apoptosis and necrosis are the most well known [28]. The way in which a cell dies depends on the cellular structures where the photosensitizer is localized at the time of treatment, the severity of the damage and light fluence rate. High fluence rates tend to induce necrosis, while low fluence rates are associated with apoptotic cell death [29]. Apoptosis is a type of programmed cell death that involves a chain of biochemical events such as cell shrinking and nuclear and DNA fragmentation. This process usually results in removal of the cell without evoking inflammatory responses [30]. Apoptosis can be induced by many pathways, such as excretion of specific hormones or growth factors. Intracellular stress and mitochondrial damage are also known to lead to apoptosis [28]. Since PpIX is localized in mitochondria, apoptosis is thought to be the most important damage mechanism of PpIX PDT [31]. Necrosis is cell death that usually occurs from acute tissue injury. It involves cell swelling, disruption of membranes and cell lysis. Rupture of the plasma membrane may release the necrotic cell content, which can be harmful to neighboring cells, provoking an inflammatory response [32]. Many lipophilic photosensitizers, like ce6, are localized in these lipid membranes, where PDT leads to membrane disruption, resulting in necrotic cell death [28].

Vascular responses during and after PDT include constriction or dilatation, and leakage of fluid from vessels into the tissue [33]. By directly damaging endothelial cells, thrombocytes adhere to vessel walls, leading to the release of vasoactive components that induce (temporary) constriction of (mainly) arterioles [34]. Severe damage to endothelial cells can result in vascular leakage. Neovasculature, which is the main type of vasculature in tumors, is usually more sensitive to this process than normal vessels. When vasculature is constricted, this disrupts the distribution of oxygen and other nutrients to the target tissue, causing indirect tumor damage due to hypoxia and starvation of nutrients. It is suggested that this extra indirect damage is necessary in addition to cellular damage to achieve complete tumor destruction [35]. Treating neovasculature in age related macular generation with BPD-MA, which localizes in the vessel endothelium, is based on this effect [8]. However, vascular shutdown during early stages of illumination decreases the transport of oxygen to the target volume, which limits the production of singlet oxygen and therefore reduces the effect of the local cellular and inflammatory

response. Treatment efficacy is therefore dependent on a fine balance between the positive and negative effects of vascular damage. Vascular responses during ALA-PDT are the subject of **chapter 3.**

PDT DOSIMETRY

The phototoxic effect of PDT is based on the interaction of light, oxygen and photosensitizer and a positive treatment outcome is dependent on the presence of all three components. It is therefore important to gain as much information on these key components as possible before, during and after therapy. Measuring these parameters is one of the main focuses of this thesis. The process of monitoring and, if needed, adapting (one of) the treatment parameters is called dosimetry. Figure 1.2 shows a schematic overview of the light-oxygen-photosensitizer interaction and the by-products of this process, which are individually all candidates for dosimetric monitoring.

The most direct way to monitor treatment outcome is by measuring the quantity of singlet oxygen formed by luminescence [36]. Although this is theoretically possible and topic of extensive preclinical research [37, 38], it is not presently feasible for clinical use. Another possibility is to measure the three key components in the measurement volume. This is termed explicit dosimetry [39, 40]. However, these components are often dependent on each other and can change dynamically during treatment.

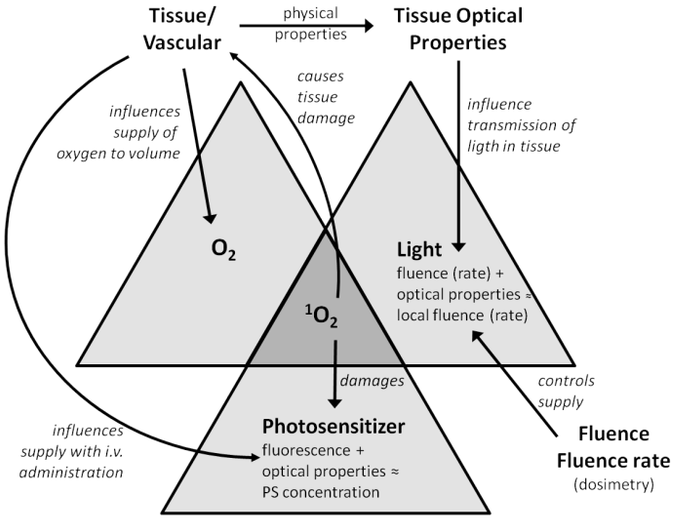

Figure 1.2: *Schematic representation of the parameters involved in PDT.*

The propagation of light in tissue is strongly influenced by the processes of absorption and scattering and as a result is not a constant factor within the treatment volume. Furthermore, the tissue optical properties change as a result of treatment, for example by changes in tissue oxygenation, blood volume or the onset of edema [41]. Photosensitizer concentration is dependent on tissue type and vascularization (in the case of systemic

administered photosensitizers). During treatment, the triplet state photosensitizer concentration depends on the amount of light available to activate the ground state photosensitizer molecule and amount of ground state molecule present, which decreases over time due to interaction with singlet oxygen. The oxygen present will decrease due to its transformation into singlet oxygen and reactive oxygen species. However, the supply of oxygen by vasculature is likely to decrease due to vascular responses. All these effects and interactions necessitate continuous measurements of all parameters, which is practically impossible without interfering with treatment. The determination of photosensitizer concentration is the subject of **chapter 5** and **chapter 6**.

One type of implicit dosimetry is the (continuous) measurement of photosensitizer fluorescence during treatment [39]. Figure 1.1 shows that an excited photosensitizer molecule can return to its ground state by sending out a fluorescent photon, which is relatively easy to detect without interfering in treatment. Fluorescence measurements before treatment can determine distribution and the relative photosensitizer concentration in the treatment area. During treatment, the degeneration of photosensitizer by oxygen radicals (photobleaching) may provide information on radical formation and therefore effectiveness of the treatment. In **chapter 2** we perform PDT with a light dose determined by the measurement of real-time PpIX photobleaching.

PDT ILLUMINATION PROTOCOLS

The success of photodynamic therapy is dependent on a complex interdependency of light, oxygen, photosensitizer and the properties of the target tissue. Before every (pre-) clinical PDT treatment, an illumination protocol is defined which dictates the timeline of the treatment. Injected photosensitizer concentration, local fluence and fluence rate (and corresponding laser settings) are the most important treatment parameters. Another important parameter is drug-light interval, which indicates the time between the time of photosensitizer administration and the start of illumination. This period is critical and based on knowledge on how the photosensitizer accumulates into the target tissue. A carefully chosen drug-light interval can also increase selective damage to tumor by taking into account knowledge on the tumor-to-normal ratio of the photosensitizer accumulation. Clinically, drug-light intervals vary from a few hours (ALA [42], ce6 [16]) to four days (mTHPC [9]).

After the discovery of re-synthesis of PpIX after illumination, a fractionated illumination protocol is developed to allow the re-synthesized PpIX to increase PDT damage [43]. This has resulted in the successful clinical application of light fractionated ALA-PDT. Although the exact mechanism of light fractionated ALA-PDT is not yet fully understood, a small first light fraction followed by a dark period of 2 hours and then a

second light fraction significantly improves the clinical success rate of the treatment of superficial basal cell carcinomas [42]. In **chapter 2 and 3** we further investigate the increased efficacy of fractionated ALA-PDT.

Photosensitizer pharmacokinetics play an important role in the determination of the drug-light interval. In **chapter 5 and 6** the pharmacokinetics and localization of photosensitizers ce6 and Bremachlorin are carefully investigated.

TISSUE OPTICAL PROPERTIES

Figure 1.2 illustrates the important role that the tissue optical properties play in monitoring and optimizing photodynamic therapy. The tissue optical properties influence the way light propagates in tissue and can be separated into effects due to absorption and scattering. In short: absorption is caused by the presence of molecules in tissue that absorb light (of a particular wavelength) and scattering is a result of refractive index differences that are present between cell and tissue structures. Both processes are described in more detail below. Knowledge of the tissue optical properties is important because they determine the distribution of light in tissue and thereby determine the delivered light dose in PDT [44]. Furthermore, tissue absorption and scattering are measurable parameters that can be related to vascular physiology in tissue [45]. Last, the detection of fluorescence light from, in case of PDT, the photosensitizer in tissue is strongly affected by tissue optical properties [46]. Knowledge of optical properties can in theory be used to determine the intrinsic photosensitizer fluorescence.

One way to investigate the absorption and scattering of tissue is to illuminate tissue with white light. The backscattered photons that are detected have interacted with the tissue, and the (calibrated) difference between the light used to illuminate the tissue and the detected light provides valuable information on the composition of the tissue [47, 48]. If light is guided through a (phantom) medium that is only scattering without absorption, the result is the detection of a reflectance spectrum that theoretically corresponds with a decreasing power law. This effect is illustrated in figure 1.3. When an absorber is present in the medium, a local minimum in observed in the reflectance spectrum where the absorber exhibits an extinction spectrum. I.e. less light is collected than would be expected in the absence of absorption when only scattering was present. With a sufficiently detailed understanding of the absorbers present and knowledge of the background scattering properties of the medium the reflectance spectrum can be decomposed into a scattering and an absorption component.

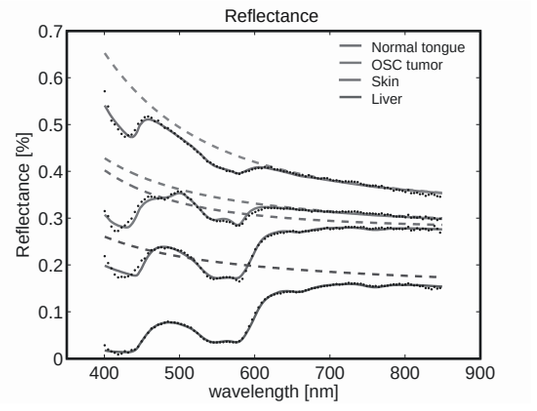

Figure 1.3: *Reflectance spectra detected on different tissues. (…) measured reflectance (---) scattering component (color) model calculation of the measured data based on best values for μ_a and μ'_s.*

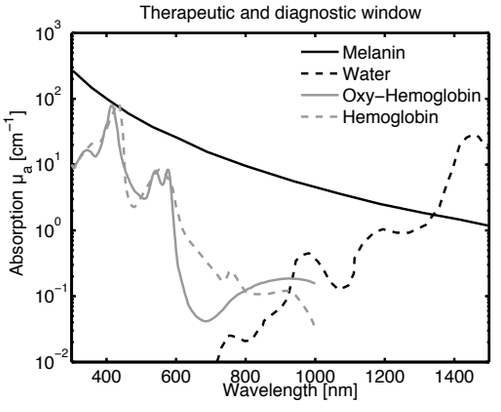

Figure 1.4: *overview of oxy- and deoxyhemoglobin absorption spectrum.*

LIGHT ABSORPTION IN TISSUE

Various endogenous molecules present in tissue, such as hemoglobin, melanin, cytochrome C and bilirubin show significant wavelength-dependent absorption in the visible region of the spectrum. An overview of the main absorbers present in tissue is given in figure 1.4. Hemoglobin is the predominant absorber in tissue and shows distinct differences in absorption spectra for its oxygenated and deoxygenated state; the double peak around 580 nm is particularly characteristic.

Absorption is quantified by the absorption coefficient μ_a, which is defined as the inverse average distance that a photon (light) can travel without being absorbed

$$\mu_a(\lambda) = \sigma_a(\lambda)\rho_N \text{ . [mm}^{-1}\text{]} \qquad (1.1)$$

Here, σ_a is the effective absorption cross-section and ρ_N is the number density of absorbing particles. The higher μ_a, the higher the probability a photon is absorbed. How much light is attenuated by the presence of an absorber is described by Beer's law

$$I(\lambda) = I_0(\lambda)e^{-\mu_a(\lambda)\langle L\rangle(\lambda)} \qquad [-] \qquad (1.2)$$

where the detected light intensity I is dependent on the original light intensity I_0, the absorption coefficient μ_a and the photon path length $\langle L \rangle$. By spectral decomposition of the measured tissue absorption spectrum into all known components present in the tissue, one can determine concentrations of these absorbers. This includes the determination of the ratio of oxygenated and deoxygenated hemoglobin present, which relates to the tissue saturation. Furthermore, physical parameters of the measurement volume, such as vessel diameter and blood volume fraction can be determined based on tissue absorption measurements. Variations in absorption and scattering properties of

tissue are under investigation for the discrimination of healthy and diseased tissue [48-51].

LIGHT SCATTERING IN TISSUE

Light propagating through tissue is also prone to scattering. Scattering is caused by spatial fluctuations in the refractive index of cellular components. When light crosses boundaries between tissues, cells and/or cell components, it will change direction. Macromolecules present in cells have a high molecular density and thus a higher refractive index than the cytoplasm. Therefore, large cellular components with lipid bilayer membranes, like mitochondria, Golgi apparatus and endoplasmic reticulum, are highly scattering components of cells, just as the cell nucleus with a high concentration of nucleic acids [52]. The scattering coefficient μ_s can be defined in a similar way to the absorption coefficient. It is the inverse distance light can travel without being scattered and can be expressed as

$$\mu_s(\lambda) = \sigma_s(\lambda)\rho_N \qquad [\text{mm}^{-1}] \qquad (1.3)$$

where σ_s is the effective scattering cross-section and ρ_N is the number density of scattering particles.

Light scattering can be divided into two regimes. Rayleigh scattering occurs when the scattering particles are smaller than the wavelength of the light. This type of scattering is isotropic. Mie theory is applicable to light scattering of spherical particles of all sizes, but is generally only used in situations where the simpler Rayleigh theory is no longer valid. Mie scattering is anisotropic, where the direction of the scattering event is indicated by the tissue phase function $P(\theta,\phi)$. The phase function can take on various forms, but as a simplification it can be expanded into a series of Legendre polynomials $P_n(\theta)$,

$$P(\cos\theta) = \sum_n (2n+1) g_n P_n(\cos\theta), \qquad [-] \qquad (1.4)$$

where g_n is the nth moment of the phase function. The first moment is the anisotropy (g), which is the mean cosine of the scattering angle and its value ranges from -1 through 0 to 1. This corresponds respectively to complete backscattering, isotropic scattering and complete forward scattering respectively. For tissue, anisotropy values range between 0.85 and 0.98 [53]. Since tissue is highly forward scattering, the reduced scattering coefficient μ'_s, is often defined to account for the longer effective distance between scattering events and is defined as

$$\mu'_s = \mu_s(1-g_1). \qquad [\text{mm}^{-1}] \qquad (1.5)$$

Similarly, the second moment of the phase function can be used to determine the phase function scattering parameter γ [54, 55]

$$\gamma = \frac{1-g_2}{1-g_1}. \qquad [-] \qquad (1.6)$$

Gamma is also a metric of the scattering angle and has been hypothesized to contain information about the nanoscale structure of tissue.

A frequently used model for tissue phase function is the Henyey-Greenstein phase function, which is introduced in 1941 to describe the light scattering of interstellar dust particles [56]. Bevilacqua and Depeursinge subsequently introduced the modified Henyey-Greenstein phase function, which incorporates an isotropic backscatter term to resemble the increased probability for backscattering that has been reported for tissue [57].

If tissue is considered as a random continuous medium, rather than a collection of spherical scatterers, analytical models can be derived to describe the angular distribution of scattered light [58]. This interpretation of tissue scattering requires a model for the refractive index correlation function, which can then be used to predict the scattering properties of the medium. Rogers et al. [59] have recently introduced a model of the refractive index correlation function, which belongs to the family of Whittle-Matérn correlation functions. This model provides a link between optical properties like μ'_s and the phase function and morphological features such as correlation length and variance of refractive index.

In contrast to physics underlying scattering over one or a few scattering events, when light travels over a relatively larger distance before detection (Dist.$\geq 3[\mu_a+\mu'_s]^{-1}$), the diffusion approximation can be used to determine optical properties. In this approach the optical properties are considered to be homogenous over this distance and the diffusion approximation assumes that light propagation is not sensitive to the tissue phase function [60]. The distribution of PDT light in the treatment volume can be described using this approximation. For smaller measurement volumes, the photon path length and the phase function have to be considered. This can be done by including the first two moments g_1 and g_2 of the phase function in the model.

FIBER OPTIC REFLECTANCE SPECTROSCOPY

Tissue absorption and scattering do not only play an important role in optimizing and monitoring PDT but they can be used as a basis for diagnosis of abnormal and malignant tissue. One way to determine the absorption and scattering properties of tissue is to use fiber optic reflectance spectroscopy. White light is transported into the tissue by optical fibers. The light propagates through the tissue, is scattered and absorbed, and a small amount of it completely reflected back exiting the tissue, and is then collected by an(other) optical fiber. Tissue absorption and scattering properties are extracted from

these detected spectra. As described above, this forms the basis of reflectance spectroscopy. Diagnosis of (pre-)malignant lesions by means of reflectance spectroscopy can be based on physiological changes that occur when tissue becomes malignant, such as variations in blood oxygen saturation, blood volume, vessel diameter or the absence or presence of certain absorbers [61]. Changes in scattering can also be utilized because these reflect differences in morphology, suggesting variations in cell size and structure, which are known to occur when a cancer develops [62]. Various approaches have been used to detect absorption and scattering by the use of fiber optic probes. The main difference between different techniques is the geometry of source and detection fibers. Generally three geometries can be identified: probes where there is a large distance between source and detector fiber (few mm to cm), probes where the distance between source and detector fiber is shorter than the transport mean free path (mfp) of light (in general <2 mm), and one single fiber serving as both source and detector.

LARGE SOURCE-DETECTOR SEPARATIONS

Classical reflectance spectroscopy devices are often based on multiple optical fibers, of which one serves as source and the other(s) as detector [63-66]. Detected light is scattered multiple times over the distance it travels from source to detector, and the exact photon path length can be calculated using diffusion theory. Here, an approximate analytical solution of the general radiation transfer equation is used. It is assumed that light propagation is insensitive to tissue phase function and therefore does not have a preferential direction of travel. Propagation of light is modeled as diffusion over a concentration gradient. This approximation is only valid when the distance light travels is large (>1 mfp to neglect the influence of the phase function on scattering) and absorption dominates over scattering [60].

Systems based on the use of multiple fibers have some drawbacks. First, the measurement volume is relatively large because of the large distance the photons travel. Optical properties are assumed to be homogenous within the measurement volume, whereas tissue is know to be heterogeneous. Furthermore, probes with this geometry are often large, which limits their practicality to skin or surgically exposed tissues. Last, since the diffusion approximation is insensitive to phase function, this probe geometry lacks the ability to provide information on the fine structure of tissue.

SMALL SOURCE-DETECTOR SEPARATIONS

In situations where light has traveled less than 1 mfp, the majority of the photons have undergone too few scattering events to be characterized by the reduced scattering coefficient only; the scattering phase function has to be accounted for [67, 68]. Since the

diffusion approximation is not valid for these short source-detector separations, other approaches have to be used to determine optical properties using small source-detector probe geometries. These approaches can be analytical or (semi-)empirical based on Monte Carlo (MC) modeling of light transport.

The most well known analytical approach to determine tissue optical properties from reflectance close to the source is the P_3 approximation, introduced by Hull and Foster [54]. This approach is based on a solution of the Boltzman transport equation, which is valid for small source-detector separations since it includes the first three moments of the phase function. However, this approach uses assumptions for the higher order Henyey-Greenstein phase function and therefore influence the determination of optical properties when a tissue has a different phase function. Recently, Vitkin et al. have introduced a phase function-corrected diffusion approximation to describe diffuse reflectance close to the source [69]. This approach combines the diffusion approximation with an approximation of the changes in reflectance due to the phase function. Although this method showed good agreement with MC simulations, a significant problem is that an assumption about the phase function has to be made. Recently, Liemert et al. have solved the three-dimensional radiation transfer equation in an anisotropically scattering medium using a two-dimensional Fourier transform and the modified spherical harmonics method [70].

One of the most widely used algorithms for the description of photon transport through turbid media is the MCML (Monte Carlo for Multi-Layered Media) code written by L. Wang [71]. This code simulates absorption and scattering events that occur with photon-tissue interactions and allows for a complete analysis of photon paths, which results in the reflectance signal collected in a specific probe geometry. MC solutions serve as a basis for (semi-)empirical, geometry-dependent models to derive tissue optical properties or can be used to create look-up tables for the correlation between reflectance and optical properties. MC simulations are used by Bevilacqua to determine the influence of the first two moments of the phase function, combined in the phase function parameter γ, on the detected reflectance spectra for small source-detector geometries [57]. Tissue refractive index, absorption coefficient, reduced scattering coefficient and γ can be empirically derived from the reflectance signal. Palmer et al. have developed a MC-based forward and inverse model to extract absorption and reduced scattering of tissue-mimicking phantoms [72].

SINGLE FIBER REFLECTANCE SPECTROSCOPY

A particularly interesting probe geometry for performing fiber optic reflectance spectroscopy is to use a single fiber for both delivery and collection of light. This method

requires an empirical model of the photon path length to be able to determine tissue absorption and phase function dependent reduced scattering. Quantification of absorption is possible using Beer's law when the relationship between single fiber diameter and path length is known. Our group has developed such a model and implemented the use of single fiber reflectance (SFR) spectroscopy. The path length model contains information on absorption and reduced scattering and is sensitive to the tissue phase function [73-75]. A single fiber with a diameter between 0.2 and 2 mm (dependent on the preferred sampling volume) is used as a probe and detected light is guided to a spectrometer by a bifurcated fiber. A schematic overview can be seen in figure 1.5a.

A reflectance setup using a single fiber provides simplicity and a small probe size, combined with a small, shallow measurement volume. The small measurement volume is advantageous when measuring for example oral mucosa, epithelium or epidermal tissue, which all have a thickness of only a few hundred micrometers. SFR is more sensitive to physiological and morphological changes due to the development of premalignant lesions in those tissues than probe geometries with a larger measurement volume are. The option of feeding a fiber optic probe through a (biopsy) needle increases the number of applications; fibers with a diameter of 200 μm can easily be fitted through needles used for fine needle aspiration (FNA), allowing interstitial measurements in a minimally invasive way [76]. By first detecting the presence of (pre-)malignant tissue in front of the biopsy/FNA device by means of a reflectance measurement, the clinician can prevent taking a false negative biopsy where the patient has to return to repeat the procedure, or reduce the number of biopsies. In theory, future biopsies could consist of only an optical measurement, but practice has shown that accurate discrimination of (pre-)malignancies and their various stages is still performed best by a trained pathologist. Last, SFR is highly sensitive to the phase function and has a potential to probe ultrastructural properties of tissue.

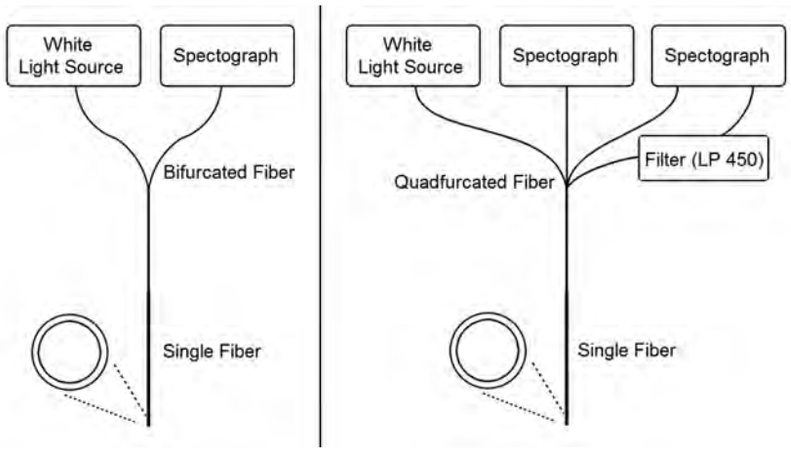

Figure 1.5: *Probe design for (a) SFR and (b) SFF.*

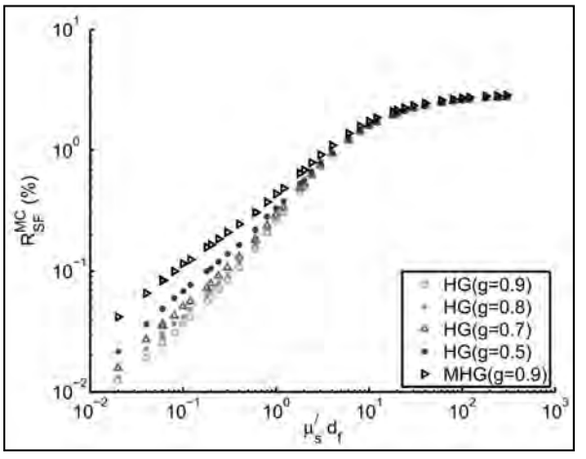

Figure 1.6: *Single fiber reflectance versus dimensionless scattering for Henyey-Greenstein phase function (g=[0.5,0.7,0.8,0.9]) and Modified Henyey-Greenstein phase function (g=[0.9]).*

MULTI DIAMETER SINGLE FIBER REFLECTANCE SPECTROSCOPY

The influence of the phase function on reflectance intensity measured close to the source has been described in literature [57, 68, 77]. Recently Kanick et al. have developed a method based on MC simulations to identify a novel mathematical formula of the reflectance intensity in terms of $\mu'_s(\lambda)$, fiber diameter d_f and the phase function parameter $\gamma(\lambda)$ [74, 78]. Figure 1.6 shows the relation between the MC simulated reflectance intensity R_{SF} and the dimensionless scattering $\mu'_s d_f$ for combinations including a wide range of μ'_s and d_f and various phase functions.

It is shown that R_{SF} becomes insensitive to the phase function for large values of $\mu'_s d_f$ [74], as can be seen in figure 1.6. By including measurements with two or more fiber diameters d_f [79] on the same measurement spot, one can discriminate the effects of scattering and phase function based on the measured reflectance. This relation is described by the empirical model

$$R_{SF} = \eta_{\lim}\left(1+\rho_3 e^{\left(-\rho_1 \mu_s d_f\right)}\right)\left[\frac{\left(\mu_s d_f\right)^{\rho_2}}{\rho_1+\left(\mu_s d_f\right)^{\rho_2}}\right], \qquad [\%] \qquad (1.7)$$

where

$$\left[\rho_1 = \xi_1\gamma^2 \quad \rho_2 = \xi_2\gamma \quad \rho_3 = \xi_3\gamma^2\right]$$

and both μ'_s and γ are determined. Performing SFR measurements with two or more fiber diameters to determine scattering and phase function information is known as multi-diameter single fiber reflectance spectroscopy (MDSFR). **Chapter 4** provides an in-vivo validation of this method.

FIBER OPTIC FLUORESCENCE SPECTROSCOPY

Fiber optic fluorescence spectroscopy is based on the same principles as reflectance spectroscopy, only in this case monochromatic laser light is transported into the tissue instead of white light. This light will be absorbed by endogenous fluorophores such as collagen and NADH, or exogenous fluorescent labeled markers and drugs such as photosensitizers [80]. These excited fluorophores emit light of a longer wavelength than the excitation light, which is detected by optical fibers. The shape and intensity of the fluorescence spectrum contain valuable information on fluorophore identity, its concentration and the local environment.

The detection of quantitative, intrinsic fluorescence in-vivo is complicated by the influence of optical properties: the total excitation light available to induce fluorescence is influenced by optical properties at the excitation wavelength, while the detected fluorescence is attenuated by the optical properties at the emission wavelength [46, 81]. Over the years, several fiber optic methods have been developed to extract the intrinsic fluorescence, based on a co-localized white light reflectance and a fluorescence measurement. The reflectance is then used to determine local optical properties for correction of fluorescence intensity. For this correction it is necessary that both measurements have coincident measurement geometries. Multi-fiber devices with separate source and detector fibers have been extensively investigated [82-84]. In this configuration, both reflectance and fluorescence light is diffusely scattered before detection and an analytical method can be applied to determine the intrinsic fluorescence independent of probe design.

SINGLE FIBER FLUORESCENCE SPECTROSCOPY

When collecting (superficial) fluorescence with a single fiber probe, the majority of collected reflectance and fluorescence photons have undergone not enough scattering events to apply the analytical models for diffusion theory. Furthermore, the sampling volume of reflectance and fluorescence differ significantly from each other for this method. Kanick et al. have developed a (semi-)empirical model to account for the influence of optical properties in fluorescence measurements and to obtain the intrinsic fluorescence, based on a combination of MDSFR and SFF [81, 85]. Correction for tissue absorption is taken care of by the use of Beer's law,

$$F_{SF} = F_{SF}^{0} e^{\left(-\mu_{a,avg}\langle L_{SFFL}\rangle\right)}. \qquad \text{[\# photons]} \qquad 1.8)$$

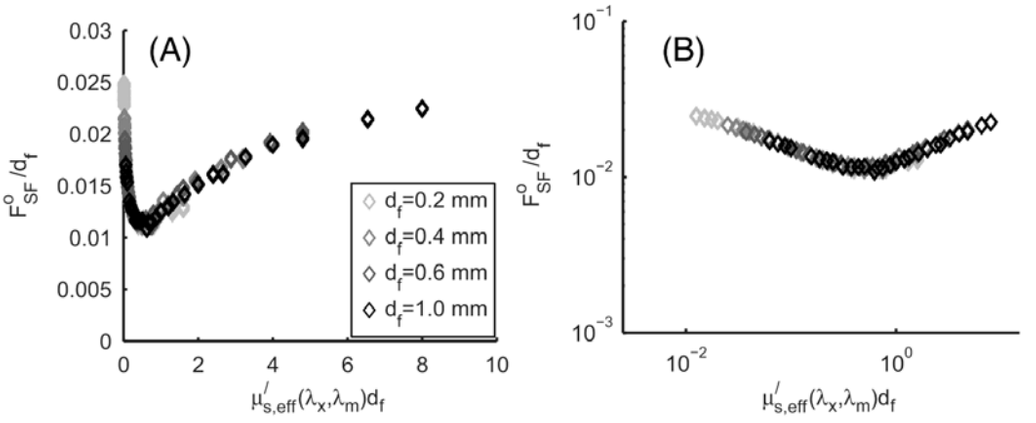

Figure 1.7: *Relation between dimensionless fluorescence intensity and the dimensionless scattering on (a) linear and (b) log scale. Results are independent of fiber diameter.*

Further, MC simulations are used to determine an empirical relation between the fluorescence ratio, effective sampling volume (V), effective escape probability (H_m^V) of fluorescent photons and the relative excitation fluence (ϕ_m^V)

$$F_{Ratio}^{SF} = \frac{F_{SF}^0}{P_{Laser}} \approx \left(\frac{\lambda_x}{\lambda_m}\right)\mu_a^f Q^f \left\langle \phi_x^V \right\rangle \left\langle H_m^V \right\rangle \left\langle V \right\rangle \quad . \text{ [-]} \tag{1.9}$$

The latter three terms can all be expressed in terms of $\mu'_s d_f$ at the excitation or emission wavelength. The fluorescent ratio is defined as the total emitted photons collected, divided by the total excitation photons launched. The correction of the detected fluorescence signal for scattering then becomes:

$$\frac{F_{Ratio}^{SF}}{\mu_a^f Q^f d_f \nu_f}\left(\frac{\lambda_m}{\lambda_x}\right) = \xi_1 \left(\mu_{s,avg} d_f + 0.00315\right)^{-\xi_2} e^{\left(\frac{-1}{\xi_2\left(\mu_s(\lambda_x)d_f\right)+1} - \frac{\xi_3}{\xi_2\left(\mu_s(\lambda_m)d_f\right)+1}\right)} \quad . \tag{1.10}$$

This equation describes the relation between the dimensionless fluorescence intensity F/d_f and the dimensionless reduced scattering $\mu'_s d_f$, which is visualized in figure 1.7. This relation is valid over a large range of $\mu'_s d_f$, μ_a and different phase functions [81, 85].

With the correct calibration procedure, the intrinsic fluorescence can be related to $Q^f \mu_a^f$, which is the product of the fluorophore quantum yield and the fluorophore absorption coefficient. In situations where quantum yield is known, this can be related to fluorophore concentration. However, in in-vivo situations quantum yield (and often μ_a^f as well) depends on the environment in which the fluorophore is located and are often not known exactly. In this thesis $Q^f \mu_a^f$ is defined as the intrinsic fluorescence. **Chapter 5** reports on the application of SFF to determine photosensitizer concentrations in-vivo.

A schematic overview of the MDSFR-SFF measurement setup used in this thesis is shown in figure 1.5b. While both reflectance and fluorescence are detected by the same fiber, separate spectrometers are needed to correctly analyze the data. The intensity of

the excitation laser light is much higher than the detected fluorescence, which requires the use of a filter to block the excitation light from the fluorescence spectrum. However, to be able to correctly determine reflectance, the complete wavelength range between 400 and 800 nm needs to be included in the analysis. We have therefore separated the detection paths of fluorescence and reflectance, in such a way that the probe can still be guided through a needle.

An important application field where measurement of intrinsic fluorescence is particularly valuable is the determination of intrinsic photosensitizer fluorescence before and during photodynamic therapy. Since oxygen is depleted during PDT, saturation levels in the measurement volume change, and consequently the optical properties. Intrinsic fluorescence allows for reliable quantification and comparison of photosensitizer fluorescence at various time points before, during and after PDT.

To determine the optimum illumination time after photosensitizer administration, knowledge of $Q^f\mu_a{}^f$ in the treatment volume and surrounding tissue is essential. Based on results of these pharmacokinetic studies in which photosensitizer $Q^f\mu_a{}^f$ is monitored over time after administration in the target tissue, one can for example determine the time point with the most photosensitizer present, or the time point with the largest tumor-to-normal ratio. Furthermore, photosensitizer molecules are often large, flat structures [86]. These molecules have the tendency to form aggregates when administered in high concentrations or under certain environmental conditions [13]. When aggregation happens, the photoactivity of the drug is much less. However, the molecules ability to fluoresce is also strongly reduced, which can be detected by intrinsic fluorescence. By measuring fluorescence after photosensitizer administration in specific target tissues, a dose escalation study can be performed to determine the optimal photosensitizer concentration for therapy. All these parameters greatly influence the treatment efficacy of PDT, and knowledge on those parameters can be used to optimize treatment efficacy.

THESIS OVERVIEW

This thesis focuses on the application of quantitative fiber optic spectroscopy and optical imaging techniques to gain insight in various PDT-related processes, and how this can contribute to the optimization of photodynamic therapy.

Specific parts of the thesis are dedicated to:

- The investigation of the relationship between vascular responses during light fractionated ALA-PDT and treatment efficacy using optical imaging and spectroscopy (chapter 2 and 3).
- The development of quantitative fiber optic fluorescence spectroscopy and its application in measuring in-vivo photosensitizer pharmacokinetics (chapter 4).
- A comparison of the pharmacokinetics and spectral properties of chlorin e_6 and Bremachlorin based on in-vivo measurements and their relationship to PDT efficacy (chapter 5, 6 and 7).

The individual chapters describe the study of one or more PDT parameters measured in-vivo before, during and/or after PDT. One chapter includes the in-vivo validation of a spectroscopic method to determine scattering of light in tissue, which is a prerequisite for quantitative fluorescence measurements that are also discussed in this thesis.

Chapter 2 describes the use of in-vivo monitoring of fluorescence during ALA-PDT. Non-contact fluorescence measurements are acquired during light fractionated ALA-PDT on healthy mouse thigh tissue. Instead of pre-determining the total delivered fluence in both fractions, we determined the length of the first light fraction based on the photobleaching kinetics of the photosensitizer PpIX. Various illumination schemes and fluence rates are investigated and evaluation of visual skin damage is chosen as a measure for treatment efficacy.

In **Chapter 3** vascular effects during the first low dose light fraction of ALA-PDT are investigated by confocal microscopy. ALA-PDT is performed in a dorsal skinfold window chamber. Confocal microscopy is used to measure variation in vessel diameter and red blood cell velocity during the first 5-13 Joules of the treatment. Photosensitizer concentration in the window chamber is determined by spectral detection using a confocal microscope. Several fluence rates have been included in this work. The time and/or light dose needed to induce vasoconstriction, together with the time vessels remain constricted, provide important knowledge in determining PDT efficacy and developing optimized treatment protocols.

The application of MDSFR spectroscopy in-vivo is described in **Chapter 4**. Reflectance measurements are performed with 0.4 and 0.8 mm fibers on mouse tongue, skin, liver and on oral squamous cell carcinoma induced in the tip of the tongue. The reduced scattering coefficient and phase function parameter γ are measured to determine whether they can be used to discriminate between tissue types.

Chapter 5 reports on the in-vivo application of single fiber fluorescence spectroscopy. Pharmacokinetics and spectral variation of both photosensitizers chlorin e_6 and Bremachlorin are investigated in mouse tongue, skin, liver and oral squamous cell

carcinoma. Analysis is based on intrinsic fluorescence spectra. Spectral variations may provide information on photosensitizer localization, since spectral shape is dependent on pH, which is known to vary between locations. Measurements are performed at various photosensitizer incubation times to gain insight in the optimal drug-light interval for PDT.

A microscopic analysis of localization of chlorin e_6 and Bremachlorin in tumor-including tongue tissue is presented in **Chapter 6**. Photosensitizer fluorescence intensities are determined in frozen tissue slices, where tumor, tumor boundary, invasive tissue and normal tissue are discriminated. An extensive comparison is made with the fiber optic results obtained in Chapter 5. Again, this knowledge may aid in finding the optimal drug-light interval for ce6 and/or Bremachlorin PDT.

In **Chapter 7** knowledge from studies described in previous chapters is combined to optimize PDT in mouse window chambers. Both chlorin e_6 and Bremachlorin are under investigation with various incubation times (chapter 5 and 6). Vascular effects occurring during PDT are analyzed (and related to findings in chapter 3), while tumor reduction/grow delay and visual tissue damage are used as indicators of treatment efficacy.

Chapter 8 provides a general discussion on the results of the studies present in this thesis, and how they contribute to the optimization of photodynamic therapy. It concludes with a brief insight in future technological perspectives.

REFERENCES

1. Von Tappeiner, H. and A. Jesionek, *Therapeutische Versuche mit fluoreszierenden Stoffen.* München Medische Wochenschrift, 1903. **47**: p. 2042-2044.
2. Raab, O., *Über die Wirkung fluoreszierender Stoffe auf Infusorien. .* Zeitschrift für Biologie, 1900. **39**: p. 524-526.
3. Dougherty, T.J., *Photosensitizers: therapy and detection of malignant tumors.* Photochemistry and photobiology, 1987. **45**(S1): p. 879-889.
4. Foote, C.S., *Definition of type I and type II photosensitized oxidation.* Photochemistry and photobiology, 1991. **54**(5): p. 659-659.
5. Babilas, P., et al., *Photodynamic therapy in dermatology: state-of-the-art.* Photodermatology, photoimmunology & photomedicine, 2010. **26**(3): p. 118-132.
6. Moore, C.M., D. Pendse, and M. Emberton, *Photodynamic therapy for prostate cancer - a review of current status and future promise.* Nature Clinical Practice Urology, 2009. **6**(1): p. 18-30.
7. Berr, F., et al., *Photodynamic therapy for advanced bile duct cancer: evidence for improved palliation and extended survival.* Hepatology, 2000. **31**(2): p. 291-298.
8. Schmidt-Erfurth, U., et al., *Photodynamic therapy with verteporfin for choroidal neovascularization caused by age-related macular degeneration: results of retreatments in a phase 1 and 2 study.* Archives of ophthalmology, 1999. **117**(9): p. 1177-1187.
9. Karakullukcu, B., et al., *mTHPC mediated interstitial photodynamic therapy of recurrent nonmetastatic base of tongue cancers: Development of a new method.* Head & neck, 2012. **34**(11): p. 1597-1606.
10. Sharman, W.M., C.M. Allen, and J.E. van Lier, *Role of activated oxygen species in photodynamic therapy.* Methods in enzymology, 2000. **319**: p. 376-400.
11. Overholt, B.F., M. Panjehpour, and D.L. Halberg, *Photodynamic therapy for Barrett's esophagus with dysplasia and/or early stage carcinoma: long-term results.* Gastrointestinal endoscopy, 2003. **58**(2): p. 183-188.
12. Grosjean, P., et al., *Clinical photodynamic therapy for superficial cancer in the oesophagus and the bronchi: 514 nm compared with 630 nm light irradiation after sensitization with Photofrin II.* British journal of cancer, 1998. **77**(11): p. 1989-1995.
13. Spikes, J.D., *New trends in photobiology: chlorins as photosensitizers in biology and medicine.* Journal of Photochemistry and Photobiology B: Biology, 1990. **6**(3): p. 259-274.
14. Nelson, J.S., W.G. Roberts, and M.W. Berns, *In vivo studies on the utilization of mono-L-aspartyl chlorin (NPe6) for photodynamic therapy.* Cancer research, 1987. **47**(17): p. 4681-4685.
15. Cunderlíková, B., L. Gangeskar, and J. Moan, *Acid-base properties of chlorin e6: relation to cellular uptake.* Journal of Photochemistry and Photobiology B: Biology, 1999. **53**(1): p. 81-90.
16. Chan, A.L., et al., *Pharmacokinetics and clinical effects of mono-L-aspartyl chlorin e6 (NPe6) photodynamic therapy in adult patients with primary or secondary cancer of the skin and mucosal surfaces.* Photodermatology, photoimmunology & photomedicine, 2005. **21**(2): p. 72-78.
17. Gomer, C.J. and A. Ferrario, *Tissue distribution and photosensitizing properties of mono-L-aspartyl chlorin e6 in a mouse tumor model.* Cancer research, 1990. **50**(13): p. 3985-3990.
18. Kato, H., et al., *Phase II clinical study of photodynamic therapy using mono-L-aspartyl chlorin e6 and diode laser for early superficial squamous cell carcinoma of the lung.* Lung Cancer, 2003. **42**(1): p. 103-111.

19. Kostenich, G., I. Zhuravkin, and E. Zhavrid, *Experimental grounds for using chlorin e6 in the photodynamic therapy of malignant tumors.* Journal of Photochemistry and Photobiology B: Biology, 1994. **22**(3): p. 211-217.

20. Mojzisova, H., et al., *Cellular uptake and subcellular distribution of chlorin e6 as functions of pH and interactions with membranes and lipoproteins.* Biochimica et Biophysica Acta Biomembranes, 2007. **1768**(11): p. 2748-2756.

21. Orenstein, A., et al., *A comparative study of tissue distribution and photodynamic therapy selectivity of chlorin e6, Photofrin II and ALA-induced protoporphyrin IX in a colon carcinoma model.* British journal of cancer, 1996. **73**(8): p. 937-944.

22. Peng, Q., et al., *5-Aminolevulinic Acid-Based Photodynamic Therapy: Principles and Experimental Research.* Photochemistry and photobiology, 1997. **65**(2): p. 235-251.

23. Kennedy, J.C. and R.H. Pottier, *New trends in photobiology: endogenous protoporphyrin IX, a clinically useful photosensitizer for photodynamic therapy.* Journal of Photochemistry and Photobiology B: Biology, 1992. **14**(4): p. 275-292.

24. de Bruijn, H.S., et al., *Microscopic localisation of protoporphyrin IX in normal mouse skin after topical application of 5-aminolevulinic acid or methyl 5-aminolevulinate.* Journal of Photochemistry & Photobiology, B: Biology, 2008. **92**(2): p. 91-97.

25. Gilissen, M.J., et al., *Effect of photodynamic therapy on the endothelium-dependent relaxation of isolated rat aortas.* Cancer research, 1993. **53**(11): p. 2548-2552.

26. de Vijlder, H.S., et al., *Acute Vascular Responses during Photodynamic Therapy using Topically Administered Porphyrin Precursors.* Photochemical & Photobiological Sciences, 2013. **In press**.

27. Dolmans, D.E., D. Fukumura, and R.K. Jain, *Photodynamic therapy for cancer.* Nature Reviews Cancer, 2003. **3**(5): p. 380-387.

28. Mroz, P., et al., *Cell death pathways in photodynamic therapy of cancer.* Cancers, 2011. **3**(2): p. 2516-2539.

29. Buytaert, E., M. Dewaele, and P. Agostinis, *Molecular effectors of multiple cell death pathways initiated by photodynamic therapy.* Biochimica et Biophysica Acta (BBA)-Reviews on Cancer, 2007. **1776**(1): p. 86-107.

30. Williams, G.T., *Programmed cell death: apoptosis and oncogenesis.* Cell, 1991. **65**(7): p. 1097-1098.

31. Kessel, D. and Y. Luo, *Mitochondrial photodamage and PDT-induced apoptosis.* Journal of Photochemistry and Photobiology B: Biology, 1998. **42**(2): p. 89-95.

32. Proskuryakov, S.Y. and V.L. Gabai, *Mechanisms of tumor cell necrosis.* Current pharmaceutical design, 2010. **16**(1): p. 56-68.

33. Fingar, V.H., et al., *The role of microvascular damage in photodynamic therapy: the effect of treatment on vessel constriction, permeability, and leukocyte adhesion.* Cancer research, 1992. **52**(18): p. 4914-4921.

34. Fingar, V.H., T.J. Wieman, and K.W. Doak, *Role of thromboxane and prostacyclin release on photodynamic therapy-induced tumor destruction.* Cancer research, 1990. **50**(9): p. 2599-2603.

35. Gollnick, S.O., et al., *Altered expression of interleukin 6 and interleukin 10 as a result of photodynamic therapy in vivo.* Cancer research, 1997. **57**(18): p. 3904-3909.

36. Gorman, A. and M. Rodgers, *Current perspectives of singlet oxygen detection in biological environments.* Journal of photochemistry and photobiology. B, Biology, 1992. **14**(3): p. 159-176.

37. Niedre, M., M.S. Patterson, and B.C. Wilson, *Direct Near-infrared Luminescence Detection of Singlet Oxygen Generated by Photodynamic Therapy in Cells In Vitro and Tissues In Vivo.* Photochemistry and photobiology, 2002. **75**(4): p. 382-391.

38. Niedre, M., et al., *Singlet oxygen luminescence as an in vivo photodynamic therapy dose metric: validation in normal mouse skin with topical amino-levulinic acid.* British journal of cancer, 2005. **92**(2): p. 298-304.

39. Wilson, B.C., M.S. Patterson, and L. Lilge, *Implicit and explicit dosimetry in photodynamic therapy: a new paradigm.* Lasers in medical science, 1997. **12**(3): p. 182-199.

40. Dysart, J.S., et al., *Relationship Between mTHPC Fluorescence Photobleaching and Cell Viability During In Vitro Photodynamic Treatment of DP16 Cells.* Photochemistry and photobiology, 2002. **75**(3): p. 289-295.

41. Wilson, B.C. and M.S. Patterson, *The physics, biophysics and technology of photodynamic therapy.* Physics in medicine and biology, 2008. **53**(9): p. R61-R109.

42. de vijlder, H.C., et al., *Light fractionation significantly improves the response of superficial basal cell carcinoma to ALA-PDT: five-year follow-up of a randomized, prospective trial.* Acta Dermatol Venereol, 2012. **92**: p. 641-647.

43. de Bruijn, H.S., et al., *Fractionated illumination after topical application of 5-aminolevulinic acid on normal skin of hairless mice: The influence of the dark interval.* Journal of Photochemistry & Photobiology, B: Biology, 2006. **85**(3): p. 184-190.

44. Wilson, B.C., W.P. Jeeves, and D.M. Lowe, *In vivo and post mortem measurements of the attenuation spectra of light in mammalian tissues.* Photochemistry and photobiology, 1985. **42**(2): p. 153-162.

45. Amelink, A., et al., *Monitoring PDT by means of superficial reflectance spectroscopy.* Journal of Photochemistry & Photobiology, B: Biology, 2005. **79**(3): p. 243-251.

46. Müller, M.G., et al., *Intrinsic fluorescence spectroscopy in turbid media: disentangling effects of scattering and absorption.* Applied optics, 2001. **40**(25): p. 4633-4646.

47. Amelink, A., et al., *Non-invasive measurement of the morphology and physiology of oral mucosa by use of optical spectroscopy.* Oral oncology, 2008. **44**(1): p. 65-71.

48. Brown, J.Q., et al., *Quantitative optical spectroscopy: a robust tool for direct measurement of breast cancer vascular oxygenation and total hemoglobin content in vivo.* Cancer research, 2009. **69**(7): p. 2919-2926.

49. Xu, R.X. and S.P. Povoski, *Diffuse optical imaging and spectroscopy for cancer.* Expert review of medical devices, 2007. **4**(1): p. 83-95.

50. Roy, H.K., et al., *Spectroscopic microvascular blood detection from the endoscopically normal colonic mucosa: biomarker for neoplasia risk.* Gastroenterology, 2008. **135**(4): p. 1069-1078.

51. Backman, V. and H.K. Roy, *Light-scattering technologies for field carcinogenesis detection: a modality for endoscopic pre-screening.* Gastroenterology, 2011. **140**(1): p. 35-41.

52. Johnsen, S. and E.A. Widder, *The physical basis of transparency in biological tissue: ultrastructure and the minimization of light scattering.* Journal of theoretical biology, 1999. **199**(2): p. 181-198.

53. Jacques, S.L., *Optical properties of biological tissues: a review.* Physics in medicine and biology, 2013. **58**(11): p. R37.

54. Hull, E.L. and T.H. Foster, *Steady-state reflectance spectroscopy in the P_3 approximation.* JOSA A, 2001. **18**(3): p. 584-599.

55. Thueler, P., et al., *In vivo endoscopic tissue diagnostics based on spectroscopic absorption, scattering, and phase function properties.* Journal of biomedical optics, 2003. **8**(3): p. 495-503.

56. Henyey, L.G. and J.L. Greenstein, *Diffuse radiation in the galaxy.* The Astrophysical Journal, 1941. **93**: p. 70-83.

57. Bevilacqua, F. and C. Depeursinge, *Monte Carlo study of diffuse reflectance at source-detector separations close to one transport mean free path.* Journal of the Optical Society of America A, 1999. **16**(12): p. 2935-2945.

58. Ishmaru, A., *Wave Propagation and Scattering in Random Media*. Vol. 2. 1978: Academic Press, Inc., New York.

59. Rogers, J.D., I.R. Capolu, and V. Backman, *Nonscalar elastic light scattering from continuous random media in the Born approximation.* Optics Letters, 2009. **34**(12): p. 1891-1893.

60. Haskell, R.C., et al., *Boundary conditions for the diffusion equation in radiative transfer.* JOSA A, 1994. **11**(10): p. 2727-2741.

61. Pouysségur, J., F. Dayan, and N.M. Mazure, *Hypoxia signalling in cancer and approaches to enforce tumour regression.* Nature, 2006. **441**(7092): p. 437-443.

62. Xu, M. and R.R. Alfano, *Fractal mechanisms of light scattering in biological tissue and cells.* Optics Letters, 2005. **30**(22): p. 3051-3053.

63. van Veen, R.L., et al., *Optical biopsy of breast tissue using differential path-length spectroscopy.* Physics in medicine and biology, 2005. **50**(11): p. 2573.

64. Chung, S., et al., *In vivo water state measurements in breast cancer using broadband diffuse optical spectroscopy.* Physics in medicine and biology, 2008. **53**(23): p. 6713.

65. Zonios, G., J. Bykowski, and N. Kollias, *Skin melanin, hemoglobin, and light scattering properties can be quantitatively assessed in vivo using diffuse reflectance spectroscopy.* Journal of Investigative Dermatology, 2001. **117**(6): p. 1452-1457.

66. Kim, A., et al., *A fiberoptic reflectance probe with multiple source-collector separations to increase the dynamic range of derived tissue optical absorption and scattering coefficients.* Optics express, 2010. **18**(6): p. 5580-5594.

67. Canpolat, M. and J.R. Mourant, *High-angle scattering events strongly affect light collection in clinically relevant measurement geometries for light transport through tissue.* Physics in medicine and biology, 2000. **45**(5): p. 1127.

68. Kienle, A., F.K. Forster, and R. Hibst, *Influence of the phase function on determination of the optical properties of biological tissue by spatially resolved reflectance.* Optics Letters, 2001. **26**(20): p. 1571-1573.

69. Vitkin, E., et al., *Photon diffusion near the point-of-entry in anisotropically scattering turbid media.* Nature communications, 2011. **2**: p. 587.

70. Liemert, A. and A. Kienle, *Light transport in three-dimensional semi-infinite scattering media.* JOSA A, 2012. **29**(7): p. 1475-1481.

71. Wang, L., S.L. Jacques, and L. Zheng, *MCML-Monte Carlo modeling of light transport in multi-layered tissues.* Computer methods and programs in biomedicine, 1995. **47**(2): p. 131-146.

72. Palmer, G.M. and N. Ramanujam, *Monte Carlo-based inverse model for calculating tissue optical properties. Part I: Theory and validation on synthetic phantoms.* Applied optics, 2006. **45**(5): p. 1062-1071.

73. Kanick, S.C., et al., *Monte Carlo analysis of single fiber reflectance spectroscopy: photon path length and sampling depth.* Physics in medicine and biology, 2009. **54**(22): p. 6991-7008.

74. Kanick, S.C., et al., *Measurement of the reduced scattering coefficient of turbid media using single fiber reflectance spectroscopy: fiber diameter and phase function dependence.* Biomedical optics express, 2011. **2**(6): p. 1687-1702.

75. Kanick, S.C., et al., *Method to quantitate absorption coefficients from single fiber reflectance spectra without knowledge of the scattering properties.* Optics Letters, 2011. **36**(15): p. 2791-2793.

76. Kanick, S.C., et al. *Incorporation of Single Fiber Reflectance Spectroscopy into Ultrasound-Guided Endoscopy (EUS-FNA) of Mediastinal Lymph Nodes*. in *Biomedical Optics and 3-D imaging*. (2010), Optical Society of America, p. BTuD89.

77. Mourant, J.R., et al., *Influence of the scattering phase function on light transport measurements in turbid media performed with small source-detector separations.* Optics Letters, 1996. **21**(7): p. 546-548.

78. Kanick, S.C., et al., *Method to quantitatively estimate wavelength-dependent scattering properties from multidiameter single fiber reflectance spectra measured in a turbid medium.* Optics Letters, 2011. **36**(15): p. 2997-2999.

79. Gamm, U.A., et al., *Measurement of tissue scattering properties using multi-diameter single fiber reflectance spectroscopy: in silico sensitivity analysis.* Biomedical optics express, 2011. **2**(11): p. 3150-3166.

80. Ntziachristos, V., *Going deeper than microscopy: the optical imaging frontier in biology.* Nature methods, 2010. **7**(8): p. 603-614.

81. Kanick, S.C., et al., *Extraction of intrinsic fluorescence from single fiber fluorescence measurements on a turbid medium.* Optics Letters, 2012. **37**(5): p. 948-950.

82. Palmer, G.M., et al., *Quantitative diffuse reflectance and fluorescence spectroscopy: tool to monitor tumor physiology in vivo.* Journal of biomedical optics, 2009. **14**(2): p. 024010-024010-8.

83. Finlay, J.C. and T.H. Foster, *Recovery of hemoglobin oxygen saturation and intrinsic fluorescence with a forward-adjoint model.* Applied optics, 2005. **44**(10): p. 1917-1933.

84. Kim, A., et al., *Quantification of in vivo fluorescence decoupled from the effects of tissue optical properties using fiber-optic spectroscopy measurements.* Journal of biomedical optics, 2010. **15**(6): p. 067006-067006-12.

85. Kanick, S., et al., *Semi-empirical model of the effect of scattering on single fiber fluorescence intensity measured on a turbid medium.* Biomedical optics express, 2012. **3**(1): p. 137-152.

86. Owens, J.W., et al., *Photophysical properties of porphyrins, phthalocyanines, and benzochlorins.* Inorganica chimica acta, 1998. **279**(2): p. 226-231.

Chapter 2

Fractionated Illumination at Low Fluence Rate Photodynamic Therapy in Mice

Tom Middelburg, Floor van Leeuwen – van Zaane, Riëtte de Bruijn, Angélique van der Ploeg – van den Heuvel, Dick Sterenborg, Arjen Amelink, Dominic Robinson

Photochemistry and Photobiology, 2010. **86**(5): p. 1140-1146

ABSTRACT

Photodynamic therapy (PDT) for actinic field cancerization is effective but painful. Pain mechanisms remain unclear but fluence rate has been shown to be a critical factor. Lower fluence rates also utilize available oxygen more efficiently. We investigated PDT effect in normal SKH1-HR mice using low and high fluence rate aminolevulinic acid (ALA) PDT and a fractionated illumination scheme. Six groups of six mice with different light treatment parameters were studied. Visual skin damage was assessed up to seven days post PDT. Fluorescence and reflectance spectroscopy during illumination provided us with real time information about PpIX photobleaching. A novel dosing approach was introduced, where we used a photobleaching percentage instead of a pre-set fluence.

Data show similar total and maximum damage scores in high and low fluence rate groups. Photobleaching of PpIX in the low fluence rate groups shows a trend towards more efficient photobleaching. Results indicate that low fluence rate PDT is as effective as, and more efficient than high fluence rate PDT in normal mouse skin. Low fluence rate PDT light protocols need to be explored in human studies in search for an effective and well-tolerated treatment for actinic field cancerization.

INTRODUCTION

Non-melanoma skin cancer and precursor lesions are a steadily increasing health care problem [1-5]. Especially extensive field cancerization necessitates the use of full field treatment options, such as photodynamic therapy (PDT). PDT using topical aminolevulinic acid (ALA) or its ester derivates, such as methyl-ALA (Metvix®) is now well accepted and used for treating actinic keratosis (AK), Bowen's disease (BD) and superficial basal cell carcinoma (sBCC). There is a consensus on the use of PDT for these indications, as presented in recent European guidelines [6-7]. Topically applied ALA is converted via the haem synthesis pathway resulting in the accumulation of the photosensitizer protoporphyrin IX (PpIX). Illumination with light of the appropriate wavelength leads to the generation of reactive oxygen species, notably singlet oxygen. This results in a range of tissue effects that include cell apoptosis, necrosis, vascular and immunological responses. The effectiveness of ALA-PDT is influenced by many variables such as fluence, fluence rate, light source, illumination scheme, the application time, the use of iron chelators and the use of penetration enhancers [8-9].

Our group observed new formation of PpIX in time after single illumination in the past and subsequently investigated this in various animal models [10-12]. A two-fold illumination scheme, separated by a substantial dark interval and a small first light fraction, increased response to PDT. We tested this light fractionated scheme in a clinical setting in sBCC's and found a significant improvement in response compared to single illumination. One year response rates in fractionated ALA PDT were 97% [13] and in another study with different light treatment parameters, 5 year response rate was 84% [14]. This approach appears to compare favorably with the results for methyl aminolevulinate (Metvix®), where two-year response rates for primary 'difficult to treat' BCC are 76% [15] and 78% for patients prone to complications and poor cosmetic outcome with conventional treatment [16].

The main disadvantage of PDT is that it is often a painful treatment [17], limiting the suitability of PDT as a treatment of first choice. Patients report a burning or tingling sensation that sometimes leads to need for local anesthesia or termination of therapy. Especially treating extensive field cancerization with actinic keratosis in the face and scalp region is painful for the patient [17-18]. The exact mechanism underlying the pain is unclear. Some authors suggested that pain increases with higher PpIX concentrations, although results are conflicting [17, 19, 20]. It has also been proposed that the methyl ester (Metvix®) produces less pain than ALA [21]. Recently a number of authors have reported significantly less pain during PDT using lower fluence rates [22-24] with low VAS

scores at 20 mW cm^{-2}. Besides the advantage in pain perception, it is well documented that using lower fluence rate PDT results in more efficient usage of the available oxygen in tissue [25-30].

We would like to incorporate the use of low fluence rate to light fractionated ALA-PDT to maintain effectiveness while minimizing pain. Therefore we designed the present study comparing high and low fluence rate PDT and several illumination schemes in hairless mouse skin. These schemes were in part the same as used in previous studies from our group at 50 mW cm^{-2} and new groups were introduced using 20 mW cm^{-2}. We delivered a cumulative total fluence (first + second light fraction) of 100 J cm^{-2} and lowered this to 50 J cm^{-2} since this is the range of fluence that was studied previously and to minimize treatment time.

There are some obstacles that must be overcome when using lower fluence rate PDT. At 20 mW cm^{-2} treatment time will be 2.5 times longer compared to 50 mW cm^{-2} when the total fluence is kept constant. For clinical purposes short treatment times are strived for. As mentioned before, low fluence rate PDT leads to more efficient use of available oxygen. This indicates that less fluence is needed at 20 mW cm^{-2}, which as a result may keep treatment times constant [19]. Here a question arises as to how much less fluence needs to be delivered to achieve the same effect. This is an issue for both the first and second illumination. Especially dosing of the relatively small first light fraction is critical for maintaining PDT efficacy, as we showed previously [11], necessitating us to employ more accurate dosing than using a predetermined fluence.

Therefore, a novel dosing method for the first light fraction was adopted, making use of PpIX fluorescence measurements. During the photodynamic process, PpIX is destroyed by singlet oxygen, in a process termed photobleaching. In ALA-PDT the rate of PpIX photobleaching is directly related to the amount of singlet oxygen produced and can potentially be used as a predictor of PDT induced response. In normal mice skin where the variations in the amount of PpIX are relatively small the normalized extent of photobleaching can be used a predictor of the PDT dose deposited [27-31]. In the present study we have used a fixed photobleaching percentage to determine when to stop the first illumination.

Our goal was to investigate if the animals that were illuminated at 20 mW cm^{-2} would react in a similar way to fractionated ALA-PDT as the animals that were illuminated at 50 mW cm^{-2} with respect to PpIX fluorescence kinetics and damage response. Visual damage

to normal hairless mouse skin was used as a measure for efficacy. We hypothesized that 20 mW cm^{-2} is as effective as 50 mW cm^{-2} in inducing visually assessed skin damage.

MATERIALS AND METHODS

ANIMALS

Thirty-six female albino hairless mice (SKH1 HR) were included in this experiment, divided into six groups that received different treatment parameters as described below. Animals were put on a chlorophyll-free diet two weeks prior to treatment to remove autofluorescence from pheophorbide-a. The study was approved by the animal experimental committee of the Erasmus University Medical Centre.

ALA APPLICATION

Animals were anesthetized with ketamine and valium before the application of 20% 5-aminolevulinic acid (ALA, Medac, Hamburg, Germany), dissolved in 3% carboxymethylcellulose and NaOH in water (pH=4) to the skin using a 7 mm round gauze, and occluded with a semi occlusive dressing (Tegaderm®). A spot on the left thigh of the mice was chosen as the illumination area. There was a four hour interval between ALA application and the delivery of the first light fraction. Prior to and during illumination animals were again anesthetized using 2-3% Isoflurane in 100% oxygen.

GROUPS OF ANIMALS AND LIGHT TREATMENT PARAMETERS

We used six different illumination schemes (n=6 animals in each group). For delivered fluences per group see also table 2.1. Groups 1-3 served as control groups for comparison with experiments performed previously at 50 mW cm^{-2}, while groups 4-6 were illuminated at 20 mW cm^{-2}. Group 1 received 100 J cm^{-2} in a single illumination at 50 mW cm^{-2}. All other groups received two light fractions, separated by a dark interval of two hours. The exact duration of the illuminations in the first light fraction in groups 2 to 6 was based on the extent of PpIX fluorescence photobleaching measured during PDT in individual animals. This individualization of the first light fraction is described in more detail in the data analysis section below. Each animal received a fluence that was needed to bleach 52% of initial PpIX in the first light fraction, with an additional fluence during the second light fraction to reach various total fluences. Groups 2 and 3 were illuminated at 50 mW cm^{-2} to a total dose of 100 and 50 J cm^{-2} respectively. Groups 4 and 5 were illuminated at 20 mW cm^{-2} to a total dose of 100 and 50 J cm^{-2} respectively. Group 6 received the same

treatment scheme as group 5 immediately followed by 50 J cm^{-2} at 50 mW cm^{-2}. This was based on a recent study, investigating the use of low fluence rates for the treatment of sBCC where PpIX photobleaching measurements were used as a method of determining the point during therapy where the fluence rate could be increased without inducing pain [23].

PDT LIGHT DELIVERY

The experimental set-up was adapted from that which we used previously [32], to maximize the amount of fluorescence light collected from the tissue and facilitate spectral fitting of the data. Figure 2.1 shows a schematic overview of the setup. During PDT, an Argon Ion laser (514 nm) was used as the treatment light source with fluences of either 20 or 50 mW cm^{-2}. Light was delivered via a 400 µm optical fiber and focused on a homogenous 7 mm treatment area on the mouse skin via a dichroic mirror using a micro lens (QLT, Vancouver, BC, Canada) and a single biconvex lens. A charged coupled device (CCD) camera (ORCA-ER, Hamamatsu, Japan) was used for taking fluorescence images, to relocate the area of interrogation and maintain a constant distance between the mouse skin and the head of the spectrograph.

FLUORESCENCE MEASUREMENTS

Fluorescence intensity was used as a measure of the PpIX concentration in the tissue. Fluorescence emission was collected from the illuminated area and focused into a 1 mm optical fiber coupled to a spectrograph (USB4000, Ocean Optics, Duiven, The Netherlands) via a 50/50 beam-splitter. Fluorescence spectra were taken continuously during the first and second illumination with integration times of 1000 ms and 2000 ms for 50 mW cm^{-2} and 20 mW cm^{-2} respectively, without interrupting PDT light delivery. Scattered excitation light was blocked using a long-pass filter (570 nm, Melles Griot, Zevenaar, The Netherlands), placed in the optical path.

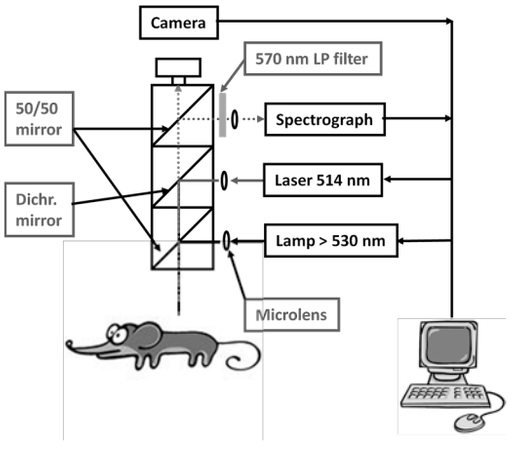

Figure 2.1: *PDT-Imaging setup.*

During the first light fraction, spectra were analyzed in real-time as described below to calculate the percentage of photobleaching and the illumination was terminated automatically when the extent of PpIX fluorescence photobleaching had reached 52% of its initial value. This value

was based on highest damage scores with this bleaching percentage in previous experiments [10].

REFLECTANCE SPECTROSCOPY

Reflectance spectra were obtained before and immediately after illumination for correcting the fluorescence spectra for changes in tissue optical properties in the fluorescence emission band. Light from a halogen lamp (0.15 mW cm^{-2}, Stortz, Tutlingen, Germany) was filtered with a long-pass filter (OG 530, Melles Griot, Zevenaar, the Netherlands) to minimize fluorescence excitation of the tissue during reflectance measurements, and delivered via another optical fiber and focused on the same 7 mm treatment area using a second 50/50 beam splitter. Reflected light was collected using the same system as the fluorescence emission. This enables fluorescence and reflection measurements being acquired using the same source-detection geometry. A white plastic reference card (Vink, Didam, The Netherlands) was used to correct spectra for small changes in light intensity and spectral output.

DATA ANALYSIS

The reflectance spectra before and after illumination were corrected for changes in light intensity, spectral lamp output and background with the use of the reference card. These spectra can be used to detect changes in tissue optical properties during illumination and correct the PpIX fluorescence intensity for this with a method first suggested by Wu et al [33]. Fluorescence spectra were analyzed in real-time during the first illumination. Spectra were analyzed as a linear combination of the basis fluorescence spectra of normal mouse skin, autofluorescence and hydroxyaldehyde chlorin photoproduct of PpIX, using a single value decomposition (SVD) algorithm. The output of this analysis yields information on the PpIX fluorescence intensity. The decrease of PpIX fluorescence intensity over time was used to determine the rate and the extent of PpIX photobleaching. The first illumination was terminated when the PpIX fluorescence was decreased by 52% of its original value. The spectra acquired during the first and second illumination were analyzed more extensively after the end of therapy. The fitted PpIX intensity values were corrected for different integration times and laser light intensities for accurate comparison and if necessary corrected for changes in tissue optical properties. These fluorescence intensities were normalized to 100% at the start of the first illumination using a second-order-decay fit [27]. The fluorescence intensity at the start of the second light fraction was either again normalized to 100%, or presented as a percentage of the fluorescence intensity at the start of the first illumination.

DAMAGE SCORE

Damage scoring was performed daily up to seven days post PDT by 2 investigators blinded from the treatment schemes (by HdeB and AvdP). We used a visual scoring system, that we have described previously [27], with a zero to five-point scale: Grade 0 means no damage; 1=minimal erythema; 2=moderate erythema; 3=severe edema or a white blister; 4=thin crust and 5=thick crust. The severity and extent of PDT response was measured and scored where different levels of severity were considered within each treatment field. The overall damage score was calculated according to the damage and the relative contribution of each region. Means were calculated per group of mice and plotted against time. The distribution of maximum damage score per group over time was evaluated using daily photographs.

STATISTICS

In a previous experiment [11] we measured a cumulative damage score of 17±4 SD (n=19) for control group 1 and 25±4 SD (n=15) for control group 2. Since we expect 20 mW cm^{-2} to be as effective in inducing skin damage as 50 mW cm^{-2}, the expected skin damage for group 4 would be equal to group 2. A power analysis with α=0.05 and β=0.80 results in n=6 per group.

For calculating differences in total damage scores between groups Student-Newman-Keuls multiple comparisons testing was performed, after calculating the total area under the curve (AUC) for subsequent daily damage scores.

RESULTS

REFLECTANCE MEASUREMENTS

Figure 2.2 shows the average reflectance spectra measured immediately before and after the first light fraction for animals treated in groups 2 and 3 (at 50 mW cm^{-2}).

Table 2.1: *Treatment group parameters*

Group	mW cm^{2}	J cm^{-2}	Delivered fluence ± SD (J cm^{-2})		Illumination Time	
			1st fraction	2nd fraction	1st fraction	2nd fraction
1	50	100	100	-	33 min	-
2	50	100	4.44 ± 0.45	95.56	1 min 29 sec	31 min 51 sec
3	50	50	5.20 ± 1.06	44.80	1 min 44 sec	14 min 56 sec
4	20	100	3.67 ± 0.34	96.33	3 min 6 sec	80 min 17 sec
5	20	50	3.74 ± 0.42	46.26	3 min 7 sec	38 min 33 sec
6	20 + 50	100	4.28 ± 0.86	45.72 + 50	3 min 35 sec	54 min 46 sec

Both spectra show the absorption features that are expected from tissue in this region of the spectrum (560-860 nm). Mice from all other groups showed the same response. There is very little change in the absorption of mouse skin before and after illumination when reflectance is measured in this geometry. Therefore, the PpIX fluorescence intensities shown in this study are not corrected for changes in tissue optical properties.

DELIVERED FLUENCE IN FIRST LIGHT FRACTION

Delivered fluences in the first and second illumination and treatment times per group are shown in table 2.1. Less fluence is needed in the low fluence rate groups and treatment times are longer.

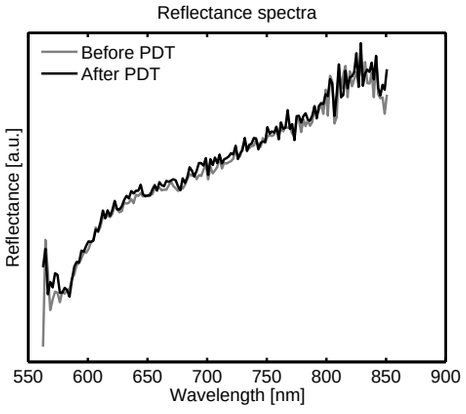

Figure 2.2: *Reflectance intensity before and after PDT in the range of 560-860 nm. Reflectance is shown as arbitrary units. The grey line represents measurement before and the black line after PDT.*

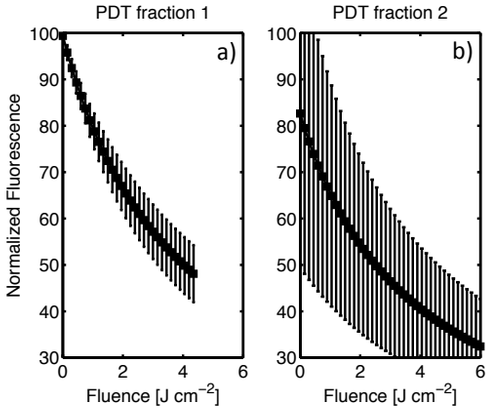

Figure 2.3: *Mean normalized PpIX photobleaching in the first (panel a) en second (panel b) illumination in groups 2 and 3 (50 mW cm^{-2}), separated by a dark interval of 2 hours. Error bars indicate one standard deviation.*

PPIX FLUORESCENCE DURING ILLUMINATION

Figure 2.3 shows the mean normalized PpIX fluorescence intensity during a two-fold illumination in which a total dose of 100 J cm^{-2} is delivered 4 and 6 hours after ALA application at a fluence rate of 50 mW cm^{-2} (group 2). Data from the first light fraction (panel a) and second light fraction (panel b) are separated by a 2 hour dark interval. The first illumination was terminated when the intensity of PpIX fluorescence had bleached by 52%. In the 2 hour dark interval PpIX fluorescence increased to over 80% of the initial value. This increase is subject to large variation, as indicated by large error bars. For both illuminations the first 6 J cm^{-2} is shown for clarity: the second light fraction continued on to a total of 100 J cm^{-2}, after which approximately 3.2% of the initial PpIX intensity at the start of the first light fraction remained.

Figure 2.4 shows the mean normalized PpIX photobleaching for the first illumination to illustrate differences with respect to fluence rate.

The 20 mW cm^{-2} groups (4, 5 and 6) show more efficient photobleaching than the 50 mW cm^{-2} groups (2 and 3). At lower fluence rates, less fluence is needed to bleach 52% of available PpIX (P=0.002). For clarity only the first 6 J cm^{-2} is shown.

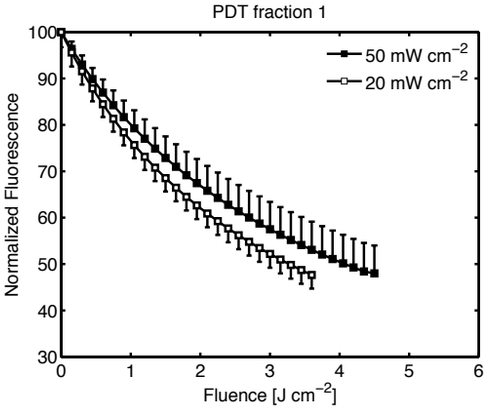

Figure 2.4: *Mean normalized PpIX photobleaching for the first illumination for different fluence rates. The full squares indicate averages at 50 mW cm^{-2} (groups 2 and 3). The open squares indicate averages at 20 mW cm^{-2} (groups 4, 5 and 6). At 20 mW cm^{-2} less fluence is needed to bleach 52% of available PpIX (P=0.002). Error bars indicate one standard deviation.*

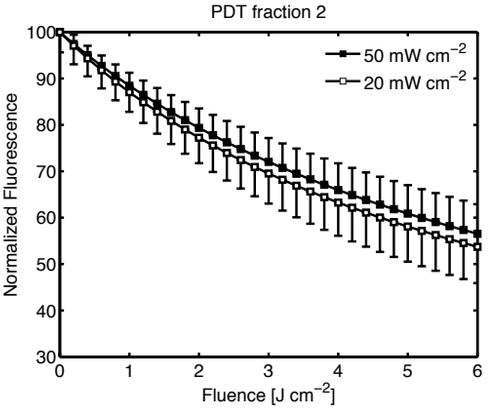

Figure 2.5: *Mean normalized PpIX photobleaching for the second illumination for different fluence rates. The open squares represent averages of the 20 mW cm^{-2} groups and full squares averages of the 50 mW cm^{-2} groups.*

Figure 2.5 shows the mean normalized PpIX photobleaching for the second illumination for different fluence rates. The 20 mW cm^{-2} groups again show a non-significant trend towards faster bleaching than the 50 mW cm^{-2} groups. In group 6, (50 J cm^{-2} at 20 mW cm^{-2} using a fractionated illumination, followed by 50 J cm^{-2} at 50 mW cm^{-2}), no change in bleaching rate was observed when the fluence rate was increased from 20 to 50 mW cm^{-2} (data not shown).

DAMAGE SCORE

Damage scores for the first seven days after PDT were measured. One day after PDT severe edema or white blister formation was visible, while damage increased over time up to day four when highest damage scores were observed.

Figure 2.6 shows the mean damage scores for each group of animals, calculated as the area under the curve (AUC) for subsequent daily damage scores.
All fractionated groups have higher total damage scores than the single illumination group and statistical differences are indicated by arrows with their P-values (ANOVA, Student-Newman-Keuls test).

In figure 2.7 the maximum score reached at any time point within the treated area is shown per group of six mice. Only in group 1, where a single illumination to 100 J cm^{-2} at 50 mW cm^{-2} is delivered, three mice had maximum scores of 3, representing severe edema or a white blister. In all other groups all mice reached maximum scores of either 4 or 5, representing a thin or thick crust respectively.

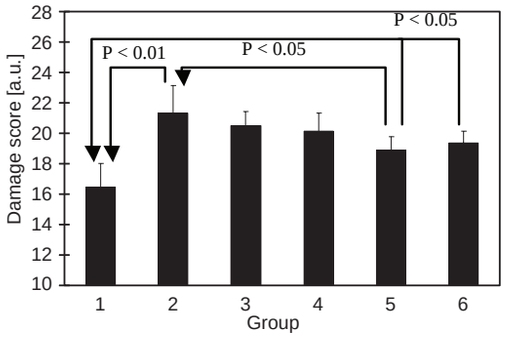

Figure 2.6: *Mean damage score for seven days after PDT for each group of animals, calculated as the area under the curve for subsequent daily damage scores. Differences between groups are illustrated by arrows and P-values (Student-Newman-Keuls test).*

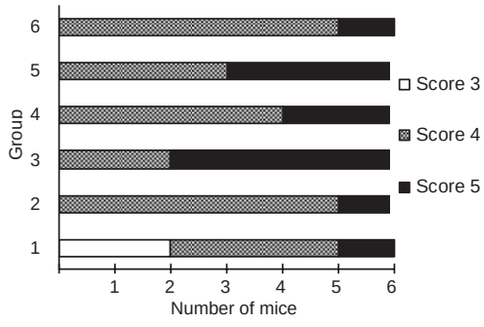

Figure 2.7: *The maximum score reached (regardless of day or size) per group of mice. Only in group 1 (single illumination group) no higher damage score than 3 was observed. Groups 2-6 appear to be similar to each other with minimum scores of either 4 or 5 (5=maximum possible score).*

DISCUSSION

This study was designed to investigate the efficacy of low fluence rate ALA-PDT in normal mouse skin. Our primary outcome was visual skin damage and this model has previously successfully been used as an indicator for clinical PDT efficacy. Our results show that low fluence rate ALA-PDT is as effective as high fluence rate PDT in inducing skin damage in normal mouse skin. We used real-time PpIX fluorescence spectroscopy to provide us with more insight into the complex mechanisms and interactions of light, PpIX formation and depletion, oxygen consumption, and photoproduct formation during PDT. Results are in line with the concept that low fluence rate ALA-PDT results in more efficient use of available oxygen. An important and novel modification in the present study was the use of a fixed PpIX photobleaching percentage for the first illumination, instead of using a fixed fluence. In normal mouse skin using the light treatment parameters we have chosen in the present study, the percentage photobleaching is likely to be well correlated to the amount of singlet oxygen formed, and therefore to the PDT dose delivered in a single light fraction. When using a fixed fluence scheme there is risk of delivering too much or too little fluence during the first light fraction due to inter-individual variations in photobleaching rate. Previously we have shown that this results in less PDT damage [11]. For this reason we used real-time fluorescence measurements to determine PpIX photobleaching as a way of standardizing the effective PDT dose for the first illumination in both high and low fluence rate groups. We stress the importance of monitoring PpIX photobleaching during illumination since it makes comparing the different illumination schemes more reliable. We chose to deliver as much fluence as needed to bleach 52% of available PpIX for the first illumination, based on previous experiments in normal mouse skin. It is important to note that the normalization step should be made with care. The fluorescence intensity variations in the skin of normal hairless mice are relatively small and of the order of 25% of the average initial PpIX intensity before the first light fraction. To accommodate large variations in the initial PpIX concentration in skin that may be present in other (clinical) lesions would require a more thorough analysis of PDT dose deposition so that the treatment parameters could be changed accordingly. It is probable that the 'optimal' bleaching dose may be different or variable for individual patients and lesions and for different dermatological conditions, which could differ in intrinsic response to PDT, blood supply and thickness of the lesion. It should also be noted that this photobleaching method is only valid for photosensitizers that undergo photobleaching mediated by singlet oxygen alone. For instance, the hematoporphyrin derivative Photofrin® can also be bleached via other mechanisms [34].

We also measured reflectance spectra before and after PDT. Previously, we always corrected the PpIX fluorescence measurements for possible changes in optical properties of the tissue layer the emitted PpIX fluorescence has to travel through. It is reasonable to assume that the tissue absorption will change, due to PDT-induced changes in blood flow and saturation. Any change in absorption of this tissue layer will bias the PpIX fluorescence intensity measurements at the skin surface. The results from our reflectance measurements, as illustrated in figure 2.2, indicate that correcting is not necessary when using our measurement method. This does not necessarily mean that the tissue optical properties in the superficial skin layer do not change; it is possible that other measurement methods could reveal such changes. The measurement volume over which the reflectance measurements are taken is much deeper than the superficial treatment effect of PDT. The influence of this dimension mismatch will be the scope of future investigation.

We were able to reproduce the results that we have found previously. The PpIX photobleaching kinetics for the two-fold illumination schemes at 50 mW cm^{-2}, as illustrated in figure 2.3, show a similar photobleaching rate as previous studies [10, 11, 27] during the first and second illumination as well as a comparable increase in PpIX fluorescence to around 80% of the initial value during the dark interval and subsequent bleaching to under 5% at the end of the second illumination. These groups of animals (groups 2 and 3) and their results therefore serve as controls for the 20 mW cm^{-2} groups.

In accordance to several previous studies, we found that illuminating at lower fluence rates (20 mW cm^{-2}) results in more efficient PDT than at higher fluence rates (50 mW cm^{-2}), as is illustrated in figure 2.4 and table 2.1. Using higher fluence rates causes depletion of available oxygen during PDT, interrupting the continuous PpIX photobleaching process. The treatment time for the first illumination is approximately two times longer in the 20 mW cm^{-2} groups than in the 50 mW cm^{-2} groups, instead of 2.5 times as would be the case if the photobleaching rate were the same. However, the amount of fluence needed (and as a result also treatment time) does not decrease proportionally with decreasing fluence rate. The consequence of this is that treatment times remain longer at lower fluence rates if the same amount of total photobleaching is desired. Our choice of low fluence rate in the present study was based on our wish to minimize pain in clinical PDT. Since it may be possible to further reduce the pain associated with the illumination by further reducing the fluence rate, it is interesting to consider the relationship between fluence rate and the fluence needed to achieve a fixed photobleaching percentage. In previous studies, we and others [26-27] have shown that

the efficiency of PpIX photobleaching was even higher when the fluence rate is reduced to 5 mW cm^{-2} and lower for fluence rates above 50 mW cm^{-2}. Finlay et al [26] have shown that the efficiency of photobleaching increases even further for lower fluence rates in rat skin. Theoretically there will be a maximum efficiency of photobleaching below 1 mW cm^{-2}, where PDT efficiency is optimal. The practical value of delivering PDT at these very low fluence rates remains unclear, since treatment times will likely be very long at very low fluence rates.

For the second illumination we also observed a trend to faster photobleaching in the 20 mW cm^{-2} groups compared to the 50 mW cm^{-2} groups, as is shown in figure 2.6. This indicates that also for the second illumination, which is longer than the first, low fluence rate photobleaching occurs somewhat more efficiently. In the first illumination the difference is much more obvious however. This may be explained by vasodilatation after the first illumination, increasing oxygen availability during the second illumination.

When comparing damage scores between groups, figures 2.6 and 2.7 illustrate different methods of damage scoring. Groups 1-3 apply illumination schemes that we have used in previous experiments and skin damage scores are consistent to the results from these previous experiments, while groups 4-6 were the low fluence rate groups. As is shown in figure 2.6, the single illumination group 1 has the lowest total damage score. All the other groups have higher scores with the highest in group 2 (100 J cm^{-2} at 50 mW cm^{-2}). Our special interest was whether the low fluence rate groups (4, 5 and 6) would score significantly better than the single group and not significantly worse than the control group 2. All low fluence rate groups have a significant higher total damage score compared to the single illumination group. Groups 4 and 6 (100 J cm^{-2} total) are not statistically different from group 2, but only group 5 (50 J cm^{-2} in total) is borderline statistically worse than group 2. Total differences between all fractionated groups are small however. A small, but statistical difference may not necessarily represent a clinically relevant difference.

We used damage to normal mouse skin as a substitute for clinical effect, because this model previously proved to be a good translational model [10-11, 13, 27]. In the present study we extended the previously used model by measuring maximum damage, which is likely to be also indicative of PDT effect. It is important however to realize that in a clinical setting, PDT effect is based on destruction of dysplastic tissue instead of normal tissue and in human skin instead of mouse skin.

From figure 2.7 it is clear that in the single illumination (group 1) maximum scores were more shifted towards lower scores than in the fractionated groups 2-6, while there is no

apparent difference in score between these fractionated groups. A difference in the results in this scoring method and the one illustrated in figure 2.6 is that group 5 (50 J cm^{-2}) has three animals with highest maximum damage scores and does not appear to be worse than any other group. Combining the different damage scoring methods, there appears to be no difference between high and low fluence rate groups in terms of inducing visual skin damage.

Taking the results from this study into account when designing a clinical trial comparing low and high fluence rate light fractionated PDT, there are additional considerations. As is clear from our results there is no proportional relationship between fluence and fluence rate for a fixed bleaching percentage. This means that treatment times will remain longer at lower fluence rates when the same amount of PpIX bleaching is used as a treatment metric.

The clinical implications of this are important because treatment times for the second illumination could be substantially longer using lower fluence rates. The duration of the first illumination is in the order of a few minutes so differences will be small and clinically irrelevant. In group 2 (100 J cm^{-2} at 50 mW cm^{-2}) the second illumination takes 31 minutes and at the end on average 3.2% (SD 1.5) of initial PpIX is left. For group 5 (50 J cm^{-2} at 20 mW cm^{-2}) the second illumination takes 40 minutes, leaving 7.7% (SD 2.7) of PpIX. In group 6 (50 J cm^{-2} at 50 mW cm^{-2} followed by 50 J cm-2 at 50 mW cm^{-2}) the second illumination takes 56 minutes and 2.9% (SD 1.0) of PpIX is left. Interestingly, the bleaching rate does not change at the point when fluence rate is increased. Probably the amount of oxygen is no longer the limiting factor for PpIX photobleaching but the concentration of PpIX is. It is unclear however what the biological advantage is of illuminating tissues with very little PpIX content. An interesting extension of the present study would be to use a fixed remaining PpIX percentage to stop the second illumination, but it will be difficult to determine this percentage.

It is also important to recognize that mouse skin is considerably thinner compared to human skin. Theoretically, deeper layers of skin may need higher total fluences since fluence rate decreases exponentially in tissue with increasing depth. Especially in the deeper bases of sBCC the fluence at depth may be an important consideration. Also the variation in vascularisation of tumor tissue results in variable light absorption and oxygen supply. Therefore it theoretically makes sense to have a clinical illumination scheme based on the illumination scheme of group 6 (50 J cm^{-2} at 20 mW cm^{-2} followed by 50 J cm^{-2} at 50 mW cm^{-2}). Effectiveness is expected to be maintained, pain is expected to be minimal and treatment times remain relatively short.

CONCLUSION

In conclusion the present study shows that low fluence rate, light fractionated ALA-PDT appears to be as effective in inducing visual skin damage in mouse skin, while PpIX photobleaching occurs more efficiently. This in part limits the duration of therapy, although lower fluence rate PDT does result in longer illuminations when the same amount of photobleaching is desired. There is need for further investigations that should include a clinical trial investigating pain and clinical efficacy using low and high fluence rate fractionated PDT, while performing PpIX fluorescence measurements. Maintaining high efficacy of therapy should be the most important consideration, while pain and treatment time must be carefully weighted against each other. Thickness of lesions must be taken into account when interpreting the results from the present study because of differences in thickness between mouse and human skin.

REFERENCES

1. Marks, R., *An overview of skin cancers. Incidence and causation*. Cancer, 1995. **75**(2 Suppl): p. 607-612.
2. Salasche, S.J., *Epidemiology of actinic keratoses and squamous cell carcinoma*. Journal of American Academia of Dermatology, 2000. **42**(1 Pt 2): p. 4-7.
3. Diepgen, T.L., V. Mahler, *The epidemiology of skin cancer.* British Journal of Dermatology, 2002. **146**(Suppl 61): p. 1-6.
4. de Vries, E., L.V. van de Poll-Franse, W.J. Louwman, F.R de Gruijl, J.W. Coebergh, *Predictions of skin cancer incidence in the Netherlands up to 2015*. British Journal of Dermatology, 2005. **152**(3): p. 481-488.
5. Trakatelli, M., C. Ulrich, V. del Marmol, S. Euvrard, E. Stockfleth, D. Abeni, *Epidemiology of nonmelanoma skin cancer (NMSC) in Europe: accurate and comparable data are needed for effective public health monitoring and interventions.* British Journal of Dermatology, 2007. **156**(Suppl 3): p. 1-7.
6. Morton, C.A., K.E. McKenna, L.E. Rhodes, *Guidelines for topical photodynamic therapy: update.* British Journal of Dermatology, 2008. **159**(6): p. 1245-1266.
7. Braathen, L.R., et al., *Guidelines on the use of photodynamic therapy for nonmelanoma skin cancer: an international consensus.* International Society for Photodynamic Therapy in Dermatology, 2005. Journal of the American Academia of Dermatology, 2007. **56**(1): p. 125-143.
8. Wilson, B.C., M.S. Patterson, *The physics, biophysics and technology of photodynamic therapy.* Physics in Medicine and Biology, 2008. **53**(9): p. R61-109.
9. Gerritsen, M.J., T. Smits, M.M. Kleinpenning, P.C. van de Kerkhof, P.E. van Erp, *Pretreatment to Enhance Protoporphyrin IX Accumulation in Photodynamic Therapy.* Dermatology, 2008. **11**: p.11.
10. de Bruijn, H.S., A. van der Ploeg-van den Heuvel, H.J.C.M. Sterenborg, D.J. Robinson, *Fractionated illumination after topical application of 5-aminolevulinic acid on normal skin of hairless mice: the influence of the dark interval.* Journal of Photochemistry and Photobiololgy, B: Biology, 2006. **85**(3):p. 184-190.
11. Robinson, D.J., H.S. de Bruijn, W.M. Star, H.J.C.M. Sterenborg, *Dose and timing of the first light fraction in two-fold illumination schemes for topical ALA-mediated photodynamic therapy of hairless mouse skin.* Photochemistry & Photobiology, 2003. **77**(3): p. 319-323.
12. van der Veen, N., H.L. van Leengoed, W.M. Star, *In vivo fluorescence kinetics and photodynamic therapy using 5-aminolaevulinic acid-induced porphyrin: increased damage after multiple irradiations.* British Journal of Cancer, 1994. **70**(5): p. 867-872.
13. de Haas, E.R., B. Kruijt, H.J.C.M. Sterenborg, H.A.M. Neumann, D.J. Robinson, *Fractionated illumination significantly improves the response of superficial basal cell carcinoma to aminolevulinic acid photodynamic therapy.* Journal of Investigative Dermatology, 2006. **126**(12): p. 2679-2686.
14. Star, W.M., A.J. van't Veen, D.J. Robinson, K. Munte, E.R. de Haas, H.J.C.M. Sterenborg, *Topical 5-aminolevulinic acid mediated photodynamic therapy of superficial basal cell carcinoma using two light fractions with a two-hour interval: long-term follow-up.* Acta Dermato-venerologica, 2006. **86**(5): p. 412-417.
15. Vinciullo, C., et al. *Photodynamic therapy with topical methyl aminolaevulinate for 'difficult-to-treat' basal cell carcinoma.* British Journa of Dermatology, 2005. **152**(4): p. 765-72.
16. Horn, M., et al., *Topical methyl aminolaevulinate photodynamic therapy in patients with basal cell carcinoma prone to complications and poor cosmetic outcome with conventional treatment.* British Journal of Dermatology, 2003. **149**(6): p. 1242-1249.

17. Grapengiesser, S., M. Ericson, F. Gudmundsson, O. Larko, A. Rosen, A.M. Wennberg, *Pain caused by photodynamic therapy of skin cancer.* Clinical Experimental Dermatology, 2002. **27**(6): p. 493-497.

18. Sandberg, C., et al., *Important factors for pain during photodynamic therapy for actinic keratosis.* Acta Dermato-venereologic, 2006. **86**(5): p. 404-408.

19. Ericson, M.B., et al., *Photodynamic therapy of actinic keratosis at varying fluence rates: assessment of photobleaching, pain and primary clinical outcome.* British Journal of Dermatology, 2004. **151**(6): p. 1204-1212.

20. Wiegell, S.R., J. Skiveren, P.A. Philipsen, H.C. Wulf. *Pain during photodynamic therapy is associated with protoporphyrin IX fluorescence and fluence rate.* British Journal of Dermatology, 2008. **158**(4): p. 727-733.

21. Moloney, F.J., P. Collins, *Randomized, double-blind, prospective study to compare topical 5-aminolaevulinic acid methylester with topical 5-aminolaevulinic acid photodynamic therapy for extensive scalp actinic keratosis.* British Journal of Dermatology, 2007. **157**(1): p. 87-91.

22. Clark, C., A. Bryden, R. Dawe, H. Moseley, J. Ferguson, S.H. Ibbotson, *Topical 5-aminolaevulinic acid photodynamic therapy for cutaneous lesions: outcome and comparison of light sources.* Photodermatology, Photoimmunology and Photomedicine, 2003. **19**(3): p. 134-141.

23. Cottrell, W.J., A.D. Paquette, K.R. Keymel, T.H. Foster, A.R. Oseroff, *Irradiance-dependent photobleaching and pain in delta-aminolevulinic acid-photodynamic therapy of superficial basal cell carcinomas.* Clinical Cancer Research, 2008. **14**(14): p. 4475-4483.

24. Wiegell, S.R., M. Haedersdal, P.A. Philipsen, P. Eriksen, C.D. Enk, H.C. Wulf, *Continuous activation of PpIX by daylight is as effective as and less painful than conventional photodynamic therapy for actinic keratoses; a randomized, controlled, single-blinded study.* British Journal of Dermatology, 2008. **158**(4): p. 740-746.

25. Langmack, K., R. Mehta, P. Twyman, P. Norris, *Topical photodynamic therapy at low fluence rates--theory and practice.* Journal of Photochemistry & Photobiology, B: Biology, 2001. **60**(1): p. 37-43.

26. Finlay, J.C., D.L. Conover, E.L. Hull, T.H. Foster, *Porphyrin bleaching and PDT-induced spectral changes are irradiance dependent in ALA-sensitized normal rat skin in vivo.* Photochemistry & Photobiology, 2001. **73**(1): p. 54-63.

27. Robinson, D.J., H.S. de Bruijn, N. van der Veen, M.R. Stringer, S.B. Brown, W.M. Star, F*luorescence photobleaching of ALA-induced protoporphyrin IX during photodynamic therapy of normal hairless mouse skin: the effect of light dose and irradiance and the resulting biological effect.* Photochemistry & Photobiology 1998. **67**(1): p. 140-149.

28. Foster, T.H., R.S. Murant, R.G. Bryant, R.S. Knox, S.L. Gibson, R. Hilf, *Oxygen consumption and diffusion effects in photodynamic therapy.* Radiation Research, 1991. **126**(3): p. 296-303.

29. Sitnik, T.M., B.W. Henderson, *The effect of fluence rate on tumor and normal tissue responses to photodynamic therapy.* Photochemistry Photobiology, 1998. **67**(4): p. 462-466.

30. Henderson, B.W., et al., *Photofrin photodynamic therapy can significantly deplete or preserve oxygenation in human basal cell carcinomas during treatment, depending on fluence rate.* Cancer Research, 2000. **60**(3): p. 525-529.

31. Robinson, D.J., H.S. de Bruijn, W.J. de Wolf, H.J.C.M. Sterenborg, W.M. Star, *Topical 5-aminolevulinic acid-photodynamic therapy of hairless mouse skin using two-fold illumination schemes: PpIX fluorescence kinetics, photobleaching and biological effect.* Photochemistry & Photobiology, 2000. **72**(6): p. 794-802.

32. de Bruijn, H.S., et al., *Light fractionation does not enhance the efficacy of methyl 5-aminolevulinate mediated photodynamic therapy in normal mouse skin.* Photochemistry & Photobiological Sciences, 2007. **6**(12): p. 1325-1331.

33. Wu, J., M. Feld, R. Rava, *Analytical model for extracting intrinsic fluorescence in turbid media.* Applied Optics, 1993. **32**(19): p. 3585-3595.

34. Finlay, J.C., S. Mitra, M.S. Patterson, T.H. Foster, *Photobleaching kinetics of Photofrin in vivo and in multicell tumour spheroids indicate two simultaneous bleaching mechanisms.* Physics in Medicine and Biology, 2004. **49**(21): p. 4837-4860.

Chapter 3

The Effect of Fluence Rate on the Acute Response of Vessel Diameter and Red Blood Cell Velocity during Topical 5-ALA Photodynamic Therapy

Floor van Leeuwen – van Zaane,
Riëtte de Bruijn, Angélique van der Ploeg – van den Heuvel,
Dick Sterenborg, Arjen Amelink, Dominic Robinson

Photodiagnosis and Photodynamic Therapy, 2014.
In press

ABSTRACT

In a previous study it is shown that for topically applied ALA-PDT, PpIX concentration correlates with vascular changes including vasoconstriction and/or vascular leakage of small vessels and arterioles in the mouse epidermis and dermis. In this study we report on vascular responses induced by ALA-PDT for different fluence rates, including both changes in vessel diameter and dynamics in blood flow in arterioles, imaged using intra-vital confocal microscopy in skinfold chambers in hairless mice. Our interest is in the dynamics of vascular changes in the early stages of illumination. We have determined the total PDT dose to be relatively low, 13 J cm^{-2}, and fluence rates of 26, 65 and 130 mW cm^{-2} were investigated. Local vascular effects occurred very soon after the start of the therapeutic illumination in ALA-PDT. In this study, we did not find a significant difference between fluence rates. Arterioles were particularly sensitive to vasoconstriction during low dose PDT, often resulting in complete vasoconstriction. When we observed complete vasoconstriction, this coincided with changes in RBC velocity. Since the therapeutic effects of PDT are dependent on a fine balance between the need for oxygen during illumination and disruption of the vasculature, the results of the present study add to our understanding of acute vascular effects during ALA-PDT and aid our efforts to optimize PDT using porphyrin pre-cursors.

INTRODUCTION

Photodynamic therapy (PDT) using topically applied porphyrin precursors is a treatment modality used for various (pre-)malignant skin lesions [1, 2]. The precursor 5-aminolevulinic acid (ALA), and its esterified derivatives methyl aminolevulinate (MAL) and hexyl aminolevulinate (HAL), are taken up by cells and converted into the endogenous photosensitizer protoporphyrin IX (PpIX) by means of the haem cycle [3]. The application of an excess of exogenous ALA leads to the accumulation of therapeutic concentrations of PpIX. During illumination, PpIX mediates the transfer of energy from light to molecular oxygen, resulting in the generation of reactive oxygen species (ROS). These ROS have a very short lifetime and diffusion radius and cause damage to nearby critical tissue structures through a combination of cellular, vascular and immunological pathways [4, 5].

Since the formation of reactive oxygen species is the initiator of local tissue damage during PDT, tissue oxygenation and therefore the local blood supply plays an important role in determining tissue response to PDT. The role of the local blood supply during PDT is multifaceted. Some (mainly intravenous administered) photosensitizers directly target the vasculature, which upon illumination results in irreversible damage to vessels and thereby destruction of the illuminated tissue. However vascular shutdown and blood flow changes during early stages of illumination decrease the transport of oxygen, which then limits the production of singlet oxygen and therefore reduces the effect of the local cellular and immunological response. Treatment efficacy is therefore dependent on a fine balance between the positive and negative effects of vascular damage. Here, light dose and fluence rate play an important role in optimizing PDT [6, 7].

Although the porphyrin-precursor ALA is usually topically applied to the skin, the precursor penetrates into the epidermis and dermis. We have recently shown accumulation of significant amounts of PpIX in vessel and arterial walls in subcutaneous tissue after topical application of ALA on skin [8]. In this circumstance the vasculature itself is a target for photodynamic therapy, and the effects of illumination on the vasculature have to be taken into account.

To overcome the problem of direct vascular shutdown and increase treatment efficacy during ALA-PDT, different illumination protocols are developed. We and others have shown that illumination with a lower fluence rate results in more PDT induced damage in normal mouse skin [7, 9]. In a hypoxic environment, the synthesis of nitric oxide stagnates, leading to direct local vasoconstriction and with that only enhancing hypoxia in the area [10]. Low fluence rate PDT is coupled with lower oxygen demand and might therefore reduce vascular shutdown during early stages of illumination. An

alternative illumination scheme that we and others are investigating is fractionated illumination with long dark intervals. In this approach a maximal efficacy is achieved when a small fluence is delivered first, separated from the second fluence by a dark interval of >90 min [6]. Although the mechanism(s) underlying this increased efficacy is not yet fully elucidated, an ischemia/reperfusion injury mechanism and/or increased reperfusion in the dark interval do not seem to be significant factors [11]. We have recently shown in-vitro that cell kill after light fractionated PDT shows a strong dependence on the concentration of PpIX at the time of the first illumination [12]; only cells incubated with low concentrations of ALA show enhanced cell death. These findings support the hypothesis that the positive effect of light fractionation is based on a cellular mechanism that leads to sub-lethally damaged cells after the first light fraction, after which these cells become more susceptible to a second light fraction two hours later.

In order to understand the interaction between PDT induced vasculature effects and tissue destruction, knowledge on vascular effects during and immediately after PDT is crucial. Various authors have reported on monitoring blood flow during and/or following ALA-PDT, showing little consistency in results [13-17]. However, these studies show large variation in experimental design on for example the average volume over which flow is determined and direct response versus long-term (clinical) response. In a previous study it is shown that for topically applied ALA-PDT, PpIX concentration correlates with vascular changes including vasoconstriction and/or vascular leakage of small vessels and arterioles in the epidermis and dermis [8]. In this study we report on vascular response induced by ALA-PDT for different fluence rates, including both changes in vessel diameter and dynamics in RBC velocity in arterioles, imaged using intra-vital confocal microscopy in skin-fold chambers in hairless mice. While previous studies investigated variations in vessel diameter pre- and post PDT, we included measurements of vessel diameter and RBC flow velocity during PDT illumination. We show that situations occurred in which vessel diameter analysis showed an uninterrupted blood supply, while flow had come to a standstill. Furthermore, we analyzed the relation between PDT illumination fluence rate, PpIX accumulation in tissue and vascular reactions in skin-fold observation chambers.

MATERIALS AND METHODS

EXPERIMENTAL DESIGN

This study focuses on the analysis of vasculature during and following ALA-PDT using intra-vital microscopy. To facilitate this, hairless mice were equipped with a one-sided

skin-fold observation chamber. Imaging was done from the subcutis, where the larger vessels were located, towards the epidermis. Red blood cells (RBCs) from a donor mouse were labeled with FITC isomer I and injected in the chamber-bearing mouse. The mouse was fixated under a confocal microscope, where high speed scanning of 1D-line perpendicular to the vessel provided information on RBC velocity. This 1D-scanning was performed during the PDT illumination and repeated 2 hours after the end of the therapeutic illumination. PDT was performed using an external light source and according to different illumination parameters, which are described in detail below. The spatial distribution of PpIX and 514 nm bright-field transmission images were recorded before, directly after and 2 hours after illumination.

ANIMAL MODEL

Dorsal skin-fold window chambers were prepared on the back of 21 inbred albino hairless mice (SKH1 HR, Charles River, Someren, the Netherlands) under general anesthesia (ketamine, 100 mg kg^{-1} b.w. and xylazine, 20 mg kg^{-1} b.w. in a volume mixture of 2:1:1 saline, ketamine, xylazine) [8]. Both sides of the chamber were covered with a 12 mm cover slide of 0.13-0.16 mm thick. Two to four days after operation, mice were included in the experiment. The window chamber frame is employed to immobilize the mice on the intra-vital microscope, to reduce motion artifacts during microscopy. Freshly prepared ALA cream (20% (v/v) ALA (Fagron BV, Capelle a/d IJssel, The Netherlands) was dissolved in water containing 3% carboxymethylcellulose and NaOH) was applied to the skin surface and occluded using a cover slide and incubated for 4 hours. During and after the incubation period animals were placed in a dark and warm environment. The committee on Animal Research of the Erasmus MC approved the experimental protocol. Animal Housing, experiments and euthanization were performed in accordance with the guidelines of this committee.

RED BLOOD CELL LABELLING

Red blood cells for labeling were obtained from a donor mouse. The labeling procedure is described in detail elsewhere [18, 19]. Every experiment day required one donor mouse, bringing the total to n=7 mice. Red blood cells were isolated (centrifuging 7 min, 2000 rpm, supernatant removed) and washed with physiological saline twice. The cells were added to 0.5 ml solution of 5 mg ml^{-1} fluorescein isothiocyanate (FITC) isomer I in phosphate buffer solution (PBS) and incubated for 2 hours at room temperature. Afterwards, cells were centrifuged, the excess solution was removed and washed twice in PBS, with 1% BSA added. Cells were then suspended in physiological saline (27 µl RBC in 0.3 ml saline). 0.1 ml RBC solution was injected i.v. per mouse, providing a fraction of

labeled RBCs that facilitated the measurement of individual fluorescent RBCs while having enough labeled cells passing during a measurement series to perform statistical analysis.

INTRA-VITAL CONFOCAL IMAGING

All imaging was performed using a confocal intra-vital microscope (Zeiss LSM510META, Carl Zeiss B.V. Sliedrecht, the Netherlands). An overview of the complete window chamber was made with bright-field transmission mode and recorded with a 20x magnification (514 nm excitation light). Higher magnification (200x) fluorescence (488 nm excitation) and transmission images were taken of a field of view including arterioles. These recordings were performed pre, post and 2 hours after PDT illumination. PpIX fluorescence was excited using the 514 nm laser of the confocal microscope and fluorescence spectral emission was detected between 601 and 676 nm using lambda mode to determine spatial distribution of photosensitizer.

VESSEL DIAMETER AND RBC VELOCITY DETERMINATION

To determine vessel diameter and RBC flow velocity before, during and after PDT, a line (256 pixels) of interest was selected, perpendicularly to the vessel of interest. This line was scanned 1000 successive times, with a scan time of approximately 1.6 ms per line (dependent on line size). 488 nm excitation light was used for excitation of FITC-labeled red blood cells. Fluorescence was collected through a 505-550 nm band pass filter, while transmitted light passed through a 530 short pass filter to block the external PDT light. Pixel size and scan times were carefully recorded for further analysis. Line scans were made pre and post PDT, and 2 hours after illumination. During PDT illumination, a line scan sequence was measured after every 0.75 J cm^{-2} delivered light dose. After illumination, this line scan sequence was continued for 3 more cycles to capture possible fast recovery effects. The focal depth of the line scan was placed in the center of the vessel by having fluorescent RBCs in the whole width of the vessel in focus (or as many as possible). Combined with an optical slice thickness of 19 µm, this covered the whole vessel lumen.

PDT ILLUMINATION PROTOCOL

PDT illumination was performed using an external laser source (Visulas, 630 nm, Carl Zeiss) coupled into a fiber and imaged through a system of lenses to illuminate the complete skin observation chamber from the skin side, while positioned under the confocal microscope. Four different illumination parameters were investigated: group A (n=6) received a total of 13 J cm^{-2} with a fluence rate of 65 mW cm^{-2}, group B (n=5)

received 13 J cm^{-2} with a fluence rate of 26 mW cm^{-2}, and group C (n=6) received 13 J cm^{-2} with a fluence rate of 130 mW cm^{-2}. Group D (n=4) served as a control group with illumination parameters equal to group A, using mice that did not receive ALA. Values for fluence and fluence rate were chosen to be comparable with previous studies using 514 nm treatment light, based on differences in PpIX absorption and photon energy [20]. Since our interest is in the dynamics of vascular changes in the early stages of illumination, we determined the total PDT dose to be relatively low, 13 J cm^{-2}.

DATA ANALYSIS

All data analysis was performed using a custom program written in Matlab 2009a (The Mathworks, Natick, MA, USA). To determine spatial PpIX concentration, we analyzed the spectral mode images. These consist of eight fluorescence emission images of consecutive emission bands (spread 11 nm, range 601-677 nm). For each pixel, intensity values of the spectral mode images form an emission spectrum, to which basis spectra for autofluorescence and PpIX fluorescence were fitted with a non-linear least squares fit method. Basis spectra were obtained by averaging recorded spectra from three group D or group A/B/C mice for autofluorescence and PpIX fluorescence respectively. Transmission images were used to draw regions of interest located in, bordering on or away from the arteriole, over which the average PpIX fluorescence was determined. The intra-arteriole and vessel wall areas covered approximately 40x160 µm, while the areas in normal tissue were larger.

The vessel diameter was determined from the transmission light image in the 1D-line scan images using a custom Matlab procedure. The 1000 consecutive lines form a gray scale image, which was converted to binary by the use of Otsu's thresholding method, dividing a gray scale image into foreground and background (tissue and vessel resp. in this case) [21]. The vessel diameter was determined as the average number of pixels determined being vessel, multiplied by pixel size.

RBC velocity was determined from the number of subsequent lines showing RBC fluorescence, where more lines indicate slower RBCs. This method is described in detail elsewhere [22]. Since the exact configuration of the blood cell in the vessel is unknown, the average RBC diameter was set to 5±3 µm (the average RBC diameters are approximately 8 µm diameter and 2 µm thickness, measured in the confocal microscopy images).

RESULTS

We were able to measure RBC velocity and vessel diameter during the complete PDT illumination in 16 of the 21 mice; two died before or during illumination, three window chambers moved out of focus during measurement. Figure 3.1, 3.2 and 3.3 show the three cases that we observed: no change in vessel diameter and flow (figure 3.2, group D), partial vasoconstriction (figure 3.3, group A), or complete vasoconstriction (figure 3.1, group B).

VESSEL DIAMETER

Analyzing the changes in vessel diameter showed results consistent with previous studies [8, 23]. 14 out of 16 mice showed a decrease in vessel diameter (diameter post PDT is 65%±46% of the diameter pre PDT), while six mice showed complete vessel occlusion directly after PDT. Variations in vessel diameter during PDT are shown in figure 3.4, where every line indicates a singe mouse. Figure 3.1 shows an example measurement series resulting in complete vasoconstriction. Confocal measurements 2 hours after PDT were, in many cases, complicated by edema formation, limiting the possibility to focus the microscope on the field of view.

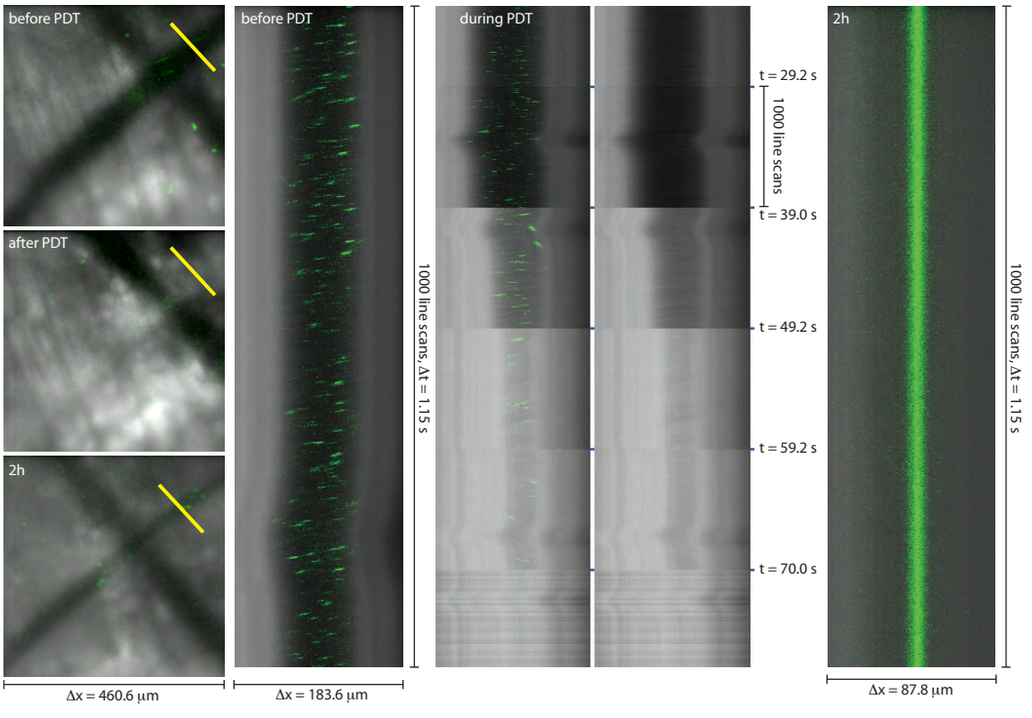

Figure 3.1: *Exemplary measurement series of complete vascular constriction. Left) Squares, overview of the area under investigation before, after and 2 hours later. Right) Line scans before, during and 2 hours after PDT illumination. In this special case re-appearance after 2 hours, but no flow.*

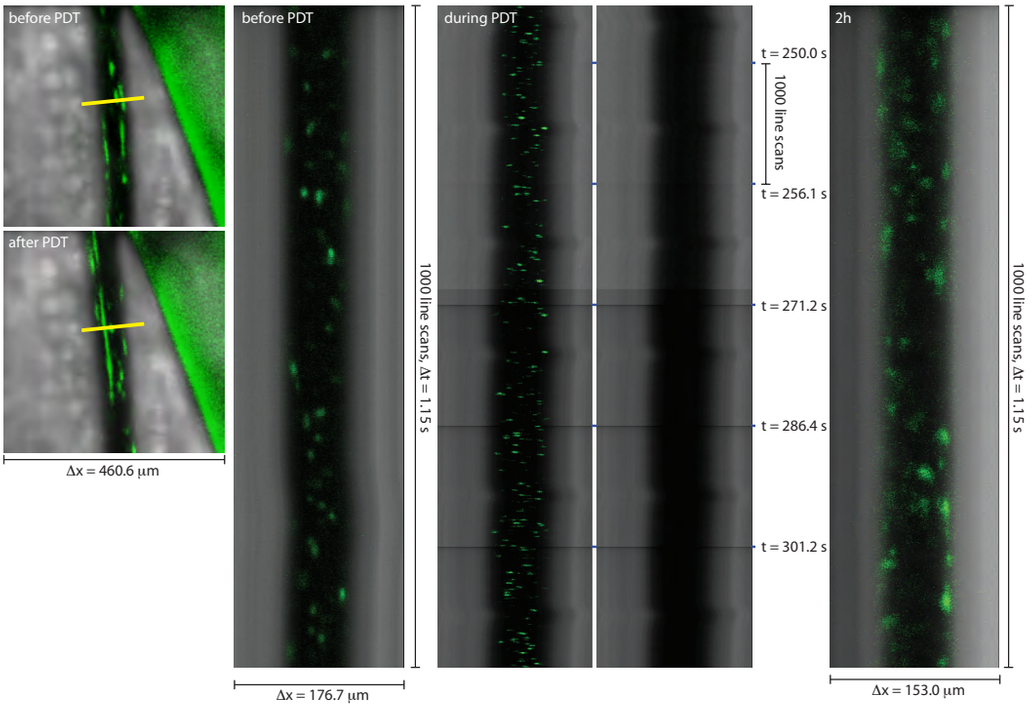

Figure 3.2: *Exemplary measurement series of control animal. Left) Squares, overview of the area under investigation before, after and 2 hours later. Right) Line scans before, during and 2 hours after PDT illumination. Without applying ALA, no vascular reaction is visible.*

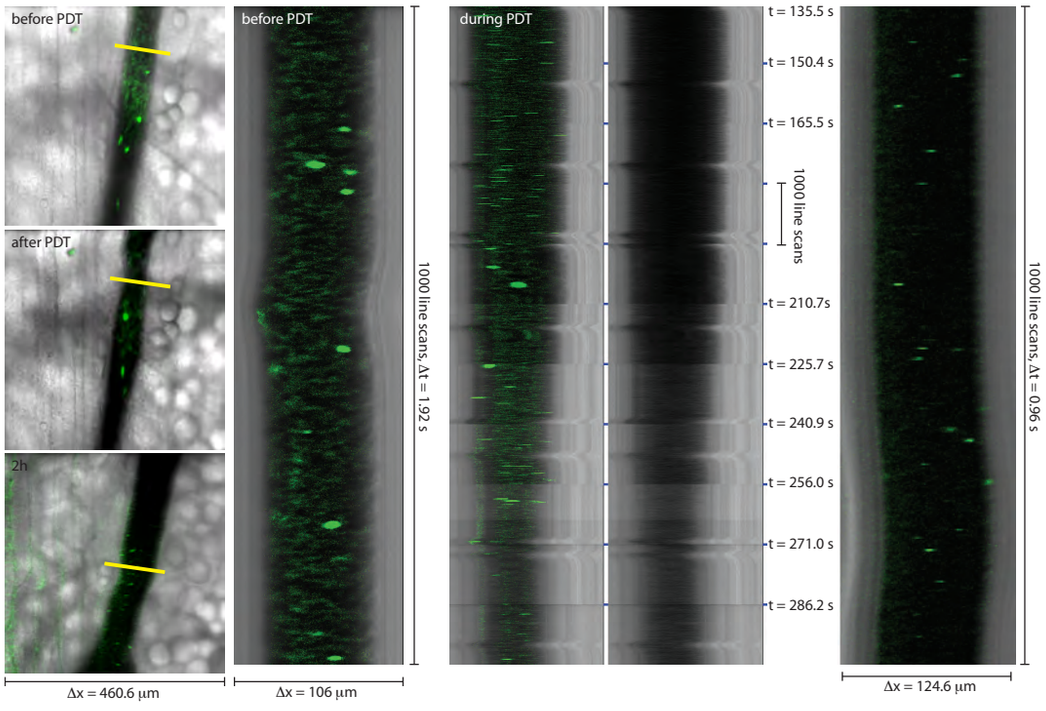

Figure 3.3: *Exemplary measurement series of partial vasoconstriction. Left) Squares, overview of the area under investigation before, after and 2 hours later. Right) Line scans before, during and 2 hours after PDT illumination. A reduction in vessel diameter during PDT can be seen, and the decrease of fluorescent dot-size at the 2 hour time point indicates an increase in RBC velocity.*

Vascular constriction seemed to be present in all PDT groups, although reactions in the 26 (figure 3.4b) and 130 mW cm^{-2} (figure 3.4c) group were more pronounced. The accumulation of PpIX in tissue varied between individual mice, due to variations in the capacity to take up and convert ALA into PpIX. However, the average PpIX levels for the three groups did not vary significantly as shown in figure 3.5 (P>0.1). The correlation between PpIX level and relative vessel diameter change as described previous [8], did not significantly show in present work, as shown in figure 3.6.

RED BLOOD CELL VELOCITY

When comparing changes in RBC velocity (figure 3.7) with changes in diameter (figure 3.4) during illumination, we found that in all cases reaching total occlusion, this was preceded by a sharp decrease in velocity to zero. When the vessel did not completely constrict, RBC velocity stayed relatively constant, as shown in figure 3.7. The large error bars on velocity measurements could be explained by different geometries in which the RBCs travelled through the vessel. RBC flow velocity was calculated using an average RBC diameter of 5 µm, while the diameter of the RBC passing the line ranged from 2 to 8 µm. The resulting variation could be assigned to variations in RBC flow velocity in one line-scan image.

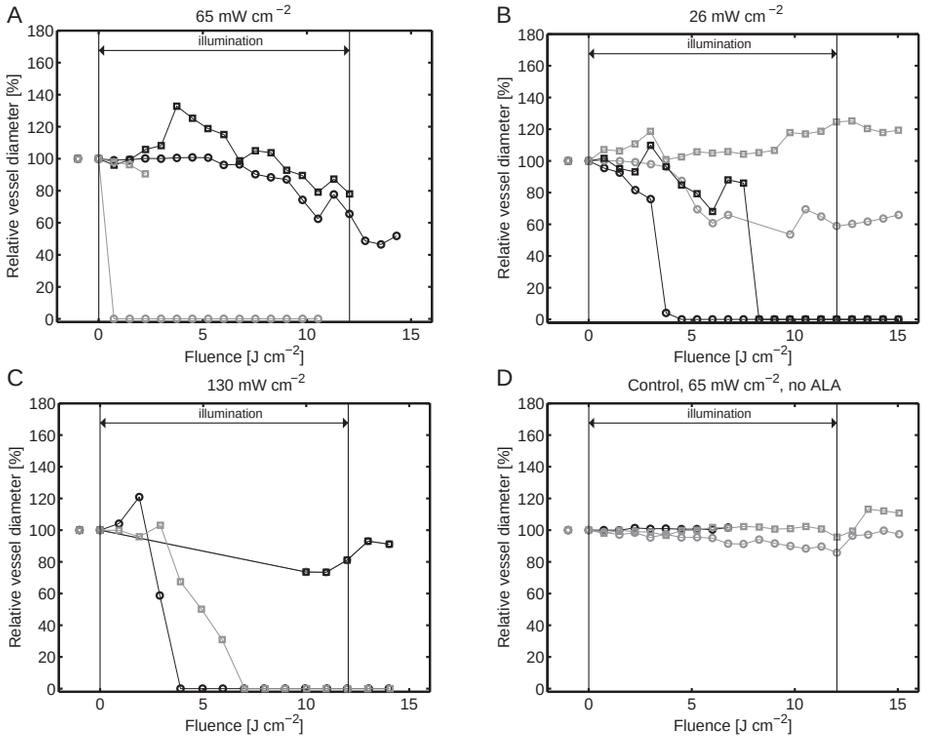

Figure 3.4: *Relative vessel diameter change vs delivered PDT fluence. Every line indicates one animal. Measurements before illumination (Fluence = -1), during illumination (Fluence = 0-13) and directly after illumination ends (Fluence = 13-15).*

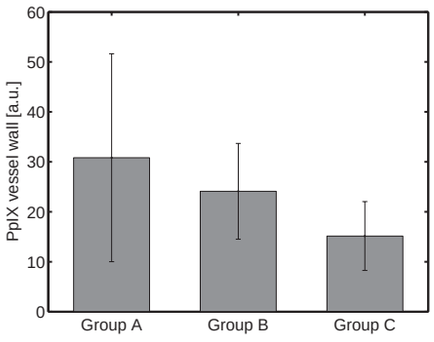

Figure 3.5: *PpIX concentration in vessel wall for three different groups does not vary significantly.*

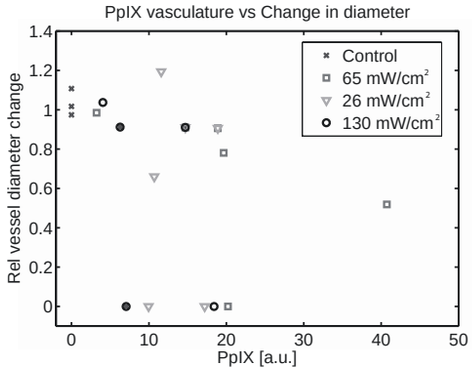

Figure 3.6: *PpIX concentration in vasculature vs. relative change in vessel diameter.*

From the six mice showing complete occlusion, one mouse showed the re-appearance of the vessel 2 hours later. This 2 hour measurement sequence is shown in figure 3.1. Although not occluded anymore, RBCs had come to a standstill. We observed this phenomenon in only one mouse. The observation that changes in vessel diameter did not necessarily correlate with changes in RBC velocity calls for discussion on how local vascular changes during and after ALA-PDT could be influencing treatment efficacy.

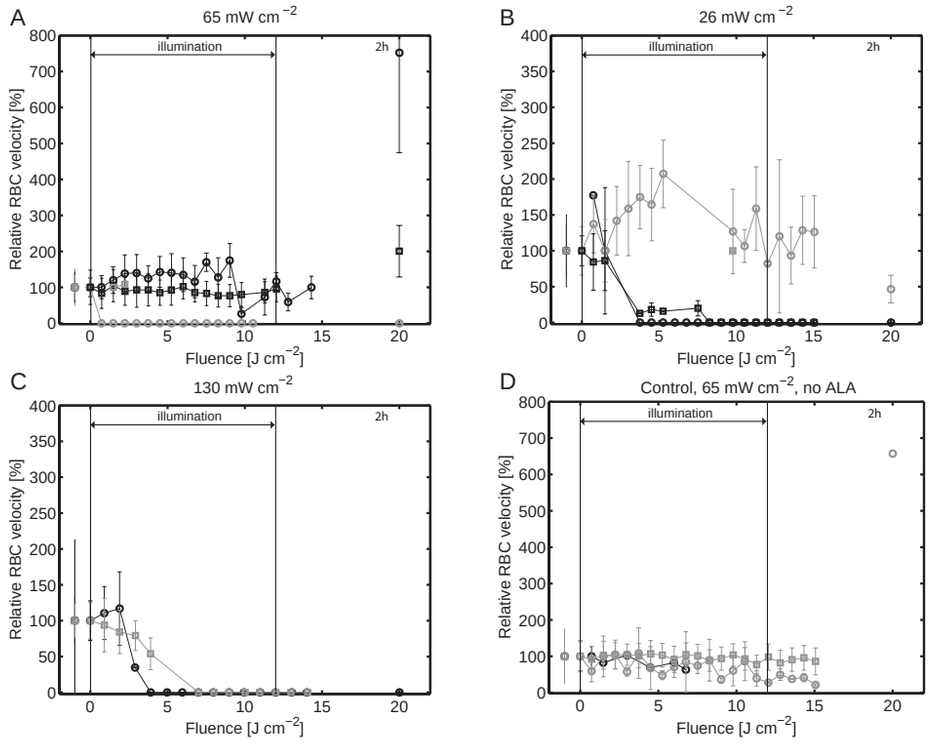

Figure 3.7: *Relative RBC velocity change vs delivered PDT fluence. Every line indicates one animal. Measurements before illumination (Fluence=-1), during illumination (Fluence=0-13) and directly after illumination ends (Fluence=13-15). 2 hours after illumination is plotted at Fluence=20. Errorbars indicate variation of RBC velocities passing the linescan during one time point.*

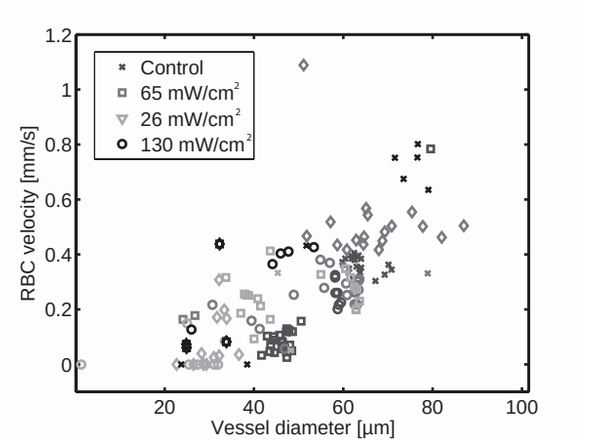

Figure 3.8: *Vessel diameter vs RBC velocity. Colors represent different groups and symbols individual mice within them.*

When relating diameter to RBC velocity, we were only able to consider variation per mouse during illumination to avoid artifacts arising from intra-animal variation in blood pressure. It is shown in figure 3.8 that in general larger diameters were related to a higher RBC velocity, as was expected from the Poiseuille equation. The RBC velocity measurements presented here were consistent with what is previously measured in skin-fold window chambers [17, 24].

DISCUSSION

In this paper we have shown that delivering a low fluence of ALA-PDT resulted in acute vascular response during the therapeutic illumination. One significant advance of the present study over our previous approaches [8, 23] to monitor acute vascular effects is the incorporation of measurement of RBC velocity rather than simply measuring changes in the diameter of blood vessels. We applied a fluence of 13 J cm^{-2}, comparable to the first small light fraction used in light fractionated PDT. We observed vasoconstriction of arterioles under investigation occurring in 77% of the mice, independent of fluence rate. Furthermore, we observed a drop in RBC velocity immediately before vessel diameter reduction set in. However, this drop in velocity was only present when total vessel constriction occurred. Interestingly, incomplete vasoconstriction did not lead to significant changes in RBC velocity. In a previous study we show no significant difference between vascular effects after low (5-10 J cm^{-2}) or high (100 J cm^{-2}) fluence PDT, indicating that the vascular effects set in early during treatment [8].

Although PpIX in tissue is not concentrated in the vasculature like intravenously administered photosensitizers are, we have recently shown that endothelial cells of epidermal and dermal vasculature do generate PpIX after the topical administration of ALA [8]. Therefore it is reasonable to expect acute vascular responses in endothelial tissue during PDT. Furthermore, when PDT illumination is started and there is a significant accumulation of PpIX in and around endothelial cells, the depletion of molecular oxygen

results in a hypoxic environment. This hypoxia inhibits the synthesis of endogenous nitric oxide. The higher the fluence rate, the faster all oxygen is depleted and the faster hypoxia sets in. Fukumura et al. [10] investigated the effect of nitric oxide inhibition on tumor microvasculature and found a decrease in RBC velocity on the venular side of the microvasculature, accompanied with a decrease of vessel diameter on the arteriolar side. Both effects result in a significant decrease in blood flow and therefore reoxygenation of the tissue. The fact that we also observed vascular shutdown in the low fluence rate group (group B) suggests that PDT efficiently inhibited the production of nitric oxide species by endothelial cells. This impairment leads to a reduction of vessel relaxation properties [25]. Furthermore inhibition of NO formation seems to play an important role in various immunological responses [26, 27], but since these responses do not evoke direct vascular changes, discussion is beyond the scope of this study.

COMPARISON WITH OTHER WORK

A number of previous studies have investigated vascular changes during ALA-PDT. For the most part these have been based on techniques that monitor changes in blood flow, RBC velocity or tissue oxygenation in relatively large measurement volumes on the order of millimeters: in diffuse correlation spectroscopy the measurement volume is approximately 1 mm [16] and in laser Doppler flowmetry the measurement volume is significantly greater than 1 mm [13]. In the present study we have measured RBC velocity in a single vessel with a diameter of less than 150 μm. This complicates direct comparison between studies, since the in a larger measurement volume, effects we observe might be counteracted by other vessels. Furthermore, measuring larger volumes, as is the case for methods based on diffuse optical techniques, can be misleading because a local (vascular) PDT effect might be overshadowed by the response of surrounding tissue to PDT. In cases where we observe a decrease in RBC velocity, this is usually followed by complete constriction of the vessel, resulting in a RBC velocity of zero. Becker et al. [16] showed a rapid drop in relative blood flow within 1-4 J after starting PDT illumination with a maximum of approximately 50% reduction (topically applied ALA, illuminated with 635 nm laser light, [75 35 10] mW cm^{-2} with a total light dose of [80 80 37.5] J cm^{-2}), followed by a recovery and overshoot of the relative blood flow. Both time and magnitude of the increase and decrease are fluence rate dependent; high fluence rate results in large decrease after ∼4 J, followed by a moderate increase, while a low fluence rate results in small decrease at ∼1 J, followed by a large overshoot of the blood flow. The time span of flow decrease of the two highest fluence rate is in the order of our total illumination time and a possible explanation that we do not see a successive increase in RBC velocity. However, our observation that most collapsed vessels are still constricted 2 hours after

illumination does not reconcile with the blood flow increase observed by Becker et al. [16]. Furthermore, we are focusing on a single vessel, while it might be hypothesized that by constriction of certain arterioles the flow velocity in neighboring vessels increases. In our experiment, velocity increase is not observed during or after deposition of the PDT dose in any of the vessels under investigation. Schacht et al. [17] used an incoherent light source (580-740 nm, 100 mW cm^{-2}), measured centerline (maximum) RBC velocity in vessels and found almost complete reduction of RBC velocity and vessel density 0.5 hours after high fluence (100 J cm^{-2}) ALA-PDT, accompanied with a strong decrease in vessel density. However, after low fluence (10 J cm^{-2}) PDT, comparable to our experiment, no significant changes were observed. Our measured initial mean RBC velocities show a large variation. Considering that for vessels <90 µm the ratio between centerline RBC velocity and mean RBC velocity approximately 1.6 [28], our data is comparable with RBC velocities reported by Schacht et al. [17]. Leveckis et al. [29] showed a decrease in vessel diameter of the cremaster muscle microcirculation within the first 20 minutes after [178 300] mW cm^{-2}, violet light, 100 J cm^{-2} ALA-PDT, but no reaction for the 105 mW cm^{-2} group. This vascular response was much stronger on the arteriolar side than for the venular side, and recovery for the arteriolar side was faster. Herman et al. [13] did not find any significant effects of ALA-PDT on blood flow of colon-26 tumors implanted in mice (633 nm laser light, 200 mW cm^{-2}, [50 100 150] J cm^{-2}).

Wang et al. [30] concluded that ALA-PDT causes a reduction in blood flow, based on comparison of PpIX fluorescence measured in patients and the results of mathematical simulations of PDT. They found that for fluence rates of both 20 and 150 mW cm^{-2} the simulations needed a stepwise decrease of blood flow velocity to correspond with patient measurements. It remains difficult to discriminate between local and regional vascular effects during PDT, since the interrogation volume is dependent on measurement techniques and considering that various mechanisms can induce vascular effects (e.g. direct vascular damage, response to inflammation or hypoxia). Our localized data may aid the modeling of local effects and their impact on the generation of reactive oxygen species, and therefore PDT efficacy.

COMPARISON WITH OUR PREVIOUS WORK

We have previously shown acute vascular effects after low dose ALA-PDT, and observed that an inhomogeneous distribution of PpIX may influence the variation in response of the local vasculature [8]. Even though ALA is topically applied to the skin, it penetrates into the dermis including the endothelial cells lining the microvasculature. These endothelial cells synthesize PpIX and are therefore prone to direct PDT damage, which then leads to vascular leakage and vasoconstriction. The later effect can also occur as a result of local

hypoxia and/or inflammatory responses involving nitric oxide. In the present study PpIX fluorescence intensities in the vascular endothelial cells showed a larger spread than previously found, while changes in vessel diameter were only loosely related to PpIX fluorescence in vessel wall or vasculature. We combined local information on vessel diameter and RBC velocity. The increase in vessel diameter measured immediately after illumination for the control group D of this study is observed previously [8]. On closer inspection our data showed a decrease in vessel diameter during the illumination, while the vessel dilated rapidly directly after the illumination ends. Small temperature changes during the control illumination may explain the cause of this vessel constriction, which was compensated for immediately after the end of the illumination. Before complete vessel constriction was observed, RBC velocity decreased over a time-span of 30-75 seconds, while no significant velocity changes were observed when the vessel was only partially constricted. This suggests that complete constriction of the vessel is not instantaneous over the whole vessel length, causing changes in RBC velocity up- or downstream from the already constricted region. In all but one case, complete vasoconstriction remained for at least 2 hours after illumination. In the one case where the vessel dilated again, only particular segments of the vessel were visible in the window chamber. It is not surprising that RBCs were not flowing in these segments. Future work will be dedicated to analyze these local vascular changes during illumination in a larger field of view.

LIMITATIONS - LOCALIZED MEASUREMENT

It is important to note that in the present study we mainly focused on the response of arterioles. This is because previous studies showed that these vessels show the largest variations in vessel diameter in response to PDT. The choice of which individual vessel to investigate is nevertheless an important consideration. There is no guarantee that vascular effects will occur at the chosen location. One should therefore keep in mind that the present study showed dynamic variation during PDT in a rather specific region of the vasculature. Information on vessel diameter up- and downstream of our field of view, was collected using low magnification images of the whole window chamber acquired before and after PDT.

LIMITATIONS - EXACT CALCULATION OF VESSEL DIAMETER

For every time point, the diameter was determined as the average diameter of all 1000 scans performed per time point. To discriminate between vessel and background in the transmission image, we used a threshold value determined using Otsu's method [21]. This method is based on minimizing the spread of pixel values on each side of the threshold.

We are aware that the result of using an automated threshold method depends heavily on the image quality. Therefore, we drew the automatically determined vessel borders in the transmission image. In situations where calculated vessel border did not correspond with what we expected based on visual examination, the threshold was adjusted manually. Evaluating the changes in diameter over time for all cases did not show deviating patterns based on manual or automatic thresholding.

LIMITATIONS - REPORTING ON THE RBC VELOCITY

The RBC velocity over the diameter of the vessel is expected to show a velocity profile dependent on vessel diameter. RBCs close to the vessel wall are slowed down by sheer stress, while the velocity is expected to be highest in the centerline of the vessel. For our calculations, we averaged all RBCs in focus. RBC velocity values in this study therefore represented real average values. This complicates comparison to average centerline values, often used in literature.

CONCLUSION

In conclusion, we have shown that during PDT illumination acute local vascular effects occurred very soon after the start of the therapeutic illumination in ALA-PDT. We observed coincident changes in both vessel diameter and RBC velocity. Arterioles were particularly sensitive to vasoconstriction during low dose PDT, often resulting in complete vasoconstriction. Since the therapeutic effects of PDT are dependent on a fine balance between the need for oxygen during illumination and disruption of the vasculature, the results of the present study add to our understanding of acute vascular effects during ALA-PDT and aid our efforts to optimize PDT using porphyrin pre-cursors.

REFERENCES

1. Morton, C., K. McKenna, and L. Rhodes, *Guidelines for topical photodynamic therapy: update.* British Journal of Dermatology, 2008. **159**(6): p. 1245-1266.
2. Braathen, L.R., et al., *Guidelines on the use of photodynamic therapy for nonmelanoma skin cancer: an international consensus.* Journal of the American Academy of Dermatology, 2007. **56**(1): p. 125-143.
3. Peng, Q., et al., *5-Aminolevulinic Acid-Based Photodynamic Therapy: Principles and Experimental Research.* Photochemistry and photobiology, 1997. **65**(2): p. 235-251.
4. Foote, C.S., *Definition of type I and type II photosensitized oxidation.* Photochemistry and photobiology, 1991. **54**(5): p. 659-659.
5. Fingar, V.H., et al., *The role of microvascular damage in photodynamic therapy: the effect of treatment on vessel constriction, permeability, and leukocyte adhesion.* Cancer research, 1992. **52**(18): p. 4914-4921.
6. de Bruijn, H.S., et al., *Fractionated illumination after topical application of 5-aminolevulinic acid on normal skin of hairless mice: The influence of the dark interval.* Journal of Photochemistry & Photobiology, B: Biology, 2006. **85**(3): p. 184-190.
7. Robinson, D.J., et al., *Fluorescence photobleaching of ALA-induced protoporphyrin IX during photodynamic therapy of normal hairless mouse skin: the effect of light dose and irradiance and the resulting biological effect.* Photochemistry and photobiology, 1998. **67**(1): p. 140-149.
8. de Vijlder, H.S., et al., *Acute Vascular Responses during Photodynamic Therapy using Topically Administered Porphyrin Precursors.* Photochemical & Photobiological Sciences, 2013. **In press**.
9. Niedre, M., et al., *Singlet oxygen luminescence as an in vivo photodynamic therapy dose metric: validation in normal mouse skin with topical amino-levulinic acid.* British journal of cancer, 2005. **92**(2): p. 298-304.
10. Fukumura, D., et al., *Role of nitric oxide in tumor microcirculation. Blood flow, vascular permeability, and leukocyte-endothelial interactions.* The American journal of pathology, 1997. **150**(2): p. 713-725.
11. van der Veen, N., H. van Leengoed, and W. Star, *In vivo fluorescence kinetics and photodynamic therapy using 5-aminolaevulinic acid-induced porphyrin: increased damage after multiple irradiations.* British journal of cancer, 1994. **70**(5): p. 867-872.
12. de Bruijn, H.t.S., et al., *Light fractionated ALA-PDT enhances therapeutic efficacy in vitro; the influence of PpIX concentration and illumination parameters.* Photochemical & Photobiological Sciences, 2013. **12**(2): p. 241-245.
13. Herman, M.A., D. Fromm, and D. Kessel, *Tumor blood-flow changes following protoporphyrin IX-based photodynamic therapy in mice and humans.* Journal of Photochemistry and Photobiology B: Biology, 1999. **52**(1): p. 99-104.
14. Henderson, B.W., et al., *Photosensitization of murine tumor, vasculature and skin by 5-aminolevulinic acid-induced porphyrin.* Photochemistry and photobiology, 1995. **62**(4): p. 780-789.
15. van der Veen, N., et al., *Photodynamic Effectiveness and Vasoconstriction in Hairless Mouse Skin after Topical 5-Aminolevulinic Acid and Single- or Two-fold Illumination.* Photochemistry and photobiology, 1999. **70**(6): p. 921-929.
16. Becker, T.L., et al., *Monitoring blood flow responses during topical ALA-PDT.* Biomedical optics express, 2011. **2**(1): p. 123-130.

17. Schacht, V., R.-M. Szeimies, and C. Abels, *Photodynamic therapy with 5-aminolevulinic acid induces distinct microcirculatory effects following systemic or topical application.* Photochemical & Photobiological Sciences, 2006. **5**(5): p. 452-458.

18. Tangelder, G.J., et al., *Velocity profiles of blood platelets and red blood cells flowing in arterioles of the rabbit mesentery.* Circulation research, 1986. **59**(5): p. 505-514.

19. Seylaz, J., et al., *Dynamic in vivo measurement of erythrocyte velocity and flow in capillaries and of microvessel diameter in the rat brain by confocal laser microscopy.* Journal of Cerebral Blood Flow & Metabolism, 1999. **19**(8): p. 863-870.

20. Robinson, D.J., et al., *Protoporphyrin IX Fluorescence Photobleaching during ALA-Mediated Photodynamic Therapy of UVB-Induced Tumors in Hairless Mouse Skin.* Photochemistry and photobiology, 1999. **69**(1): p. 61-70.

21. Otsu, N., *A threshold selection method from gray-level histograms.* Automatica, 1975. **11**(285-296): p. 23-27.

22. Jones, E., et al., *Measuring hemodynamic changes during mammalian development.* American Journal of Physiology-Heart and Circulatory Physiology, 2004. **287**(4): p. H1561-H1569.

23. Middelburg, T., et al., *Topical Hexylaminolevulinate and Aminolevulinic Acid Photodynamic Therapy: Complete Arteriole Vasoconstriction Occurs Frequently and Depends on Protoporphyrin IX Concentration in Vessel Wall.* Journal of Photochemistry and Photobiology B: Biology, 2013. **126**: p. 26-32.

24. Leunig, M., et al., *Angiogenesis, microvascular architecture, microhemodynamics, and interstitial fluid pressure during early growth of human adenocarcinoma LS174T in SCID mice.* Cancer research, 1992. **52**(23): p. 6553-6560.

25. Gilissen, M.J., et al., *Effect of photodynamic therapy on the endothelium-dependent relaxation of isolated rat aortas.* Cancer research, 1993. **53**(11): p. 2548-2552.

26. Reeves, K.J., M.W. Reed, and N.J. Brown, *Is nitric oxide important in photodynamic therapy?* Journal of Photochemistry and Photobiology B: Biology, 2009. **95**(3): p. 141-147.

27. Ho, J.D., H.J. Man, and P.A. Marsden, *Nitric oxide signaling in hypoxia.* Journal of molecular medicine, 2012. **90**(3): p. 217-231.

28. Lipowsky, H.H. and B.W. Zweifach, *Application of the two-slit photometric technique to the measurement of microvascular volumetric flow rates.* Microvascular research, 1978. **15**(1): p. 93-101.

29. Leveckis, J., N. Brown, and M. Reed, *The effect of aminolaevulinic acid-induced, protoporphyrin IX-mediated photodynamic therapy on the cremaster muscle microcirculation in vivo.* British journal of cancer, 1995. **72**(5): p. 1113-1119.

30. Wang, K.K.-H., et al., *Simulations of measured photobleaching kinetics in human basal cell carcinomas suggest blood flow reductions during ALA-PDT.* Lasers in surgery and medicine, 2009. **41**(9): p. 686-696.

Chapter

4

In-Vivo Quantification of the Scattering Properties of Tissue using Multi Diameter Single Fiber Reflectance Spectroscopy

Floor van Leeuwen – van Zaane,
Ute Gamm, Pieter van Driel, Thomas Snoeks, Riëtte de Bruijn
Angélique van der Ploeg – van den Heuvel, Isabel Mol,
Clemens Löwik, Dick Sterenborg, Arjen Amelink,
Dominic Robinson

Biomedical Optics Express, 2013. **4**(5): p. 696-708

ABSTRACT

Multi diameter single fiber reflectance (MDSFR) spectroscopy is a non-invasive optical technique based on using multiple fibers of different diameters to determine both the reduced scattering coefficient (μ_s') and a parameter γ that is related to the angular distribution of scattering, where $\gamma = (1-g_2)/(1-g_1)$ and g_1 and g_2 the first and second moment of the phase function, respectively. Here we present the first in-vivo MDSFR measurements of $\mu_s'(\lambda)$ and $\gamma(\lambda)$ and their wavelength dependence. MDSFR is performed on nineteen mice in four tissue types including skin, liver, normal tongue and in an orthotopic oral squamous cell carcinoma. The wavelength-dependent slope of $\mu_s'(\lambda)$ (scattering power) is significantly higher for tongue and skin than for oral cancer and liver. The reduced scattering coefficient at 800 nm of oral cancer is significantly higher than that of normal tongue and liver. Gamma generally increases with increasing wavelength; for tumor it increases monotonically with wavelength, while for skin, liver and tongue $\gamma(\lambda)$ reaches a plateau or even decreases for longer wavelengths. The mean $\gamma(\lambda)$ in the wavelength range 400-850 nm is highest for liver (1.87±0.07) and lowest for skin (1.37±0.14). Gamma of tumor and normal tongue falls in between these values where tumor exhibits a higher average $\gamma(\lambda)$ (1.72±0.09) than normal tongue (1.58±0.07). This study shows the potential of using light scattering spectroscopy to optically characterize tissue in-vivo.

INTRODUCTION

Reflectance spectroscopy is frequently used to determine the absorption and scattering coefficients of biological tissue. A range of fiber optic devices with different probe geometries have been developed to retrieve these optical properties, within various regimes of tissue-light propagation [1-3]. The absorption coefficient of tissue is related to physiological parameters such as micro-vascular blood oxygenation, blood volume fraction and micro vessel diameter, as well as to the concentration of chromophores such as bilirubin and cytochrome C. Scattering in tissue results from variations in refractive index between the various cell and tissue components and their surroundings.

At large source-detector separations, light transport can be considered diffuse and is therefore only dependent on the absorption coefficient (μ_a) and the reduced scattering coefficient (μ_s'), given by $\mu_s' = \mu_s(1-g_1)$ where $g_1 = \langle\cos(\theta)\rangle$ is the first moment of the scattering phase function (PF), also called the scattering anisotropy. At these large distances, light transport is insensitive to the exact shape of the PF. However, in device configurations with small source-detector separations, an additional, PF dependent variable γ is necessary to describe the effect of large angle scattering events on the reflectance signal [4-7]. This parameter γ is defined as

$$\gamma = \frac{1-g_2}{1-g_1} \tag{4.1}$$

where g_2 is the second Legendre moment of the PF [5].

Our group has previously developed single fiber reflectance spectroscopy (SFR), where one fiber serves as both source and detector. One advantage of this geometry is that SFR is sensitive to superficial tissues and their microvasculature, which are susceptible to early changes in morphology caused by (pre-)malignant disease. Furthermore, the diameter of a single fiber probe is such that it can be easily guided through the working channel of an endoscope to sample internal organs. The analysis of SFR spectra is performed using a semi-empirical model (cf. equation 4.2) that describes the PF-dependent relationship between SFR signal and the dimensionless reduced scattering (which is defined as the product of the reduced scattering coefficient and the fiber diameter $\mu_s'd_f$) [6]. This semi-empirical model was based on Monte-Carlo simulations and validated in tissue mimicking phantoms [8, 9]. SFR spectroscopy allows us to determine tissue absorption without prior knowledge of the scattering coefficient [10]. Recently, SFR has been extended to multi-diameter single fiber reflectance spectroscopy (MDSFR), in which two fiber diameters can be used to determine the μ_s' and γ [7, 11, 12]. An MDSFR measurement consists of several co-localized SFR measurements using different fiber diameters [11], which are each

individually corrected for absorption [10], resulting in the reflectance in the absence of absorption, R_{SF}^{0}, for every SFR measurement. The co-localized, multi-fiber diameter R_{SF}^{0} values are then simultaneously fitted to the model described in equation 4.2,

$$R_{SF}^{0}(\lambda, d_f) = \eta_{\lim}\left(1 + p_1 e^{-p_3 \mu_s'(\lambda) d_f}\right) \cdot \left[\frac{\left(\mu_s'(\lambda) d_f\right)^{p_2}}{p_3 + \left(\mu_s'(\lambda) d_f\right)^{p_2}}\right] \tag{4.2}$$

where η_{lim} is the diffuse limit of the single fiber collection efficiency and [p_1 p_2 p_3] are $\gamma(\lambda)$-dependent coefficients, the values of which are derived from Monte Carlo simulations. The spectral shape of $\mu_s'(\lambda)$ is constrained according to a biologically realistic power law decay. Solving the equation with two unknown variables for two different fiber diameters allows wavelength dependent quantification of both μ_s' and γ. The MDSFR approach has been validated both in-silico and in optical phantoms containing polystyrene microspheres over a wide range of biologically relevant values for $\mu_s'(\lambda)$ and $\gamma(\lambda)$, with and without the presence of absorbers [7, 12].

In the current study we present, for the first time, differences in the wavelength dependence of μ_s' and γ in-vivo, measured using MDSFR. We have acquired MDSFR spectra in-vivo from tumor, normal tongue tissue, skin and liver in an orthotopic xenograft model for oral cancer in mice using consecutive SFR measurements of two different fiber diameters (0.4 and 0.8 mm).

MATERIALS AND METHODS

MDSFR REFLECTANCE MODEL

First, the Beer-Lambert law is used to correct the measured SFR intensities $R_{SF}(d_f)$ for absorption to obtain $R_{SF}^{0}(d_f)$:

$$R_{SF}(d_f) = R_{SF}^{0}(d_f)\, e^{-\mu_{a,Tiss}\langle L\rangle} \tag{4.3}$$

where $R_{SF}^{0}(d_f)$ is given by equation 4.2, $\mu_{a,\,Tiss}$ is the absorption coefficient of tissue and $\langle L\rangle$ is the effective photon path length, given by [8]

$$\frac{\langle L\rangle}{d_f} = \frac{C_{PF}\,1.54}{\left(\mu_s'(\lambda) d_f\right)^{0.18}\left(0.64 + \mu_a d_f\right)^{0.64}}. \tag{4.4}$$

The absorption coefficient of tissue is expressed as the sum of the absorption of blood $\mu_{a,blood}$ and the absorption of bilirubin μ_a^{bil}:

$$\mu_{a,Tiss}(\lambda) = \mu_{a,blood}(\lambda) + \mu_a^{bil}(\lambda). \tag{4.5}$$

The absorption coefficient of blood can be described as the product of the specific blood absorption coefficients and blood volume fraction:

$$\mu_{a,blood}(\lambda) = C_{cor}(\lambda) \times bvf\left[StO_2\mu_a^{HbO2,spec}(\lambda) + (1 - StO_2)\mu_a^{Hb,spec}(\lambda)\right] \quad (4.6)$$

where StO_2 is the blood oxygen saturation, bvf is blood volume fraction assuming the concentration of hemoglobin in whole blood to be 150 g L^{-1}, and $\mu_a^{HbO2,spec}$ and $\mu_a^{Hb,spec}$ are the specific absorption coefficients of oxygenized and deoxygenized blood, respectively. C_{cor} is the correction factor that accounts for flattening of spectral features resulting from the inhomogeneous distribution of blood in tissue and the confinement of blood in vessels [13, 14]. For whole blood, the correction factor is given by:

$$C_{cor} = \left\{1 - \exp\left[\mu_{a,blood}(\lambda)D_v\right]\right\} / \left[\mu_{a,blood}(\lambda)D_v\right] \quad (4.7)$$

and is related to the average vessel diameter D_v. The total tissue absorption $\mu_{a,tiss}$ can then be described as the absorption of blood $\mu_{a,blood}$, dependend on blood volume fraction, and the absorption of bilirubin, which is the product of the specific absorption coefficient $\mu_a^{bil,spec}$ and the bilirubin concentration c_{bil}:

$$\mu_{a,Tiss}(\lambda) = \mu_{a,blood}(\lambda) + c_{bil}\mu_a^{bil,spec}(\lambda) \quad (4.8)$$

The small but distinct gfp fluorescence emission peak present in the white light reflectance spectra of tumor was accounted for using a fit component $Em_{GFP}(\lambda)$ to be included in the reflectance model:

$$R_{SF}(d_f) = R_{SF}^0(d_f)e^{-\mu_{a,Tiss}\langle L\rangle} + c_{GFP}Em_{GFP}(\lambda) \quad (4.9)$$

This Em_{GFP} basis spectrum was previously acquired by fluorescence measurements of the tongue tumors, corrected for optical properties and system transmission. We attempted to include the absorption of gfp (determined from in-vitro cells) in the SFR analysis in the same way bilirubin is treated in equation 4.8. This did not result in a significant improvement of the fit, and gfp absorption was therefore omitted form the fit procedure.

The aim of this first step of the analysis is to remove the effects of absorption on the individual SFR spectra. It was shown previously that accurate absorption coefficients from individual SFR spectra can be obtained without prior knowledge of the tissue scattering properties [7, 10] if an optimized set [p_1 p_2 p_3 C_{PF}] is used, i.e. p_1=1.55, p_2=0.969, p_3=6.82, and C_{PF}=0.944. The background scattering model used in this first step of individual analysis of each SFR spectrum is based on a 4th order polynomial, i.e.

$$\mu_s'(\lambda) = a_1\left(\frac{\lambda}{\lambda_0}\right)^{-1} + a_2\left(\frac{\lambda}{\lambda_0}\right)^{-2} + a_3\left(\frac{\lambda}{\lambda_0}\right)^{-3} + a_4\left(\frac{\lambda}{\lambda_0}\right)^{-4}. \quad (4.10)$$

This model allows sufficient degrees of freedom to correct for the physically incorrect assumption that [p_1 p_2 p_3 C_{PF}] are independent of γ. This aspect of the model will be further addressed in the discussion section. After removal of the effect of absorption on

the individual SFR spectra, the MDSFR analysis is performed by solving equation 4.2 for multiple fiber diameters simultaneously. Here, the reduced scattering coefficient is modeled using the power law function

$$\mu_s'(\lambda) = a_1\left(\frac{\lambda}{\lambda_0}\right)^{-a_2} \tag{4.11}$$

and equation 4.2 and Equation 4.4 are adapted to yield a wavelength-dependent γ by replacing the coefficients [p_1 p_2 p_3] with $p_1 = 0.63\gamma^2$ $p_2 = 0.57\gamma$ $p_3 = 2.31\gamma^2$ in equation 4.2 [11] and $C_{PF} = 0.68\gamma^{0.6}$ in equation 4.4. A Levenberg-Marquart non-linear fit procedure is used to estimate the variables $\mu_s'(\lambda)$ and $\gamma(\lambda)$ from the MDSFR spectra of two different fiber diameters simultaneously.

Finally, since the MDSFR analysis yields estimates of $\mu_s'(\lambda)$ and $\gamma(\lambda)$, these values can now be used in the individual SFR fits to re-estimate the absorption coefficient. In the first step, the absorption coefficient was estimated without knowledge of the scattering properties by assuming fixed (wavelength independent) values for [p_1 p_2 p_3 C_{PF}] and using a 4th order polynomial for $\mu_s'(\lambda)$; the accuracy of that approach is now verified by using the extracted wavelength dependent estimates of γ and using a biologically realistic shape for $\mu_s'(\lambda)$, i.e. a power law.

EXPERIMENTAL SETUP

The illustration in figure 4.1 represents a single probe-unit of the MDSFR spectroscopic setup. During reflectance measurements, white light emitted by a halogen light source (HL-2000-FHSA; Ocean Optics; Duiven, NL) is directed through the first fiber of a quadfurcation into a solid core fiber optic probe and guided onto the tissue. A small fraction of the light is reflected from the tissue into the acceptance cone of the probe fiber and directed via a second fiber of the quadfurcation into a spectrometer (SD-2000; Ocean Optics; Duiven, NL) for detection and further analysis. After the reflectance measurement, a low power fluorescence measurement is performed, using a 405 nm laser directed into another fiber of the quadfurcation to illuminate the tissue through the same

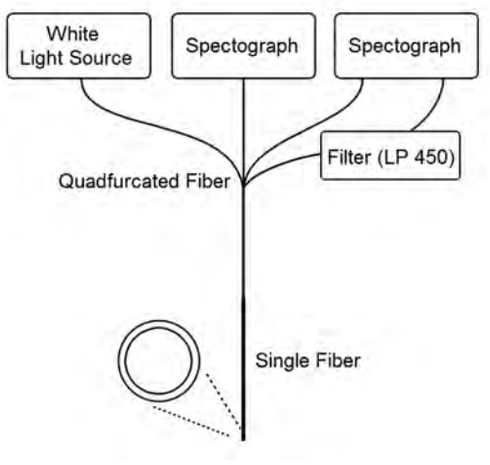

Figure 4.1: *Schematic diagram of the measurement setup. Reflectance and fluorescence are measured through a single fiber of either 0.4 or 0.8 mm. Two identical setups are used to accommodate two fiber diameters.*

probe. The emitted fluorescence is then guided through the last fiber of the quadfurcation, which leads through a 450 nm long-pass filter into a second spectrograph (QE-65000; Ocean Optics; Duiven, NL). The fluorescence measurement is incorporated to ensure the presence of tumor cells, retro-virally infected with gfp, in the measurement volume. The complete MDSFR system consists of two identical probe-units containing fiber diameters of 0.4 and 0.8 mm. The fiber probes are sequentially placed in contact with the tissue under investigation. All probes are polished under an angle of 15^{o} to minimize internal specular reflections from the probe tip. A calibration procedure was performed as described previously [7], consisting of a measurement in water in a dark container (I_{water}) and a measurement in a liquid phantom containing 20% Intralipid diluted to yield μ_s'(800nm)=1.2 mm^{-1}, (I_{IL}^{cal}), where

$$R_{SF}^{meas} = I_{IL}^{sim}\left[\frac{I_{meas} - I_{water}}{I_{IL}^{cal} - I_{water}}\right] \tag{4.12}$$

and I_{IL}^{sim} is the absolute SFR signal obtained through Monte Carlo simulations.

ANIMAL MODEL

The study protocol was approved by the Animal Welfare Committee of the Leiden University Medical Center. Housing of BALB/cByJ nu/nu female mice (aged 4-6 weeks; Charles River Laboratories), the experiments and euthanazation were performed in accordance with the guidelines of this committee. Chlorophyll free food and sterilized water were provided without restriction. A set of 19 mice were injected with OSC19 cells lenti-virally transfected with luc and gfp (6x10^4 cells, Biocat, Heidelberg, Germany) [15, 16]. After an incubation period of 10-13 days, animals were included in the study and anesthetized with 2-3% Isoflurane. Reflectance spectra were acquired from tumor, normal tongue tissue (both five measurements), and skin and liver (both three measurements). The consecutive measurements were taken by removing and carefully repositioning the fiber between measurements, without imparting undue pressure on each tissue. For tumor, the fiber tip was positioned directly on top of the visible tumor. An additional MDSFR measurement of liver was carried out immediately before animals were sacrificed. After the animals were sacrificed, the tongue was harvested for microscopic tissue analysis.

DATA REDUCTION AND STATISTICAL ANALYSIS

To verify the presence of tumor tissue in the measurement volume with the probe on top of the tumor, co-localized fluorescence spectra are acquired with both the 0.4 and 0.8 mm fiber. Since the quantum yield of Cop-gfp, incorporated to identify tumor tissue, is

high, qualitative analysis of these spectra was sufficient to exclude measurements where tumor tissue was not present in the measurement volume. Two animals did not develop a visual tumor, and lacked gfp fluorescence in all five tumor measurements for both fiber diameters. These animals were excluded from the analysis of optical properties of tumor tissue.

Variation in probe pressure and probe location in consecutive measurements may lead to slight variations in outcome, which can interfere with a proper analysis of the averaged MDSFR data. Therefore, all SFR spectra with R(800 nm) deviating >2σ from the average value of R(800 nm) of the consecutive measurements on each tissue site, were removed from the analysis after the first analysis step. To account for remaining variations in subsequent SFR measurements, the standard deviation of R(800 nm) for each fiber diameter was used as a weight factor in the non-linear MDSFR fit procedure. Therefore, SFR fiber measurements with large variations contribute less to the best-fit outcome. Statistical analysis of optical properties for various tissues is done by using a paired Student T-test with $P<0.05$ as the level of significance.

RESULTS

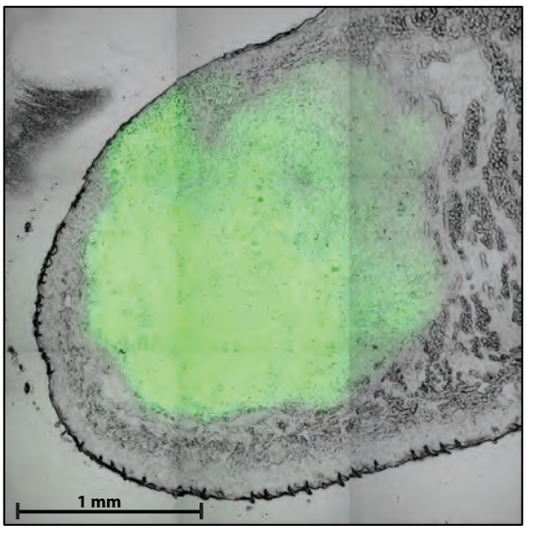

Figure 4.2: *Confocal fluorescence microscopy image of mouse tongue, using 488 nm excitation and 520-540 nm detection, showing the distribution of gfp-expressing OSC tumor in green and transmitted 488 nm light in grey. Scale bar 1 mm.*

After an incubation period of 10-13 days, 17 mice had a visible tumor at the tip of the tongue. Figure 4.2 shows a representative example of a combined confocal fluorescence and bright-field transmission microscopy image of a frozen section cut vertically through the center of the tongue. In this example the fiber tip was positioned in contact with the surface of the tongue in the upper left region of the image where tumor cells are close to the surface of the tongue. The image shows a thin but variable layer of epithelium overlying the gfp-fluorescent tumor at the tip of the tongue. A total of 588 reflectance spectra taken from 19 mice were analyzed in this study.

Figure 4.3 shows representative reflectance

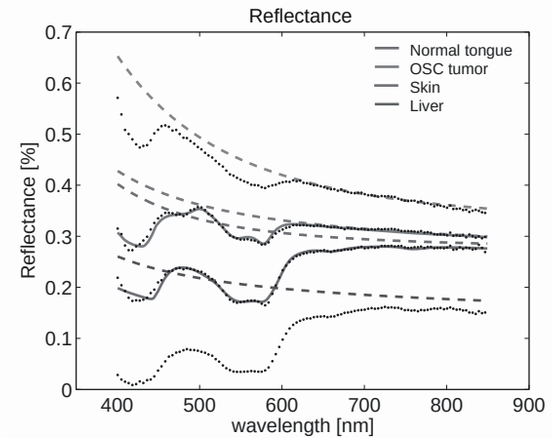

Figure 4.3: *Typical 0.8 mm SFR data. Plotted are the measured R_{SF} (black dots), individual SFR fits (solid lines) and calculated R_{SF}^0 (dashed lines) for normal tongue, tumor, skin and liver tissue.*

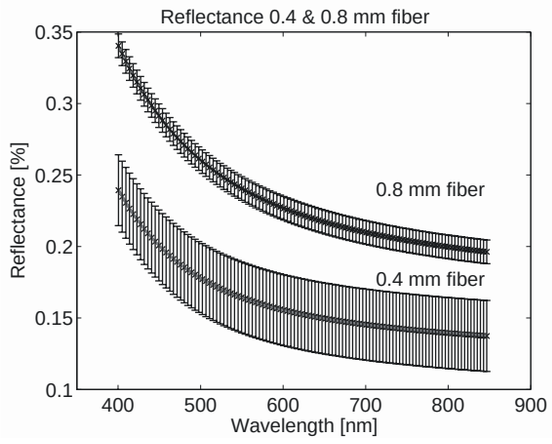

Figure 4.4: *Averaged SFR spectra of normal tongue tissue; fiber diameters are 0.4 and 0.8 mm.*

4

spectra of tumor, tongue, skin and liver tissue, together with their best fits and calculated absorption-corrected reflectance R_{SF}^0 for a 0.8 mm fiber (after the 3rd analysis step, based on power-law scattering and wavelength-dependent γ).

In this example, the spectra taken on skin show a significantly higher reflectance over the whole wavelength range compared to normal tongue and tumor tissue, while reflectance for liver is lowest. R_{SF}^0 spectra (dashed lines in figure 4.3) of five consecutive co-localized measurements per fiber diameter are averaged, and these averaged spectra and their standard deviations serve as input for the MDSFR analysis. Figure 4.4 shows the average R_{SF}^0 spectra of normal tongue tissue in a single mouse, fitted with the MDSFR model. As expected, a larger fiber diameter results in a higher reflectance.

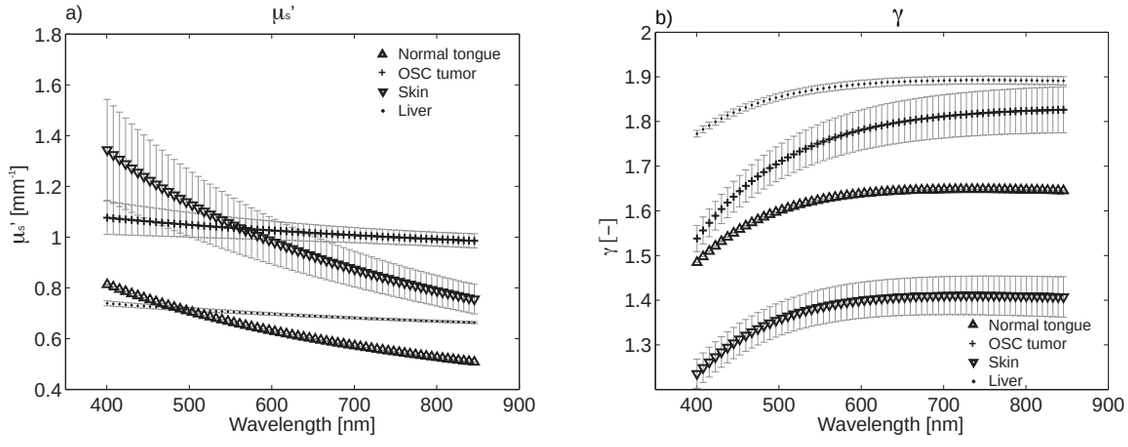

Figure 4.5: μ_s' *(a) and* γ *(b) for different tissues, measured in one representative mouse.*

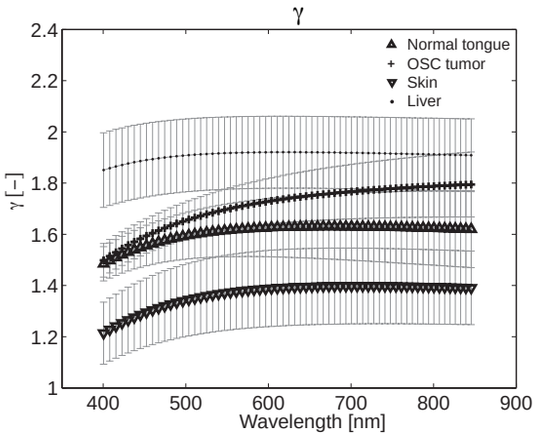

Figure 4.6: *Gamma per tissue, averaged over n=19.*

Figure 4.5a and b show $\mu_s'(\lambda)$ and $\gamma(\lambda)$ resulting from MDSFR fits on different tissues for a representative mouse. For all locations, μ_s' decreases with increasing wavelength [17]. It is helpful to describe μ_s' in terms of two parameters, the reduced scattering coefficient at 800 nm μ_s'(800nm), and its wavelength dependent slope, which is often termed the scattering power (resp. a_1 and a_2 in equation 4.11).

It has been shown that the scattering power is related to the refractive index correlation function of the measured tissue, and therefore has a direct relation with tissue structure [18-20]. In general we can conclude from all measurements that skin is most easily distinguishable from the other tissues by having a higher value for the scattering power. The differences between tumor and normal tongue tissue are more subtle, but tumor tends to have a lower scattering power than normal tongue tissue. Liver also shows a very low scattering power. The wavelength dependence of γ (figure 4.5b) shows an increase with wavelength for the low wavelength region, for all tissue types. For higher wavelengths, γ either plateaus or decreases after reaching a maximum, except for tumor tissue, for which γ continues to increase with wavelength.

In figure 4.6, we show the average $\gamma(\lambda)$ for the four different tissue types, based on the measurements on all 19 mice. Figure 4.7a-c show the median and quartiles of μ_s'(800), the scattering power, and γ averaged over the 400-850 nm wavelength range, for normal tongue, tumor tissue, skin and liver.

Both figure 4.6 and figure 4.7c clearly show that γ is lowest for skin and highest for liver. Furthermore, γ for tumor increases monotonically with increasing wavelength, and increases more over the measured wavelength range than for normal tissue, although this difference is not significant. Table 4.1 summarizes the average values for scattering power, μ_s'(800) and average γ for the four tissue types.

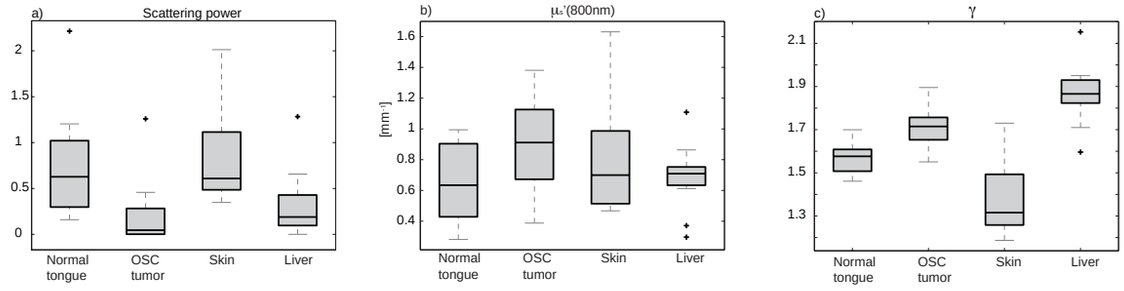

Figure 4.7: *Average scattering power (a), μ_s' (800nm) (b) and Gamma (c) of 19 mice, for four different tissues.*

From figure 4.7a and table 4.1, it can be seen that the scattering powers of tumor and liver are significantly lower than for normal tongue and skin (Paired t-test, P<0.05). The μ_s'(800nm) for tumor is significantly higher than for normal tongue and liver. The average value for γ of skin differs significantly from all other tissues.

Table 4.1: *Scattering power, μ_s'(800nm) and average γ for four different tissues*

	Scattering power	**μ_s' (800nm) [mm^{-1}]**	γ
Normal tongue	0.63±0.35	0.64±0.25	1.58±0.07
OSC tumor	0.13±0.16	0.90±0.29	1.72±0.09
Skin	0.86±0.49	0.81±0.37	1.37±0.14
Liver	0.24±0.20	0.71±0.08	1.87±0.07

An interesting observation is that although the reflectance is highest for skin, the $\mu_s'(\lambda)$ is not. This suggests that the angular distribution of scattering represented by $\gamma(\lambda)$ can strongly influence the observed reflectance. The low $\gamma(\lambda)$ for skin indicates that scattering is more directed backwards for skin than for other tissues, resulting in a higher total reflectance. For liver the opposite occurs; the low reflectance in this tissue is not a result of a low $\mu_s'(\lambda)$, but the high $\gamma(\lambda)$ which indicates that most of the scattered light is directed forward.

DISCUSSION

In this paper we have presented the first in-vivo measurements of $\mu_s'(\lambda)$ and $\gamma(\lambda)$ obtained using multi-diameter single fiber reflectance spectroscopy. We determined $\mu_s'(\lambda)$ and $\gamma(\lambda)$ for four different types of mouse tissue, including skin, liver, normal tongue and oral squamous cell carcinoma. Measurements of $\mu_s'(\lambda)$ and $\gamma(\lambda)$ show distinct differences between tissue types.

COMPARISON TO PREVIOUS STUDIES: $\mu_s'(\lambda)$

A number of previous studies have performed measurements to determine the optical (scattering) properties of tissues in ex-vivo and in-vivo tissue samples. The often significant limitations of measuring tissue optical properties in ex-vivo samples are well recognized [21]. The measurement of tissue optical properties in-vivo has for the most part been based on the use of diffuse reflectance spectroscopy or the measurement of interstitial fluence rate and angularly resolved radiance [21]. A range of tissue types have been investigated, in general for wavelengths above 630 nm. In the wavelength region between 630 and 850 nm the reduced scattering coefficient typically ranges from 0.4-1.31 mm^{-1}, with tissues such as brain and stomach yielding higher values. These values are well within the range of those found in the present study. Thus far, the only data reported for shorter wavelengths is in the stomach [22] where the absolute value of μ_s' is slightly higher than the range we obtained for our investigated tissues, but this is likely to be a consequence of the different tissue type.

The scattering power is related to the shape of the refractive index correlation function and has recently been suggested to be an important factor in identifying tissue structure. Ex-vivo data of various organs have been published [23, 24]. Yi and Backman have reported for rat liver a scattering power of 1.64±0.11, measured by inverse spectroscopic optical coherence tomography on excised organs. Hall et al. found the scattering power for fixed muscle tissue slices of mice to be 1.30±0.12 by measuring the angular distribution of light scattered through the sample, and fitting these observations to Monte Carlo simulations to obtain the optical properties of the sample under investigation. Although our in-vivo scattering powers are low compared to these values, they are still within the range of $0<a_2<2$, which is typical for tissue [25]. A recently published paper on in-vivo measurements of the correlation length in colorectal field carcinogenesis reported scattering powers of $0.2<a_2<0.5$ [26]. This aligns well with the relatively low a_2 values we have found in the present in-vivo study. Whether the differences in scattering power are related to differences between in-vivo and ex-vivo scattering properties or due to differences in the optical methods remains a topic of investigation.

COMPARISON TO PREVIOUS STUDIES: $\gamma(\lambda)$

We observe marked differences when comparing our findings of the wavelength dependence of γ to the in-vivo data published by Thueler et al. [22]. We have extracted γ values between 1.2 and 1.9 with γ generally increasing with wavelength; γ varied between 1.5 and 1.9 for tongue and tumor tissue, and between 1.2 and 1.5 for skin, which are within the range of expected values for tissue [7, 27, 28]. Thueler et al. report

measurements on stomach epithelium with an approximately constant γ with values around 2.0, and a slight increase in the low wavelength region. Whether these differences in γ are related to differences between tissue types or due to differences in the used optical methods remains to be investigated.

It is interesting to consider that the spectral shape of γ can be linked to the correlation function of the refractive index in the tissue under investigation. The spectral shape of γ is determined by the first two Legendre moments of the phase function, which are wavelength dependent. The phase function and its derived metrics anisotropy (g_1) and γ are, similar to the (reduced) scattering coefficient, related to the refractive index correlation function [20, 23]. The tissue refractive index correlation function has recently been modeled by the Whittle-Matérn correlation function, which contains three variables: the deterministic factor D, the length scale of the correlation l_c, and the scaling factor N_c. While the scattering power is directly related to the deterministic factor D, the length scale of the correlation l_c is related to both μ_s' and γ. In theory it is possible to express γ and its wavelength dependence in terms of l_c, and use the combined measurements of μ_s' and γ to calculate the physical properties of the correlation function, D and l_c. However, this is beyond the scope of this paper and will be presented in future work.

STEP-ANALYSIS OF FIT PROCEDURE

MDSFR is based on the reflectance in the absence of absorption. In the vast majority of in-vivo situations, where absorption is present, one first needs to determine the contribution of absorption to the total reflectance intensity using the model that we previously developed for individual SFR measurements. To achieve this, our analysis of tissue absorption and scattering in an individual SFR measurement was based on a background scattering model consisting of a polynomial (n=4), together with an optimized set of wavelength-independent coefficients representing γ [10]. The choice of such a non-physical background scattering model is necessary in order to correct for the ill-posed assumption that γ is wavelength independent; the background scattering model needs sufficient freedom in this first step to correct for this assumption. It is important to emphasize that in the first step, we only need to remove the effect of absorption on the individual SFR spectra by implementing the approach reported previously [11]. The MDSFR analysis itself is then performed with the physically realistic power-law scattering model (that follows from the definition of the Whittle-Matérn correlation function), which yields values for the reduced scattering coefficient (defined by the scattering power and μ_s'(800nm)) and γ. To verify that the absorption was correctly estimated in the first step, the extracted values for γ from the MDSFR analysis were used to re-analyse the individual

SFR measurements using the power-law scattering model and the extracted wavelength-dependent γ. We found that the absorption spectra extracted in the first step were almost identical to the absorption spectra extracted using the power-law scattering model and the wavelength dependent γ, as indicated by an average Pearson correlation coefficient of R^2=0.99 between extracted absorption spectra.

Clearly when more information becomes available about the wavelength dependence of γ, that knowledge could be used to spectrally constrain γ and thus complete an MDSFR fit in a single step fitting routine.

LIMITATIONS

A - Probe replacement

A potential limitation of the present study is caused by the fact that multiple fibers with different diameters are used sequentially. Therefore, slight differences in measurement volume are not only due to different fiber diameters but can also occur from measuring a slightly different spot in each measurement. Sequentially measuring the exact same tissue location with the exact same pressure for various fiber diameters is not only time consuming, but also makes the current measurement procedure cumbersome and sensitive to measurement artifacts. Clearly the use of a single measurement probe that is capable of rapidly changing its effective aperture would be a major step forward. New technological developments should overcome this problem in the near future and provide true co-localized measurement positions for various fiber diameters [29]. Despite the uncertainty in probe repositioning, the standard deviations for an individual mouse on the MDSFR fitted values for μ_s' and γ (figure 4.5a and b) are all within 10% of the fitted value (with the exception of μ_s' for skin), which is very encouraging.

B- Layered tissue

It is well known that skin and oral mucosa are comprised of layered tissue. In skin the stratum corneum and epidermis overlay the underlying dermis. In the oral cavity the normal tongue is comprised of a superficial keratinized layer with underlying epithelial layer and deeper lying connective tissue comprised of orthogonal muscle fiber bundles. The two, 0.4 and 0.8 mm, fibers are expected to probe the relatively homogeneous layers of tissue comprising mouse epithelium and dermis in the skin and the tongue epithelium and underlying connective tissue in normal tongue. OSC in the tongue develops beneath the superficial keratinized layer but can potentially be overlain by a layer of epithelial tissue of variable thickness. Microscope images of sections of OSC in the tongue (figure 4.2) show variation in thickness of the tissue layer covering the tumor between animals. Although tumor size and position varied somewhat between animals, placing the fiber

probe on a position where the tumor was visible minimized the distance between tumor and fiber tip. Since the measurement volume and depth increase with increasing fiber diameter, the smallest fiber diameter was specifically chosen to be 0.4 mm to incorporate tumor within the measurement volume. However, the contribution of the top layer of the tongue epithelium to the total acquired signal will be slightly different for each fiber diameter. Given these concerns we analyzed spectra acquired using each fiber diameter at a single location. This analysis showed consistent values for scattering power between fiber diameters. While this result suggests that the influence of epithelium overlying the tumor is small, it could be a reason why we observe only a relatively small difference in scattering signature between normal tongue and tumor tissue. The potential confounding effect of overlying epithelium could be removed in the future by studying a chemically induced model of oral cancer in animals or interrogating superficial human OSC.

FUTURE DEVELOPMENTS

Quantification of tissue optical properties does not only yield direct diagnostic information, it also facilitates the use of quantitative in-vivo fluorescence measurements. To quantify the concentration of an (exogenous) fluorophore in tissue, for example to monitor photodynamic therapy, knowledge of local tissue optical properties is necessary to correct for the effects of scattering and absorption on the collected fluorescence [30]. Our setup allows for reflectance and fluorescence measurements to be taken with the same probe, providing a method to determine fluorescence corrected for the influence of tissue optical properties, which opens the way to quantitatively compare fluorescence from different tissues and patients.

CONCLUSION

In conclusion, we have presented the first in-vivo MDSFR analysis of four different tissue types, based on measurements of 19 animals. Analysis of scattering power, reduced scattering at 800nm and average γ resulted in significant differences for the four tissue types studied. Future work will address the relation between $\mu_s'(\lambda)$ and $\gamma(\lambda)$ and the properties of the tissue refractive index correlation function D and l_c.

REFERENCES

1. Reif, R., O. A'Amar, and I.J. Bigio, *Analytical model of light reflectance for extraction of the optical properties in small volumes of turbid media.* Applied optics, 2007. **46**(29): p. 7317-7328.
2. Amelink, A., et al., *In vivo measurement of the local optical properties of tissue by use of differential path-length spectroscopy.* Optics Letters, 2004. **29**(10): p. 1087-1089.
3. Zonios, G., et al., *Diffuse Reflectance Spectroscopy of Human Adenomatous Colon Polyps In Vivo.* Applied optics, 1999. **38**(31): p. 6628-6637.
4. Tian, H., Y. Liu, and L. Wang, *Influence of the third-order parameter on diffuse reflectance at small source-detector separations.* Optics Letters, 2006. **31**(7): p. 933-935.
5. Bevilacqua, F. and C. Depeursinge, *Monte Carlo study of diffuse reflectance at source-detector separations close to one transport mean free path.* Journal of the Optical Society of America A, 1999. **16**(12): p. 2935-2945.
6. Kanick, S.C., et al., *Measurement of the reduced scattering coefficient of turbid media using single fiber reflectance spectroscopy: fiber diameter and phase function dependence.* Biomedical optics express, 2011. **2**(6): p. 1687-1702.
7. Gamm, U.A., et al., *Quantification of the reduced scattering coefficient and phase-function-dependent parameter Gamma of turbid media using multidiameter single fiber reflectance spectroscopy: experimental validation.* Optics Letters, 2012. **37**(11): p. 1838-1840.
8. Kanick, S.C., et al., *Monte Carlo analysis of single fiber reflectance spectroscopy: photon path length and sampling depth.* Physics in medicine and biology, 2009. **54**(22): p. 6991-7008.
9. Kanick, S.C., H. Sterenborg, and A. Amelink, *Empirical model of the photon path length for a single fiber reflectance spectroscopy device.* Optics Express, 2009. **17**(2): p. 860-871.
10. Kanick, S.C., et al., *Method to quantitate absorption coefficients from single fiber reflectance spectra without knowledge of the scattering properties.* Optics Letters, 2011. **36**(15): p. 2791-2793.
11. Kanick, S.C., et al., *Method to quantitatively estimate wavelength-dependent scattering properties from multidiameter single fiber reflectance spectra measured in a turbid medium.* Optics Letters, 2011. **36**(15): p. 2997-2999.
12. Gamm, U.A., et al., *Measurement of tissue scattering properties using multi-diameter single fiber reflectance spectroscopy: in silico sensitivity analysis.* Biomedical optics express, 2011. **2**(11): p. 3150-3166.
13. Van Veen, R.L.P., W. Verkruysse, and H. Sterenborg, *Diffuse-reflectance spectroscopy from 500 to 1060 nm by correction for inhomogeneously distributed absorbers.* Optics Letters, 2002. **27**(4): p. 246-248.
14. Rajaram, N., et al., *Experimental validation of the effects of microvasculature pigment packaging on in vivo diffuse reflectance spectroscopy.* Lasers in surgery and medicine, 2010. **42**(7): p. 680-688.
15. Yokoi, T., et al., *Establishment and characterization of a human cell line derived from a squamous cell carcinoma of the tongue.* Tumor Research, 1988. **23**: p. 43-57.
16. Carlotti, F., et al., *Lentiviral vectors efficiently transduce quiescent mature 3T3-L1 adipocytes.* Molecular Therapy, 2004. **9**(2): p. 209-217.
17. Cerussi, A.E., et al., *Sources of absorption and scattering contrast for near-infrared optical mammography.* Academic Radiology, 2001. **8**(3): p. 211-218.
18. Turzhitsky, V., et al., *Multiple scattering model for the penetration depth of low-coherence enhanced backscattering.* Journal of biomedical optics, 2011. **16**(9): p. 097006-097006.

19. Turzhitsky, V., et al., *A predictive model of backscattering at subdiffusion length scales.* Biomedical optics express, 2010. **1**(3): p. 1034-1046.

20. Rogers, J.D., I.R. Capolu, and V. Backman, *Nonscalar elastic light scattering from continuous random media in the Born approximation.* Optics Letters, 2009. **34**(12): p. 1891-1893.

21. Welch, A.J. and M. van Gemert, *Optical-Thermal Response of Laser Irradiated Tissue*1995: Plenum Press, New York.

22. Thueler, P., et al., *In vivo endoscopic tissue diagnostics based on spectroscopic absorption, scattering, and phase function properties.* Journal of biomedical optics, 2003. **8**(3): p. 495-503.

23. Yi, J. and V. Backman, *Imaging a full set of optical scattering properties of biological tissue by inverse spectroscopic optical coherence tomography.* Optics Letters, 2012. **37**(21): p. 4443-4445.

24. Hall, G., et al., *Goniometric measurements of thick tissue using Monte Carlo simulations to obtain the single scattering anisotropy coefficient.* Biomedical optics express, 2012. **3** (11): p. 2707-2719.

25. Xu, M. and R.R. Alfano, *Fractal mechanisms of light scattering in biological tissue and cells.* Optics Letters, 2005. **30**(22): p. 3051-3053.

26. Gomes, A.J., et al., *In vivo measurement of the shape of the tissue-refractive-index correlation function and its applicationto detection of colorectal field carcinogenesis.* Journal of biomedical optics, 2012. **17**(4): p. 047005-047005.

27. Bevilacqua, F., et al., *In Vivo Local Determination of Tissue Optical Properties: Applications to Human Brain.* Applied optics, 1999. **38**(22): p. 4939-4950.

28. Chamot, S., et al., *Physical interpretation of the phase function related parameter Y studied with a fractal distribution of spherical scatterers.* Optics express, 2010. **18**(23): p. 23664-23675.

29. Hoy, C.L., et al., *Use of a coherent fiber bundle for multi-diameter single fiber reflectance spectroscopy.* Biomedical optics express, 2012. **3**(10): p. 2452-2464.

30. Wilson, B.C., M.S. Patterson, and L. Lilge, *Implicit and explicit dosimetry in photodynamic therapy: a new paradigm.* Lasers in medical science, 1997. **12**(3): p. 182-199.

Intrinsic Photosensitizer Fluorescence Measured using Multi Diameter Single Fiber Spectroscopy *In-Vivo*

chapter 5

Floor van Leeuwen – van Zaane,
Ute Gamm, Pieter van Driel, Thomas Snoeks, Riëtte de Bruijn
Angélique van der Ploeg – van den Heuvel, Clemens Löwik,
Dick Sterenborg, Arjen Amelink, Dominic Robinson

Journal of Biomedical Optics, 2014. **19**(1): 015010

ABSTRACT

Quantification of fluorescence in-vivo is complicated by the influence of tissue optical properties on the collected fluorescence signal. When tissue optical properties in the measurement volume are quantified, one can obtain the intrinsic fluorescence, which equals the product of fluorophore absorption coefficient and quantum yield. We applied this method to in-vivo single fiber fluorescence (SFF) spectroscopy measurements on mouse tong, skin, liver and oral squamous cell carcinoma, where we detected intrinsic fluorescence spectra of the photosensitizers chlorin e_6 (ce6) and Bremachlorin at t = [3 4.5 6 24 48] hour incubation time. We observed a tissue dependent maximum of 35% variation in the total correction factor over the visible wavelength range. Significant differences in spectral shape over time between sensitizers were observed. While the wavelength position of the fluorescence intensity maximum for ce6 shifted to the red, Bremachlorin showed a blue-shift. Furthermore, the Bremachlorin peak appeared to be broader than the ce6 fluorescence peak. Intrinsic fluorescence intensity, which can be related to photosensitizer concentration, was decreasing for all time points, but showed significantly more Bremachlorin present compared to ce6 at long incubation times. Results from this study can be used to define an optimal treatment protocol for Bremachlorin-based photodynamic therapy.

INTRODUCTION

In-vivo optical spectroscopy is under investigation both as a diagnostic tool and as a method for monitoring a number of therapeutic modalities [1-4]. Reflectance spectroscopy provides information on the presence and concentration of tissue absorbers, while scattering can be related to information on morphology and ultrastructure of tissue [5, 6]. Fluorescence spectroscopy enables the detection of endogenous molecules such as collagen and NADH, as well as exogenous fluorophores such as fluorescent labeled markers and drugs [7, 8]. The shape and intensity of the fluorescence spectrum contain valuable information on fluorophore identity, its concentration and the local environment. The interrogation of fluorescent drugs in various tissue types is one of the major applications of in-vivo fluorescence spectroscopy and has been widely incorporated in photodynamic therapy (PDT) research and in clinical practice. Photosensitizing agents are well known for their fluorescent properties. It is shown that knowledge of photosensitizer fluorescence intensity and/or changes in photosensitizer spectral properties before and during treatment may be related to therapeutic efficacy and can be used to monitor PDT [9-12].

Despite the potential usefulness of in-vivo fluorescence spectroscopy, the exact quantification of fluorescent signals is proven to be very challenging. When measuring fluorescence in-vivo, the number of collected photons is strongly influenced by optical properties of the tissue under investigation. The local fluence rate is influenced by tissue optical properties at the excitation wavelength (λ_x), while the number of emitted fluorescence photons detected depends on the optical properties at the emission wavelength (λ_m). We are interested in the intrinsic fluorescence, where the influence of tissue optical properties is removed from the measured fluorescence spectrum and which can therefore be related to the fluorophore absorption coefficient and thereby to fluorophore concentration. Intrinsic fluorescence enables quantitative comparison of fluorescence intensity and spectral shape measured on tissues with different and/or varying optical properties.

Several methods have been developed previously to extract intrinsic fluorescence spectra in turbid media such as biological tissue. To provide accessibility to various tissues, system designs for in-vivo use are generally based on fiber optic probes. Many techniques combine white light reflection measurements to obtain tissue optical properties with a fluorescence measurement, and then use analytical or empirical models [4, 13, 14] to extract the intrinsic fluorescence. A complication of using optical properties obtained

from a reflectance measurement to correct fluorescence data is the discrepancy of measurement geometries between the two. Multi-fiber fluorescent probes with separate source(s) and detector(s), where the detected light is diffuse and the sampling volume is in the order of mm^3, have been extensively investigated [3, 4, 13, 15, 16]. In this geometry, both reflectance and (a large part of the) fluorescent light are diffusely scattered. After determination of the optical properties, an analytical model to retrieve intrinsic fluorescence can be used that is independent of specific probe design. Another approach is to use a source and detection fiber with a small separation distance and therefore probing a much smaller sample volume directly below the fiber tip. In this configuration, the majority of detected reflectance and fluorescence photons have undergone too few scattering events to apply diffusion theory and sample volumes for reflectance and fluorescence differ significantly from each other. Therefore, approaches to remove the influence of optical properties from fluorescence are based on (semi-) empirical models and are usually device and measurement geometry-specific. A specific situation of small source-detector separation is to use a single fiber for illumination and detection of both reflected and fluorescent light [17-20].

Our group has recently developed a fiber optic system based on the combination of multi-diameter single fiber reflectance (MDSFR) spectroscopy and single fiber fluorescence (SFF) spectroscopy; the former functioning to determine tissue absorption and scattering properties, the latter to detect tissue fluorescence [21-23]. Illumination and detection are performed by a single optical fiber probe for both reflectance and fluorescence measurements. The measurement volume is confined to shallow depths of the order of the fiber diameter [24, 25]. It is shown that acquiring two successive single fiber reflectance measurements with different fiber diameters (termed MDSFR) enables quantification of both the reduced scattering coefficient and the phase function parameter γ. This parameter is defined as

$$\gamma = \frac{1-g_2}{1-g_1} \tag{5.1}$$

where g_1 and g_2 are the first and second Legendre moment of the phase function, and has to be included due to the shallow measurement geometry [21, 26]. Intrinsic fluorescence is determined using a semi-empirical model based on Monte Carlo simulations and phantom studies. This model incorporates the effect of optical properties on local excitation fluence and fluorescence photon escape probability within the whole sample volume [23, 27].

An important application field where measurement of intrinsic fluorescence is particularly valuable is the determination of photosensitizer fluorescence before and during photodynamic therapy. Since oxygen is depleted during PDT, saturation levels in the measurement volume will change, and hence the optical properties. Other direct effects of PDT include changes in blood volume fraction and vessel diameter influencing absorption and the onset of acute edema, which influences scattering [11, 28-30]. Intrinsic fluorescence allows for reliable quantification and comparison of photosensitizer fluorescence at various time points before, during and after PDT.

Chlorins are a class of second generation photosensitizers that exhibit low dark toxicity and have enhanced absorption in the optical window between 600 and 800 nm. Chlorin e_6 (ce6) is a member of this family of photosensitizers and has been studied intensively for over two decades [31-33]. Preclinical studies comparing localization and photo toxicity of ce6 with other photosensitizers are performed [34, 35]. Ce6-PVP, in which the ce6 molecule is bound to a polyvinylpyrrolidone carrier, is used in PDT of urological oncological lesions [36]. The second-generation photosensitizer mono-L-aspartylchlorin-e6 has been used successfully in phase I studies for cutaneous lesions [37], solid tumors [38] and mucosal surfaces [39]. It is shown that in-vitro analysis of cellular uptake of ce6 has a strong dependence of spectral shape on pH of the solution, resulting in a shift of both the absorption and fluorescence spectrum and a decrease of fluorescence intensity [32, 33]. By analyzing both intensity and spectral shape, we should be able to distinguish between intensity decreases due to clearance of the photosensitizer from the tissue, and intensity changes due to re-localization to an environment with a different pH. One important aspect of the use of ce6 is its relatively low lipophilicity; this means that it is metabolized rapidly and cleared from the body quickly via the urinary system. This has advantages in, for example, reducing skin photosensitivity but a short clearance time limits its effective localization in neoplastic tissue. A new photosensitizing compound, Bremachlorin, consists largely (~80%) of ce6, combined with the photosensitizing agents purpurin 5 (~15%) and chlorin p_6 (~5%) [40, 41]. The main active component of Bremachlorin is thought to be purpurin 5, because of its rapid interaction with albumin and low-density lipoproteins that enables it to be delivered to cancerous tissues [42]. Although purpurin 5 in itself is too hydrophobic to be administered in aqueous solution, combined with ce6 and cp6 it achieves the chemical stability required for both intravenous administration and storage. It is expected that the combined purpurin 5 and ce6 in Bremachlorin results in an overall photosensitizing effect that is greater than the individual concentrations of both photosensitizers [40].

In the present study we have for the first time used quantitative single fiber fluorescence spectroscopy in-vivo to analyze fluorescence spectra of both ce6 and Bremachlorin in-vivo. Analysis of variations in both fluorescent spectral shape and intensity yields information on clearance and localization of both photosensitizers under investigation. This analysis is applied on healthy tongue tissue, oral squamous cell carcinoma tissue at the tip of the tongue, skin and liver, for time points ranging from 3 to 48 hours after photosensitizer injection.

MATERIALS & METHODS

CORRECTION THEORY

To measure intrinsic fluorescence, it is necessary to correct the measured raw fluorescence signal for the influence of μ'_s and μ_a. The method of determining μ'_s and μ_a from MDSFR spectra has been described in detail elsewhere [21, 22, 43]. Furthermore, a semi-empirical model is developed, based on Monte-Carlo simulations and phantom studies to account for the influence of tissue optical properties on a fluorescence signal [23, 27]. To obtain the fluorescence in the absence of absorption F^0_{SF} from the measured fluorescence F_{SF} a modified form of Beer's law is used [27]

$$F_{SF} = F^0_{SF} e^{\left(-\mu_{a,avg}\langle L_{SFF}\rangle\right)}. \tag{5.2}$$

Here, $\mu_{a,avg}$ is the average μ_a at the excitation and emission wavelength and the fluorescence photon path length L_{SFF} is defined as

$$\langle L_{SFF}\rangle = \langle Z\rangle \frac{1+\kappa\sqrt{\left(\mu_{s,avg}d_f\right)}}{1+\left(\mu_{a,avg}d_f\right)}, \tag{5.3}$$

where $\mu'_{s,avg}$ is the average μ'_s at excitation and emission wavelength, d_f is the fiber diameter and κ represents a single fitted parameter which has a value of κ =1.81±0.01 [23]. Z is the effective sampling depth, defined as

$$\langle Z\rangle = d_f A_2 \left(\mu_{s,avg}d_f\right)^{-A_3}, \tag{5.4}$$

and can be related to the effective sampling volume

$$\langle V\rangle = A_1 \langle Z\rangle d_f^2. \tag{5.5}$$

In this equation, A_1 is a proportionality factor that depends on the geometrical shape of the effective volume and A_2 and A_3 are determined empirically to be 0.71±0.01 and 0.36±0.01 respectively [23, 27].

A model is previously developed to relate F^0_{SF} to the intrinsic fluorescence spectrum $\mu^f_a Q^f$, which is the product of fluorophore absorption coefficient and quantum yield, integrated over wavelength [27]

$$F^{SF}_{Ratio} = \frac{F^0_{SF}}{P_{Laser}} \approx \left(\frac{\lambda_x}{\lambda_m}\right)\mu^f_a Q^f \left\langle \phi^V_x \right\rangle \left\langle H^V_m \right\rangle \langle V \rangle \quad . \tag{5.6}$$

Here $\langle V \rangle$, $\left\langle \phi^V_x \right\rangle$ and $\left\langle H^V_m \right\rangle$ are the effective sampling volume, excitation fluence and escape probability respectively, which can all be described as a function of μ'_s and d_f. The factor $\frac{\lambda_x}{\lambda_m}$ accounts for difference in photon energy between emission and excitation wavelength. F^{SF}_{Ratio} is the ratio between the total excitation photons launched (related to P_{laser}) and the emitted photons detected (related to F^0_{SF}). The product of equation 5.6 and the expressions for $\langle V \rangle$, $\left\langle \phi^V_x \right\rangle$ and $\left\langle H^V_m \right\rangle$ yields

$$\frac{F^{SF}_{Ratio}}{\mu^f_a Q^f d_f \nu_f}\left(\frac{\lambda_m}{\lambda_x}\right) = \zeta_1 \left(\mu_{s,avg} d_f + 0.00315\right)^{-\zeta_2} e^{\left(\frac{-1}{\zeta_2\left(\mu_s(\lambda_x)d_f\right)+1} - \frac{\zeta_3}{\zeta_2\left(\mu_s(\lambda_m)d_f\right)+1}\right)} \tag{5.7}$$

where [ζ_1 ζ_2 ζ_3] are fitted parameters with values [0.0935±0.003, 0.31±0.01, 1.61±0.05] and λ_x and λ_m the excitation and emission wavelength respectively [27]. Since our measurements, and therefore the intrinsic fluorescence spectra did not only contain photosensitizer fluorescence, but also included autofluorescence and gfp fluorescence in measurements on tumor tissue, the contribution of the latter two to the intrinsic fluorescence spectra was determined by spectral deconvolution and both components were subtracted, resulting in photosensitizer intrinsic fluorescence spectra. We note that equation 5.7 includes a value of 0.00315 to be able to apply the model in the very low scattering regime. Including this factor results in a theoretical maximum value for equation 5.6 of 0.041 for μ'_s=0 mm^{-1}, which corresponds with the analytically derived maximum fluorescence in the situation of no scattering and no absorption using an NA=0.22 fiber in a medium with a refractive index of n_0=1.33 [44].

MEASUREMENT SETUP

The illustration in figure 5.1 represents a single probe unit of the combined MDSFR-SFF spectroscopic setup. Two of those probe units were used, with the only difference in fiber diameter of the probe and quadfurcation, to be able to perform measurements with both 0.4 and 0.8 mm probes. Positioning of the probes was done manually.

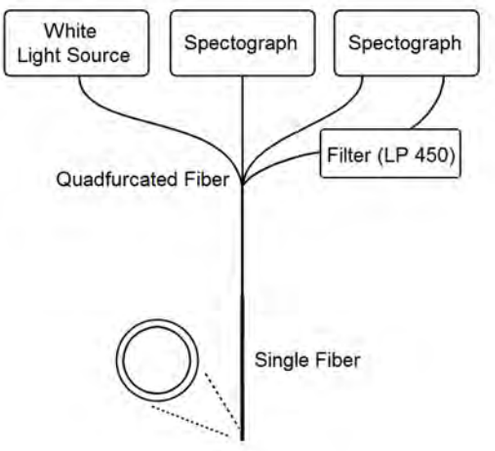

Figure 5.1: *Schematic diagram of the measurement setup. Reflectance and fluorescence are measured through a single fiber of either 0.4 or 0.8 mm. Two identical setups are used to accommodate the two fiber diameters.*

The measurements consisted of a subsequent reflectance and fluorescence measurement without probe repositioning. During a reflectance measurement, white light emitted by a halogen light source (HL-2000-FHSA; Ocean Optics; Duiven, NL) was directed through the first leg of a quadfurcation into a solid core fiber optic probe and guided onto the tissue. A small fraction of the white light was reflected from the tissue into the acceptance cone of the probe fiber and directed via a second leg of the quadfurcation into a spectrometer (SD-2000; Ocean Optics; Duiven, NL) for detection and further analysis. After the reflectance measurement, the fluorescence measurement was performed, using low power 405 nm excitation light coupled into one leg of the quadfurcation to illuminate the tissue through the same solid core probe as the reflectance. The emitted fluorescence was then guided through the last leg of the quadfurcation, which leads through a 450 nm long-pass filter into a second spectrograph (QE-65000; Ocean Optics; Duiven, NL) by the use of a solid core 0.2 mm fiber. The complete MDSFR-SFF system consists of two identical probe-units containing probe core diameters of 0.4 and 0.8 mm, combined with a 4x0.1 mm and a 4x0.2 mm quadfurcation respectively. The fiber probes were sequentially placed in contact with the tissue under investigation. Both probes were polished under an angle of 15^{o} to minimize internal specular reflections from the probe tip. The calibration procedure using a diluted Intralipid 20% phantom included correction for fiber alignment and transmission efficiency and is described elsewhere [45].

ANIMAL MODEL

For this study, 19 mice (BALB/c nu/nu female mice, aged 4-6 weeks; Charles River Laboratories) were injected with metastatic oral squamous cell carcinoma cell line OSC19, lenti-virally transfected with luc2 (Biocat, Heidelberg, Germany) and Cop-gfp (Evrogen, Moscow, Russia). $6x10^{4}$ cells, diluted in 20 µl PBS, were injected to induce an oral squamous cell carcinoma at the tip of the tongue after an incubation period of 10-13 days [43, 46-48]. Gfp was included in the cell line to easily assess the inclusion of tumor tissue in the measurement volume. After tumor incubation, animals were restrained and

injected with chlorin e_6 (16 mg kg^{-1} in 100 µl PBS, Frontier Scientific, Inc., Logan, USA) or Bremachlorin (20 mg kg^{-1}, form stock solution of 3.5 g l^{-1}, Rada-pharma International BV, The Netherlands). At t = [3 4.5 6 24 or 48] hours after photosensitizer injection, animals were anesthetized with an injection of ketamine/xylazine and spectroscopic reflectance measurements with both fiber diameters and fluorescence measurements with the 0.4 mm fiber were performed on normal tongue tissue, OSC tumor (both five measurements per fiber diameter), skin and liver (both three measurements per fiber diameter), after which the animals were sacrificed. The consecutive measurements were taken by removing and carefully repositioning the fiber between measurements, without imparting undue pressure on each tissue. For tumor, the fiber tip was positioned directly on top of the visible tumor. The study protocol was approved by the Animal Welfare Committee of the Leiden University Medical Center. Housing of BALB/c nu/nu female mice, the experiments and euthanazation were performed in accordance with the guidelines of this committee. Chlorophyll free food and sterilized water were provided without restriction.

DATA ANALYSIS

All data analysis was performed using custom applications running in Matlab (release 2009b, The Mathworks, Natick, MA, USA). Reflectance spectra were fitted with a combination of basis spectra by using a Levenberg-Marquart non-linear fit procedure to estimate μ_a. μ'_s was determined by averaging the absorption-corrected reflectance spectra per fiber diameter and fitting a model through those averaged reflectance spectra of both fiber diameters, as previously described [43]. Individual measurements that were excluded from the MDSFR fit were excluded from SFF analysis as well. Spectra were excluded from the analysis when (i) fluorescence measurements did not indicate the presence of tumor tissue in the tumor measurement, (ii) we were unable to fit µa to the individual reflectance spectrum (iii) we could not successfully fit μ'_s or γ to the averaged absorption-corrected reflectance spectra. The fluorescence spectra from all individual measurements were corrected for absorption and scattering as described above. These corrected fluorescence spectra were then divided into autofluorescence, gfp fluorescence and photosensitizer fluorescence by spectral deconvolution. The autofluorescence and gfp were then subtracted to obtain the intrinsic fluorescence spectrum. Basis spectra for gfp and autofluorescence were constructed from fluorescence measurements on >5 animals before fluorophore injection, where normal tongue and tumor were fitted with an identical autofluorescence spectrum. Skin and liver were both analyzed with their tissue-dependent autofluorescence basis spectrum. Spectral deconvolution was again based on a Levenberg-Marquart non-linear fit procedure. The resulting intrinsic photosensitizer fluorescence spectrum was related to the product of photosensitizer

absorption coefficient and quantum yield $\mu^f_a Q^f$ by integration over wavelength. To quantify variations in the shape of the spectral emission, two Gaussians were fitted to the main ce6/Bremachlorin peak present in the intrinsic photosensitizer fluorescence spectrum; one covering the high-intensity emission peak, fitted between 650 and 680 nm and a skewed Gaussian to determine the width and intensity of the emission shoulder at the right side of the maximum between 680 and 800 nm. This skewed function is defined as

$$f(\lambda) = b_1 e^{\frac{-(\lambda - b_2)^2}{2b_3^2}} \left(1 + erf\left(b_4 \frac{\lambda - b_2}{\sqrt{2}}\right)\right). \quad (5.8)$$

The parameters b_1-b_4 were fitted using a least-mean-square method to describe the shape of the right hand sight of the spectra. From these fitted Gaussian curves we were able to determine the intrinsic fluorescence intensity, peak wavelength, FWHM of both fitted Gaussians and the ratio between different fit parameters. The underlying reasons for and implications of these spectral shifts are discussed below.

RESULTS

For this experiment, 299 spectra were included in the analysis. In biological tissue, largest variations of absorption in the visible range is found in the 400-600 nm range, while scattering is decreasing with increasing wavelength.

Figure 5.2 shows a typical example of MDSFR spectra taken on tumor tissue, using a 0.4 and 0.8 mm fiber, together with their corresponding scattering background model in the absence of absorption. Around 500 nm, a peak could be distinguished, caused by strong gfp fluorescence of the tongue tumor, excited by white light used to acquire the reflectance spectra.

THE MAGNITUDE OF THE CORRECTION FOR TISSUE OPTICAL PROPERTIES

The correction factor was calculated over the whole spectral range for both absorption and scattering for the four different tissues, averaged over all mice. These are shown in figure 5.3a and b. The error bars indicate the SD of all measurements per tissue.

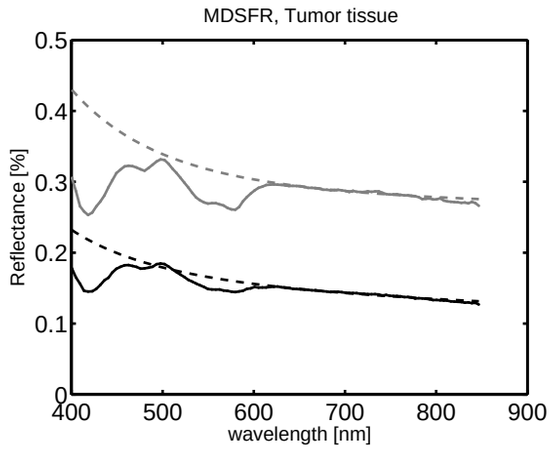

Figure 5.2: *Reflectance measurement of tongue tumor tissue. Black) 0.4 mm fiber, Grey) 0.8 mm fiber. Shown are the reflectance spectrum (o) and the scattering background model (--), averaged over five consecutive measurements.*

The correction factors were dependent on the tissue type and illustrated the importance of our technique for the recovery of intrinsic fluorescence in different tissue types: absorption was significantly stronger in liver where there was a high concentration of blood, whereas skin had the lowest absorption. Scattering correction did not vary significantly with tissue type (figure 5.3b). The spectral variation of oxygenated and deoxygenated blood was observed in tumor and normal tongue absorption coefficients. The variation in the total correction factor over the visible wavelength range for both the absorption and scattering is shown in figure 5.4, where the maximum value of the absorption or scattering based correction factor is divided by the minimum value. This figure shows clearly that correction for tissue absorption was most important with regards to analysis of spectral shape. Scattering varied less over wavelength, although the contribution of the scattering correction to the total correction procedure was larger than that of absorption. Therefore, incorrect scattering correction will result in an incorrect calculation of the fluorophore concentration but much less in incorrect conclusions on spectral shape. Applying both absorption and scattering correction results in the intrinsic fluorescence spectrum.

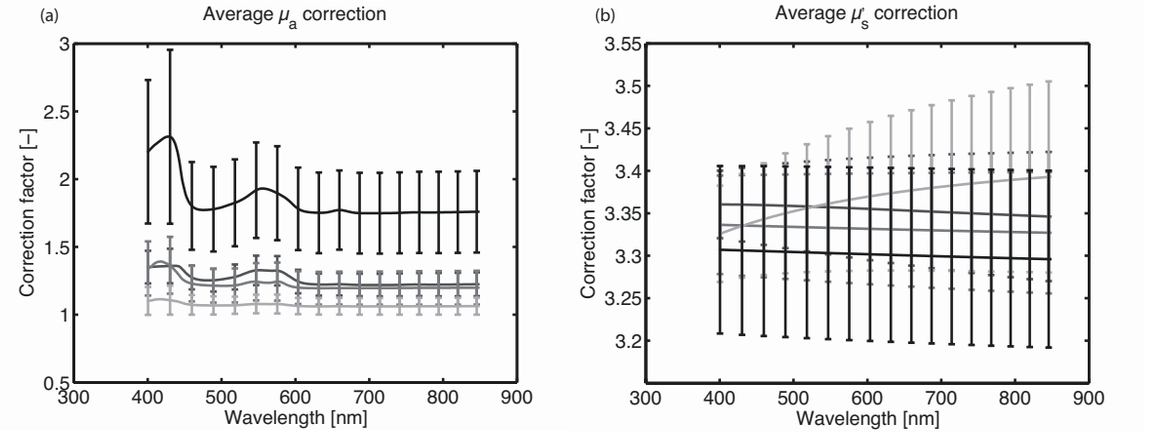

Figure 5.3: *(a) Average μ_a factor spectrum for four different tissues. Since μ_a was wavelength dependent, the absorption correction is too. Calculation is based on equation 5.2. (b) Average scattering correction factor spectrum for four different tissues, resulting from equation 5.7.*

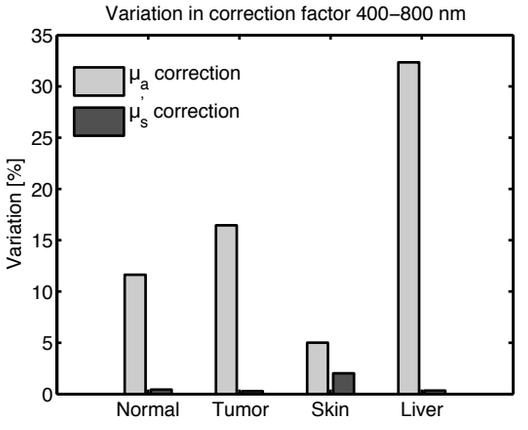

Figure 5.4: *Variation over the visible wavelength range (400-800 nm) of the corrections for absorption and scattering. Maximum value in that range divided by minimum value.*

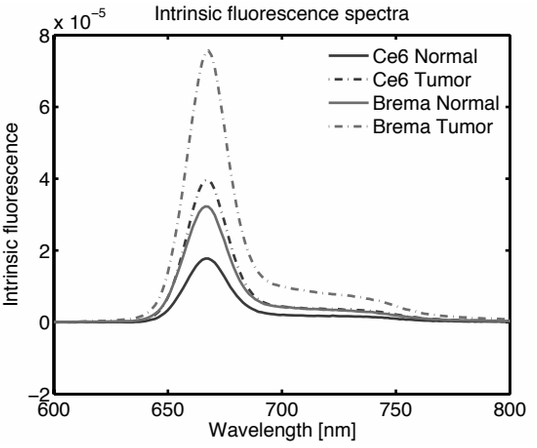

Figure 5.5: *Typical ce6 and Bremachlorin spectrum in normal tongue and tumor, 3 hours after photosensitizer injection.*

When comparing intrinsic fluorescence spectra of Bremachlorin and ce6 of normal and tongue tumor tissue in figure 5.5, Bremachlorin showed higher fluorescence intensity than ce6 did for both tissues. Furthermore, the tumor tissue intensity was much higher than that of normal tissue.

To illustrate the spectral variations of ce6 and Bremachlorin in different tissues at different time points, figure 5.6a and b shows normalized spectra acquired from different tissues and time points. Between 3 and 24 hours after injection the ce6 peak shifted towards longer wavelengths, while for Bremachlorin a shift towards lower wavelengths was measured. Furthermore, clear differences in peak width and the contribution of the longer wavelength shoulder were observed over time after photosensitizer administration.

To quantify these spectral variations in the intrinsic photosensitizer fluorescence spectrum, the fluorescence was characterized by two fitted Gaussian distributions as shown in figure 5.7; one covered the high-intensity emission peak, fitted between 650 and 680 nm and a skewed Gaussian determined the width and intensity of the emission shoulder at the right side of the maximum between 680 and 800 nm.

INTENSITY AND RATIO

Both ce6 and Bremachlorin showed the highest intrinsic fluorescence intensity in liver and lowest in normal tissue.

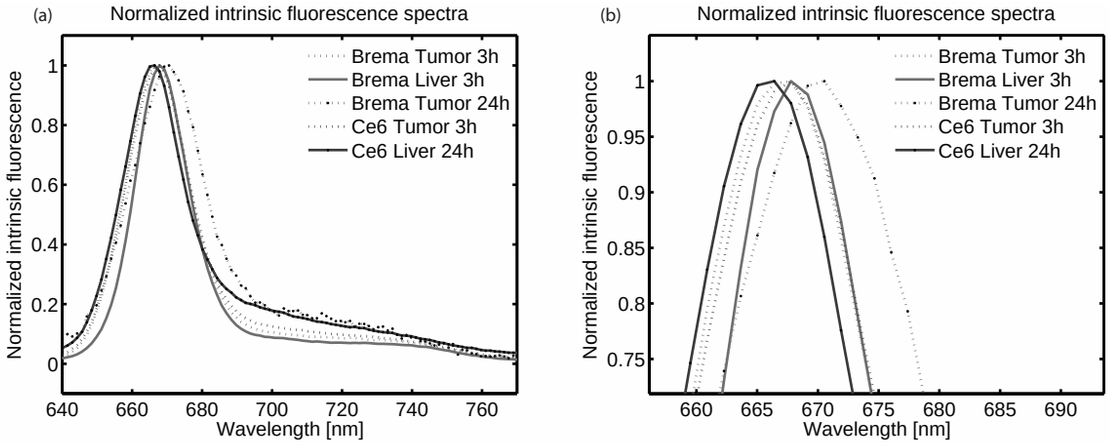

Figure 5.6: *(a) Characteristic intrinsic photosensitizer fluorescence spectrum for varying tissue, time and photosensitizer, normalized. (b) Close up of peak position*

Furthermore, fluorescence intensity of Bremachlorin was significantly higher in all tissues at all time points (except 3 and 6 hour measurements in liver, where the difference is not significant), as can be seen in figure 5.8a. The fluorescence intensity was measured as the maximum value of the fluorophore intrinsic fluorescence spectrum. It is evident from the data (figure 5.8a) that there was relatively less ce6 present in time as it was cleared more rapidly than Bremachlorin. This may have significant implications for the use of Bremachlorin as a photosensitizer and will be discussed in more detail elsewhere. Figure 5.8b shows the intensity ratio of the main peak and the shoulder on the right side. For this, the maximum values of both fitted Gaussian distributions were divided by each other. Ce6 showed ratios between 8.4 and 11.0, significantly larger than Bremachlorin (ratios between 5.9 and 7.5) for 3, 4.5 and 6 hours after injection in all tissues, indicating a lower shoulder for ce6 compared with Bremachlorin ($P<0.02$ for all time points and tissues).

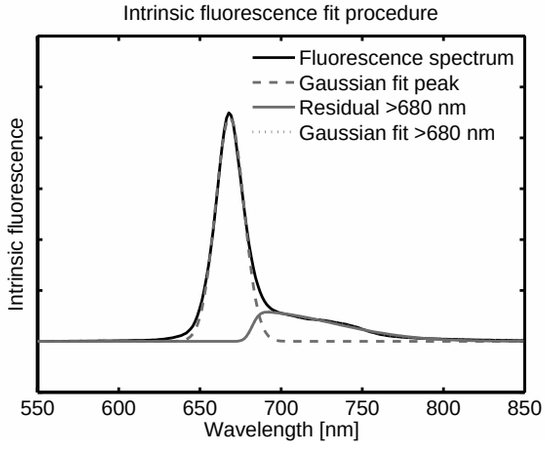

Figure 5.7: *Fluorescence intensity is fitted with a Gaussian distribution between 650 and 680 nm, and a skewed Gaussian distribution between 680 and 800 nm.*

The 24 and 48 hour time points were not considered in this analysis because the fluorescence intensity of the shoulder was in many cases too low to be fitted accurately. For each photosensitizer, differences over time and tissue were small and rarely significant, as indicated in figure 5.8b.

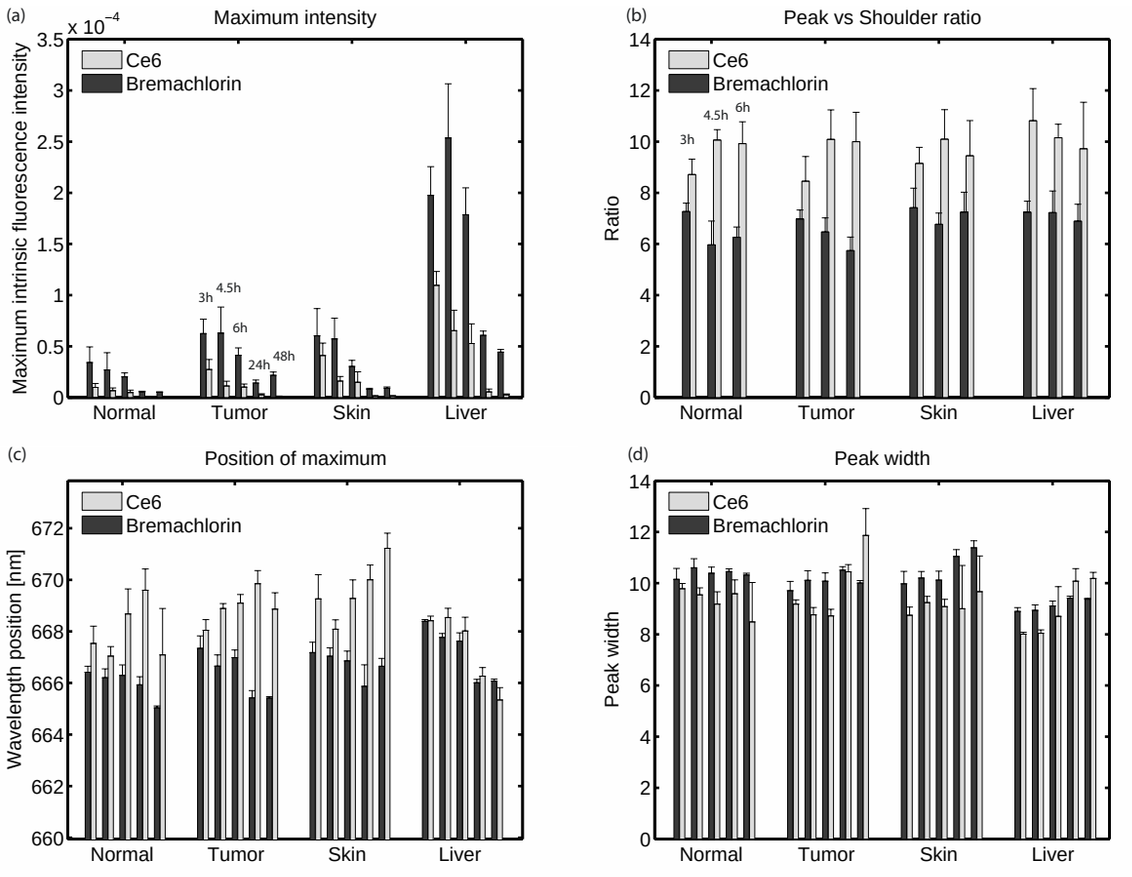

Figure 5.8: *(a) Maximum intrinsic fluorescence intensity. This parameter correlates with the product of photosensitizer concentration and quantum yield at the peak wavelength. (b) Ratio between maximum intrinsic fluorescence intensity and the fitted intensity parameter of the skewed Gaussian. This represents the ratio between peak and shoulder of the ce6 / Bremachlorin fluorescence spectrum. (c) Wavelength that represents maximum intrinsic fluorescence peak position. (d) FWHM of the Gaussian representing the main intrinsic fluorescence peak.*

PEAK POSITION

Figure 5.8c shows that the wavelength of the maximum intrinsic fluorescence intensity was shifted more towards the red for ce6 compared with Bremachlorin for tongue tissue, tumor tissue and skin. The peak position of Bremachlorin ranged from 667-665 nm, while ce6 ranged from 665-671 nm. This discrepancy was significant ($P<0.05$) for all time points in normal tongue tissue, tumor tissue and skin. Liver showed a blue-shift of the peak wavelength over time for both photosensitizers, that did not significantly differ from each other for t= [3 6 24] hours. Bremachlorin showed a decrease of peak position wavelength over time for all four tissues, while, although not always significant, ce6 showed an increasing trend for tongue tissue, tumor and skin. From figure 5.8b and 5.8c, we can conclude that for ce6, a shift of the peak to a higher wavelength corresponded with an

increase in the peak/shoulder ratio. Possible explanations for the observed wavelength shifts can be found in the discussion section.

WIDTH

When comparing the width of the main fluorescence emission peak of both photosensitizers in figure 5.8d, it can be seen that in general the width of the spectrum of ce6 peak was significantly smaller than that of Bremachlorin. It should be noted that the 24 and 48 hour measurements of ce6 were associated with large uncertainty caused by the very low fluorescence intensity, compared to Bremachlorin, as shown in figure 5.8a. This was reflected in an increased fit uncertainty. Over the first 6 hours after injection, Bremachlorin showed a stable peak width for all tissues under investigation, while ce6 showed a steady but not significant decrease over time for tumor and normal tissue.

DISCUSSION

In this paper we have demonstrated for the first time that in-vivo application of SFF is possible. We report on variations in spectral shape of the fluorescence emission of two photosensitizers ce6 and Bremachlorin in various tissues after intravenous injection. To compare fluorescence intensity and spectral shape in different tissues and of multiple animals, we extracted the intrinsic fluorescence by removing the influence of tissue optical properties on the raw fluorescence signal.

SPECTRAL VARIABILITY IN CE6

It is shown in-vitro that both the fluorescence peak intensity and the peak position of ce6 are strongly influenced by pH of the solution [32]. For ce6 in PBS a decrease in pH in the range of 7.5-3.5 results in a peak shift from 661 to 647 nm, combined with a decrease in intensity of the main fluorescence peak when the spectrum is normalized at 720 nm [32]. The range of peak positions for ce6 that we have observed was in the range of 665-671 nm, which is higher than reported by Cunderlikova et al. It is shown for the spectral properties of ce6 in more physiologically relevant environments containing serum (by adding FCS, BSA, LDL/HDL) or measured in-vivo, that the binding of ce6 significantly shifts the peak position to higher wavelengths [40]. Studies of ce6 or ce6-conjugates in solution show a peak wavelength range comparable with what was found in this study [35, 40, 49]. Changes in pH influence binding affinity and thus the spectral shape represents the relative contributions of the differently bound ce6. The data in figure 5.8b and 5.8c showed a trend of increasing peak/shoulder ratio corresponding with increasing peak

position wavelength in time after photosensitizer injection for tumor, normal tissue and skin. According to Cunderlikova et al. [32], the increase of peak/shoulder ratio and peak position suggests a transition into a higher pH environment in an in-vitro situation. In the range of biological relevant pH values, the peak shift associated with pH variations is small. How this transfers to the in-vivo situation remains to be determined.

COMPARISON OF CE6 AND BREMACHLORIN

It is clear from figure 5.8b and 5.8c that although ratio and peak position increased for ce6, Bremachlorin showed the opposite; a blue-shift in peak position accompanied by a decrease in shoulder ratio. This might suggest re-localization of the drug to an environment with a lower pH. Furthermore, binding of ce6 to low-density lipoproteins is also linked with a blue-shift of the peak position, compared to albumin bound ce6. This suggests that ce6 in Bremachlorin may be preferably bound to these LDL proteins, providing for uptake in (malignant) cells. Unbound ce6 is mainly accumulated in the plasma membrane of cells. The width of the peak, which could also be associated with pH, did not change significantly.

Bremachlorin consists of a mixture of ce6, purpurin 5 and cp6, in which both ce6 and purpurin 5 are know to have photodynamic effect. In the administered mixture, ce6 also acts as a solvent, since purpurin 5 is too hydrophobic to be administered in aqueous solution. Purpurin has a high binding affinity to LDL proteins, allowing the drug to enter malignant cells via endocytosis [50]. Since ce6 accounts for the largest fraction in Bremachlorin, we expected the spectral shape to be dominated by ce6. The influence of the other two components – purpurin 5 and chlorin p_6 – on the spectral shape and behavior is unknown. Both purpurin 5 and chlorin p_6 are known to have an emission spectrum similar to ce6 when analyzed separately [51, 52]. Our results showed that a mixture of ce6, cp6 and purpurin 5 clearly behaved differently than pure ce6. Bremachlorin is more lipophilic than pure ce6 [42], and it is therefore expected that the localization of Bremachlorin differs from pure ce6. It could not be determined from this experiment if the spectral variations between Bremachlorin and ce6 were a result of spectral influences of the two extra components, or if they were variations in ce6 spectra caused by changes in environment. However, our experiments did show that Bremachlorin has different spectral properties than pure ce6 and should therefore be investigated as a new photosensitizer, including optimization of the treatment protocol.

FLUORESCENCE CORRECTION METHOD

The method to use MDSFR for measuring the absorption and reduced scattering in-vivo to recover the intrinsic photosensitizer fluorescence is developed based on the use of Monte Carlo simulations and phantom studies. In these optimized circumstances, theory is validated and empirical parameters are included in the model [23]. However, applying this method in-vivo is much less straightforward considering spatial heterogeneity and the potential for the confounding effects of tissue layers. In this study MDSFR was performed using consecutive placement of two fiber diameters on the same spot. Therefore, slight differences in measurement volume were not only due to different fiber diameters but could also occur from measuring a slightly different sampling volume in each measurement. Therefore the μ'_s used to correct the fluorescence was based on an average value and did not necessarily exactly represent the μ'_s in the fluorescence sample volume. New technological developments should overcome this problem in the near future and provide true co-localized measurement positions for various fiber diameters [45]. Although we repositioned the probe on each tissue up to five times per mouse, the variation of variables compared within measurements of one mouse was at least four times smaller than the maximum variation between animals. Therefore, the size of the error bars was predominately due to inter-animal variations.

IMPLICATIONS AND FUTURE WORK

In this work we investigated spectral variations of chlorin e_6 and Bremachlorin. Clear differences were observed in fluorescence intensity, peak/shoulder ratio and peak position for both sensitizers over time after injection. Furthermore, although Bremachlorin consists of approximately 80% of ce6, spectra showed distinct differences, suggesting variations in localization and/or clearance pathways. The more blue-shifted peak of Bremachlorin, together with the wider peak, suggests Bremachlorin was bound to LDL proteins more than ce6. This might result in a higher uptake of the photosensitizer in the cell. It is shown that internalization of the photosensitizer results in more PDT induced damage than photosensitizers located on the cell membrane [53]. Furthermore, this may explain the prolonged detection of significant amounts of photosensitizer fluorescence in tissue compared to ce6.

Although results in this study look promising for using the ce6 in Bremachlorin as photosensitizer, purpurin 5 is known to have strong photodynamic activity as well. Spectral analysis showed mainly variations in ce6. How this ce6 behavior relates to behavior and localization of purpurin 5 and influences PDT outcome remains to be

investigated. In future studies we aim to analyze the microscopic distribution of ce6 and Bremachlorin in tongue/tumor tissue.

CONCLUSION

In the present study we used for the first time quantitative single fiber fluorescence spectroscopy in-vivo to analyze fluorescence spectra of both ce6 and Bremachlorin in-vivo. Influence of optical properties on fluorescence varied up to 35% over the visible wavelength range and was tissue dependent. We analyzed variations in spectral shape of the intrinsic fluorescence in normal tongue tissue, OSC tongue tumor, skin and liver at t=[3 4.5 6 24 48] hours after photosensitizer injection. We observed significant differences in spectral shape over time between sensitizers. While the wavelength position of the fluorescence intensity maximum underwent a red-shift over time for ce6, Bremachlorin showed a blue-shift. Furthermore, the Bremachlorin peak appeared to be broader than the ce6 fluorescence peak. Intrinsic fluorescence intensity, which can be related to photosensitizer concentration, was decreasing for all time points, but showed significantly more Bremachlorin present compared to ce6 at long incubation times. In conclusion, although Bremachlorin consists for ~80% of chlorin e_6, they behaved significantly different in-vivo. These differences may be explored to define an optimal treatment protocol for Bremachlorin-based photodynamic therapy.

ACKNOWLEDGEMENTS

We kindly thank Laura Mezzanotte for her work on the lentiviral transduction and production of the Luc2-gfp-OSC19 cell line, and the University Medical Centre Leiden for providing those cells for this study.

REFERENCES

1. Georgakoudi, I. and J. Van Dam, *Characterization of dysplastic tissue morphology and biochemistry in Barrett's esophagus using diffuse reflectance and light scattering spectroscopy.* Gastrointestinal endoscopy clinics of North America, 2003. **13**(2): p. 297-308.
2. Drezek, R., et al., *Light scattering from cervical cells throughout neoplastic progression: influence of nuclear morphology, DNA content, and chromatin texture.* Journal of biomedical optics, 2003. **8**(1): p. 7-16.
3. Palmer, G.M., et al., *Quantitative diffuse reflectance and fluorescence spectroscopy: tool to monitor tumor physiology in vivo.* Journal of biomedical optics, 2009. **14**(2): p. 024010-024010-8.
4. Kim, A., et al., *Quantification of in vivo fluorescence decoupled from the effects of tissue optical properties using fiber optic spectroscopy measurements.* Journal of biomedical optics, 2010. **15**(6): p. 067006-067006-12.
5. Boustany, N.N., S.A. Boppart, and V. Backman, *Microscopic imaging and spectroscopy with scattered light.* Annual review of biomedical engineering, 2010. **12**: p. 285.
6. Thueler, P., et al., *In vivo endoscopic tissue diagnostics based on spectroscopic absorption, scattering, and phase function properties.* Journal of biomedical optics, 2003. **8**(3): p. 495-503.
7. Ntziachristos, V., *Going deeper than microscopy: the optical imaging frontier in biology.* Nature methods, 2010. **7**(8): p. 603-614.
8. Kollias, N., G. Zonios, and G.N. Stamatas, *Fluorescence spectroscopy of skin.* Vibrational Spectroscopy, 2002. **28**(1): p. 17-23.
9. Robinson, D.J., et al., *Protoporphyrin IX Fluorescence Photobleaching during ALA-Mediated Photodynamic Therapy of UVB-Induced Tumors in Hairless Mouse Skin.* Photochemistry and photobiology, 1999. **69**(1): p. 61-70.
10. Robinson, D.J., et al., *Fluorescence photobleaching of ALA-induced protoporphyrin IX during photodynamic therapy of normal hairless mouse skin: the effect of light dose and irradiance and the resulting biological effect.* Photochemistry and photobiology, 1998. **67**(1): p. 140-149.
11. Karakullukcu, B., et al., *Clinical feasibility of monitoring mTHPC mediated photodynamic therapy by means of fluorescence differential path-length spectroscopy.* Journal of Biophotonics, 2011. **4**(10): p. 740-751.
12. Robinson, D.J., et al., *Optical spectroscopy to guide photodynamic therapy of head and neck tumors.* Selected Topics in Quantum Electronics, IEEE Journal of, 2010. **16**(4): p. 854-862.
13. Finlay, J.C. and T.H. Foster, *Recovery of hemoglobin oxygen saturation and intrinsic fluorescence with a forward-adjoint model.* Applied optics, 2005. **44**(10): p. 1917-1933.
14. Wu, J., M.S. Feld, and R.P. Rava, *Analytical model for extracting intrinsic fluorescence in turbid media.* Applied optics, 1993. **32**(19): p. 3585-3595.
15. Müller, M.G., et al., *Intrinsic fluorescence spectroscopy in turbid media: disentangling effects of scattering and absorption.* Applied optics, 2001. **40**(25): p. 4633-4646.
16. Zhang, Q., et al., *Turbidity-free fluorescence spectroscopy of biological tissue.* Optics Letters, 2000. **25**(19): p. 1451-1453.
17. Diamond, K.R., M.S. Patterson, and T.J. Farrell, *Quantification of fluorophore concentration in tissue-simulating media by fluorescence measurements with a single optical fiber.* Applied optics, 2003. **42**(13): p. 2436-2442.
18. Stepp, H., et al., *Measurement of fluorophore concentration in turbid media by a single optical fiber.* Medical Laser Application, 2007. **22**(1): p. 23-34.

19. Amelink, A., et al., *Quantitative fluorescence spectroscopy in turbid media using fluorescence differential path length spectroscopy.* Journal of biomedical optics, 2008. **13**(5): p. 054051-054051-8.

20. Pogue, B.W. and G. Burke, *Fiber optic bundle design for quantitative fluorescence measurement from tissue.* Applied optics, 1998. **37**(31): p. 7429-7436.

21. Gamm, U.A., et al., *Measurement of tissue scattering properties using multi-diameter single fiber reflectance spectroscopy: in silico sensitivity analysis.* Biomedical optics express, 2011. **2**(11): p. 3150-3166.

22. Gamm, U.A., et al., *Quantification of the reduced scattering coefficient and phase-function-dependent parameter Gamma of turbid media using multidiameter single fiber reflectance spectroscopy: experimental validation.* Optics Letters, 2012. **37**(11): p. 1838-1840.

23. Kanick, S., et al., *Semi-empirical model of the effect of scattering on single fiber fluorescence intensity measured on a turbid medium.* Biomedical optics express, 2012. **3**(1): p. 137-152.

24. Kanick, S.C., et al., *Monte Carlo analysis of single fiber reflectance spectroscopy: photon path length and sampling depth.* Physics in medicine and biology, 2009. **54**(22): p. 6991-7008.

25. Kanick, S.C., H. Sterenborg, and A. Amelink, *Empirical model of the photon path length for a single fiber reflectance spectroscopy device.* Optics Express, 2009. **17**(2): p. 860-871.

26. Bevilacqua, F. and C. Depeursinge, *Monte Carlo study of diffuse reflectance at source-detector separations close to one transport mean free path.* Journal of the Optical Society of America A, 1999. **16**(12): p. 2935-2945.

27. Kanick, S.C., et al., *Extraction of intrinsic fluorescence from single fiber fluorescence measurements on a turbid medium.* Optics Letters, 2012. **37**(5): p. 948-950.

28. de Bruijn, H.S., et al., *Microscopic localisation of protoporphyrin IX in normal mouse skin after topical application of 5-aminolevulinic acid or methyl 5-aminolevulinate.* Journal of Photochemistry & Photobiology, B: Biology, 2008. **92**(2): p. 91-97.

29. Amelink, A., et al., *Monitoring PDT by means of superficial reflectance spectroscopy.* Journal of Photochemistry & Photobiology, B: Biology, 2005. **79**(3): p. 243-251.

30. de Vijlder, H.S., et al., *Acute Vascular Responses during Photodynamic Therapy using Topically Administered Porphyrin Precursors.* Photochemical & Photobiological Sciences, 2013. **In press**.

31. Nelson, J.S., W.G. Roberts, and M.W. Berns, *In vivo studies on the utilization of mono-L-aspartyl chlorin (NPe6) for photodynamic therapy.* Cancer research, 1987. **47**(17): p. 4681-4685.

32. Cunderlíková, B., L. Gangeskar, and J. Moan, *Acid-base properties of chlorin e6: relation to cellular uptake.* Journal of Photochemistry and Photobiology B: Biology, 1999. **53**(1): p. 81-90.

33. Mojzisova, H., et al., *Cellular uptake and subcellular distribution of chlorin e6 as functions of pH and interactions with membranes and lipoproteins.* Biochimica et Biophysica Acta Biomembranes, 2007. **1768**(11): p. 2748-2756.

34. Kostenich, G., I. Zhuravkin, and E. Zhavrid, *Experimental grounds for using chlorin e6 in the photodynamic therapy of malignant tumors.* Journal of Photochemistry and Photobiology B: Biology, 1994. **22**(3): p. 211-217.

35. Orenstein, A., et al., *A comparative study of tissue distribution and photodynamic therapy selectivity of chlorin e6, Photofrin II and ALA-induced protoporphyrin IX in a colon carcinoma model.* British journal of cancer, 1996. **73**(8): p. 937-944.

36. Chin, W.W.L., et al., *Fluorescence imaging and phototoxicity effects of new formulation of chlorin e6-polyvinylpyrrolidone.* Journal of Photochemistry and Photobiology B: Biology, 2006. **84**(2): p. 103-110.

37. Taber, S.W., et al., *Photodynamic therapy using mono-L-aspartyl chlorin e6 (Npe6) for the treatment of cutaneous disease: a Phase I clinical study.* Clinical cancer research, 1998. **4**(11): p. 2741-2746.

38. Lustig, R.A., et al., *A multicenter Phase I safety study of intratumoral photoactivation of talaporfin sodium in patients with refractory solid tumors.* Cancer, 2003. **98**(8): p. 1767-1771.

39. Chan, A.L., et al., *Pharmacokinetics and clinical effects of mono-L-aspartyl chlorin e6 (NPe6) photodynamic therapy in adult patients with primary or secondary cancer of the skin and mucosal surfaces.* Photodermatology, photoimmunology & photomedicine, 2005. **21**(2): p. 72-78.

40. Douillard, S., et al., *In vitro evaluation of Radachlorin sensitizer for photodynamic therapy.* Journal of Photochemistry and Photobiology B: Biology, 2010. **98**(2): p. 128-137.

41. Douillard, S., D. Olivier, and T. Patrice, *In vitro and in vivo evaluation of Radachlorin sensitizer for photodynamic therapy.* Photochemical & Photobiological Sciences, 2009. **8**(3): p. 405-413.

42. Uzdensky, A., et al., *Photodynamic effect of novel chlorin e6 derivatives on a single nerve cell.* Life sciences, 2004. **74**(17): p. 2185-2197.

43. van Leeuwen - van Zaane, F., et al., *In vivo quantification of the scattering properties of tissue using multi-diameter single fiber reflectance spectroscopy.* Biomedical optics express, 2013. **4**(5): p. 696-708.

44. Gamm, U.A., et al., *Extraction of intrinsic fluorescence from single fiber fluorescence measurements on a turbid medium: experimental validation.* Biomedical optics express, 2014. **In press**.

45. Hoy, C.L., et al., *Use of a coherent fiber bundle for multi-diameter single fiber reflectance spectroscopy.* Biomedical optics express, 2012. **3**(10): p. 2452-2464.

46. Yokoi, T., et al., *Establishment and characterization of a human cell line derived from a squamous cell carcinoma of the tongue.* Tumor Research, 1988. **23**: p. 43-57.

47. Carlotti, F., et al., *Lentiviral vectors efficiently transduce quiescent mature 3T3-L1 adipocytes.* Molecular Therapy, 2004. **9**(2): p. 209-217.

48. Mezzanotte, L., et al., *Evaluating reporter genes of different luciferases for optimized in vivo bioluminescence imaging of transplanted neural stem cells in the brain.* Contrast Media & Molecular Imaging, 2013. **8**(6): p. 505-513.

49. Mitra, S. and T.H. Foster, *In vivo confocal fluorescence imaging of the intratumor distribution of the photosensitizer mono-L-aspartylchlorin-e6.* Neoplasia, 2008. **10**(5): p. 429-438.

50. Jori, G. and E. Reddi, *The role of lipoproteins in the delivery of tumour-targeting photosensitizers.* International journal of biochemistry, 1993. **25**(10): p. 1369-1375.

51. Garbo, G.M., *Purpurins and benzochlorins as sensitizers for photodynamic therapy.* Journal of Photochemistry and Photobiology B: Biology, 1996. **34**(2): p. 109-116.

52. Zenkevich, E., et al., *Photophysical and photochemical properties of potential porphyrin and chlorin photosensitizers for PDT.* Journal of Photochemistry and Photobiology B: Biology, 1996. **33**(2): p. 171-180.

53. Agostinis, P., et al., *Photodynamic therapy of cancer: an update.* CA: a cancer journal for clinicians, 2011. **61**(4): p. 250-281.

chapter 6

Microscopic Analysis of the Localization of Two Chlorin-Based Photosensitizers in OSC19 Tumors in the Mouse Oral Cavity

Floor van Leeuwen – van Zaane,
Pieter van Driel, Ute Gamm, Thomas Snoeks, Riëtte de Bruijn
Angélique van der Ploeg – van den Heuvel, Clemens Löwik,
Dick Sterenborg, Arjen Amelink, Dominic Robinson

Lasers in Surgery and Medicine,
published online January 2014

ABSTRACT

The effect of photodynamic therapy (PDT) is dependent on the localization of photosensitizer in the treatment volume at the time of illumination. Investigation of photosensitizer pharmacokinetics in and around the treatment volume aids in determining the optimal drug-light interval for PDT. In this paper we have investigated the distribution of the photosensitizers chlorin e_6 and Bremachlorin in the oral squamous cell carcinoma cell-line OSC19-Luc-Gfp in a tongue tumor, tumor boundary, invasive tumor boundary and normal tongue tissue by the use of confocal microscopy of frozen sections. Tongues were harvested at t = [3 4.5 6 24 48] hours after injection. Both photosensitizers showed a decreasing fluorescence with increasing incubation time, and at all time points higher fluorescence was measured in tumor boundary than in tumor itself. For short incubation times, a higher fluorescence intensity was observed in invasive tumor border and normal tissue compared to tumor tissue. Bremachlorin showed a small increase in tumor to normal ratio at 24 and 48 hours incubation time. Ce6 was undetectable at 48 hours. We did not find a correlation between photosensitizer localization and the presence of vasculature. It can be concluded that Bremachlorin at 24 and 48 hour incubation times provides us with both a concentration suitable for PDT and a small tumor/tumor boundary to normal selectivity of between 1.2 and 2.5. This selectivity after long incubation times provides the possibility to spare normal tissue and it may therefore be worthwhile to investigate the efficacy of Bremachlorin PDT with long incubation times.

INTRODUCTION

Photodynamic therapy (PDT) is the treatment of choice for several (pre-)malignant skin lesions [1]. There have been many (pre-)clinical studies focusing on the use of PDT for the treatment of epithelial malignancies and solid tumors and PDT has been used clinically for the treatment of tumors of the head & neck and the prostate [2-5]. The principle of PDT is based on the generation of reactive oxygen species (ROS). These ROS, which have a very short life time and diffusion length, cause damage in nearby tissue structures resulting in cellular, vascular and immunological responses [6]. ROS are generated when a photosensitizing agent, the photosensitizer, is illuminated with light of a specific wavelength in the presence of molecular oxygen. The photosensitizer facilitates the transfer of energy from light to molecular oxygen, resulting in the formation of highly reactive singlet oxygen. Over the last 30 years, different photosensitizing agents have been synthesized and tested. These photosensitizers vary in how reactive oxygen species are generated, where they are located in tissue and how they are metabolized [7].

It is desirable for photosensitizers to have a preferential uptake in tumor tissue over normal tissue. When the concentration photosensitizer is (much) higher in tumor than in its surrounding tissue, selective tissue damage may be achieved when using an appropriate illumination protocol [8, 9]. There are various ways to achieve this selective tissue damage. Intravascular administered photosensitizers such as mTHPC rely for selectivity on the leaky neovasculature in and surrounding the tumor. It is expected that the somewhat loose structure of endothelial cells in tumor neovasculature allows for easier passage of intravascular substances into the surrounding tissue, together with a selective affinity for proliferating neovasculature. When performing PDT with intravascular administrated chlorin e_6 (ce6) based photosensitizer, additional environmental factors such as pH may enhance selectivity [10]. In-vitro it has been shown that a decrease of pH from 8.5 to 7.0 enhances the lipophilicity and therefore increases the binding prevalence of ce6 from serum albumin towards low-density lipoproteins (LDL) in the blood stream [10, 11]. Lipoproteins, and therefor the photosensitizer, are internalized via the endocytosis pathway. Since the pH of tumor stroma is decreased compared to normal tissue [12], the liphophilicity may favor the cellular uptake of ce6 by tumor tissue.

The localization of the photosensitizer at the time of therapy determines which cellular and tissue structures are damaged by PDT generated reactive oxygen species. Some (mainly intravenous administered) photosensitizers directly target the vasculature, which upon illumination leads to in irreversible damage to vessels supplying oxygen and

nutrients to the tumor, resulting in its destruction [13]. However, vascular shutdown and blood flow changes during early stages of illumination decrease the transport of oxygen, which may limit the production of singlet oxygen and thereby inhibit the induction of local cellular and immunological responses. Treatment efficacy is therefore dependent on a fine balance between the positive and negative effects of vascular damage. By varying PDT treatment protocols, one can determine the effects on particular tissue structures [8]. Directly after intravenous administration of the photosensitizer one expects it to be present in the vessels and partly in tissue closely surrounding the vasculature. The longer the time between drug administration and illumination the more the photosensitizer is expected to diffuse into the surrounding tissue and not only localize around vasculature [8]. However, differences in metabolism and clearance between tissues result in concentration gradients several hours to days after injection. The investigation of in-vivo pharmacokinetics is therefore a very important tool to identify the drug distribution that is thought to represent the most favorable treatment conditions [14].

The photosensitizer ce6 has been studied intensively for over two decades [15]. It is a second generation photosensitizer, which shows low dark toxicity and an enhanced absorption in the red wavelength region between 600 and 800 nm. Ce6-PVP, in which the ce6 molecule is bound to a polyvinylpyrrolidone carrier, has been used in PDT of urological tumors [16]. Various preclinical studies with the photosensitizer mono-L-aspartylchlorin-e6 (Npe6) have been performed and NPe6 is clinically approved for the treatment of early stage superficial squamous cell carcinomas in lung in Japan [17, 18], and it is also under investigation for skin malignancies [19]. It is known that the in-vitro spectral shape of ce6 is strongly dependent on pH of the solution; variations in pH result in a shift of both the absorption and fluorescence spectrum and a decrease of fluorescence intensity [10, 11]. By analyzing both intensity and spectral shape, it is, in theory, possible to distinguish between intensity decreases due to clearance of the photosensitizer from the tissue, and intensity changes due to relocalization to an environment with a different pH. An important characteristic of ce6 is its relatively low lipophilicity, resulting in rapid excretion from the body via the urinary system. A positive effect of this short clearance time is reduced skin photosensitivity, which prevents patients from spending days or even weeks in the dark. A drawback is that short clearance times can limit the effective localization in neoplastic tissue.

A new photosensitizing compound, Bremachlorin, consists largely (~80%) of ce6, combined with the photosensitizing agents purpurin 5 (~15%) and chlorin p_6 (~5%) [20]. The number of (pre-)clinical studies performed with Bremachlorin is limited but covers a number of malignancies and treatment protocols [21-23]. The main active component of

Bremachlorin is thought to be purpurin 5, partly because its rapid interaction with albumin and low-density lipoproteins that enables it to be delivered to cancerous tissues [24]. Although purpurin 5 in itself is too hydrophobic to be administrated in aqueous solution, combined with ce6 and cp6 it achieves the chemical stability required for both intravenous administration and storage. Although the exact role of the three separate constituents of Bremachlorin on the biodistribution and potential PDT induced response is unclear, it is expected that the combined purpurin 5 and ce6 in Bremachlorin results in an overall photosensitizing effect that is greater than the individual concentrations of both photosensitizers [20]. The confocal microscopy approach of the present manuscript does not provide the possibility to discriminate between the individual constituents of Bremachlorin.

In this paper, we compare the localization of the clinically registered formulation of Bremachlorin with ce6 in oral squamous cell carcinomas and surrounding tissue in tongue, at various time points after i.v. administration by means of confocal microscopy. Recently we have reported on variations in intensity and spectral shape between Bremachlorin and ce6 while using non-invasive in-vivo fiber optic intrinsic fluorescence spectroscopy [25]. In this paper we continue that investigation by studying concentration gradients between tumor, tumor boundary, invasive tumor border and tissue showing normal histology by the use of confocal microscopy. Furthermore, localization of photosensitizer around vasculature is investigated over time. The aim of this study is to distinguish localization differences between the two photosensitizers on a microscopic scale, and compare this with fiber optic results.

MATERIALS AND METHODS

ANIMAL MODEL

Forty BALB/c nu/nu hairless mice (aged 4-6 weeks; Charles River Laboratories) were incubated with orthotopic oral squamous cell carcinoma's at the tip of the tongue. This cell line was transduced with luciferase 2 (luc2) and green fluorescent protein (gfp) to create the cell line OSC-19-luc2-cgfp, as described previously [26-28]. $6x10^4$ cells, suspended in 20 µL phosphate-buffered saline were submucosally implanted in the tip of the tongue of the mice. Two weeks later, mice were randomized in 10 groups and injected with either Bremachlorin (20 mg kg^{-1}, from a 3.5 g L^{-1} stock solution; Rada-pharma International B.V. ,The Netherlands) or ce6 (16 mg kg^{-1}, dissolved in 100 µl PBS, Frontier Scientific, Inc., Logan, USA). At a pre-assigned incubation times (t = [3 4.5 6 24 48] hours),

mice were anesthetized, sacrificed by cervical dislocation and tongues were removed and snap frozen for further investigation. The study protocol was approved by the Animal Welfare Committee of the Leiden University Medical Center. Housing of mice, the experiments and euthanazation were performed in accordance with the guidelines of this committee. Chlorophyll free food and sterilized water were provided without restriction.

CONFOCAL IMAGE ANALYSIS

Tongues were harvested and snap frozen in liquid nitrogen at a preset time after photosensitizer injection. Samples were stored in dark containers at -80^{o}C. From every tongue, three frozen sections with a slice thickness of 20 µm were prepared for confocal microscopy. Every slice was followed by a subsequent 5 µm thick slice to allow for hematoxylin & eosin (H&E) staining and histological analysis. Sample preparation and storage was performed under dark conditions to prevent photobleaching of the photosensitizer present in the samples. Confocal microscopy was performed using a Zeiss LSM 510 confocal laser scanning microscope equipped with an 8-channel photomultiplier tube for semi-spectral detection of fluorescence (Zeiss LSM510META, Carl Zeiss B.V. Sliedrecht, the Netherlands). In every section, three locations containing various tissue structures were chosen for analysis. Locations contained tumor and tumor boundary, invasive tumor border or normal tongue tissue.

A spectral image of the photosensitizer fluorescence under 405 nm excitation was generated recording fluorescence at 16 wavelengths ranging from 588-748 nm. Confocal images of gfp fluorescence and autofluorescence were recorded of the same location, directly after each other. Detailed settings can be found in table 6.1. Simultaneous with each fluorescence image, a bright-field 514 nm transmission image was recorded which shows histological data. Exact coordinates of the measurement locations within a

Table 6.1: *Confocal microscopy settings*

Fluorophore	***λ_{ex} (nm)***	***$\lambda_{detection}$ (nm)***	***Slice thickness***	***Scan Speed (µs/pixel)***	***Magni-fication***
gfp, Tumor tissue	488	505-530 BP	<10 µm	1.60	200x
Autofluorescence	405	420-480 BP	<10 µm	1.60	200x
ce6 / Bremachlorin Spectral detection	405	588-748 nm 10 nm res.	<10 µm	1.60	200x
CD31, endothelial cells	633	650 LP	<10 µm	1.60	200x

microscope slide were carefully recorded. After this imaging session, samples were stained with Alexa Fluor® 647 anti-mouse CD31 (2.5 µg ml^{-1}; BioLegend Inc., San Diego, USA) for 12 hours at 4°C. Afterwards, samples were rinsed with PBS and analyzed with the confocal microscope to visualize vasculature at the exact same locations as the three previous recordings were made. Details of the imaging parameters are shown in table 6.1.

DATA ANALYSIS

Analysis of the images was performed using Matlab (release 2010b, The Mathworks, Natick, MA, USA). The spectral fluorescence images were averaged over 2x2 pixels to reduce noise levels. Every cluster of pixels was then spectrally deconvolved using basis spectra for autofluorescence and ce6 fluorescence. Autofluorescence was determined to be a multiple of an exponential decay curve with a power of -0.03, equation 6.1,

$$basisspectrum = a \cdot \exp^{(-0.03 \cdot \lambda)}, \quad (6.1)$$

where a is a fit factor and λ the wavelength. This autofluorescence basis spectrum is based on spectra measured (in identical configuration as the measurements) on 18 locations in three reference tongues without photosensitizer. One autofluorescence basis spectrum could be applied to both tumor, normal tissue and invasive tumor border. Photosensitizer basis spectra were derived from 19 locations containing a high photosensitizer fluorescence intensity, after the removal of autofluorescence. Since the spectral resolution of the microscope is quite low (10 nm), we did not discriminate between basis spectra for ce6 and Bremachlorin. There was substantial variation in autofluorescence between tissues. Spectrally deconvolving the photosensitizer fluorescence images resulted in a measure of the photosensitizer present not influenced by autofluorescence variations.

Images of autofluorescence and tumor cell gfp fluorescence aided in determining which pixels to include in analysis. To discriminate between tissue autofluorescence or gfp fluorescence and system or background noise, the Matlab function 'grayslice' was used. This function converts gray scale images to indexed images using multilevel thresholding. Every pixel with threshold ≥1 was included as tissue or tumor using autofluorescence or gfp fluorescence respectively. If a location contains tumor (gfp-positive) and tumor boundary (gfp-negative) pixels, pixels containing gfp fluorescence are counted as tumor, while the rest of the image is considered boundary.

Pixels with very high intensity fluorescence spots in the photosensitizer and autofluorescence images caused by section preparation artifacts were not included in the analysis. The average photosensitizer concentration was calculated for the following tissues: OSC tongue tumor (including only gfp-fluorescence positive pixels), tumor boundary, invasive tumor border and histologically normal tongue tissue. This resulted in

an average photosensitizer concentration for every tissue at each time point, for both ce6 and Bremachlorin.

CO-LOCALIZATION WITH VASCULATURE

To assess the degree of co-localization of photosensitizer with vasculature, a vessel staining procedure was used, where tissue was incubated with CD31 for 12 hours. However, due to the hydrophilic nature of ce6 and Bremachlorin, this staining procedure removed photosensitizer from the tissue. Therefore, images of photosensitizer and gfp were recorded before staining. A 514 nm bright-field transmission image of the whole tongue was made to show tissue histology. Locations of fluorescence images were mapped on these histological images. After staining of the vasculature, the tissue was again imaged, at the exact same location. The required position of the slide was determined based on the histological features in the bright-field transmission image. Resulting vasculature images were analyzed using the function 'grayslice' to determine which pixels were identified as vasculature (threshold ≥1). Only pixel clusters larger than 30 bordering pixels were considered vasculature. In situations where there was non-specific staining of tissue, all pixel clusters belonging to vasculature were manually selected and non-specific staining was ignored. Automated analysis of photosensitizer fluorescence intensity versus distance to nearest vessel was performed by calculating the distance in pixels to the nearest pixel stained for vasculature. When the distance was determined for all pixels, it was binned in steps of 20 pixels (=18 μm) and pixels within that distance were averaged per bin. This resulted in an intensity profile around the vasculature. Since not all tissue locations had the same number of distance bins (less vasculature results in larger distances), only the bins containing data points of at least three different locations were included in the analysis.

RESULTS

A total of 276 locations on tongue coupes of 36 mice were analyzed. Every tongue was cut into three slices, on which three locations per slice were analyzed. The different tissue types were determined using the histological information from the 514 nm bright-field transmission images, as shown in figure 6.1.

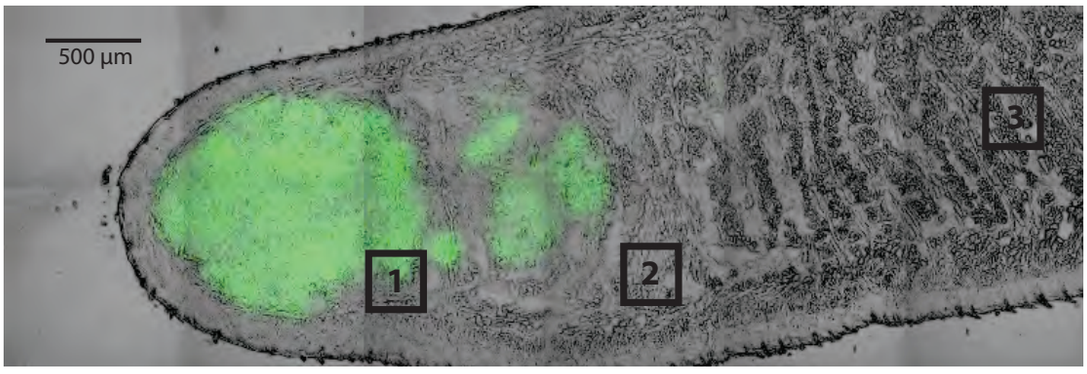

Figure 6.1: *Tongue overview (100x magnification). Green indicates tumor (gfp fluorescence). Locations: 1) tumor and tumor border 2) invasive tissue 3) normal tissue.*

All locations were labeled tumor/tumor boundary, invasive tumor border or normal tissue. The tumor is located in the tip of the tongue, with islands of tumor cells invading the tongue tissue. In this example tumor is clearly visible in the tip. Figure 6.1, location 1 indicates a possible microscopy location containing tumor and tumor boundary. The majority of the tip of the tongue consisted of invasive tumor border (figure 6.1, location 2), while only the most right part of the tongue showed normal tongue histology (figure 6.1, location 3), consisting mainly of muscle fibers. The main tumor and tumor islands showed an abrupt, easy distinguishable border.

PHOTOSENSITIZER FLUORESCENCE

The average photosensitizer fluorescence intensities at t = [3 4.5 6 24 and 48] hours were determined for the four different histological tissue sites described above for ce6 and Bremachlorin. Figure 6.2 shows an example of the results of a fit over the average spectrum of four pixels.

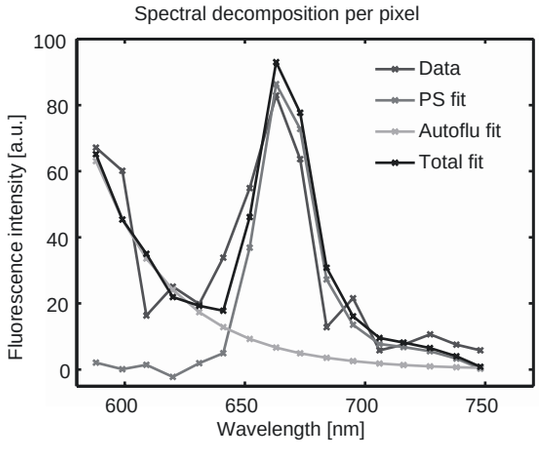

Figure 6.2: *Photosensitizer and background fit per pixel.*

We have previously shown that Bremachlorin and ce6 vary spectrally over time using fiber optic spectroscopy [25]. However, the spectral resolution obtained by the photomultiplier detector of the confocal microscope is 10 nm, which was not sensitive enough to distinguish these changes. Therefore, only the intensity of the fluorescence was analyzed. An overview of average fluorescence intensities is shown in figure 6.3a and b.

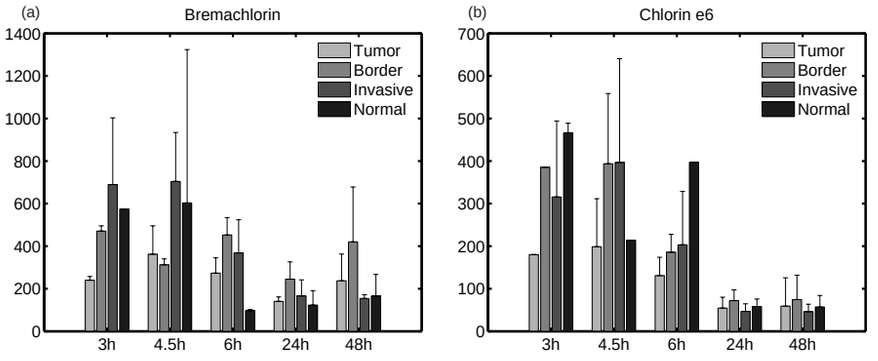

Figure 6.3: a) *Bremachlorin. Average per tissue type per time point. b) Chlorin e6. Average per tissue type per time point.*

At the 24 and 48 hour time points of ce6 in figure 6.3b, the photosensitizer fluorescence was very low compared to autofluorescence. This limited the possibilities for deconvolution of the photosensitizer fluorescence spectral image and explains the lack of significant differences between the two time points. For the late Bremachlorin time points 24 and 48 hours (figure 6.3a) a tumor/tumor boundary to normal selectivity of 1.2 to 2.5 was observed; the photosensitizer fluorescence intensity of tumor tissue was higher than that of normal tissue. After short incubation times, fluorescence intensity was higher in normal tissue at most times a comparable or higher Bremachlorin fluorescence intensity than normal tissue. For ce6 we do not observe consistently higher values for invasive tumor border compared to normal tissue, although both are significantly higher than the photosensitizer fluorescence intensity in tumor tissue.

Figure 6.3 shows that for short incubation times the concentration of both ce6 and Bremachlorin was generally higher in the tumor boundary than in the tumor itself. The invasive tumor border also showed higher photosensitizer concentration than tumor, for both ce6 and Bremachlorin. Histologically normal tissue showed relatively low fluorescence intensity. The difference between tumor and tumor boundary concentration was clearly visible at short incubation times. An example of this pattern of distribution is shown in figure 6.4, where figure 6.4a and b show the gfp (green) and photosensitizer (red) fluorescence on a background of histological information. Figure 6.4c shows gfp and photosensitizer fluorescence in one image, which shows the lack of photosensitizer present in tumor tissue.

When investigating the localization of ce6 and Bremachlorin in normal and invasive tumor border for short incubation time points, it was observed that both showed a high degree of co-localization with muscle fiber bundles. An example this effect for Bremachlorin at 3 hours is shown in figure 6.5a and b, where figure 6.5b shows the localization in relation to

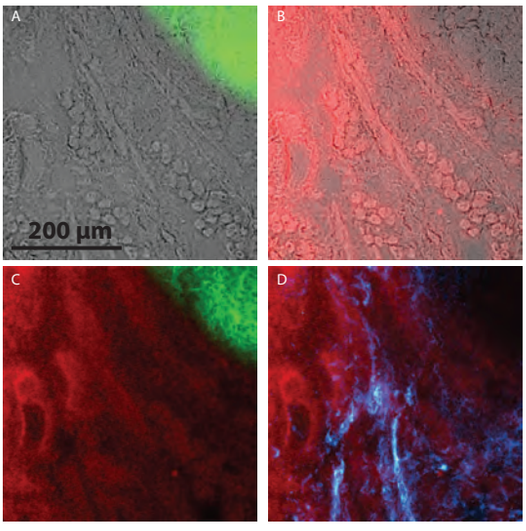

Figure 6.4: *Photosensitizer fluorescence intensity in tumor and tumor border 3 hours after injection. Red: Photosensitizer, Green: tumor, Blue: vasculature. a,b) fluorescence overlay on histological transmission image. c) localization of photosensitizer and tumor tissue. d) localization of vessels in relation to photosensitizer fluorescence.*

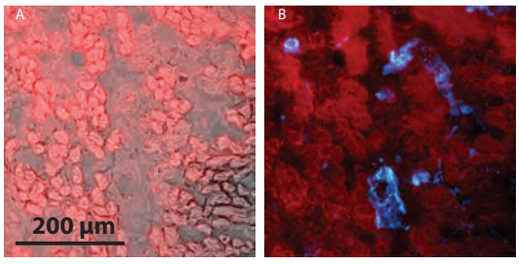

Figure 6.5: *Photosensitizer in normal tissue is mainly located in muscle fiber bundles at 3 hours after injection. a) transmission histology image with a photosensitizer overlay (red). b) photosensitizer fluorescence intensity in relation to vessels (blue).*

the vasculature (blue). A high degree of co-localization was observed for both ce6 and Bremachlorin.

Comparison of 24 and 48 hour time points for both photosensitizers showed that ce6 was present in much lower concentrations than Bremachlorin. Furthermore, there was no longer co-localization of ce6 and Bremachlorin with muscle fiber bundles. Fluorescence intensity images showed a low, quite homogenous level.

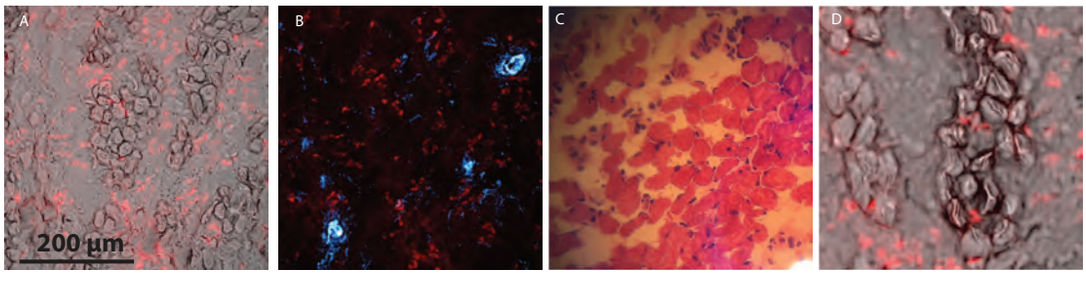

Figure 6.6: *At 48 hour incubation time, photosensitizer is localized in relatively high intensity spots on a low background. a) transmission histology image with a photosensitizer overlay (red). b) photosensitizer fluorescence intensity in relation to vessels (blue). c) H&E stained microscopy image of normal tongue tissue. d) transmission image of normal tongue tissue with corresponding PS localization (red).*

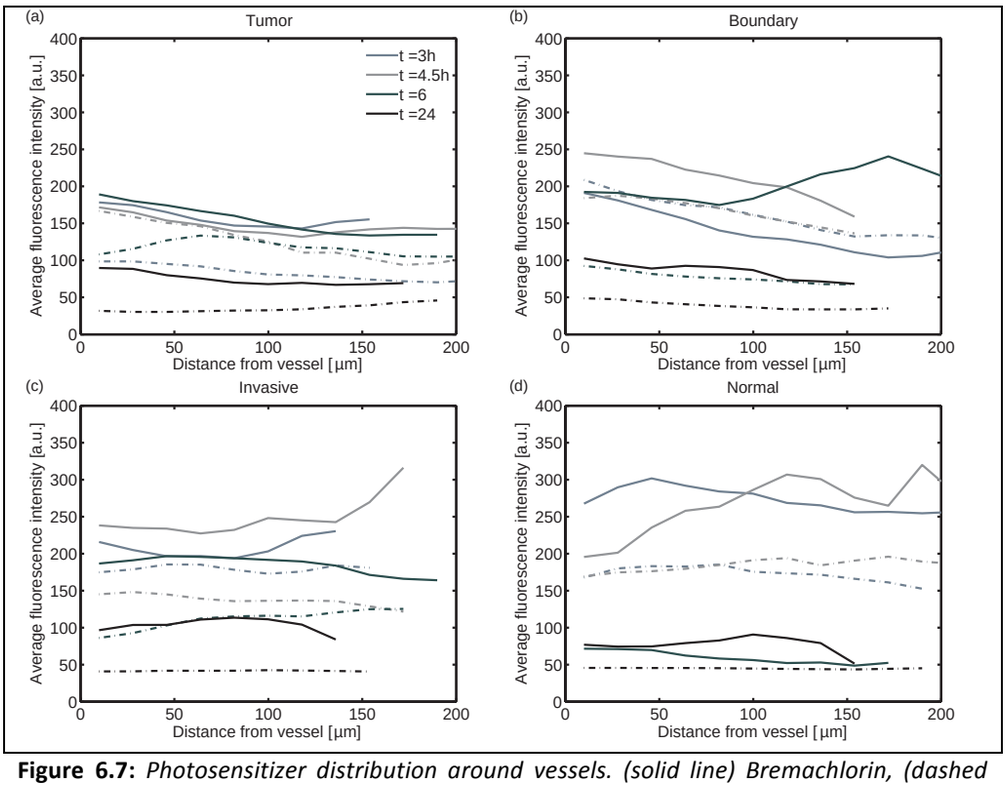

Figure 6.7: *Photosensitizer distribution around vessels. (solid line) Bremachlorin, (dashed line) ce6.*

For both photosensitizers, the intensity ce6 in the tumor remained lower than the surrounding (invasive) boundary, while the Bremachlorin concentration in normal tissue was even lower than in tumor. Interestingly, at these later time points, small spots of high intensity fluorescence were present in all of the tissues investigated, although their presence in tumor was significantly less. This punctate distribution did not co-localize with identifiable tissue structures in the bright-field transmission images (figure 6.6a) and in particular was not coincident with the vasculature (figure 6.6b). A comparison of the location and pattern of these high concentrations of Bremachlorin and – to a lesser extend- ce6 with H&E histological sections suggests that these high concentrations are associated with cell nuclei (figure 6.6c and d).

VESSEL CO-LOCALIZATION

Figure 6.7 shows the photosensitizer fluorescence intensity against distance from the nearest vessel, averaged over all locations with that particular photosensitizer, tissue type and incubation time. In figure 6.7a to d, results for the different tissue types are shown. The number of averaged tissue locations ranged from 3 to 20. In general, the Bremachlorin (solid lines) intensity was higher than the ce6 intensity (dashed lines). For

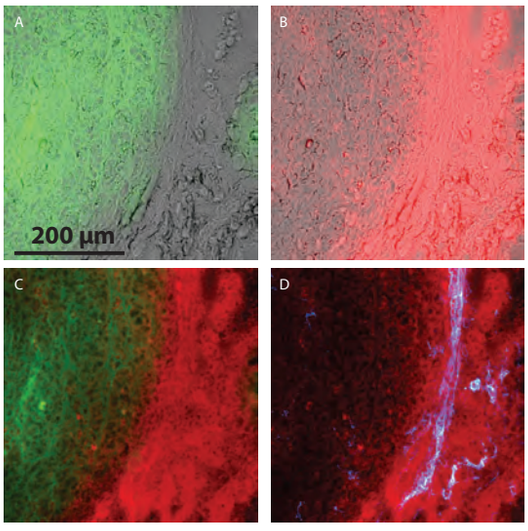

Figure 6.8: *Bremachlorin after 3 hour incubation time. No direct correlation between photosensitizer (red) and vasculature (blue) can be seen. Photosensitizer is much lower in tumor tissue (green).*

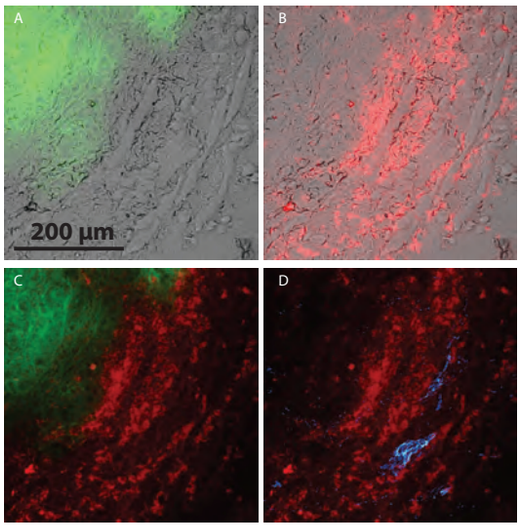

Figure 6.9: *Bremachlorin after 48 hour incubation time. No direct correlation between photosensitizer (red) and vasculature (blue) can be seen. Photosensitizer is much lower in tumor tissue (green).*

tumor tissue and tumor boundary it was observed that for short incubation times the photosensitizer concentration was highest around the vasculature and showing a decreasing concentration gradient with distance from the vasculature. This dependency decreased with increasing incubation time, suggesting a re-localization from vasculature to a homogenous distribution in the tissue. Invasive tumor border and normal tissue did not show this relationship. Although the variation in measurements was large and the observed relations were not significantly different, they represent an undeniable trend in the data. When comparing ce6 vessel co-localization with that of Bremachlorin, a difference in the concentration gradients was not observed in the graphs. It was observed that tumor boundary contained relatively many vessels. Photosensitizer was distributed around these vessels in the stroma. Some long incubation time locations showed a negative relationship between vessel staining and photosensitizer in tumor stroma, suggesting that the photosensitizer was present in the tissue, but not in the vasculature.

Figure 6.8 and figure 6.9 show the highly vascularized tumor boundary. Figure 6.8 shows a 3 hour Bremachlorin time point at which a decrease in photosensitizer concentration around the vessel could not be discriminated (figure 6.8d). Figure 6.9 shows Bremachlorin at 48 hours, were it was observed that photosensitizer is localized around, but mostly not coincident with the vasculature (figure 6.9d).

DISCUSSION

In this paper we report on the microscopic localization of the photosensitizers Bremachlorin and ce6. We have previously performed non-invasive in-vivo fiber optic intrinsic fluorescence pharmacokinetics measurements on normal tongue and orthotopic oral squamous cell carcinoma in the tip of the tongue [25]. This study is an extension of that analysis using confocal microscopy.

PHOTOSENSITIZER LOCALIZATION

The concentration of photosensitizer in the four tissues that were investigated - tumor, tumor boundary, invasive tumor border and normal tissue- showed a general decreasing trend over time, although not all time points were significantly different from each other. Photosensitizer fluorescence intensity was lower in tumor tissue than in the invasive tumor border for both Bremachlorin and ce6. Normal tissue, consisting of muscle fibers, showed a high fluorescence at short incubation times. Comparing photosensitizer localization with the presence of vasculature showed a decrease in fluorescence intensity with increasing distance from vessels for short incubation times in tumor and tumor boundary. This suggests that photosensitizer was predominantly present in and around the vasculature. The reason we did not observe this in invasive tumor border and normal tissue might be due to the localization of photosensitizer in muscle fibers in these tissues, where the pharmacokinetics may differ from those in tumor/tumor boundary. Since the localization of vasculature and muscle fibers did not directly correlate, the photosensitizer distribution around a vessel was mainly dependent on the presence of muscle fiber bundles. A correlation between photosensitizer localization and vasculature, and then in particular the smaller vessels surrounding muscle fibers, might be observed when analyzing even shorter incubation times.

The localization of photosensitizer in bright spots after 24 and 48 hour incubation time did not co-localize with identifiable tissue structures in the bright-field transmission images. H&E images taken from slides of the same tong were compared with the bright-field transmission images. Direct comparison of these images was complicated, since i) H&E and confocal images not being taken from the same coupes, and ii) although the confocal and the H&E coupe consist of subsequent tissue slices, the processing of the two methods results in differences in appearance. However, it allowed for qualitative analysis of histological structures that matched the fluorescent pattern on size and localization.

It can be seen in figure 6.6c and d that the relative location and density of the bright spots in figure 6.6d show close resemblance to the cell nuclei stained purple in figure 6.6c. Bright spots are only located at the edge of muscle bundles, not in the middle.

Furthermore, in areas where the bright spots do not coincide with muscle bundles, they appear to be closely together present in a ribbon-like structure. A qualitative comparison of the location and pattern of these high photosensitizer concentrations with the H&E histological sections suggested that the bright fluorescent photosensitizer spots visible at 24 and 48 hour incubation time were associated with cell nuclei. Both ce6 and Bremachlorin are known to be internalized via endocytosis, after which the photosensitizer is subcellular localized in the lysosomes. These intracellular vesicles accumulate near the cell nucleus [29, 30] and could therefore very well be the source of the high fluorescent spots.

COMPARISON WITH FIBER OPTIC RESULTS

We have previously reported on pharmacokinetics of Bremachlorin and ce6 measured with single fiber fluorescence spectroscopy (SFF) which enabled the discrimination between normal and tumor tissue [25]. Based on these measurements, a much larger decrease of ce6 and Bremachlorin over time than shown in figure 6.3 was expected in the present study [25]. Although quantitative comparison between fluorescence intensity measured using confocal microscopy and fiber optic spectroscopy is not possible due to differences in sample volume, light delivery and reflectance within the sample, it is possible to perform qualitative analysis. The exact reason for this discrepancy is not immediately clear. Sample degradation due to photobleaching is a potential explanation for this observation. The fact that high photosensitizer concentration samples are more prone to decreased intensity underlines this hypothesis. A larger decrease was observed in the short incubation times, corresponding with high photosensitizer concentration. Another factor that could contribute to the diminished fluorescence in early time points using microscopy is the removal of most blood from the tissue. For short incubation times, high concentration of photosensitizer might be expected to be present in the blood, due to its hydrophilic nature. In SFF measurements, this is included in the measurements, while for confocal imaging of tissue slides the contribution of blood is expected to be much less. At late time points, the photosensitizer is already cleared from the blood and therefore the variation between SFF and confocal measurements due to the inclusion of blood should be minimal.

The fiber optic pharmacokinetic measurements showed a significantly higher fluorescence intensity in tumor tissue compared to normal tissue both for Bremachlorin and ce6. Furthermore, at long incubation times (24 and 48 hours), there is still a significant amount of Bremachlorin present, while ce6 is (almost) completely cleared. Comparing these results with our microscopic findings in the present study, tumor shows lower fluorescence intensity than normal tissue. Considering the histology of the tumor in

the tongue (figure 6.1) it can be seen that although the tumor is mostly located in the tip of the tongue, there is still a layer of tumor boundary and some invasive tumor border covering the tumor at the tongue tip. When performing fiber optic measurements, this tissue is included in the measurement volume. We can therefore not discriminate between tumor and tumor boundary in the fiber optic measurements. In the present microscopic analysis the tumor boundary showed a much higher fluorescence intensity than normal tissue. This explains the high concentration of photosensitizer measured in what were identified as tumor measurements. A direct quantitative comparison of fluorescence intensity acquired with fiber optic measurements and with confocal microscopy is therefore not possible. Since the fiber optic measurements of normal tissue were all taken at the back of the tongue we can safely compare those with microscopically normal histology. In this paper we show that for long incubation times (24 and 48 hours), there is more Bremachlorin present in tumor than in normal tissue. Although fiber optic measurement showed tumor-selectivity at all incubation times, the tumor to normal ratio of the photosensitizer increased significantly for Bremachlorin at 24 and 48 hours. This corresponds with the trend found microscopically. Due to the relatively low spectral resolution possible in the present study, a spectral comparison of the two photosensitizers over time was not feasible.

When analyzing the microscopic distribution of photosensitizer, the photosensitizer was much less homogenously distributed than was expected based on the fiber optic measurements. We showed differences in localization that were not possible using SFF. The presence of photosensitizer in muscle fiber bundles in normal and invasive tumor border is somewhat surprising. Although the photosensitizer distribution is investigated extensively in-vitro [29, 30], microscopic analysis of localization in an orthotropic tumor model was necessary to reveal this. The same was true for the highly vascularized tumor boundary, where the highest concentration photosensitizer was shown to be present. This border is for example not clearly distinguishable when implanting the same tumor cell line in a dorsal skinfold window chamber [unpublished data]. It is important to perform pharmacokinetic measurements in an (orthotopic) environment as close to the (pre-)clinical situation as possible. In clinical mTHPC-PDT of the oral cavity, damage to normal tissue is a limiting factor. The tongue model used for this study is therefore of significant interest to study the potential for Bremachlorin biodistribution and PDT effects on normal tissue. The high photosensitizer uptake of muscle compared to tumor after short incubation times suggests that long incubation times may be more effective in sparing normal tongue.

COMPARISON WITH OTHERS

Ce6 has been extensively researched in vitro. It is known that both quantum yield and spectral shape are pH dependent; reducing the pH in the range pH7-pH9 results in a decrease in fluorescent quantum yield and a red shift of the fluorescence emission [10, 11]. A decrease in pH also causes an increase in lipophilicity, resulting in a preferred binding to low density lipoproteins (LDL) over albumin. These LDL are considered a delivery system of lipophilic photosensitizers, where internalization occurs via LDL-specific endocytosis. It has been suggested that the relatively low pH of tumor environment, together with an over-expression of LDL-receptors on the cell surface in proliferating tissue, results in a higher photosensitizer accumulation in tumor than in normal tissue [31]. Our results in OSC tumors did not show this effect. In fact we found a lower photosensitizer concentration in tumor than in normal tissue. A reason for this might be relatively low vascularization of the encapsulated tumor in the mouse tongue. It should be noted that humans have a different HDL/LDL profile than rodents and further studies are necessary in other species to confirm the results above.

Mitra et al. [32] investigated the microscopic distribution of NPe6, a derivative of ce6, in an intradermal EMT6 tumor model in mouse skin using intra-vital microscopy. They showed NPe6 is localized in the vasculature for the first hours after administration and redistributes throughout the extravascular regions between 1 and 3 hours. This effect is observed for both tumor and normal vasculature. Although our study focused on a different range of incubation times starting at 3 hours, the distribution of NPe6 versus distance is similar to our findings in OSC tumors in the tongue; a slight but steady decrease with distance from vessel over time. The fact that we have shown different pharmacokinetics of ce6 and Bremachlorin in normal tissue may be a consequence of the differences in tumor models. Another possibility is that the different pharmacokinetics are a consequence of differences between NPe6 and ce6 and Bremachlorin. Large experimental tumors in the tongue are known to have a higher interstitial pressure than the relatively flat tumors grown in a window chamber [33]. This influences the results of preclinical pharmacokinetic studies. We have already observed that in normal tongue, most photosensitizer was located in the muscle bundles present in tongue, whereas the larger vessels were quite randomly distributed in tissue. This resulted in high fluorescence intensity peaks at random distances from vasculature, which was evened out when averaging over multiple locations. When focusing an investigation on the relation between photosensitizer localization and vasculature, more appropriate models such as mouse skin in a dorsal skinfold chamber may be considered. However, when determining pharmacokinetics to optimize PDT, it is advised to study the tissue that is treated with PDT. Since in the head & neck area PDT is used to treat tumors in the tongue, it is normal

tongue tissue (muscle) that needs to be spared. The current model is appropriate for that. When investigating other head and neck areas that are treated with PDT, such as the floor of mouth or the lining mucosa, other models might be more appropriate.

CONFOCAL MICROSCOPY

Analyzing thin tissue samples on the presence of a photosensitizer without bleaching the sample remains challenging. To prevent bleaching, samples were prepared under conditions as dark as possible and the samples were stored in a closed dark container. When performing confocal microscopy, determining of the right location and placing the sample in focus was done visually using a very small amount of light. With the sample in the right location, the first image acquired was always that to determine the distribution of photosensitizer fluorescence. Furthermore, multiple locations on one same sample were chosen to be located away from each other to prevent photobleaching due to previous recordings.

Localization of vasculature was performed by staining with CD31. Since this procedure involved washing and incubating with PBS, this had to be performed after recording of photosensitizer; the hydrophilicity of ce6 and to a lesser extend Bremachlorin caused the photosensitizer to be removed from the tissue during the vessel staining. Finding the exact same location when re-imaging the sample after vascular staining proved challenging but not impossible. Due to hydration of the tissue the structure did change somewhat, but not significantly. Therefore the location of the vasculature in one recording is very likely to identify vasculature in other recordings.

IMPLICATIONS OF CE6 AND BREMACHLORIN PHARMACOKINETICS FOR PDT

An important result of the present study is the relatively low concentrations for ce6 and Bremachlorin in tumor itself. This may be a concern when we consider therapeutic efficacy. We have found however that the OSC tumor boundary contained high concentrations of photosensitizer. This well vascularized tissue maintains the supply of blood and nutrients to the tumor. Although we did not find a co-localization between photosensitizer and vascular wall, the high local photosensitizer concentration may result in damage to the vasculature of the tumor boundary when performing PDT. This may indirectly destroy tumor tissue. At early time points, the concentration of both ce6 and Bremachlorin was higher in normal tissue than in tumor. At long incubation times of 24 and 48 hours, the Bremachlorin concentration in tumor appears to be higher than in normal tissue, although the total amount of photosensitizer present in tissue at these time points was much lower. However, it has been shown before that clinical efficacy of PDT is not directly related to photosensitizer concentration. Therefore, the low

concentrations found at 24 and 48 hours might very well result in efficient PDT. Clinically, PDT with ce6 and its derivatives is usually combined with an incubation time of <6 hours [17, 34]. Results form this study suggest that this is not the most optimal time point to directly damage tumor tissue, while preventing normal tissue damage. A 24 hour drug-light interval appears to be an encouraging option for Bremachlorin PDT, showing a relatively high tumor-to-normal ratio and a homogenously spread photosensitizer distribution.

CONCLUSION

In this paper we report on the microscopic analysis of the photosensitizers Bremachlorin and ce6 in mouse tongues containing OSC tumors. Incubation times of t = [3 4.5 6 24 and 48] hours were investigated. For both photosensitizers, more fluorescence was measured in tumor boundary than in tumor itself. Normal and invasive tumor border showed higher fluorescence intensity than tumor tissue for short incubation times. Only at 24 and 48 hour incubation times, the Bremachlorin concentration in tumor and tumor boundary was higher than that in normal tissue, providing the possibility for selective tissue damage. In normal tissue and the invasive tumor border tissue, photosensitizer was mainly present in normal muscle, although for longer incubation times the distribution became more homogenous. For the investigated time points between 3 and 48 hours, we did not find a correlation between the localization of photosensitizer and vasculature. It can be concluded that Bremachlorin at 24 and 48 hour incubation time provides us with both a concentration suitable for PDT and a small tumor/tumor boundary to normal selectivity of between 1.2 and 2.5. This tumor selectivity opens up the possibility to investigate Bremachlorin PDT with long incubation times, where normal muscle may be spared and only tumor tissue is affected by PDT.

ACKNOWLEDGEMENTS

We kindly thank Laura Mezzanotte for her work on the lentiviral transduction and production of the Luc2-gfp-OSC19 cell line, and the University Medical Centre Leiden for providing those cells for this study.

REFERENCES

1. Babilas, P., et al., *Photodynamic therapy in dermatology: state-of-the-art.* Photodermatology, photoimmunology & photomedicine, 2010. **26**(3): p. 118-132.
2. van der Snoek, E.M., et al., *Photodynamic therapy with systemic meta-tetrahydroxyphenylchlorin in the treatment of anal intraepithelial neoplasia, grade 3.* Lasers in surgery and medicine, 2012. **44**(8): p. 637-644.
3. Karakullukcu, B., et al., *Clinical feasibility of monitoring mTHPC mediated photodynamic therapy by means of fluorescence differential path-length spectroscopy.* Journal of Biophotonics, 2011. **4**(10): p. 740-751.
4. Dunn, J., et al., *A randomised controlled trial of ALA vs. Photofrin photodynamic therapy for high-grade dysplasia arising in Barrett's oesophagus.* Lasers in medical science, 2013. **28**(3): p. 707-715.
5. Weersink, R.A., et al., *Techniques for delivery and monitoring of TOOKAD (WST09)-mediated photodynamic therapy of the prostate: clinical experience and practicalities.* Journal of Photochemistry and Photobiology B: Biology, 2005. **79**(3): p. 211-222.
6. Dolmans, D.E., D. Fukumura, and R.K. Jain, *Photodynamic therapy for cancer.* Nature Reviews Cancer, 2003. **3**(5): p. 380-387.
7. Allison, R.R., et al., *Photosensitizers in clinical PDT.* Photodiagnosis and photodynamic therapy, 2004. **1**(1): p. 27-42.
8. Chen, B., et al., *Combining vascular and cellular targeting regimens enhances the efficacy of photodynamic therapy.* International Journal of Radiation Oncology* Biology* Physics, 2005. **61**(4): p. 1216-1226.
9. Cramers, P., et al., *Foscan uptake and tissue distribution in relation to photodynamic efficacy.* British journal of cancer, 2003. **88**(2): p. 283-290.
10. Cunderlíková, B., L. Gangeskar, and J. Moan, *Acid-base properties of chlorin e6: relation to cellular uptake.* Journal of Photochemistry and Photobiology B: Biology, 1999. **53**(1): p. 81-90.
11. Mojzisova, H., et al., *Cellular uptake and subcellular distribution of chlorin e6 as functions of pH and interactions with membranes and lipoproteins.* Biochimica et Biophysica Acta Biomembranes, 2007. **1768**(11): p. 2748-2756.
12. Gerweck, L.E. and K. Seetharaman, *Cellular pH gradient in tumor versus normal tissue: potential exploitation for the treatment of cancer.* Cancer research, 1996. **56**(6): p. 1194-1198.
13. Mroz, P., et al., *Cell death pathways in photodynamic therapy of cancer.* Cancers, 2011. **3**(2): p. 2516-2539.
14. Andrejevic-Blant, S., et al., *Photodynamic therapy of early squamous cell carcinoma with tetra (m-hydroxyphenyl) chlorin: optimal drug-light interval.* British journal of cancer, 1997. **76**(8): p. 1021-1028.
15. Nelson, J.S., W.G. Roberts, and M.W. Berns, *In vivo studies on the utilization of mono-L-aspartyl chlorin (NPe6) for photodynamic therapy.* Cancer research, 1987. **47**(17): p. 4681-4685.
16. Chin, W.W.L., et al., *Fluorescence imaging and phototoxicity effects of new formulation of chlorin e6-polyvinylpyrrolidone.* Journal of Photochemistry and Photobiology B: Biology, 2006. **84**(2): p. 103-110.
17. Kato, H., et al., *Phase II clinical study of photodynamic therapy using mono-L-aspartyl chlorin e6 and diode laser for early superficial squamous cell carcinoma of the lung.* Lung Cancer, 2003. **42**(1): p. 103-111.

18. O'Connor, A.E., W.M. Gallagher, and A.T. Byrne, *Porphyrin and nonporphyrin photosensitizers in oncology: preclinical and clinical advances in photodynamic therapy.* Photochemistry and photobiology, 2009. **85**(5): p. 1053-1074.

19. Chan, A.L., et al., *Pharmacokinetics and clinical effects of mono-L-aspartyl chlorin e6 (NPe6) photodynamic therapy in adult patients with primary or secondary cancer of the skin and mucosal surfaces.* Photodermatology, photoimmunology & photomedicine, 2005. **21**(2): p. 72-78.

20. Douillard, S., D. Olivier, and T. Patrice, *In vitro and in vivo evaluation of Radachlorin sensitizer for photodynamic therapy.* Photochemical & Photobiological Sciences, 2009. **8**(3): p. 405-413.

21. Bae, S.-M., et al., *Photodynamic Effects of Radachlorin on Cervical Cancer Cells.* Cancer Research and Treatment, 2004. **36**(6): p. 389-394.

22. Ji, W., et al., *The effect of Radachlorin PDT in advanced NSCLC: A pilot study.* Photodiagnosis and photodynamic therapy, 2013. **10**(2): p. 120-126.

23. Kochneva, E.V., et al., *Photosensitizer Radachlorin: Skin cancer PDT phase II clinical trials.* Photodiagnosis and photodynamic therapy, 2010. **7**(4): p. 258-267.

24. Uzdensky, A., et al., *Photodynamic effect of novel chlorin e6 derivatives on a single nerve cell.* Life sciences, 2004. **74**(17): p. 2185-2197.

25. van Leeuwen - van Zaane, F., et al., *Intrinsic photosensitizer fluorescence measured using multi-diameter single fiber spectroscopy in-vivo.* Journal of biomedical optics, 2014. **19**(1): p. 015010.

26. van Leeuwen - van Zaane, F., et al., *In vivo quantification of the scattering properties of tissue using multi-diameter single fiber reflectance spectroscopy.* Biomedical optics express, 2013. **4**(5): p. 696-708.

27. Mezzanotte, L., et al., *Evaluating reporter genes of different luciferases for optimized in vivo bioluminescence imaging of transplanted neural stem cells in the brain.* Contrast Media & Molecular Imaging, 2013. **8**(6): p. 505-513.

28. Carlotti, F., et al., *Lentiviral vectors efficiently transduce quiescent mature 3T3-L1 adipocytes.* Molecular Therapy, 2004. **9**(2): p. 209-217.

29. Chin, W.W.L., et al., *Effect of polyvinylpyrrolidone on the interaction of chlorin e6 with plasma proteins and its subcellular localization.* European Journal of Pharmaceutics and Biopharmaceutics, 2010. **76**(2): p. 245-252.

30. Soukos, N.S., M.R. Hamblin, and T. Hasan, *The Effect of Charge on Cellular Uptake and Phototoxicity of Polylysine Chlorine6Conjugates.* Photochemistry and photobiology, 1997. **65**(4): p. 723-729.

31. Kratz, F., A. Wunder, and B. Elsadek, *Serum Proteins as Drug Carriers of Anticancer Agents*. Drug Delivery in Oncology: From Basic Research to Cancer Therapy, ed. F. Kratz, P. Senter, and H. Steinhagen2011: Wiley-VHC GmbH & Co. KGaA, Weinheim, Germany. 747-803.

32. Mitra, S. and T.H. Foster, *In vivo confocal fluorescence imaging of the intratumor distribution of the photosensitizer mono-L-aspartylchlorin-e6.* Neoplasia, 2008. **10**(5): p. 429-438.

33. Gutmann, R., et al., *Interstitial hypertension in head and neck tumors in patients: correlation with tumor size.* Cancer research, 1992. **52**(7): p. 1993-1995.

34. Lustig, R.A., et al., *A multicenter Phase I safety study of intratumoral photoactivation of talaporfin sodium in patients with refractory solid tumors.* Cancer, 2003. **98**(8): p. 1767-1771.

Chapter 7

The Effect of the Drug-Light Interval on Chlorin e_6 Photodynamic Therapy on Oral Squamous Cell Carcinoma in Mice

Floor van Leeuwen – van Zaane,
Pieter van Driel, Ute Gamm, Thomas Snoeks, Riëtte de Bruijn
Angélique van der Ploeg – van den Heuvel, Dick Sterenborg,
Clemens Löwik, Dominic Robinson

Photodiagnosis and Photodynamic Therapy
Submitted December 2013

ABSTRACT

The effect of photodynamic therapy (PDT) is dependent on the presence of oxygen, light and photosensitizer in the treatment volume. It has been recently shown that for the chlorin e_6-based photosensitizer Bremachlorin, pharmacokinetics showed promising results for PDT using a drug-light interval of 24-48 hours. In this paper, the effect of the drug-light interval on PDT using chlorin e_6 and Bremachlorin was investigated. Oral squamous cell carcinomas were induced in dorsal window chambers on the back of mice and treated with PDT after a drug-light interval of 5 or 24 hours. Acute vascular effects were analyzed using recordings of the window chamber vasculature during illumination. Two hours after illumination, vascular leakage and stasis were investigated by intra-vital confocal microscopy. 48 hours after treatment, chambers were inspected for microscopic vascular damage such as hemorrhage and tissue was removed and sectioned for histological analysis of PDT-related cell damage. Most acute vascular effects were observed during Bremachlorin PDT with a 24 hour drug-light interval, followed by ce6 PDT 5 hours after injection. Leakage and stasis were more evident in Bremachlorin treated animals independent of incubation time. The PDT-induced histological responses were most severe in Bremachlorin PDT with a 24 hour drug-light interval. PDT-related damage to tumor cells was related to the onset of acute vascular effects during PDT illumination. We can conclude that for both ce6 and Bremachlorin PDT with a 24 hour drug-light interval was most effective in inducing damage to tumor cells. This is in contrast with the short-incubation times that are currently used for ce6-based photosensitizers in (pre-)clinical research.

INTRODUCTION

Photodynamic therapy (PDT) has been under investigation for over four decades and is now applied clinically for the treatment of various (pre-)malignant lesions [1-4]. Its working principle is based on the interaction between a photoactive drug, the photosensitizer, oxygen and light of an appropriate wavelength. Treatment light energy is absorbed by the photosensitizer, which is promoted to an excited singlet state. One of the ways for this unstable molecule to lose its excess energy is to transform into a triplet state by intersystem crossing. In this triplet state, the photosensitizer can interact with oxygen to generate highly reactive oxygen species, notably singlet oxygen, which causes direct tissue damage [5].

PDT-induced direct cell damage can result in two distinct response pathways: apoptosis, and necrosis [6]. Apoptosis is the process of regulated cell death, involving a series of biological events. Many pathways and signals can induce apoptosis, including the release of hormones, cytokines and stress. Direct mitochondrial damage results in the release of cytochrome C into the intra-cellular space, which represents the onset of apoptotic cell death. Several photosensitizers are known to directly target mitochondria (PpIX [7]), or activate the translocation of damage-inducing proteins to the mitochondria (NPe6 [8]), resulting in apoptosis of tumor cells. Necrosis is cell death resulting from acute tissue injury and is characterized by pyknotic nuclei, cytoplasmic swelling and disintegration of cell membranes. Necrosis is associated with the induction of a wide range of immunological responses that can have a significant influence on the overall outcome of PDT [6]. The extent to which PDT indices apoptosis and/or necrosis depends on many factors including cell type, subcellular photosensitizer localization, oxygen tension (apoptosis requires the availability of oxygen) and light fluence rate; high fluence rates tend to induce necrosis, while low fluence rates are associated with apoptotic cell death [9]. Immunological responses to PDT include the activation of autophagy, but exactly how these autophagic effects influence the outcome of PDT are still under investigation [10]. In general cells use autophagy as a defense against ROS mediated damage by clearing the cell of damaged organelles. Depending on the type of ROS and degree of oxidative injury, PDT may stimulate autophagy and induce cell death [11].

Many different photosensitizers have been used clinically for a variety of applications [2, 3, 12, 13]. Although all photosensitizers' mechanism of action are based on the principle of generation of reactive oxygen species, exactly which tissue or cellular structures these ROS interact with depends on their localization [14, 15]. Most photosensitizers are administered intravenously, after which they diffuse into the surrounding tissue. The rate

at which this occurs is dependent on the physiochemical properties of the photosensitizer, but varies from hours (for example chlorin e_6) to days (for example mTHPC and Photofrin) [16-19]. Pre-formed photosensitizers such as m-THPC, ce6 and its derivatives are normally administered intravascular, but have tumor tissue as their target. In certain circumstances the uptake of photosensitizer in tumor tissue may be higher than in normal tissue. The underlying mechanism for this selectivity is the EPR effect, caused by the leaky nature of the neovasculature and reduced lymphatic drainage in tumors compared to normal tissue [20]. Furthermore, ce6 is thought to profit from the relatively low pH of tumor stroma, resulting in a shift in binding affinity and a more efficient cellular internalization [21, 22].

Photosensitizer pharmacokinetics, cellular uptake and subsequent localization are critical determinants of PDT efficacy. The first determines how the amount of photosensitizer present in a tissue under investigation develops over time and is influenced by metabolism and clearance of the photosensitizer.

Many photosensitizers are known to not only affect tumor cells in the treatment volume, but also have the vasculature itself as a target [23]. Previous studies with topically applied 5-aminolevulinic acid (ALA), a precursor for the endogenous photosensitizer protoporphyrin IX (PpIX) showed that PpIX is synthesized in the mitochondria of cells in the epidermis and dermis [24]. It is known that even (epi-) dermally located endothelial cells generate PpIX, which upon illumination results in damage to the vasculature [25, 26]. NPe6, a ce6 conjugate, is known to induce stasis in tissue vasculature [27]. Although this disrupts the blood and nutrient supply to the tumor and/or lesion, which can be favorable for treatment outcome, the oxygen supply necessary for PDT is also disrupted. The effect of PDT induced vascular damage is therefore multifaceted and the overall result is known to depend strongly on treatment parameters such as fluence, fluence rate and drug-light interval [25, 28-30].

Photosensitizers based on chlorin e_6 are known to be quite hydrophilic. Since this prevents the photosensitizer from being internalized by cells, ce6 is quickly metabolized and cleared from the tissue via the urinary system. The in-vivo response of tumors following ce6 based PDT has been investigated in a limited number of studies [31]. Many more studies have been performed with ce6-based conjugates such as ce6-PVP, in which ce6 is conjugated with a polyvinylpyrrolidone carrier [32], or ce6 derivatives such as NPe6 (mono-L-aspartylchlorin-e_6) [18]. These chemical modifications are designed to increase the cellular uptake of the photosensitizer, thereby increasing efficacy. Various preclinical studies on the effects of NPe6-PDT on vasculature have been performed [27, 33, 34].

NPe6 is approved for clinical use on early stage superficial squamous cell carcinomas in lung in Japan [35, 36], and it is also under investigation for skin malignancies [13, 37].

Bremachlorin is a mixture of photosensitizers consisting of ce6 (~80%), chlorin p_6 (~5%) and purpurin 5 (~15%) [38]. It is less hydrophilic than ce6 and is therefore expected to have a higher binding affinity for low density lipoproteins (LDL) and thereby being internalized in cells by means of endocytosis and intra-cellular transported in lysosomes towards the nucleus [39]. The number of (pre-)clinical tests performed with Bremachlorin is limited but covers a number of malignancies and treatment protocols [38, 40-43].

Previously, we have studied the fluorescence of both ce6 and Bremachlorin. In-vivo, photosensitizer intrinsic fluorescence spectra were acquired in mouse tissue (tongue and oral squamous cell carcinoma in tongue) using single fiber fluorescence spectroscopy at various times after photosensitizer injection [44]. Furthermore, we have investigated the microscopic localization of ce6 and Bremachlorin in frozen tongue samples using confocal microscopy [45]. We showed that for both ce6 and Bremachlorin the photosensitizer concentration is highest in the tumor border. The photosensitizer concentration in normal tissue is much lower, and microscopically we found that although tumor border has a high concentration, the tumor itself contains a relatively low concentration of photosensitizer. However, 24 hours after administration the concentration of Bremachlorin in tumor exceeds that of normal tissue. At this time point, ce6 is mostly excreted from the body. After short incubation times in normal and the invasive tumor border, photosensitizers are preferentially located in muscle fiber bundles. After 24 or 48 hours, this effect is less pronounced, showing a more homogenous level of photosensitizer concentration for Bremachlorin. Ce6 is undetectable at these time points. Clinically, ce6-based photosensitizers usually have a drug-light interval of 4-6 hours [13]. These results suggest that a longer drug-light interval may be more favorable for Bremachlorin based PDT, which takes advantage of the higher selectivity in tumor compared to normal tissue.

In the present study we have performed PDT in dorsal skinfold chambers in mice containing OSC19 oral squamous cell carcinoma. The primary purpose of the study is to determine if our previous findings on the pharmacokinetics of ce6 and Bremachlorin result in more effective photodynamic therapy after a long drug-light interval (24 hours), compared to a short 5 hour drug-light interval. Treatment efficacy is measured based on a combination of tumor reduction, visual macroscopic damage and histological damage observations.

MATERIALS AND METHODS

ANIMAL MODEL

A dorsal skin fold window chamber was prepared on the back of 28 mice (BALB/c nu/nu female mice, aged 4-6 weeks; Charles River Laboratories) using a procedure described in detail elsewhere [46-48]. In short, mice were anesthetized (ketamine, 100 mg kg^{-1} b.w. and xylazine, 20 mg kg^{-1} b.w. in a volume mixture of 2:1:1 saline, ketamine, xylazine) and the skin was dissected leaving the fascia and the opposing skin. The skin-fold was then sandwiched between two frames, fixed with two light metal bolts and sutures. Cells from the oral squamous cell carcinoma cell line OSC19, transfected with luc2 (Biocat, Heidelberg, Germany) and Cop-gfp (Evrogen, Moscow, Russia), were injected in the fascia ($4x10^5$ cells) [49-52]. Afterwards, both sides of the frame were covered with a 12 mm microscope cover glass to allow for analysis of tumor and vasculature over time. All experiments were performed under isoflurane (2-3%) anesthesia. The study protocol was approved by the Animal Welfare Committee of the Erasmus Medical Center. Housing of BALB/c nu/nu mice, the experiments and euthanazation were performed in accordance with the guidelines of this committee. Chlorophyll free food and sterilized water were provided without restriction.

TUMOR SIZE DETERMINATION

After a 6-7 days incubation time, 24 hours before PDT, tumor size was analyzed by means of bioluminescence imaging (IVIS, PerkinElmer, Walthma, MA, USA). Animals were anesthetized (2-3% isoflurane), injected with luciferin (150 mg kg^{-1}, VivoGlo, Promega Corporation, Madison, WI, USA) and tumor size was determined after five minutes using bioluminescence imaging. This process was repeated two days after therapy, after which the animals were euthanized and tissue harvested for further investigation.

PHOTODYNAMIC THERAPY

Animals were divided into four treatment groups 1-4 (n=6) and one control group 0 (n=4). Two photosensitizers, ce6 (16 mg kg^{-1} in 100 µl PBS, Frontier Scientific, Inc., Logan, USA) and Bremachlorin (20 mg kg^{-1}, form stock solution of 3.5 g l^{-1}, Rada-pharma International B.V., The Netherlands) were investigated at two drug-light intervals (5 and 24 hours). Treatment parameters were as follows: all animals received 200 J cm^{-2} at a fluence rate of 150 mW cm^{-2} (corresponding to 23 minutes illumination) using a 532 nm laser light source. Group 1: Bremachlorin, 5 hours. Group 2: ce6, 5 hours. Group 3: Bremachlorin, 24 hours. Group 4: ce6, 24 hours. The control group 0 received the same fluence and fluence

rate as all other groups, without the administration of photosensitizer. Illumination was performed with the mouse placed in a specially designed setup, shown in figure 7.1, so that the window chamber could be illuminated homogenously from the top (skin-side), while recording the chamber from below (muscle and vascular layer) to monitor vascular effects during treatment. Before illumination, fluorescent images of the treatment area were recorded to analyze: i) photosensitizer fluorescence (λ_{ex} 532 nm, $\lambda_{detection}$ bandpass 640-680 nm detection filter) and ii) gfp (tumor) fluorescence (λ_{ex} 405 nm, $\lambda_{detection}$ bandpass 480-520 nm filter). The treatment efficacy was determined based on tumor reduction as measured from comparing tumor bioluminescence before and after treatment. Furthermore, macroscopic damage (necrosis, crust formation etc.) was recorded two days after treatment. Tissue from the window chamber was harvested after euthanazation of the animal and processed for H&E staining. This allowed for microscopic analysis of damage to the target tissue.

VASCULAR EFFECTS

Vascular effects during and after PDT were determined in three ways: acute vascular damage, short term vascular leakage and stasis, and long term (vascular) damage.

Acute vascular effects

Acute vascular damage was determined by recording window chamber vasculature during illumination using 532 nm bright-field transmission imaging. Images were recorded every 10 sec. These images were separately inspected to determine arterial closure, venous closure, reopening of vessels, muscular movement or hemorrhage.

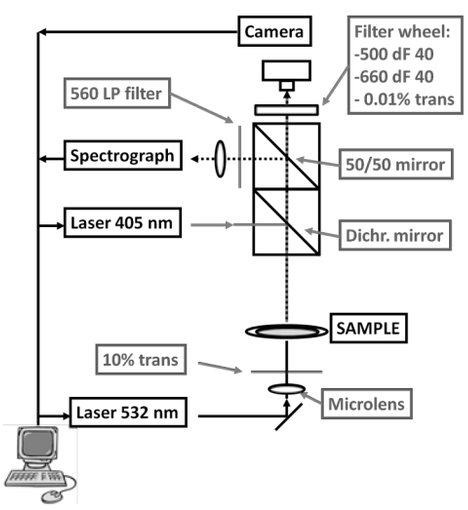

Figure 7.1: *PDT illumination setup.*

Short term leakage and stasis

Two hours after PDT, blood flow and vasculature were investigated using intravital microscopy (Zeiss LSM510META, Carl Zeiss B.V. Sliedrecht, the Netherlands) where the mouse was anesthetized using Isoflurane 2-3%. Mice were i.v. injected with 100 µl (48 µmol kg^{-1}) long half life Rho-PEG-L liposomes [48] to visualize the chamber vasculature and vascular leakage. Vascular leakage becomes visible when the vascular dye is extraverted into the extravascular regions showing diffuse fluorescence rather than a vascular angiogram.

Various locations in and outside the tumor were recorded and analyzed for vascular damage. The vascular dye was imaged with the following confocal parameters: (λ_{ex} 633 nm, 650 LP filter, optical slice thickness <12 µm). Tumor gfp was imaged: λ_{ex} 488 nm, 505-550 BP filter, optical slice thickness <48 µm. The optical slice thickness for tumor detection was purposely chosen to be large to include the complete tumor thickness in an overview image. Where possible, several areas within tumor and normal tissue were recorded. Chambers were inspected for the presence of leakage (the blood marker flows out of the contained vessel area) or stasis (the blood marker does not reach certain vessels).

(VASCULAR) DAMAGE AT 48 HOURS

Two days after the therapeutic illumination, the IVIS measurement was repeated. This provided an indication on PDT efficacy in the way of tumor size reduction. Furthermore, IVIS measurements provided an image of the window chamber vasculature, which was compared with the image before PDT. Finally, images of the window chambers before animal euthanization were visually inspected.

MICROSCOPIC TISSUE DAMAGE AT 48 HOURS

After euthanization, the tissue from window chambers was removed, embedded in paraffin, cut in 4 µm sections and stained with H&E. Sections were digitalized (Nanozoomer, Hamamatsu) and inspected to asses the tissue for the presence of apoptotic, necrotic and inflammatory markers, together with a general assessment of tumor and normal tissue viability.

RESULTS

ACUTE VASCULAR EFFECTS

For every animal, we determined the occurrence and/or time point of the following events during illumination: arterial constriction, venule constriction, relaxation of the vascular lumen, cutaneous-muscle contraction and hemorrhage. As expected, the control group (no photosensitizer) did not show any of these events during illumination. The occurrence of these events is shown in figure 7.2. One animal of group 2 died before illumination started, resulting in 23 treated animals and four controls.

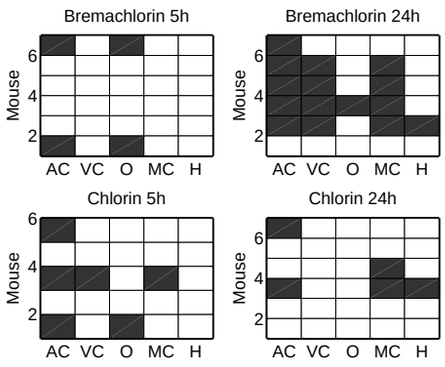

Figure 7.2: *Overview of acute vascular effects during PDT illumination for individual mice. The effects scored are arterial closure (AC), venous closure (VC), vascular relaxation (O), cutaneous muscle contraction (MC) and hemorrhage (H). Observed effects are indicated with a black box.*

For Bremachlorin with a 5 hour drug-light interval we observed arterial constriction for two animals, occurring between 130 and 170 s after the start of illumination. Both arteries returned to their initial condition respectively 150 and 1070 s later. Muscle contraction and bleeding did not occur.

Animals treated with Bremachlorin PDT at 24 hours showed vascular effects in five of the six animals. We observed both arterial and venule constriction. In animals that showed both, we also observed severe muscle contraction, visible by the displacement of the vasculature in the window chamber. Sometimes this displacement happened gradually during the later half of PDT illumination (figure 7.3, vessels in lower right corner), in other situations all vasculature could be completely rearranged within two minutes, as can be seen in figure 7.5 One animal showed strong hemorrhage and leaking vessels during illumination. Some example image sequences during therapy are presented in figure 7.3-7.5, where figure 7.5 shows severe muscle contraction and hemorrhage.

A 5 hour drug-light interval using ce6 resulted in three out of five animals showing acute vascular effects. In the only animal showing muscular contraction, we observed both arterial and venule constriction.

Ce6 PDT after a 24 hour drug-light interval did not result in significant vascular constriction. We observed arterial constriction in two animals and muscle contraction in two animals, of which one did not show any acute vascular effects. The animals that exhibited both arterial constriction and muscle contraction did however show dramatic shifts in dermal layers, followed by copious bleeding that originated from the tumor.

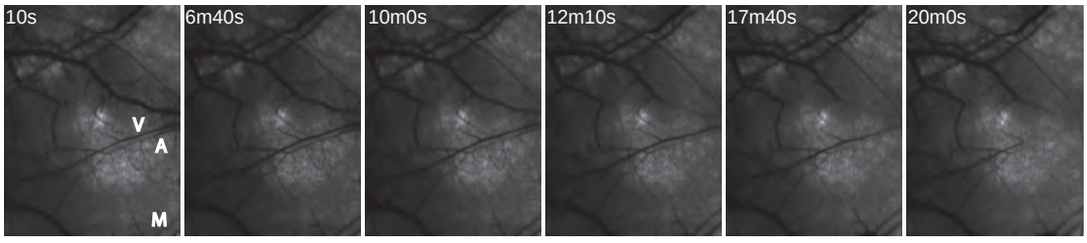

Figure 7.3: *Chlorin e6 PDT after 5 hour drug-light interval. Acute vascular effects like arterial constriction (A), venule constriction (V) and constriction of cutaneous muscles (M).*

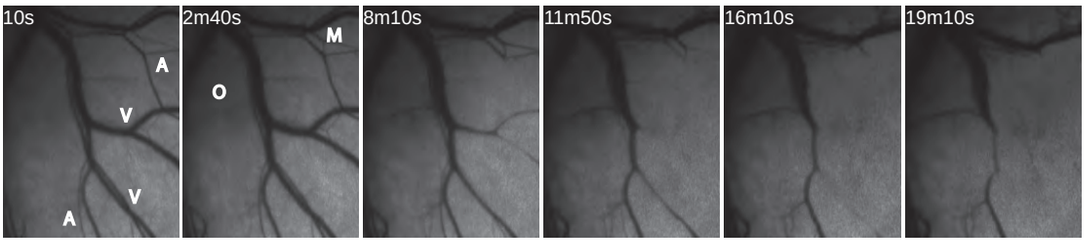

Figure 7.4: *Bremachlorin PDT after 24 hour drug-light interval. Acute vascular effects like arterial constriction (A), venule constriction (V), opening of arteries (O) and constriction of cutaneous muscles (M).*

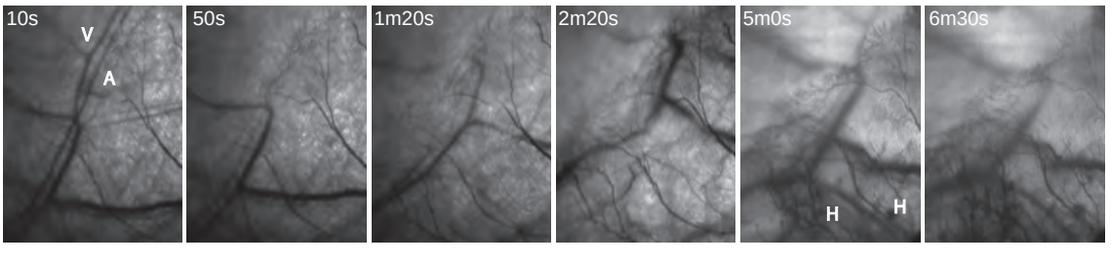

Figure 7.5: *Bremachlorin PDT after 24 hour drug-light interval. Immediate vascular shutdown (V,A) followed by severe muscle contractions and hemorrhage (H).*

Only four animals (2x Bremachlorin 5 hours, 1x Bremachlorin 24 hours and 1x ce6 5 hours) showed relaxation of the vessels during treatment.

VASCULAR LEAKAGE AND STASIS

The detection of vascular effects by confocal microscopy was in some cases confounded by the formation of edema directly after therapy. This prevented focusing on the focal plain containing the vasculature. Therefore, the present analysis only includes a partial set of animals. Where possible, animals not suitable for confocal microscopy were analyzed using conventional white light microscopy.

During confocal microscopy various vascular responses were observed. Some locations showed stasis (figure 7.6), others showed vascular leakage (figure 7.7) and visually we observed vessel constriction and hemorrhage in the window chambers. However, there were also animals where these effects did not occur.

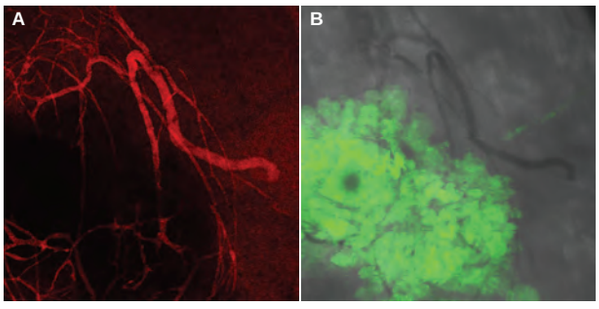

Figure 7.6: *Vasculature (Red) and Tumor (Green). Stasis is locally observed in tumor vessels.*

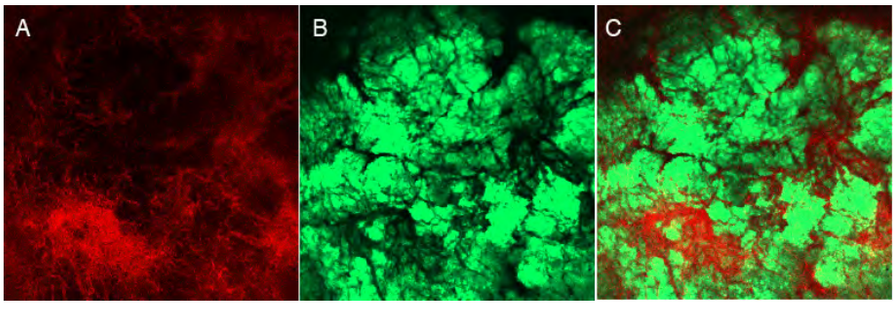

Figure 7.7: *Vasculature (Red) and Tumor (Green). Vascular stasis (upper left) and leakage (lower left) of vessels 2 hours after PDT.*

There were relatively more vascular effects visible for animals treated with Bremachlorin compared to Ce6. An overview of this is shown graphically in figure 7.8 where we discriminate between leakage (L) and stasis (S).

VASCULAR RESPONSE AFTER 48 HOURS

Forty eight hours after illumination the most damage was observed in the group treated with Bremachlorin and a drug-light interval of 24 hours. Four of the five animals showed macroscopic vascular damage in the form of hemorrhage and discontinuity of the vasculature. However, every treatment group showed at least one animal with similar observations. We found that animals showing these macroscopic characteristics of discontinuous vasculature two days after treatment all showed acute vascular effects during treatment. The animals in which this effect was found were distributed over all treatment groups, including both photosensitizers and incubation times. However, not all animals with acute vascular effects showed macroscopic vascular damage. We did not find a correlation between the vascular effects during treatment and the observation of hemorrhage and partial occlusion of the vasculature 48 hours after illumination.

Tumor size reduction was only measured qualitatively, where we compared the area of the tumor bioluminescence signal one day before and two days after treatment. A relation between tumor size reduction and treatment group was not observed. It is interesting to note that all animals showing a lower tumor mass after treatment were

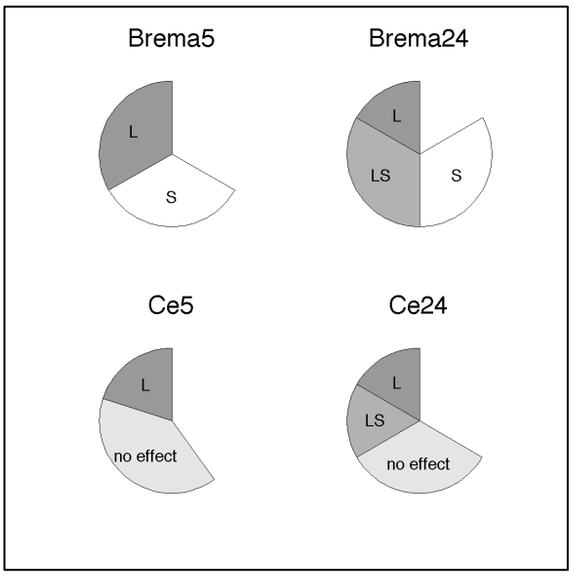

Figure 7.8: *Overview of vascular leakage and stasis as observed using confocal microscopy 2 hours after PDT illumination. (L) leakage, (S) stasis (LS) leakage and stasis.*

animals in which we observed vascular damage and therefore acute vascular effects. Again, we also observed animals with vascular damage having a much higher tumor load than before treatment.

HISTOLOGICAL RESPONSE AT 48 HOURS

The normal histological state of control window chambers differs from healthy normal skin due to inflammatory reactions caused by the window chamber. These include a thickening of the stratum corneum and lymphocyte infiltration in the upper and lower dermis. The fascia, in contact with the cover glass of the window, may show abundant infiltration and edema irrespective of the presence of tumor.

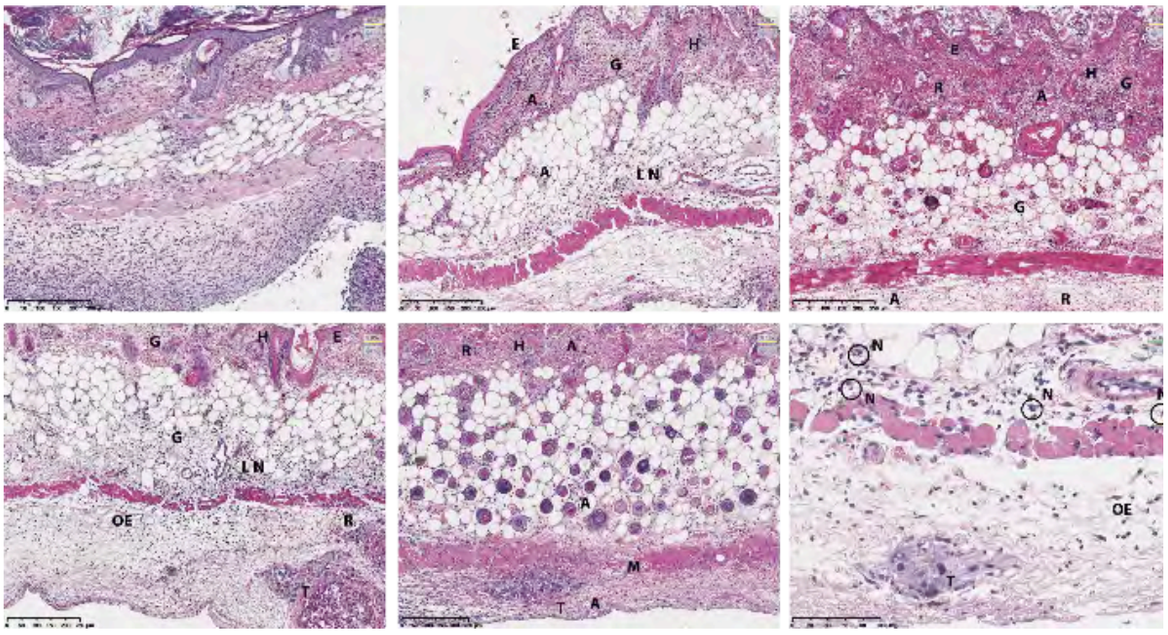

Figure 7.9: *histological PDT-induced tissue effects. a) control no treatment. b) Group 2 ce6 5 hours. c) Group 4 ce6 24 hours. d) Group 1 Bremachlorin 5 hours. e) Group 3 Bremachlorin 24 hours. All magnifications 100x f) Group 3, 300x magnification. Infiltrate consist of both lymphocytes and neutrophils. Arrows indicate abnormal histological structures: (E) loss of cell structure in epithelium (A) apoptotic bodies (H) damaged hair follicle (R) extravagated red blood cells (T) tumor tissue (N) neutrophils (L) lymphocytes (OE) edema (Gen) general loss of tissue structure (M) muscle damage.*

Typical pathological characteristics for PDT induced damage are the presence of interstitial inflammatory infiltrate consisting of polymorphonuclear cells (neutrophils and eosinophils) and mononuclear cells (lymphocytes, monocytes, and plasma cells) in the tissue, apoptotic bodies, necrosis-related homogenization of the tissue structure and loss of cell borders, the loss of cell adhesion, damaged cells and edema. Vascular damage is indicated by red blood cell extravasation throughout the tissue. The vitality of the tumor after PDT is determined based on damaged tumor cells, infiltration of lymphocytes and neutrophils, the presence of red blood cells, apoptotic bodies and the observation of pyknotic nuclei and eosinophilic homogeneous cytoplasm.

Figure 7.9 shows some typical examples of PDT affected normal and tumor tissue in relation to a section of a control animal. Figure 7.9a shows histological state of a window chamber. Some inflammatory infiltration can be seen in the upper dermis and the fascia. The epidermis was completely intact and hair follicles and sebaceous glands were present throughout the whole dermis. The lower dermis (adipose cell layer) showed intact cells, which were closely connected to each other. The muscle layer was continuous and showed the striped pattern characteristic for cutaneous muscle.

Homogenization of the tissue structure in the epithelial layer for PDT treated animals (figure 7.9b-e) was observed, indicated by the loss of hematoxylin staining and recognizable cellular shapes. This effect was reported in 12 PDT treated animals, which included all animals treated in group 3, and half of the animals in group 1, 2 and 4. Most of these animals combined the loss of cell structures in the epidermis with damaged hair follicles and sebaceous glands. The observation of a severed epithelial layer was in most cases linked to abnormal tissue histology in dermis and adipose layer as well.

PDT related damage to the upper dermis included inflammatory infiltrate, both lymphocytes and neutrophils, edema, clusters of apoptotic bodies and extravasation of red blood cells throughout the tissue. The extravasation of RBCs, indicating hemorrhages and/or leaking vasculature, appeared more often after treatment with a 24 hour drug-light interval for both photosensitizers.

The lower dermis (adipose cell layer) showed the most PDT related damage when animals were treated with a 24 hour drug-light interval (group 3 and 4). This included the loss of the characteristic round shape of the adipose cells (as in figure 7.9c), infiltrate and apoptotic bodies through the whole layer. Animals treated with a 5 hour drug-light interval (groups 1 and 2) showed an increase in inflammatory infiltrate compared to the normal reaction to the window chamber, and some animals showed the presence of edema.

The normal structure of the cutaneous muscle was partially lost in three of the four animals in group 3. Other groups did not show any abnormal muscle tissue, except from some edema around the muscle fibers. The fascia of three animals showed some edema, while in three other animals, all part of group 3 or 4, we observed extravasation of RBCs, apoptosis and loss of cell structure in the fascia.

To determine the vitality of the tumor after PDT, tumor tissue in the histological sections was analyzed. Viability of tumor and/or normal tissue was determined in histological sections from 23 animals (in four animals harvesting of tissue two days after illumination was not possible). In 15 samples tumor tissue was identified in the sections under analysis, from which three were unaffected control animals. In only six of the remaining 12 mice vital tumor tissue was observed.

An overview of the impact of PDT on normal and tumor tissue for the different treatment schemes is shown in table 7.1. The percentage of animals per group that showed PDT effects in normal or tumor tissue is shown. Animals categorized as having affected normal tissue showed PDT-related deviation from normal tissue histology, as described above. In mice having affected tumor tissue the tumor did show only little vital tumor cells. The PDT-induced histological abnormalities in both normal and tumor tissue were more severe when the illumination was performed after a 24 hour drug-light interval for both photosensitizers. Ce6 PDT with a 5 hour drug-light interval was least effective in causing damage, both in normal and tumor tissue. None of the four tumors present appeared to be affected by PDT, while two of the four animals showed PDT-induced histological markers in normal tissue. We did not observe selective tumor damage, in which normal tissue was still intact but tumor tissue was destroyed.

Table 7.1: *Overview of microscopic tissue damage 2 days after PDT*

Photo-sensitizer	***Drug-light interval (h)***	***Animals with affected normal tissue (%)***	***N (affected : total)***	***Animals with affected tumor tissue (%)***	***N (affected : total)***
Bremachlorin	5	67	4 : 6	60	3 : 5
Bremachlorin	24	100	4 : 4	100	2 : 2
Chlorin e_6	5	50	2 : 4	0	0 : 4
Chlorin e_6	24	80	4 : 5	100	1 : 1

DISCUSSION

In this paper we have investigated PDT induced damage on OSC19 tumor in dorsal window chambers in mice. The photosensitizers under investigation are Bremachlorin and ce6, and drug-light intervals of 5 and 24 hours are applied. Previous findings on photosensitizer pharmacokinetics suggest that long drug-light intervals may result in more effective PDT. Here we showed that illuminating 24 hours after photosensitizer administration was more effective than a 5 hour drug-light interval in causing vascular and tissue responses for both ce6 and Bremachlorin. Furthermore, Bremachlorin caused an increase in acute vascular effects during PDT illumination compared to ce6, together with more evidence of microscopically and macroscopically PDT-induced tissue damage two days after illumination.

ACUTE EFFECTS OF PDT IN THE DORSAL SKINFOLD WINDOW CHAMBER

During the therapeutic illumination we were able to detect acute vascular and tissue response by imaging the vasculature and tissue in the window chamber. We observed constriction of arteries and venules, some constrictions lasted for at least 2 hours, other constricted arteries relaxed within 2 hours. Relaxation of the vessel lumen during PDT has been observed previously by Fingar et al. [53] during Photofrin PDT using a 24 hour drug-light interval. In the present study, two animals showed severe hemorrhage in the window chamber during illumination. Direct vascular effects were most often observed in animals treated with Bremachlorin using a 24 hour drug-light interval, and ce6 with a 5 hour drug-light interval.

Even though it is known from previous studies that the amount of Bremachlorin present in the vasculature is highest after short incubation times [44], the acute vasoconstriction and tissue displacement that we observe for Bremachlorin in the present study are more pronounced using a 24 hour drug-light interval. Furthermore, the investigation of the response of the vasculature 2 hours following PDT using confocal microscopy combined with the injection of a fluorescent dye in the vasculature showed vascular leakage and stasis. These effects were observed for both ce6 and Bremachlorin, but were more pronounced for 24 and 5 hours Bremachlorin PDT, where all animals under investigation showed leakage and/or stasis. Our results are contrary to the absence of vascular constriction reported in a study by McMahon et al. on the effect of NPe6 PDT on vasculature in the rat cremaster muscle using a 4 and 24 hour drug-light interval [27]. The complete vascular stasis as reported by McMahon does correspond with our observations, although we observed similar results in the groups with both the 4 hour and 24 hour drug-light interval. It is hypothesized that platelets are damaged by PDT and play

a role in the induction of stasis, as previously described for ALA-PDT [54] and Photofrin PDT [55].

A number of animals showed severe muscle contraction in the window chamber that caused displacement of the vasculature and in some cases the tumor. In two cases this included the dislocation of the fascia relative to the (epi)dermal layer. This movement suggests that the cutaneous muscle layer was strongly affected during the PDT illumination. Although the mechanism behind this muscle activation is unknown, it is a well known effect that arteries, including their muscle layer, often constrict as a acute response to PDT [56]. We have previously observed severe muscle spasms during the treatment of anal intraepithelial neoplasia using systemic mTHPC [1], which also suggests a reaction of muscle fibers as a PDT related effect. The activation of muscle fibers during PDT is probably related to the presence of Bremachlorin and ce6 that we have previously observed in OSC19 tumors in muscle after a 24 hour drug-light interval [45].

HISTOLOGICAL EFFECTS AFTER PDT AT 48 HOURS

The microscopic observations on histological PDT-induced effects made two days after illumination corresponded with what has previously been reported [57, 58] in humans. PDT results in a combination of apoptotic and necrotic cell death. In PDT treated animals, we observed signs of apoptotic and necrotic cell death in normal tissue in 15 of the 19 chambers. In tumor tissue, apoptotic and necrotic markers were only observed in 6 of the 12 sections containing tumor material. Animals treated after a 24 hour drug-light interval showed more cell-kill related effects than those treated 5 hours after photosensitizer administration. Although the probability of PDT effects in normal or tumor tissue is higher in animals showing acute vascular effects after illumination, we found no clear relation between the two. It should be noted that we analyzed six tissue sections per chamber, with an equal intermittent histological slice separation. How these locations correspond with the regions of interest showing vasoconstriction or tissue movement during PDT is unknown and small tumors may not have always been included in our analysis of histological sections.

There appears to be no correlation between vascular effects during or 2 hours after illumination and the histological response 48 hours after illumination. Analysis showed most histological characteristics of direct cell damage, both for tumor and normal tissue cells, for 24 hour incubation time for both Bremachlorin and ce6. This is in contrast with what might be expected for ce6. Apparently, the very low concentration of ce6 present 24 hours after administration was sufficient to evoke significant PDT induced effects.

Previous studies have reported that the efficacy of PDT is greater when it is applied using short drug-light intervals. It is important to note that in the present study we have only investigated the histological tissue response after two days, while tumor re-growth may be a better assessment of treatment efficacy. McMahon et al. [27] have reported similar tissue response for both 4 and 24 hour incubation times in NPe6-PDT after 48 hours, only to show tumor regrowth for the 24 hour group.

The relationship between acute vascular effects and histological PDT effects is relevant, since it provides an indication of tumor vitality. Analysis of acute vascular effects in animals from which we were able to determine histological PDT effects on normal and tumor cells showed that in 4 out of 6 and 10 out of 15 animals we observed both vascular effects and histological damage to tumor and normal cells respectively. Similarly, from the animals that did not show histological indications of apoptosis or necrosis to tumor or normal tissue, respectively 4 out of 6 and 3 out of 4 animals did not show any acute vascular effects. Therefore, although not significant, the observation of acute vascular effects during PDT illumination correlates with PDT induced tissue damage on a microscopic level.

Microscopic analysis of the cutaneous muscle layer did in most cases not show direct response in muscle fibers. Only two animals showed a disruption of the layer, although edema and inflammatory infiltrate were in more cases observed around the bundles. If pharmacokinetics in skin compare with those observed in the tongue [44, 45], muscle fiber should contain a relatively high concentration of photosensitizer, but does not appear to be substantially affected. The valid theory for ALA-PDT suggests that muscle fibers are more susceptible for PDT damage than epithelial layers surrounding it [59] which results in intact epithelial layers on top of severely damaged musculature in the esophagus. For ce6-PDT however, this theory does not seem to apply.

COMPARISON WITH PREVIOUS EXPERIMENTS

We have recently reported on the pharmacokinetics of Bremachlorin and ce6 in OSC19 tumors in the mouse tongue [44, 45]. We showed that the amount of photosensitizer present is highest in the tumor border, while the concentration in normal and tumor tissue is much lower. It is only after incubation times of 24 hours or longer that the concentration in normal tongue tissue becomes lower than in tumor tissue. Although ce6 is at those time points almost completely metabolized and cleared from tissue, Bremachlorin is still present in significant amounts. When comparing in-vivo intrinsic fluorescence measurements using single fiber fluorescence spectroscopy (SFF) [44] and ex-vivo analysis of tongue sections using confocal microscopy, the decrease over time

found in microscopic sections was much smaller than in SFF measurements. Therefore, it has been hypothesized that most of the photosensitizer is present in the vasculature after short incubation times.

Although specific tumor targeting of PDT effects was not observed, it is clear that 24 hour incubation time induced more effect than 5 hours did. Even ce6, which was mostly metabolized at 24 hours after administration, showed acute vascular effects during and tissue damage after illumination at late time points, more so than observed after a 5 hour incubation time.

The study presented in this paper was designed to show PDT-effects related to cell death after treatment of an oral squamous cell carcinoma. In this study, the mouse dorsal skinfold chamber was our model of choice, due to its accessibility and visualizing ability during imaging. Although this study was designed based on pharmacokinetics in the tongue, it provides us with important insights into PDT in OSC19 tumors in general. Since the induction of the tumor in a different, non-orthotopic environment may result in different pharmacokinetics, these insights could not automatically assumed to be true for OSC19 tumors in tongue. The next step in the investigation of long drug-light interval Bremachlorin and ce6 PDT of oral squamous cell carcinoma will be performing PDT an orthotopic model, where PDT efficacy is determined based on growth delay. However, execution of growth delay studies is complicated by the large natural variability present in biological tissue and treatment response. Analysis of acute PDT response as performed in this study provides us with insights that cannot easily be derived from growth delay studies.

IMPLICATIONS FOR CLINICAL USE

Based on in-vivo pharmacokinetic studies, ce6-based photosensitizers are (pre-)clinically used in combination with a short drug-light interval of around 5 hours [13]. However, most studies apply a ce6-based conjugate to reduce the hydrophilicity of pure ce6 and increase cellular internalization. Bremachlorin consists of a solution in which pure ce6 is the photo-active substance. This and previous studies showed that when using Bremachlorin as photosensitizer, investigation of drug-light intervals in the order of days is worthwhile.

CONCLUSION

For the photosensitizer mixture Bremachlorin and, to a lesser extend, ce6, most PDT-related effects were observed after a 24 hour incubation time. This was the case for acute vascular effects during PDT and 2 hours after PDT, and histological analysis of PDT treated tissue 48 hours after illumination. These findings are in contrast with current (pre-)clinical

practice, in which mostly short drug-light intervals are used for PDT with ce6-based photosensitizers, based on the much higher concentration photosensitizer present at those time points. How the observation of PDT-effects after 48 hours relates to tumor reduction and/or cure is the topic of future research.

REFERENCES

1. van der Snoek, E.M., et al., *Photodynamic therapy with systemic meta-tetrahydroxyphenylchlorin in the treatment of anal intraepithelial neoplasia, grade 3.* Lasers in surgery and medicine, 2012. **44**(8): p. 637-644.
2. Karakullukcu, B., et al., *mTHPC mediated interstitial photodynamic therapy of recurrent nonmetastatic base of tongue cancers: Development of a new method.* Head & neck, 2012. **34**(11): p. 1597-1606.
3. Babilas, P., et al., *Photodynamic therapy in dermatology: state-of-the-art.* Photodermatology, photoimmunology & photomedicine, 2010. **26**(3): p. 118-132.
4. Pech, O., et al., *Long-term results of photodynamic therapy with 5-aminolevulinic acid for superficial Barrett's cancer and high-grade intraepithelial neoplasia.* Gastrointestinal endoscopy, 2005. **62**(1): p. 24-30.
5. Dougherty, T.J., et al., *Photodynamic therapy.* Journal of the National Cancer Institute, 1998. **90**(12): p. 889-905.
6. Mroz, P., et al., *Cell death pathways in photodynamic therapy of cancer.* Cancers, 2011. **3**(2): p. 2516-2539.
7. Kennedy, J., R. Pottier, and D. Pross, *Photodynamic therapy with endogenous protoporphyrin: IX: basic principles and present clinical experience.* Journal of Photochemistry and Photobiology B: Biology, 1990. **6**(1): p. 143-148.
8. Usuda, J., et al., *Increased cytotoxic effects of photodynamic therapy in IL-6 gene transfected cells via enhanced apoptosis.* International journal of cancer, 2001. **93**(4): p. 475-480.
9. Buytaert, E., M. Dewaele, and P. Agostinis, *Molecular effectors of multiple cell death pathways initiated by photodynamic therapy.* Biochimica et Biophysica Acta (BBA)-Reviews on Cancer, 2007. **1776**(1): p. 86-107.
10. Kessel, D., M.G.a.H. Vicente, and J.J. Reiners, *Initiation of apoptosis and autophagy by photodynamic therapy.* Lasers in surgery and medicine, 2006. **38**(5): p. 482-488.
11. Sasnauskiene, A., et al., *Apoptosis, autophagy and cell cycle arrest following photodamage to mitochondrial interior.* Apoptosis, 2009. **14**(3): p. 276-286.
12. Bozzini, G., et al., *Photodynamic therapy in urology: What can we do now and where are we heading?* Photodiagnosis and photodynamic therapy, 2012. **9**(3): p. 261-273.
13. Chan, A.L., et al., *Pharmacokinetics and clinical effects of mono-L-aspartyl chlorin e6 (NPe6) photodynamic therapy in adult patients with primary or secondary cancer of the skin and mucosal surfaces.* Photodermatology, photoimmunology & photomedicine, 2005. **21**(2): p. 72-78.
14. Dolmans, D.E., D. Fukumura, and R.K. Jain, *Photodynamic therapy for cancer.* Nature Reviews Cancer, 2003. **3**(5): p. 380-387.
15. Kessel, D., et al., *The role of subcellular localization in initiation of apoptosis by photodynamic therapy.* Photochemistry and photobiology, 1997. **65**(3): p. 422-426.
16. Mitra, S. and T.H. Foster, *In vivo confocal fluorescence imaging of the intratumor distribution of the photosensitizer mono-L-aspartylchlorin-e6.* Neoplasia (New York, NY), 2008. **10**(5): p. 429.
17. Cramers, P., et al., *Foscan uptake and tissue distribution in relation to photodynamic efficacy.* British journal of cancer, 2003. **88**(2): p. 283-290.
18. Gomer, C.J. and A. Ferrario, *Tissue distribution and photosensitizing properties of mono-L-aspartyl chlorin e6 in a mouse tumor model.* Cancer research, 1990. **50**(13): p. 3985-3990.

19. Roberts, W.G. and M.W. Berns, *In vitro photosensitization I. Cellular uptake and subcellular localization of mono-L-aspartyl chlorin e6, chloro-aluminum sulfonated phthalocyanine, and photofrin II.* Lasers in surgery and medicine, 1989. **9**(2): p. 90-101.

20. Roberts, W.G. and T. Hasan, *Role of neovasculature and vascular permeability on the tumor retention of photodynamic agents.* Cancer research, 1992. **52**(4): p. 924-930.

21. Mojzisova, H., et al., *Cellular uptake and subcellular distribution of chlorin e6 as functions of pH and interactions with membranes and lipoproteins.* Biochimica et Biophysica Acta (BBA)-Biomembranes, 2007. **1768**(11): p. 2748-2756.

22. Cunderlíková, B., et al., *Increased binding of chlorin e6 to lipoproteins at low pH values.* The International Journal of Biochemistry & Cell Biology, 2000. **32**(7): p. 759-768.

23. Chen, B., et al., *Combining vascular and cellular targeting regimens enhances the efficacy of photodynamic therapy.* International Journal of Radiation Oncology* Biology* Physics, 2005. **61**(4): p. 1216-1226.

24. de Bruijn, H.S., et al., *Microscopic localisation of protoporphyrin IX in normal mouse skin after topical application of 5-aminolevulinic acid or methyl 5-aminolevulinate.* 2008. **92**(2): p. 91-97.

25. de Vijlder, H.S., et al., *Acute Vascular Responses during Photodynamic Therapy using Topically Administered Porphyrin Precursors.* Photochemical & Photobiological Sciences, 2013. **In press**.

26. van Leeuwen - van Zaane, F., et al., *The Effect of Fluence Rate on the Acute Response of Vessel Diameter and Red Blood Cell Flow Velocity during Topical 5-Aminolevulinic Acid Photodynamic Therapy.* Photodiagnosis and photodynamic therapy, 2014. **In press**.

27. McMahon, K.S., et al., *Effects of photodynamic therapy using mono-L-aspartyl chlorin e6 on vessel constriction, vessel leakage, and tumor response.* Cancer research, 1994. **54**(20): p. 5374-5379.

28. de Bruijn, H.S., et al., *Fractionated illumination after topical application of 5-aminolevulinic acid on normal skin of hairless mice: The influence of the dark interval.* Journal of Photochemistry & Photobiology, B: Biology, 2006. **85**(3): p. 184-190.

29. Sitnik, T.M. and B.W. Henderson, *The effect of fluence rate on tumor and normal tissue responses to photodynamic therapy.* Photochemistry and photobiology, 1998. **67**(4): p. 462-466.

30. Henderson, B.W., T.M. Busch, and J.W. Snyder, *Fluence rate as a modulator of PDT mechanisms.* Lasers in surgery and medicine, 2006. **38**(5): p. 489-493.

31. Kostenich, G., I. Zhuravkin, and E. Zhavrid, *Experimental grounds for using chlorin e6 in the photodynamic therapy of malignant tumors.* Journal of Photochemistry and Photobiology B: Biology, 1994. **22**(3): p. 211-217.

32. Chin, W.W.L., et al., *Fluorescence imaging and phototoxicity effects of new formulation of chlorin e6-polyvinylpyrrolidone.* Journal of Photochemistry and Photobiology B: Biology, 2006. **84**(2): p. 103-110.

33. Nakagawa, H., et al., *Expression of vascular endothelial growth factor by photodynamic therapy with mono-l-aspartyl chlorin e6 (NPe6) in oral squamous cell carcinoma.* Oral oncology, 2007. **43**(6): p. 544-550.

34. Moy, W.J., et al., *Preclinical in vivo evaluation of Npe6-mediated photodynamic therapy on normal vasculature.* Lasers in surgery and medicine, 2012. **44**(2): p. 158-162.

35. Kato, H., et al., *Phase II clinical study of photodynamic therapy using mono-L-aspartyl chlorin e6 and diode laser for early superficial squamous cell carcinoma of the lung.* Lung Cancer, 2003. **42**(1): p. 103-111.

36. O'Connor, A.E., W.M. Gallagher, and A.T. Byrne, *Porphyrin and nonporphyrin photosensitizers in oncology: preclinical and clinical advances in photodynamic therapy.* Photochemistry and photobiology, 2009. **85**(5): p. 1053-1074.

37. Taber, S.W., et al., *Photodynamic therapy using mono-L-aspartyl chlorin e6 (Npe6) for the treatment of cutaneous disease: a Phase I clinical study.* Clinical cancer research, 1998. **4**(11): p. 2741-2746.

38. Douillard, S., D. Olivier, and T. Patrice, *In vitro and in vivo evaluation of Radachlorin sensitizer for photodynamic therapy.* Photochemical & Photobiological Sciences, 2009. **8**(3): p. 405-413.

39. Chin, W.W.L., et al., *Effect of polyvinylpyrrolidone on the interaction of chlorin e6 with plasma proteins and its subcellular localization.* European Journal of Pharmaceutics and Biopharmaceutics, 2010. **76**(2): p. 245-252.

40. Bae, S.-M., et al., *Photodynamic Effects of Radachlorin on Cervical Cancer Cells.* Cancer Research and Treatment, 2004. **36**(6): p. 389-394.

41. Ji, W., et al., *The effect of Radachlorin PDT in advanced NSCLC: A pilot study.* Photodiagnosis and photodynamic therapy, 2013. **10**(2): p. 120-126.

42. Privalov, V.A., et al. *Clinical trials of a new chlorin photosensitizer for photodynamic therapy of malignant tumors*. in *Proc. SPIE 4612, Optical methods for tumor treatment and detection: mechanisms and techniques in photodynamic therapy XI*. (2002), International Society for Optics and Photonics, p. 178-189.

43. Kochneva, E.V., et al., *Photosensitizer Radachlorin: Skin cancer PDT phase II clinical trials.* Photodiagnosis and photodynamic therapy, 2010. **7**(4): p. 258-267.

44. van Leeuwen - van Zaane, F., et al., *Intrinsic photosensitizer fluorescence measured using multi-diameter single fiber spectroscopy in-vivo.* Journal of biomedical optics, 2014. **19**(1): p. 015010.

45. van Leeuwen - van Zaane, F., et al., *Microscopic Analysis of the Localization of Two Chlorin-Based Photosensitizers in OSC19 Tumors in the Mouse Oral Cavity.* Lasers in Surgery and Medicine, 2014. **In press**.

46. Falkvoll, K., et al., *A transparent chamber for the dorsal skin fold of athymic mice.* Pathobiology, 1984. **52**(4): p. 260-268.

47. Papenfuss, H.D., et al., *A transparent access chamber for the rat dorsal skin fold.* Microvascular research, 1979. **18**(3): p. 311-318.

48. Seynhaeve, A.L., et al., *Tumor necrosis factor alpha mediates homogeneous distribution of liposomes in murine melanoma that contributes to a better tumor response.* Cancer research, 2007. **67**(19): p. 9455-9462.

49. van Leeuwen - van Zaane, F., et al., *In vivo quantification of the scattering properties of tissue using multi-diameter single fiber reflectance spectroscopy.* Biomedical optics express, 2013. **4**(5): p. 696-708.

50. Yokoi, T., et al., *Establishment and characterization of a human cell line derived from a squamous cell carcinoma of the tongue.* 1988.

51. Carlotti, F., et al., *Lentiviral vectors efficiently transduce quiescent mature 3T3-L1 adipocytes.* 2004. **9**(2): p. 209-217.

52. Mezzanotte, L., et al., *Evaluating reporter genes of different luciferases for optimized in vivo bioluminescence imaging of transplanted neural stem cells in the brain.* Contrast Media & Molecular Imaging, 2013. **8**(6): p. 505-513.

53. Fingar, V.H., et al., *The role of microvascular damage in photodynamic therapy: the effect of treatment on vessel constriction, permeability, and leukocyte adhesion.* Cancer research, 1992. **52**(18): p. 4914-4921.

54. Zieve, P.D., H.M. Solomon, and J.R. Krevans, *The effect of hematoporphyrin and light on human platelets. I. Morphologic, functional, and biochemical changes.* Journal of cellular physiology, 1966. **67**(2): p. 271-279.

55. Henderson, B., et al., *Effects of photodynamic treatment of platelets or endothelial cells in vitro on platelet aggregation.* Photochemistry and photobiology, 1992. **56**(4): p. 513-521.

56. Gilissen, M.J., et al., *Effect of photodynamic therapy on the endothelium-dependent relaxation of isolated rat aortas.* Cancer research, 1993. **53**(11): p. 2548-2552.

57. Fantini, F., et al., *Pathologic changes after photodynamic therapy for Basal cell carcinoma and Bowen disease: a histologic and immunohistochemical investigation.* Archives of dermatology, 2008. **144**(2): p. 186-194.

58. Tosca, A.D., et al., *Photodynamic treatment of skin malignancies with aminolevulinic acid.* Dermatologic surgery, 1996. **22**(11): p. 929-934.

59. Van den Boogert, J., et al., *Timing of illumination is essential for effective and safe photodynamic therapy: a study in the normal rat oesophagus.* British journal of cancer, 1999. **79**(5/6): p. 825-830.

chapter 8

Discussion

Floor van Leeuwen – van Zaane

GENERAL DISCUSSION

This thesis focuses on the application of quantitative fiber optic spectroscopy and optical imaging techniques to provide an insight into various PDT-related processes, which can contribute to the optimization of photodynamic therapy. It can be divided into three principle sections.

- The investigation of the relationship between vascular responses during light fractionated ALA-PDT and treatment efficacy using optical imaging and spectroscopy.
- The development of quantitative fiber optic fluorescence spectroscopy and its application in measuring in-vivo photosensitizer pharmacokinetics.
- A comparison of the pharmacokinetics and spectral properties of chlorin e_6 and Bremachlorin based on in-vivo measurements and their relationship to PDT efficacy.

The primary goal is to use results from these investigations to optimize treatment protocols for PDT with the aim of maximizing treatment efficacy and minimizing side effects. Although this thesis only covers preclinical research, it demonstrates the first in-vivo implementation of fully quantitative reflectance and fluorescence fiber optic spectroscopy. The next translational step: fully quantitative clinical spectroscopy would clearly benefit clinical PDT research.

This chapter provides the reader with a general discussion of conclusions of the individual studies, how they relate to each other and how they relate to the overall goal of optimization of PDT.

INVESTIGATION OF THE ROLE OF THE FIRST LIGHT FRACTION IN LIGHT FRACTIONATED ALA-PDT

In **chapter 2** and **chapter 3** the extensive research on light fractionated ALA-PDT that has been carried out over the last two decades is extended. Interest in light fractionated ALA-PDT was piqued by the clinical observation that PpIX fluorescence re-appeared after therapeutic illumination [W.M. Star, personal communication]. This led to numerous studies investigating (a) the mechanism(s) underlying light fractionation and (b) how efficacy might be maximized by changing the length of the dark interval and light treatment parameters. Preclinical results applying this treatment protocol have been promising [1]. It has been shown that the increase in response is highest when a low dose fraction is followed by a 2 hour dark interval and a subsequent high dose fraction [2]. The

choice of fluence (rate) for the first fraction has been shown to be critical. The increased effect of light fractionated ALA-PDT was subsequently confirmed in a clinical study of treatment of superficial basal cell carcinomas [3]. The exact mechanism(s) underlying the increased response are still under investigation, but we have shown that cells are rendered sensitive to the second light fraction by a *small* PDT dose and a 2 hour dark interval [4]. This is the reason why the light treatment parameters of the first light fraction and their influence on the acute physiological response to PDT are critical.

The higher efficacy of a low dose first fraction over a high dose first fraction may be explained by the onset of vascular constriction early in the treatment, which then has the chance to recover during the dark interval. Vasoconstriction is thought to be caused by rapid oxygen depletion during the first few minutes of PDT and therefore a lower fluence rate is expected to lead to less or slower vasoconstriction. When the vasculature is damaged, the oxygen supply to the target tissue is severed and PDT is rendered ineffective. Therefore, it would be expected that lower fluence rates increase the efficacy of fractionated PDT even more. An additional advantage of using low fluence PDT is the reduced pain experienced by the patient. ALA-PDT is known to be very painful during treatment, which in some cases leads to discontinuation of the treatment. It has been reported that illumination with a lower fluence rate results in less painful side effects [5].

In **chapter 2** we compare PDT damage to normal tissue for various fractionated PDT illumination protocols, including 20 and 50 mW cm^{-2}. This study confirms the increased damage of fractionated PDT over a single illumination and demonstrates the importance of the choice of fluence as the fluence rate is reduced.

In **chapter 3** the focus lies on a thorough investigation of the onset of vasoconstriction during the first fraction of PDT. Fluence rates of 26, 65 and 130 mW cm^{-2} (corresponding to 20, 50 and 100 mW cm^{-2} corrected for green vs. red laser light photon energy) are investigated. Although vasoconstriction is observed, these observations are present in all three groups. A control group without ALA application does not show vasoconstriction. The results of these two studies suggest that fluence rate does not play a key role in occurrence of vascular effects and the increased efficacy of fractionated PDT.

Although low fluence rate 20 mW cm^{-2} PDT may not result in increased tissue damage and vasoconstriction, it does not differ significantly in damage from 50 mW cm^{-2}, which is currently used clinically for the treatment of superficial basal cell carcinomas. The positive effect of decreasing the fluence rate to 20 mW cm^{-2} is that it is suggested to reduce the pain patients experience when undergoing treatment [5]. However, decreasing fluence rate from 50 mW cm^{-2} to 20 mW cm^{-2} while simultaneously achieving the same total dose is clinically unfeasible due to the 2.5 times longer illumination time (given an identical fluence of 100 J cm^{-2}). **Chapter 2** shows that when using a fluence rate

of 20 mW cm^{-2} a total dose of 50 J cm^{-2} leads to similar tissue damage as 100 J cm^{-2}. Therefore, with only a small increase in clinical illumination time it may be feasible to reduce the pain patients experience during treatment. Although clinical research is required to confirm the decrease in pain sensation while maintaining treatment efficacy, these results may lead to a significant improvement in how patients experience ALA-PDT.

Recently it is discovered in-vitro that cells incubated with low concentrations of ALA show enhanced cell death after light fractionated PDT over incubation with high ALA concentrations [4]. It is suggested that the delivery of a small PDT dose followed by a dark interval will bring the tumor cells in a pre-lethal phase making them more vulnerable for death by apoptosis or autophagy. PpIX concentrations measured in the dermis in general and dermal epithelial cells in particular are low, but may therefore be more vulnerable for light fractionated PDT. A possible application of this result is to use the amount of PpIX synthesis as a measure for the optimum drug-light interval compared to the predetermined two hours period that is currently used in the clinic. Intrinsic fluorescence measurements by single fiber fluorescence spectroscopy (SFF) could be used in this context to monitor PpIX fluorescence before and during treatment. Recently, spectroscopic measurements of PpIX using SFF have been performed during clinical ALA-PDT of actinic keratosis [T. Middelburg, manuscript submitted]. It should be noted that it is probably not feasible to determine small differences in localization associated with differences in PpIX between dermal tissue and endothelial cells.

DEVELOPMENT OF QUANTITATIVE IN-VIVO FLUORESCENCE SPECTROSCOPY

Fluorescence spectroscopy is under investigation both as a diagnostic tool and as a method for monitoring a number of therapeutic modalities. The (semi-)quantification of fluorescent drugs in various tissue types is one of the major applications of in-vivo fluorescence spectroscopy and is widely incorporated in PDT research and in clinical practice. Despite the potential usefulness of in-vivo fluorescence spectroscopy, the exact quantification of fluorescent signals is complicated by the effect of tissue optical properties on light. This thesis therefore focuses on intrinsic fluorescence, where the influence of those tissue optical properties is removed from the measured fluorescence spectrum and which can be related to fluorophore concentration. Intrinsic fluorescence enables quantitative measurement of fluorescence intensity and spectral shape in tissues with different and/or varying optical properties. A limiting factor in determining the intrinsic fluorescence in-vivo up to now has been the need for quantitative information on tissue scattering properties. With the development of multi-diameter single fiber reflectance spectroscopy (MDSFR), a method is now available to determine these

scattering properties, and -with minimal adaptation of the device- intrinsic fluorescence measurements are feasible.

Chapter 4 reports on the first in-vivo demonstration of MDSFR. In-vivo values for scattering power are determined for four different tissues, together with the scattering phase function parameter γ. This illustrates the potential for the use of optical spectroscopy as diagnostic tool to discriminate tissue types. Although the skin types compared in this thesis are easily distinguishable even without the inclusion of MDSFR, the development of this method paves the way for the possibility to discriminate normal from dysplastic tissue. This application is very promising in, among other things, selecting biopsy sites to prevent the taking of false negative biopsies, or for first line health care providers to use optical diagnostics to determine referral of patients with suspect lesions in the skin or in the oral cavity and oropharynx.

The physical interpretation of reduced scattering and especially γ are difficult. Scattering of light is caused by changes in refractive index between the different cellular and intracellular compartments in tissue. It should therefore theoretically be possible to relate scattering to morphological parameters as size and shape of scatterers. Tumor morphology differs significantly from that of normal tissue, which makes scattering a potentially diagnostic tool. Recently, research in this area has shifted towards the consideration of the refractive index correlation function, which is modeled by the Whittle-Matérn correlation function [6]. This is a generic phase function model, of which the often used Henyey-Greenstein phase function is one of the possible solutions. The Whittle-Matérn correlation function contains three variables: the deterministic factor D, the length scale of the correlation l_c, and the scaling factor N_c. While the scattering power is directly related to the deterministic factor D, the length scale of the correlation l_c is related to both μ_s' and γ. It is possible to express γ and its wavelength dependence in terms of l_c and use the combined measurements of μ_s' and γ to calculate the physical properties of the correlation function, D and l_c. Knowledge on D and l_c can be related to morphological features, which enables spectroscopic measurements to provide information on tissue micro- and ultrastructure. In early carcinogenesis, tissue undergoes small-scale morphological and architectural changes that occur even before histological abnormalities become apparent. By characterizing the effects of light scattering, these changes may be detectable [7]. The changes may even be present beyond the site of the lesion [8].

Extending MDSFR to fluorescence spectroscopy requires the addition of an excitation laser, two extra bifurcations of the fiber and a separate spectrograph equipped with a filter to block excitation light. A semi-empirical model is developed in which the contribution of tissue scattering and absorption to the fluorescence signal is determined

and removed, which provides the intrinsic fluorescence. This process is described and applied in **chapter 5**. When discriminating between the influence of scattering and absorption, it is observed that the absorption correction is responsible for a spectral correction while scattering correction mainly results in an adaptation of the fluorescence intensity.

The intrinsic fluorescence as outcome of SFF measurements is wavelength dependent and proportional to the product of the fluorophore quantum yield and absorption at the excitation wavelength. This can be easily linked to fluorophore concentration when fluorophore quantum yield and its absorption spectrum are known. When measuring fluorescence in vivo, fluorophore concentration is much harder to obtain, since both quantum yield and absorption of the fluorophore can be dependent on environmental factors such as pH. **Chapter 5** therefore focuses on the measurement of the intrinsic fluorescence $Q^f\mu_a{}^f$.

The fluorescence measurements presented in this thesis are still based on subsequent measurements with two different fiber diameters on the same location. This situation is not ideal; repositioning of fibers inevitably leads to a variation in measurement volume between both fibers. The development of a fiber bundle probe to partially overcome this problem is in progress, where measurements can be done without replacing the probe. Probe design is based on a coherent fiber bundle acting as a single fiber with a variable diameter [9]. It is obvious that measurement volumes of measurements performed with different fiber diameters are never exactly the same. But the coherent fiber bundle allows for inclusion of the complete small diameter volume into the large diameter volume, which is a vast improvement over the repositioning of a different fiber as applied in **chapter 5** of this thesis. Before finalization of the coherent fiber bundle, two intermediate solutions have been used in (pre-)clinical investigations. The first being a probe with two adjacent fibers very close to each other, which removed the variation in localization between fibers. Second, a probe with three concentric rings – imitating fiber diameters - containing a total of 19 fibers is used, which has the advantage of having the measurement volume of the small fiber diameter included in the volume of larger fiber diameters [10]. First results of liquid phantom sample measurements use with the coherent fiber bundle are promising, but a carefully designed robust and often repeated calibration procedure appears critical. Slight variations in fiber positioning or laser output result in significant variations in measured fluorescence.

The dependency on calibration is expected to also be an important factor for the SFF procedure described in **chapter 5**. Its influence is somewhat overshadowed by the relocation of fibers and consecutive averaging of measurements. Furthermore, the variations in calibration are mainly distinguishable as variations in intensity; spectral

deviations are not expected to originate from this calibration error. However, the design of a stable system configuration and a validated and robust calibration method are critical factors for the correct use of SFF measurements.

The introduction of intrinsic fluorescence as the parameter of choice when performing in-vivo fluorescence measurements allows for quantification of fluorophore concentration. The determination of photosensitizer in a PDT treatment volume is an important application of SFF in a clinical environment. Initial photosensitizer concentration and the rate of photobleaching during treatment provide important information that could potentially help in determining a patient-dependent optimal PDT treatment protocol. Since it is expected that tissue absorption and scattering are affected by PDT itself, intrinsic fluorescence is the logical option to monitor photosensitizer concentration.

A rapidly emerging field in medical practice is fluorescence imaging, where fluorescent dyes are accumulated in tumor tissue and tumor resection is performed under excitation light to visualize the tumor and its margins. However, the superiority of intrinsic fluorescence over the simple detection of emitted fluorescence light is not yet recognized in this field. One could argue that for tumor visualization the latter is more than sufficient, however this reasoning is contradicted by the development of very sensitive fluorescent systems for exactly this purpose. Tumor resection takes place in a bloody environment that causes very large differences in optical properties, which will severely influence the detected fluorescence. Combining image guided surgery with point measurements of SFF provides a very useful concept where the bulk tumor is removed based on the fluorescence imaging, and the cavity from which the tumor is resected is analyzed for remaining tumor tissue, invisible due to absorption of blood, using SFF.

DETERMINING THE OPTIMAL DRUG-LIGHT INTERVAL FOR CHLORIN e_6 AND BREMACHLORIN PDT

In this thesis, the SFF method is applied preclinically to investigate two photosensitizers. The first, chlorin e_6 (ce6), has been under investigation for many years. The relatively high hydrophilicity of ce6 means that it is rapidly cleared and may not accumulate in tumor tissue. The second photosensitizer, Bremachlorin, is a solution that consists for 80% ce6. The remaining 20% is composed of purpurin 5 and chlorin p_6, both photosensitizing agents in themselves. Furthermore, these two substances are side products of ce6 synthesis. Therefore, less purification steps are necessary for Bremachlorin, which makes it commercially interesting. The behavior of both photosensitizers is compared in-vivo using intrinsic SFF measurements (**chapter 5**) and confocal microscopy (**chapter 6**) to analyze localization over different length scales. It can be concluded that there are subtle but significant spectral variations between the two photosensitizers in-vivo over 3 to 48

hour incubation times. Ce6 is almost completely metabolized and removed from the tissues after 24 hours. Bremachlorin is still present in significant quantities at 48 hours. The tumor-to-normal ratio of 2-3 for these late time points, is higher than for short incubation times and might be utilized for performing tumor selective PDT. However, it is questionable whether these tumor-to-normal ratios are sufficient to achieve this. The spectral variations observed between Bremachlorin and ce6 over time suggest a relocalization of the photosensitizer in a different environment. Ce6 behaves in a way similar to previously reported in-vitro [11, 12]. We have observed a red-shift of the fluorescence peak position accompanied by an increase in peak/shoulder ratio. According to Cunderlikova et al. [11] this indicates a shift to an environment with a higher pH. It is shown however, that peak shift with pH change is absent in solutions containing FCS. How this translates to an in-vivo situation remains to be determined. Bremachlorin shows the opposite effect; a blue-shift accompanied by a decrease in peak/shoulder ratio. This suggests that Bremachlorin relocates to a lower pH environment over time. When comparing these observations with our microscopic results, we do not see an obvious relocation during the first 6 hours of incubation. We again find Bremachlorin present after 24 and 48 hours, while ce6 has been almost completely removed from the tissue.

Microscopic analysis shows that although it is concluded, based on fiber optic measurements, that there is more photosensitizer present in tumor than in normal tissue, this is not actually the case at the microscopic level. Photosensitizer concentration in tumor tissue is relatively low, only at 24 and 48 hours is it higher than normal tissue for Bremachlorin. Rather it is the immediate tumor border that contains most photosensitizer. When performing fiber optic measurements, this border is, due to measurement geometry, included in measurements containing tumor tissue, incorrectly showing a high photosensitizer concentration in tumor tissue. This example shows that no matter what optical measurement method is used, the interpretation of the results will always be dependent on the sample volume of that particular method. Many fiber optic fluorescence devices require multiple fibers and are based on diffusion theory. This requires a large interrogation volume in the order of mm^3. For our superficial measurements of mouse tongue, the sample volume of SFF (around 200 µm in depth) is much more suitable. A diffuse reflectance measurement volume would include almost the whole thickness of the tongue. However, to determine photosensitizer localization on tissue level, SFF sample volume may still be too large. It is therefore important to choose a method that fits the volume of interest. Another option is to relinquish the non-invasive nature of SFF and insert an MDSFR/SFF probe into the tumor.

Intrinsic fluorescence measurements which can reveal spectral variations in-vivo over time are very useful in increasing our understanding of photosensitizer pharmacokinetics. Based on extensive knowledge of these pharmacokinetics, an informed decision on duration of the drug-light interval in PDT can be made.

PDT EFFECTS ON TISSUE AND VASCULATURE AFTER VARIOUS DRUG-LIGHT INTERVALS

Based on the pharmacokinetics of ce6 and Bremachlorin in-vivo in various tissues presented in **chapter 6**, we have designed a therapeutic study **(chapter 7)**. Ce6 PDT is performed with short drug-light intervals, varying from 4-6 hours [13]. Previous measurements show that this drug-light interval is well chosen because ce6 is hardly detectable after 24 hours. Similar measurements suggest that for Bremachlorin, a drug-light interval of 24 hours may be favorable, which shows a tumor-to-normal ratio of 2-3. Although the primary cellular targets of ce6-based photosensitizers are lysosomes, acute vascular effects during PDT are reported for these photosensitizers [14]. To be able to draw conclusions with respect to vascular effects, the vasculature is recorded during treatment and vessel leakage and stasis are analyzed two hours after illumination using confocal microscopy. PDT-related effects on tumor and normal tissue are assessed based on histology two days after illumination.

The results from **chapter 7** confirm the hypothesis which followed from the research performed in **chapter 5** and **chapter 6**: Bremachlorin PDT after a 24 hour drug-light interval does induce more (acute) vascular effects and cell damage than after a 5 hour drug-light interval. Confocal microscopy two hours after illumination proves that not only is vasoconstriction observed during illumination, but also that PDT induces stasis and vascular leakage in most of the animals treated with Bremachlorin and a 24 hour drug-light interval. Furthermore, the observation of acute vascular effects during illumination is, although not significant, related to histological characteristics of PDT-induced tissue damage. Unexpectedly we found that ce6 produces more damage to both normal and tumor tissue after 24 hour incubation than after 5 hours, when very little photosensitizer is measured with in-vivo spectroscopy and microscopic analysis. This underlines the hypothesis that PDT-related damage is not only dependent on the photosensitizer concentration present, but that there are other factors that influence PDT-related damage, such as subcellular localization and vascularization. Investigation and, if required, monitoring of those factors before and during PDT may aid in defining the most effective treatment protocol.

The conclusion that Bremachlorin-PDT is more effective after a 24 hours incubation time, is predicted based on intrinsic fluorescence measurements in-vivo, but does not correspond with current clinical practice of ce6-based photosensitizers.

Spectroscopy proves to be a useful tool in photosensitizer concentration and localization analysis. Vessel analysis during PDT by the use of (confocal) microscopy provides relevant insight in vascular PDT effects and can be related to PDT outcome. This shows that a thorough investigation of the PDT related parameters can aid in therapy optimization.

APPLICATION OF SPECTROSCOPIC METHODS TO OPTIMIZE AND MONITOR PDT

In this thesis, it is demonstrated how various spectroscopic methods can be applied to research on the optimization of photodynamic therapy. Tissue saturation and vessel diameters can be determined by single fiber reflectance and MDSFR, which provide useful information on the availability of oxygen. In this thesis, monitoring the vascular effects that occur during fractionated ALA-PDT has been facilitated using optical microscopy. At a later stage, when the importance of vascular effects is better understood, fiber optic spectroscopy could play a critical role in monitoring vascular effects during PDT.

Intrinsic fluorescence spectroscopy performed with SFF provides a quantitative measure of photosensitizer concentration. This is a powerful tool in preclinical research for the measurement of photosensitizer pharmacokinetics and in the optimization of the PDT treatment protocol. Knowledge of tissue scattering and absorption and their variation during treatment may be applied in order to compensate the delivered light dose in the treatment volume real-time. However, this technique is not yet ready to be implemented in a clinical application. A more realistic solution may be to adjust the illumination protocol before treatment based on patient-dependent optical properties.

An important factor to be considered in the application of fiber optic spectroscopic methods to monitor PDT is the interference with the PDT illumination field. Depending on the dimensions of the treatment area and the measurement probe, shielding of tissue from light may prove problematic. Therefore, most studies applying SFFL are based on pre- and post measurements only, or by shortly interrupting the therapeutic illumination to take a measurement. In large solid tumors treated with interstitial PDT, for example in the head & neck area, multiple catheters are implemented. It is common practice that illumination is performed in one or more catheters at the time, while the other catheters contain monitoring devices to measure changes in tissue during therapy [15]. Here, the change in the light field is relatively minor. For superficial tumors, an improvement can be made by the equipment of fluorescence imaging devices with the technology to detect tissue optical properties. Although this brings us some very interesting theoretical and technical challenges, the development of imaging devices capable of detecting intrinsic fluorescence will be a major step forward in fluorescence monitoring during PDT.

REFERENCES

1. Robinson, D.J., et al., *Topical 5 Aminolevulinic Acid photodynamic Therapy of Hairless Mouse Skin Using Two fold Illumination Schemes: PpIX Fluorescence Kinetics, Photobleaching and Biological Effect.* Photochemistry and photobiology, 2000. **72**(6): p. 794-802.
2. de Bruijn, H.S., et al., *Fractionated illumination after topical application of 5-aminolevulinic acid on normal skin of hairless mice: The influence of the dark interval.* Journal of Photochemistry & Photobiology, B: Biology, 2006. **85**(3): p. 184-190.
3. de vijlder, H.C., et al., *Light fractionation significantly improves the response of superficial basal cell carcinoma to ALA-PDT: five-year follow-up of a randomized, prospective trial.* Acta Dermatol Venereol, 2012. **92**: p. 641-647.
4. de Bruijn, H.t.S., et al., *Light fractionated ALA-PDT enhances therapeutic efficacy in vitro; the influence of PpIX concentration and illumination parameters.* Photochemical & Photobiological Sciences, 2013. **12**(2): p. 241-245.
5. Cottrell, W.J., et al., *Irradiance-dependent photobleaching and pain in 5-aminolevulinic acid-photodynamic therapy of superficial basal cell carcinomas.* Clinical cancer research, 2008. **14**(14): p. 4475-4483.
6. Rogers, J.D., I.R. Capolu, and V. Backman, *Nonscalar elastic light scattering from continuous random media in the Born approximation.* Optics Letters, 2009. **34**(12): p. 1891-1893.
7. Subramanian, H., et al., *Optical methodology for detecting histologically unapparent nanoscale consequences of genetic alterations in biological cells.* Proceedings of the National Academy of Sciences, 2008. **105**(51): p. 20118-20123.
8. Roy, H.K., et al., *Association between rectal optical signatures and colonic neoplasia: potential applications for screening.* Cancer research, 2009. **69**(10): p. 4476-4483.
9. Hoy, C.L., et al., *Use of a coherent fiber bundle for multi-diameter single fiber reflectance spectroscopy.* 2012. **3**(10): p. 2452-2464.
10. Hoy, C.L., et al., *Method for rapid multidiameter single-fiber reflectance and fluorescence spectroscopy through a fiber bundle.* Journal of biomedical optics, 2013. **18**(10): p. 107005-107005.
11. Cunderlíková, B., L. Gangeskar, and J. Moan, *Acid-base properties of chlorin e6: relation to cellular uptake.* Journal of Photochemistry and Photobiology B: Biology, 1999. **53**(1): p. 81-90.
12. Mojzisova, H., et al., *Cellular uptake and subcellular distribution of chlorin e6 as functions of pH and interactions with membranes and lipoproteins.* Biochimica et Biophysica Acta (BBA)-Biomembranes, 2007. **1768**(11): p. 2748-2756.
13. Chan, A.L., et al., *Pharmacokinetics and clinical effects of mono-L-aspartyl chlorin e6 (NPe6) photodynamic therapy in adult patients with primary or secondary cancer of the skin and mucosal surfaces.* Photodermatology, photoimmunology & photomedicine, 2005. **21**(2): p. 72-78.
14. McMahon, K.S., et al., *Effects of photodynamic therapy using mono-L-aspartyl chlorin e6 on vessel constriction, vessel leakage, and tumor response.* Cancer research, 1994. **54**(20): p. 5374-5379.
15. Karakullukcu, B., et al., *Clinical feasibility of monitoring mTHPC mediated photodynamic therapy by means of fluorescence differential path-length spectroscopy.* Journal of Biophotonics, 2011. **4**(10): p. 740-751.

chapter 9

Summary / Samenvatting

Dankwoord

Portfolio

About the Author

Floor van Leeuwen – van Zaane

SUMMARY

The aim of this thesis is to optimize photodynamic therapy (PDT) by the application of spectroscopic and microscopic techniques. Treatment efficacy of PDT is dependent on the interaction between light, oxygen and a photoactive agent, the photosensitizer. Only when these three components are present in a certain concentration or amount will tissue damage -the goal of PDT- occur in the treatment volume. However, the availability of all three components is dependent on various biological processes. In this thesis we apply various spectroscopic and microscopic methods to determine the optimal and most effective treatment protocol for performing PDT.

Chapter 2 and **Chapter 3** focus on the first light fraction in light fractionated ALA-PDT in mice. Previous studies show the timing and duration of this fraction to be critical for treatment efficacy.

Chapter 2 reports on in-vivo monitoring of photosensitizer fluorescence during ALA-PDT. Six treatment groups are investigated and the length of the first light fraction is dependent on photobleaching of photosensitizer. Fluence rates of 20 and 50 mW cm^{-2} and total fluences of 50 and 100 J cm^{-2} are considered, together with a single 50 mW cm^{-2}, 100 J cm^{-2} group and a variable fluence rate group. No significant differences in damage scores are observed between all fractionated illumination groups, while a single illumination induced significantly less damage. The finding that a lower fluence rate accompanied with a lower fluence did induce the same damage is very valuable for clinical PDT; a lower fluence rate is thought to cause less pain during therapy, and combined with a lower fluence the increase of treatment time is thought to be within practical limits.

In **Chapter 3,** vascular effects during the first light fraction of ALA-PDT by confocal microscopy are investigated. ALA-PDT is performed in a dorsal skinfold window chamber on the back of a mouse. Confocal microscopy is used to measure variations in vessel diameter and red blood cell velocity during the first 13 J of the treatment using fluence rates of 26, 65 and 130 mW cm^{-2}. For all fluence rates, vascular effects occur in at least one animal and set in quickly after the start of illumination. Only when a vessel is completely constricted does red blood cell velocity drop. Because the therapeutic effects of PDT are dependent on a fine balance between a need for oxygen during illumination and disruption of the vasculature, understanding acute vascular effects during ALA-PDT plays an important role in optimizing PDT using porphyrin pre-cursors.

The application of multi-diameter single fiber reflectance spectroscopy (MDSFR) in-vivo is described in **Chapter 4**. Using multiple fibers of various diameters allows for quantitative measurements of tissue scattering and the phase function parameter. Reflectance measurements are successfully performed with 0.4 and 0.8 mm fibers on mouse tongue, skin, liver and on oral squamous cell carcinoma induced in the tip of the tongue. The reduced scattering coefficient μ_s' and phase function parameter γ show significant differences between tissues.

In **Chapter 5** and **Chapter 6**, the focus is on application of fluorescence spectroscopy and microscopy to acquire knowledge on the pharmacokinetics of the photosensitizers chlorin e_6 and Bremachlorin.

Chapter 5 reports on the in-vivo application of single fiber fluorescence spectroscopy. We have investigated pharmacokinetics and spectral variation of both photosensitizers chlorin e_6 (ce6) and Bremachlorin in mouse tongue, skin, liver and oral squamous cell carcinoma for incubation times of t=[3 4.5 6 24 48] hours. With determination of quantitative scattering as described in chapter 4, it is possible to correct the detected fluorescence signal for tissue absorption and scattering, resulting in the intrinsic fluorescence. Between the two photosensitizers, significant differences in spectral shape, peak position and fluorescence intensity are observed. There is significantly more Bremachlorin present compared to ce6 at long incubation times. Insight in photosensitizer pharmacokinetics may aid in determining the optimal drug-light interval for PDT of a particular tissue.

A microscopic analysis of the localization of ce6 and Bremachlorin in tongue and tongue tumor is presented in **Chapter 6**, again after t=[3 4.5 6 24 and 48] hour incubation times. Photosensitizer fluorescence intensities are determined in frozen tissue slices, where we discriminate tumor, tumor boundary, invasive tissue and normal tissue. Highest photosensitizer concentrations are found in the tumor border, while concentration in the tumor itself is very low. For Bremachlorin, the photosensitizer concentration is higher in tumor than in normal tissue after 24 and 48 hours. In normal and invasive tissue, photosensitizer is mainly localized in muscle fibers, while after longer incubation times photosensitizer is spread more homogenously. There is no direct correlation between location of vasculature and photosensitizer for both ce6 and Bremachlorin.

In **Chapter 7** some of the analyses described in previous chapters are combined when performing PDT in mouse window chambers. Both ce6 and Bremachlorin are under investigation with 5 and 24 hour incubation times (chapter 5 and 6). Vascular effects occurring during PDT are analyzed (related to chapter 3) and related to hemorrhage,

disrupted vasculature, vascular leakage and stasis and histological characteristics of cell damage as indications of treatment efficacy. Bremachlorin PDT after 24 hour drug-light interval is most effective in inducing acute vascular effects, followed by ce6 with a 5 hour drug-light interval. Cellular tissue damage is, although not significant, related to the onset of acute vascular effects during illumination. The positive effect of PDT on tissue damage after a 24 hour drug-light interval with Bremachlorin was hypothesized based on research conducted in previous chapters, and the research in chapter 7 confirms this.

A general discussion on the results of the studies presented in this thesis is provided in **Chapter 8**. Results are discussed in relation to each other and on their contributions to the optimization of photodynamic therapy. It concludes with a brief insight in future technological perspectives.

SAMENVATTING

Het doel van dit proefschrift is het optimaliseren van fotodynamische therapie (PDT) door het gebruik van microscopische en spectroscopische technieken. Hoe effectief PDT is wordt bepaald door de interactie tussen licht, zuurstof en de fotosensitizer, een stof die wordt geactiveerd door licht. Uitsluitend wanneer deze drie componenten voldoende aanwezig zijn in het te behandelen gebied zal schade aan het weefsel optreden,het doel van PDT. Of de componenten ook in de juiste hoeveelheid aanwezig zijn is afhankelijk van verschillende biologische processen. In dit proefschrift gebruiken we verschillende spectroscopische en microscopische technieken om de optimale omstandigheden voor PDT te bepalen. De resultaten kunnen worden gebruikt in het opstellen van een zo effectief mogelijk behandelprotocol.

In **Hoofdstuk 2** en **Hoofdstuk 3** ligt de nadruk op de eerste belichting van ALA-PDT met een gefractioneerd belichtingsprotocol in muizen. Het is eerder aangetoond dat de timing en duur van de eerste belichting voor een groot deel de effectiviteit van PDT bepalen.

Hoofdstuk 2 beschrijft het in-vivo monitoren van de hoeveelheid fotosensitizer in het behandelvolume tijdens ALA-PDT. We onderzoeken zes behandelgroepen, waarbij de lengte van de eerste belichting wordt bepaald door de afname van de fotosensitizer fluorescentie. De behandelgroepen zijn verdeeld in een lichtintensiteit van 20 of 50 mW cm^{-2} en een totale lichtdosis van 50 of 100 J cm^{-2}, één groep met een enkele belichting van 50 mW cm^{-2} bij 100 J cm^{-2} en een groep met variabele lichtintensiteit. Tussen de verschillende groepen met gefractioneerde belichting is geen significant verschil in weefselschade waargenomen, terwijl een enkele belichting resulteert in minder schade.

Het feit dat belichting met een lagere lichtintensiteit en een lagere totale lichtdosis resulteert in gelijke weefselschade is goed nieuws voor de klinische toepassing van ALA-PDT bij huidaandoeningen. Een lagere lichtintensiteit wordt geassocieerd met minder pijn tijdens de behandeling, maar was niet praktisch toepasbaar door de significant langere behandeltijd. Nu blijkt dus dat met een lagere lichtdosis hetzelfde resultaat wordt bereikt met een minimale toename van behandeltijd ten opzichte van het huidige protocol.

In **Hoofdstuk 3** worden, met behulp van confocale microscopie, vaateffecten tijdens de eerste belichting van gefractioneerde ALA-PDT onderzocht. Voor dit onderzoek hebben muizen een kamertje op de rug waardoor de vaatstructuur in de huid in beeld gebracht kan worden met een microscoop tijdens PDT. Tijdens de belichting worden variaties in vaatdiameter en snelheid van rode bloedcellen gemeten tijdens de eerste 13 J van de behandeling met lichtintensiteiten van 26, 65 en 130 mW cm^{-2}. In alle groepen vaateffecten treden vaateffecten op bij een aantal muizen, vrij snel na het starten van de belichting. Als vaten compleet dichtklappen stoppen ook de rode bloedcellen met stromen, maar bij gedeeltelijke vaatversmalling is geen significante afname van de snelheid van rode bloedcellen te zien. Het effect van PDT wordt tweezijdig beïnvloed door vaateffecten in de zin dat de zuurstof – en dus intacte vasculatuur- nodig is voor PDT, maar schade aan de vaten ook schade aan de tumor oplevert. Het is daarom van belang de interactie tussen deze effecten te begrijpen en hiermee gefractioneerde ALA-PDT te optimaliseren.

De eerste in-vivo toepassing van *multi-diameter single fiber reflectie spectroscopie* (MDSFR) wordt beschreven in **Hoofdstuk 4**. Door het gebruik van meerdere fibers met een verschillende diameter kan op een kwantitatieve manier verstrooiing in weefsel gemeten worden. Deze metingen zijn uitgevoerd met fiber diameters van 0.4 en 0.8 mm op tong, tong tumor, huid en lever van muizen. De verstrooiings-coëfficiënt μ_s' en fase-functie parameter γ verschillen significant van elkaar voor de verschillende weefsels, waaruit geconcludeerd kan worden dat MDSFR gebruikt kan worden voor diagnostiek.

Hoofdstuk 5 en **Hoofdstuk 6** richten zich op fluorescentie spectroscopie en microscopie voor het onderzoeken van de verspreiding van de fotosensitizer in het weefsel over tijd (farmacokinetiek). Dit onderzoek omvat de fotosensitizers chlorine e_6 (ce6) en Bremachlorine.

In **Hoofdstuk 5** wordt het eerste gebruik van single fiber fluorescentie spectroscopie beschreven. Voor beide fotosensitizers zijn de intensiteit en de vorm van het fluorescentiespectrum onderzocht, waarbij gekeken is naar tong, tong tumor, huid en lever van een muis. De incubatietijd van de fotosensitizer is t = [3 4.5 6 24 48] uur. Met de

kwantificering van de weefselverstrooiingscoëfficiënt zoals beschreven in hoofdstuk 4 kan het gemeten fluorescentiesignaal worden gecorrigeerd voor absorptie en verstrooiing van het weefsel. Dit resulteert in de intrinsieke fluorescentie, een kwantitatieve maat voor fluorescentie. De twee fotosensitizers verschillen significant in vorm, intensiteit en positie van het fluorescentiespectrum. Er is significant meer Bremachlorine dan ce6 aanwezig in weefsel na lange incubatietijd. Inzicht in farmacokinetiek van de fotosensitizers is nodig om de optimale tijd tussen toediening van het medicijn en belichting te bepalen voor een specifiek weefsel.

De lokalisatie van ce6 en Bremachlorine na t = [3 4.5 6 24 48] uur is op microscopisch niveau onderzocht voor tong en tongtumor in **Hoofdstuk 6**. De fluorescentie van fotosensitizers is gemeten in vriescoupes van tongen, waarbij we tumor, tumorrand, invasief weefsel en normaal weefsel onderscheiden. De concentraties fotosensitizer is het hoogst in tumorrand, terwijl de concentratie in tumor relatief laag is. Pas na 24 en 48 uur is de concentratie Bremachlorine in tumor hoger dan in normaal weefsel. In normaal en invasief weefsel wordt de fotosensitizer vooral gevonden in spierweefsel, maar voor langere incubatietijden verdeelt het zich meer homogeen over het weefsel. Voor beide fotosensitizers lijkt er geen directe correlatie te bestaan tussen de lokalisatie van fotosensitizer en vasculatuur.

In **Hoofdstuk 7** worden een aantal analyses uit vorige hoofdstukken gebruikt tijdens PDT in het kamertjesmodel in muizen, waarin we een tumor hebben geïnduceerd. We onderzoeken ce6 en Bremachlorine voor een incubatietijd van 5 en 24 uur. Tijdens de belichting zijn acute vaateffecten geanalyseerd en deze zijn gerelateerd aan de volgende kenmerken van PDT-gerelateerde schade: bloedingen, onderbreking van vaten, vaatlekkage, stroomsnelheid van rode bloedcellen en histologische kenmerken van weefselschade. De meeste acute vaateffecten werden geïnduceerd door Bremachlorine na een incubatietijd van 24 uur, gevolgd door ce6 na 5 uur incubatie. Cellulaire weefselschade is gerelateerd aan het optreden van acute vaateffecten tijdens de belichting, al is dit resultaat niet significant. De hypothese van verhoogde effectiviteit van Bremachlorine-PDT na 24 uur incubatietijd was gebaseerd op onderzoek uit de vorige hoofdstukken, en het onderzoek van hoofdstuk 7 bevestigt dit vermoeden.

Dit proefschrift sluit af met een algemene discussie van de resultaten in **Hoofdstuk 8**. Zowel de samenhang tussen resultaten in verschillende hoofdstukken als de bijdrage aan het optimaliseren van fotodynamische therapie worden besproken. Tenslotte wordt er een korte blik geworpen op mogelijke nieuwe technologische ontwikkelingen.

DANKWOORD

Het dankwoord. Misschien wel het meest gelezen hoofdstuk van een proefschrift, de afsluiting. En zo voelt het ook, want verder is alles klaar. Met een bijna euforisch gevoel en een goed glas wijn kan ik nu reflecteren op de afgelopen ruim vijf jaar. Want er is veel gebeurd, en er is ook zeker zoveel niet gebeurd. Grootse plannen moesten bijgesteld worden, om uiteindelijk als eenzaam puntje op de publicatielijst te eindigen. Daartegenover staat dat resultaten van een klein experiment de grondslag kunnen vormen van een compleet proefschrift. Het resultaat heeft u hier in uw handen. Maar wat het uiteindelijke onderwerp van het onderzoek ook is, één ding staat vast: alleen had ik het niet kunnen volbrengen.

Allereerst wil ik Dick Sterenborg bedanken, als mijn promotor, maar vooral ook als de persoon die alles in een breder daglicht plaatst. Je laat je niet beperken door de (on)mogelijkheden binnen de medische technologie; tomaten en zelfs melk kunnen ook interessant zijn! De vele lunchdiscussies leidden vaker wel dan niet tot ideeën voor verrassende toepassingsgebieden van bekende natuurkundige verschijnselen.

Where Dick showed me how to broaden my scientific horizon, Dominic Robinson helped me to determine the exact direction of my research. Dom, I couldn't have found a better co-promotor if I tried. Your calm, determined confidence in a positive ending of my PhD was what kept me going on many occasions. You were always available for any questions I had, took time to review -and greatly improve- my writing and of course for the occasional Belgium Beer at a sidewalk café. Thank you for everything Dom, it is very much appreciated.

Ute, too bad you're not here to stand next to me, but I know you think of me anyway. Together we shared the though life of being a PhD student: driving along the US East coast, cycling across a tiny island in Sweden and even the crazy idea of playing roller derby together. You made the office a lot less quit in the beginning, and we kept that up through the years. You were a great roomie and colleague, and you are a great friend – albeit somewhat far away at the moment. Thanks for everything!

En dan de lange dagen in het lab, die zonder de geweldige steun van Riëtte en Lique niet mogelijk geweest zouden zijn. Allereerst vanwege jullie kennis en kunde – je denkt toch niet dat ik een muis oppak!? – en zeker niet onbelangrijk, doordat we de lange donkere uren wachten gezellig hebben volgekletst zonder dat we in slaap vielen. Ontzettend veel gelachen, maar serieus als dat nodig was. Jullie mogen ook trots zijn op het werk in dit

boekje, jullie hebben daarin een sleutelrol gespeeld! Riëtte, natuurlijk ook bedankt dat je mijn paranimf wil zijn.

Of course I'd like to thank all colleagues and ex-colleagues at the CODT. Arjen, you were my hero when it came to technical problems: calibration of setups, higher-level tissue optics and those bloody confidence intervals on fit parameters, you always got me out of the woods. Chad, Chris and Jan Bonne, you all helped me in some way to get to the point where I am now. And Sander, Threes, Jasper, Giju, Robert, Slavka, Manzoor, Zoë and Bastiaan, without you the office just wouldn't have been the same!

Verder wil ik ook mijn collega's van het LUMC bedanken voor de gezellige maar ook productieve samenwerking. Thomas, Pieter, Isabel, prof. Löwik, en natuurlijk de rest die aan het project mee heeft gewerkt, ontzettend bedankt.

Ook wil ik graag alle leden van mijn commissie bedanken.

Dan is het nu tijd voor de personen voor wie de wetenschappelijke inhoud van dit proefschrift ondergeschikt is aan dit dankwoord. Rianne, Leonie, Elsbeth, Aimee, Anna en Mariska, al weer 12 jaar geleden zijn we over het hele land uitgewaaid, maar de gezamenlijke middagen en etentjes blijven. Dat er nog maar veel vriendinnenmiddagen mogen volgen!

Kasper, mijn paranimf, je moet er maar durven staan. En dat doe je! Merel, ik ben de trotste tante die je kan bedenken. En de trotste zus!

Pap en Mam, jullie hebben me altijd mijn eigen weg laten gaan, en stonden daarbij vooraan om te helpen verhuizen. Jullie zijn nog net zo geïnteresseerd in en enthousiast over waar ik mee bezig ben als dag één op de universiteit, ook al kost uitleggen nu soms wat meer tijd. Zonder jullie onvoorwaardelijke steun en vertrouwen in een goede afloop, had ik hier niet gestaan. Jullie zijn de beste!

En lieve Bas, hier een hele alinea speciaal voor jou. Maar dat is te kort om op te noemen waarvoor ik je allemaal wil bedanken. Daarom hierbij de belangrijkste redenen: Bedankt dat je het woordje 'the' altijd weghaalt uit mijn teksten en dat je zulke mooie plaatjes hebt gemaakt. Bedankt ook dat je me toch maar weer door liet typen als jij al sliep. Maar vooral ook bedankt voor je troostende schouder en opbeurende woorden als ik het niet zag zitten. Voor de gezellige avonden en heerlijke vakanties waarin ik geen seconde aan werk dacht. En boven alles, bedankt dat je mijn ontzettend lieve man bent. Dit feestje heb jij net zo hard verdiend.

LIST OF PUBLICATIONS

PEER REVIEWED PUBLICATIONS

1. De Vijlder, H.C., H.S. de Bruijn, A. van der Ploeg – van den Heuvel, F. van Zaane, D. Schipper, T.L.M. ten Hagen, H.J.C.M. Sterenborg, E.R.M. de Haas, D.J. Robinson, *Acute Vascular Responses during Photodynamic Therapy using Topically Administered Porhpyrin Precursors*, Photochemical & Photobiological Sciences, 2014. **In press**

2. Gamm, U.A., F. van Leeuwen – van Zaane, S.C. Kanick, H.J.C.M. Sterenborg, D.J. Robinson, A. Amelink, *Fully quantitative intrinsic single fiber fluorescence spectroscopy*, Journal of Biomedical Optics, 2014. **In press**

3. Van Leeuwen – van Zaane, F., P.B.A.A. van Driel, U.A. Gamm, T.J.A. Snoeks, H.S. de Bruijn, A. van der Ploeg – van den Heuvel, H.J.C.M Sterenborg, C.W.G.M. Löwik, D.J. Robinson, *The Effect of the Drug-Light Interval on Chlorin e_6 Photodynamic Therapy on Oral Squamous Cell Carcinoma in Mice*, Photodiagnosis and Photodynamic Therapy, submitted December 2013

4. Van Leeuwen – van Zaane, F., H.S. de Bruijn, A. van der Ploeg – van den Heuvel, H.J.C.M. Sterenborg, A. Amelink, D.J. Robinson, *The Effect of Fluence Rate on Acute Response of Vessel Diameter and Red Blood Cell Velocity During Topial 5-ALA Photodynamic Therapy,* Photodiagnosis and Photodynamic Therapy, 2014. **In press**.

5. Van Leeuwen – van Zaane, F., P.B.A.A. van Driel, U.A. Gamm, T.J.A. Snoeks, H.S. de Bruijn, A. van der Ploeg – van den Heuvel, C.W.G.M. Löwik, H.J.C.M. Sterenborg, A. Amelink, D.J. Robinson, *Microscopic Analysis of the Localization of two Chlorin-based Photosensitizers in OSC19 Tumors in the Mouse Oral Cavity,* Lasers in Surgery and Medicine, 2014. Published online January 2014, DOI: 10.1002/lsm.22220

6. Van Leeuwen – van Zaane, F., U.A. Gamm, P.B.A.A. van Driel, T.J.A. Snoeks, H.S. de Bruijn, A. van der Ploeg – van den Heuvel, H.J.C.M Sterenborg, C.W.G.M. Löwik, A. Amelink, D.J. Robinson, *Intrinsic Photosensitizer Fluorescence Measured using Multi-Diameter Singel Fiber Spectroscopy In Vivo,* Journal of Biomedical Optics, 2014. **19**(1): 015010

7. Van Leeuwen – van Zaane, F., U.A. Gamm, P.B.A.A. van Driel, T.J.A. Snoeks, H.S. de Bruijn, A. van der Ploeg – van den Heuvel, I.M. Mol, C.W.G.M. Löwik, H.J.C.M. Sterenborg, A. Amelink, D.J. Robinson, *In Vivo Quantification of the Scattering Properties of Tissue using Multi-Diameter Single Fiber Reflectance Spectroscopy,* Biomedical Optics Express, 2013. **4**(5): p. 696-708

8. Van Zaane, F., D. Subbaiyan, A. van der Ploeg – van den Heuvel, H.S. de Bruijn, E. Margallo – Balbas, G. Pandraud, H.J.C.M. Sterenborg, P.J. French, D.J. Robinson, *A Telemetric Light Delivery System for Metronomic Photodynamic Therapy (mPDT).* Journal of Biophotonics, 2010. **3**(5-6): p. 347-355

9. Middelburg, T.A., F. van Zaane, H.S. de Bruijn, A. van der Ploeg – van den Heuvel, H.J.C.M. Sterenborg, H.A.M. Neumann, E.R.M. de Haas, D.J Robinson, *Fractionated Illumination at Low Fluence Rate Photodynamic Therapy in Mice*, Photochemistry & Photobiology, 2010. **86**(5): p. 1140-1146

CONFERENCE PROCEEDINGS AND PAPERS

1. Van Zaane, F., T.A. Middelburg, H.S. de Bruijn, A. van der Ploeg – van den Heuvel, E.R.M. de Haas, H.J.C.M. Sterenborg, H.A.M. Neumann, D.J. Robinson, *Correction of Fluorescence for Depth-Specific Optical and Vascular Properties using Reflectance and Differential Path-length Spectroscopy during PDT,* Proceedings of SPIE 7380 (2009): Photodynamic Therapy: Back to the Future, 73803Q

2. Amor Río, J., E. Margallo-Balbás, B. Song, G. Pandraud, D. Subbaiyan, F. van Zaane, D.J. Robinson, H. Zandbergen, P.J. French, *Microlamp for In Situ Tissue Spectroscopy for the Dosimetry of Photodynamic Therapy*, Proceedings of Eurocensors XXQV, 2010. Procedia Engineering, 2010. **5**: p. 323-326

PHD PORTFOLIO

Name student:	Floor van Leeuwen – van Zaane
Erasmus MC department:	Radiation Oncology
PhD period:	June 2008 - April 2014
Research school:	Postgraduate school Molecular Medicine
Promotor:	Prof. dr. H.J.C.M Sterenborg
Co-promotor:	Dr. D.J. Robinson

PHD TRAINING

Courses		*Year*
Valorisation workshop		2009
Basic and translational oncology		2009
Animal imaging workshop by AMIE		2010
Introduction to statistics by NIHES		2010
Biophotonics '11, summer school in Ven, Sweden		2011
Workshop on Photoshop and Illustrator		2011
Workshop on InDesign		2011
Seminars and research meetings		
Department research meetings	Oral presentations	2008-2013
MolMedDay 2010	Oral presentation	2010
MolMedDay 2011	Poster presentation	2011
Biophotonics '11, Ven, Sweden	Poster presentation	2011
Symposium Sound Light	Attendant	2011
Symposium Optical Imaging Center, Erasmus MC	Attendant	2012
International Conferences		
IPA, Seattle	Oral presentation	2009
IPA, Innsbrück	Oral + Poster	2011
Gordon Research Conference, Holderness NH, USA	Poster presentation	2012
Teaching		
Supervision of bachelor student in physics		2011-2012
Invited lecture Haagse Hogeschool		2011

ABOUT THE AUTHOR

Floor van Zaane was born on February 24th, 1984 in Zaandam, where she lived during her primary education and high school period. In 2002 she graduated from the gymnasium department of the Pascal College in Zaandam, following the 'Natuur & Techniek' program combined with courses in biology, management & organization and Latin. After graduation she decided to continue her education at the University of Twente, enrolling in the Bachelors program Biomedical Engineering. This program was finished successfully with a Bachelors thesis on determination of the D-loop in mitochondrial DNA using atomic force microscopy, at the Biophysical Engineering group at the University of Twente. In 2005 she continued with the Biomedical Engineering Masters program focusing on biomedical optics. This program included an internship at Perimed AB (Stockholm, Sweden) working for 10 weeks on optical transcutaneous oxygen measurements and laser-Doppler imaging of skin. The Masters program was completed in January 2008 with a thesis project performed at the Biophotonics group at Philips Research (Eindhoven, The Netherlands) working on the development of a fiber optic laser-Doppler flow velocimeter for intravenous application. In April 2008 Floor obtained a Bachelors degree in Health Care Engineering & Management with a thesis on digital pathology at the Philips Health Care Incubator.

After graduating, Floor started working on her PhD at the Erasmus medical Center (Rotterdam, The Netherlands) at the Center for Optical Diagnostics and Therapy under guidance of Prof. dr. Sterenborg. Although her research initially focussed on a telemetric brain implant for metronomic PDT, it moved slowly by steadily towards the development of new optical spectroscopy and imaging methodologies and their application for monitoring photodynamic therapy. The culmination of this work is presented in this thesis.

Floor is currently working at Quantib BV as assistant Quality Manager, The development and maintenance of the quality management system as required for medical devices is her responsibility, together with analysis of the clinical (radiology) workflow for the design of new products.